Oceanologia

Official Journal of the Polish Academy of Sciences: Institute of Oceanology and Committee on Maritime Research

This journal is supported by the Ministry of Science and Higher Education, Warsaw, Poland

Indexed in: ISI Journal Master List, Science Citation Index Expanded, Scopus, Current Contents, Zoological Record, Thomson Scientific SSCI, Aquatic Sciences and Fisheries Abstracts, DOAJ

IMPACT FACTOR ANNOUNCED FOR 2018 IN THE 'JOURNAL CITATION REPORTS' IS 1.988; 5-year IF is 2.112. CITESCORE ANNOUNCED FOR 2018 IS 2.16

Publisher
Elsevier Sp. z o.o.
22, Jana Pawła II Avenue
00-133 Warsaw, Poland

Associate Publisher
Chen Lin
c.lin@elsevier.com
+86-10-8520 8768

ISSN 0078-3234

Oceanologia (2019) 61, 401—411

Available online at www.sciencedirect.com

ScienceDirect

journal homepage: www.journals.elsevier.com/oceanologia/

ORIGINAL RESEARCH ARTICLE

Tide and mean sea level trend in the west coast of the Arabian Gulf from tide gauges and multi-missions satellite altimeter

Nada Abdulraheem Siddig *, **Abdullah Mohammed Al-Subhi, Mohammed Ali Alsaafani**

Department of Marine Physics, Faculty of Marine Sciences, King Abdulaziz University, Jeddah, Saudi Arabia

Received 17 December 2018; accepted 8 May 2019
Available online 24 May 2019

KEYWORDS
Sea level change;
Long term data;
Tidal constituents;
Residual mean sea level;
Arabian gulf costal region

Summary Hourly data of the relative sea level from seven stations on the west coast of the Arabian Gulf, for the period 1979—2008 have been analyzed. The harmonic constituents of tide show pure diurnal tide at Murjan Island, semidiurnal type at Mina Salman and mixed type with semidiurnal dominance at the remaining five stations. Based on Multi-Missions Satellite Altimetry data, the mean sea level trend estimate was about 2.8 ± 0.4 mm/year for global ocean and about 3.6 ± 0.4 mm/year for the Arabian Gulf. Among the seven tide gauge stations, the highest sea level trend is found at Mina Salman (3.4 ± 0.98 mm/year) that agrees with the local estimate from the Multi-Missions Satellite Altimetry data. The minimum trend is found at Jubail (1.6 ± 0.71 mm/year) and Ras Tanura (0.7 ± 0.31 mm/year). At Arrabiyah Island station, the sea level trend is about 2.4 ± 0.66 mm/year, which is obtained after removing the interruptions from a relatively longer duration (15 years) data. This is in agreement with other stations and the estimates from the altimetry. The tidal analysis and trend estimation for Jubail station (29 years) have been conducted for the first time. At Murjan Island, the decadal cycle is evident from the long sea level data, giving the current estimate of trend more reliability as compared with previous studies.

* Corresponding author at: Department of Marine Physics, Faculty of Marine Sciences, King Abdulaziz University, P. O. Box 80207 Jeddah 21589, Saudi Arabia. Tel.: +966 509226141.
E-mail address: nsiddique@stu.kau.edu.sa (N.A. Siddig).
Peer review under the responsibility of Institute of Oceanology of the Polish Academy of Sciences.

ELSEVIER Production and hosting by Elsevier

https://doi.org/10.1016/j.oceano.2019.05.003

1. Introduction

The Arabian Gulf (AG), a semi-enclosed marginal sea covers a total area of about 239 $\times$ 10^3 km^2 with an average depth of about 36 m (Emery, 1956). Coastal areas in the northwest and the west are shallow. The average length of the AG is 990 km (Fig. 1). The main water exchange between the AG and the Indian Ocean is through the Strait of Hormuz. The wind (Shamal) blowing from north and northwest in the AG, that blow through winter and summer, is characterized by strong wind speeds during winter due to high atmospheric pressure disturbances and by a relatively lower intensity during summer (Perrone, 1979). The wind speed at the coast reaches as high as 15 m s^{-1} (Reynolds, 1993). The annual evaporation over the AG is about 2 m/year (Ahmad and Sultan, 1991; Hastenrath and Lamb, 1979; Meshal and Hassan, 1986; Privett, 1959; Xue and Eltahir, 2015), while fresh water input by precipitation is ~0.15 m/year (Johns et al., 2003). The main source of freshwater (mostly in the northern end of the AG) was the Shatt Al Arab river and its convergence with the Euphrates, Tigris and Karun rivers. However, the discharge of rivers is very small compared to evaporation.

Tides in the AG are complex, and the major tide is varying in nature from being semidiurnal, diurnal, and mixed type (Reynolds, 1993). Semidiurnal tides have two amphidromical points in the north-west and south, while the diurnal tide has one amphidromical point in the center of the AG, near the Kingdom of Bahrain. It also shows that the primary constituents are M2, S2, K1, and O1 (Najafi, 1997). The tidal propagation in the AG basin is counterclockwise from the Iranian coast north to the Saudi Arabia coast south.

The sea level variations in the west and northwest coasts of the AG have been the focus of the researchers (e.g. Al-Subhi, 2010; Alothman et al., 2014; Khalilabadi and Dariush, 2013; Reynolds, 1993; Sharaf El Din, 1988; Sultan et al., 2000). Sultan et al. (2000) calculated the meteorological effects causing (up to 75%) the seasonal signals of mean sea level in the AG, out of which the atmospheric pressure is contributed by 62% and wind stress by 12%.

Since 1992, high-quality satellite altimeters (TOPEX/Poseidon, ERS-2, GFO, Jason-1, Envisat, Jason-2 and Jason-3) lead to accurate estimates of the sea-level rise in global measurements. Gornitz (1995) estimated the rate of sea-level changes from long-term records, which show 1–2 mm/year increase globally, while altimetry data (short-term) show the increase around 3 mm/year (Antonov et al., 2005; Bindoff et al., 2007). Church et al. (2008) found that the sea level records from both tide gauge data and satellite altimeter data show sea level rising by more than 3 mm/year. Sultan et al. (2000) found that the sea level trend at Ras Tanura during 1980 and 1994 is 1.70 mm/year. Alothman and Ayhan (2010) analyzed the sea levels in 13 stations in the northwestern coast of the AG and found a relative rise of about 1.96 mm/year by correcting the vertical land motion.

Figure 1 A map of the study area shows the name and location of the stations.

The subsequent study (Alothman et al., 2014) in the northwestern part of the AG found a trend of 2.20 mm/year when the vertical land motion trend was 1.50 mm/year.

Several studies describe the tidal constituents, with the four major tidal constituents (M2, S2, O1, and K1) that computes the amplitudes and phase (Kämpf and Sadrinasab, 2006; Lardner et al., 1982; Le-Provost, 1984; Najafi, 1997; Sultan et al., 1995; Thompson et al., 1994). John (1992) studied the tidal components from the current data and found that it changes from mixed with a dominant semidiurnal component at the northwestern region to mixed with a dominant diurnal component in the southwestern region. He also identified that the tides from the coast of Abu Ali Pier to Ras Tanura are semidiurnal type. Poul (2016) found similar results using tide gauge data for one year. Al-Mahdi et al. (2007) found that the tide in the eastern side of the AG is mixed with dominant semidiurnal component and the tidal range is over 2.50 m. Khalilabadi (2016) analyzed one-year tide gauge data at four locations along the south coast of Iran and concluded that the semidiurnal constituent was dominant in this region. Akbari et al. (2016) analyzed 8 tidal harmonic constituents (S2, M2, N2, K2, K1, P1, O1 and Q1) at 3 stations in the AG and found that the tide is generally mixed with a semidiurnal component, except near the amphidromic points. Sharaf El Din (1988) studied major harmonic constituents at 8 stations, including 6 ARAMCO tide gauges during 1980–1987 and found that the tide has diurnal and semidiurnal patterns with a dominant semidiurnal component. Al-Subhi (2010) carried out a tidal analysis for Juaymah during 2000 and 2005, and found that the tide is mixed with a dominant semidiurnal component. Table 1 summarizes the findings of all the above studies.

AG is an important area being an extension of the Indian Ocean across the Strait of Hormuz, with great economic importance (industry, commerce, and oil) and marine life.

The aim of this study is to investigate both tidal characteristics and sea level trend from seven stations on the west coast of the AG.

This is for the first time, a study incorporates records from seven tide gauge stations covering the west coast of the AG from 1979 to 2008 for analyzing tidal characteristics and linear trend together. Along with this, it is also utilizing all satellite altimetric data available from (1993–2018) for analysis of mean sea level trend.

2. Data and methods

The data used in this study include tide gauge data obtained from the Saudi Aramco Company for six stations along Saudi Arabian coast of the AG and Permanent Service for Mean Sea Level (PSMSL) data for the Kingdom of Bahrain region. The station names, coordinates and the data duration are listed in Table 2.

The satellite altimetry data (available from 1993 to 2018) were obtained from (NOAA) National Oceanic and Atmospheric Administration (https://www.star.nesdis.noaa.gov/sod/lsa/SeaLevelRise/LSA_SLR_timeseries.php).

The shortest recorded period in this study is 9 years for the Abu Ali Pier station and for the longest period recorded at Mina Salman – Ras Tanura and Jubail for 29 years.

Analysis of tide gauge data was conducted by employing World Tide MATLAB Software (WTWC) (Boon, 2004), which applies a selective least squares harmonic analysis to discriminate tidal component and prediction of tides and tidal currents, using up to 35 tidal components. It can analyze the sea level data and retain the residual sea level which is caused by forces other than the tide, which is mainly due to the meteorological forces.

By mathematical application to analysis the predict tidal, we obtain the equation

$$h(t) = h_0 + \sum_{j=1}^{m} f_j H_j \cos(\omega_j t + u_j - \kappa_j^*), \quad (1)$$

where t is the time in serial hours, $h(t)$ is a predicted water level at t, h_0 is the mean water level, f_j is a lunar node factor for the jth constituent, H_j is the mean amplitude for the jth constituent over 18.6-year lunar node cycle, ω_j is the frequency of the jth constituent, u_j is the nodal phase for the jth constituent, κ_j* is the phase of the jth constituent for the period origin is utilized (midnight beginning December 31, 1899) and m is a number of constituents.

For purely solar constituents, $f_j = 1$ and $u_j = 0$.

The amplitude (H_j) and phase (κ_j*) of the tidal constituent analysis by using the least squares method.

To identify the tidal type in each station, the form factor F (Defant, 1961) was estimated.

$$F = (K1 + O1/M2 + S2). \quad (2)$$

For $F < 0.25$ the tide is semidiurnal; for F between 0.25 and 1.5, the tide is mixed, mainly semidiurnal; for F between 1.5 and 3.0 the tide is mixed, mainly diurnal; and finally, for $F > 3.0$, the tide is diurnal.

Tide gauge (long-term) data were analyzed to acquire the monthly mean sea level elevations. As shown in Table 2, the period of the data varies from station to station; some stations have gaps of days or months. At Mina Salman, station

Table 1 The previous studies of the tidal constituents in the Arabian Gulf.

Study	Number of stations	Type of tide	Period of data
John (1992)	4	Diurnal and semidiurnal	1986–1987
Poul (2016)	31	Diurnal and semidiurnal	375 days
Al-Mahdi et al. (2007)	3	Semidiurnal	1993–1994
Khalilabadi (2016)	4 (3 inside the AG)	Semidiurnal	2009
Akbari et al. (2016)	9 (3 inside the AG)	Diurnal and semidiurnal	200 days
Sharaf El Din (1988)	6	Diurnal and semidiurnal	1980–1987
Al-Subhi (2010)	2	Semidiurnal	2000–2005

Table 2 The location of tide gauge stations in the western coast of the Arabian Gulf.

No.	Station	Longitude	Latitude	Period
1	Murjan Island	49.63°	28.45°	1986–2008
2	Arrabiyah Island	50.17°	27.77°	1985–2000
3	Abu Ali Pier	49.68°	27.31°	2000–2008
4	Jubail	49.91°	26.86°	1980–2008
5	Ras Tanura	50.16°	26.64°	1980–2008
6	Qurayyah Pier	50.11°	25.88°	1980–2000
7	Mina Salman	50.61°	26.20°	1979–2007

the data extend from 1979 to 2007 with seven-year gaps in 1981 and 1998–2003. The statistical mean of the residual sea level has been calculated to remove the seasonal effect. The monthly averaged residual sea level has been used to estimate the linear trend. Before fitting any linear model, the time series has been statistically tested for the significance of trend using the method of Mann–Kendall, which tests whether to reject the null hypothesis (H0, no trend) or accept the alternative hypothesis (Ha, if trend is present). Then the Least-Squares Line LSL method is used to fit the trend, which usually approximate the general patterns of the time series over its period (Crum, 1925; Hoshmand, 1997).

Fitting of linear trend through the Method of LSL is accomplished as follows:

The linear equation in general is

$$y = a + bx(i), \tag{3}$$

where a and b, can be expressed as follows:

$$a = \frac{y}{c}, \tag{4}$$

where c is the length of data,

$$x_m = \sum_{i=1}^{N} x_i - \tilde{x}. \tag{5}$$

The sum of square coefficient of the element x

$$X^2 = \sum_{i=1}^{N} x_{m(i)}^2. \tag{6}$$

Write the sum of y

$$y = \sum_{i=1}^{N} y_i. \tag{7}$$

We may rewrite these equations as

$$b = \frac{XY}{X^2}. \tag{8}$$

In order to estimate the value of the linear trend, Eqs. (4) and (8) are substituted in Eq. (3).

The standard error is calculated by dividing the standard deviation from the mean as

$$se = \frac{\sqrt{\frac{1}{N-1}\sum_{i=1}^{N}(x_i - x_m)^2}}{\sqrt{N}}. \tag{9}$$

We used XLSTAT software (http://www.xlstat.com/en/) for calculating the probability value (P-value), and hypothesis testing. The Mann–Kendall test was applied to assess the significance of mean sea level trend, as follows

$$S = \sum_{k=1}^{n-1} \sum_{j=k+1}^{n} sgn(X_j - X_k), \tag{10}$$

where the data collected over time = $X1$, $X2$, $X3$, …, Xn. $(X_j - X_k)$ is the difference between current values and all

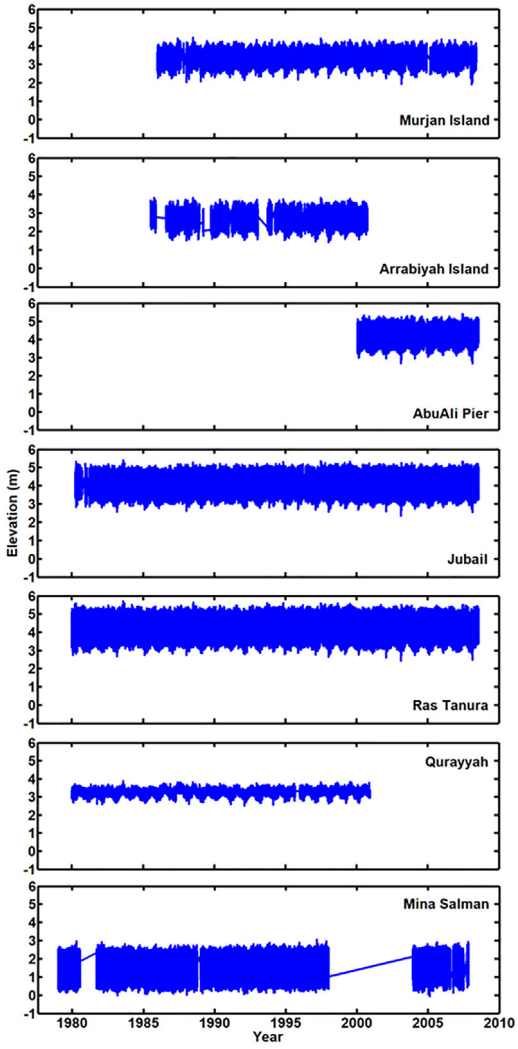

Figure 2 Time series of the tide gauge readings for seven stations.

Table 3 The highest astronomical tide (HAT) and lowest astronomical tide (LAT) elevation values for each station.

Station	HAT [m]	LAT [m]	Data recording time [day]
Murjan Island	0.56	−0.44	8187
Arrabiyah Island	0.92	−0.67	5556
Abu Ali Pier	0.88	−0.40	3110
Jubail	1.00	−1.01	10,074
Ras Tanura	1.13	−1.13	10,440
Qurayyah Pier	0.15	−0.19	7649
Mina Salman	1.02	−1.10	10,535

previous values, where $j > k$, that takes on the values of 1, 0, or −1.

Finally, the merged mean sea level from all the altimeters was analyzed to find the linear trend. The data filtered to approximately 10-days' time interval of $1^\circ \times 1^\circ$ grids with seasonal signals removed. The monthly mean sea level was calculated for both global data (66°S to 66°N) and for the AG region.

3. Results and discussion

Time series of the observed tide gauge data from all the stations are shown in Fig. 2. Over the study period, the tidal range (between HAT and LAT) is inconsistent from station to station. The highest range of about 2.00 m has been observed at Ras Tanura, Jubail and Mina Salman stations. The tidal range at Murjan Island is mostly about 1.00 m, while that at Arrabiyah Island is 1.60 m and at Abu Ali Pier is 1.27 m. The lowest tidal range is at Qurayyah Pier, which is about 0.34 m. Few stations, for instance, Abu Ali Pier, have discontinuities in data due to an error in recording or missing data from the source (Aramco). Mina Salman has discontinuity in the time series during 1998 and 2003.

Using the World Tides Package, the tidal and non-tidal components have been acquired for each time series. The Highest Astronomical Tide (HAT) and Lowest Astronomical Tide (LAT) in each station are shown in Table 3.

To estimate the tidal harmonic constituents, we selected uninterrupted one-year data for each station. However, the data for Arrabiyah in 1992 have a discontinuity of seven days in early February, which does not have an effect on the estimation of the tidal constituent.

4. The astronomical tides

The results of the harmonic analysis are listed in Table 4. The tidal type at each station is estimated by calculating the *F* ratio (see Eq. (2)). The major constituents M2 and K1 are determined as the most important semidiurnal and diurnal constituents. The results of the tidal harmonic constituents are plotted in Figs. 3–10.

Table 4 The amplitudes of the major tidal harmonic constituents in the west coast of Arabian Gulf; the constituents used for estimation of the form factor are bolded.

Stations	Amplitude of tide constituent								*F*-ratio	Type of tide
	Q1	O1	P1	K1	N2	M2	S2	K2		
Murjan Island	0.04	**0.21**	0.09	**0.32**	0.01	**0.05**	**0.03**	0.01	6.62	Diurnal
Arrabiyah Island	0.02	**0.14**	0.05	**0.19**	0.07	**0.34**	**0.13**	0.04	0.70	Mixed mainly semidiurnal
Abu Ali Pier	0.02	**0.13**	0.05	**0.16**	0.08	**0.41**	**0.14**	0.04	0.52	Mixed mainly semidiurnal
Jubail	0.02	**0.13**	0.05	**0.16**	0.10	**0.51**	**0.18**	0.06	0.42	Mixed mainly semidiurnal
Ras Tanura	0.02	**0.11**	0.04	**0.14**	0.12	**0.60**	**0.21**	0.07	0.30	Mixed mainly semidiurnal
Qurayyah Pier	0.002	**0.01**	0.01	**0.02**	0.01	**0.08**	**0.02**	0.01	0.30	Mixed mainly semidiurnal
Mina Salman	0.01	**0.07**	0.02	**0.11**	0.15	**0.68**	**0.22**	0.08	0.20	Semidiurnal

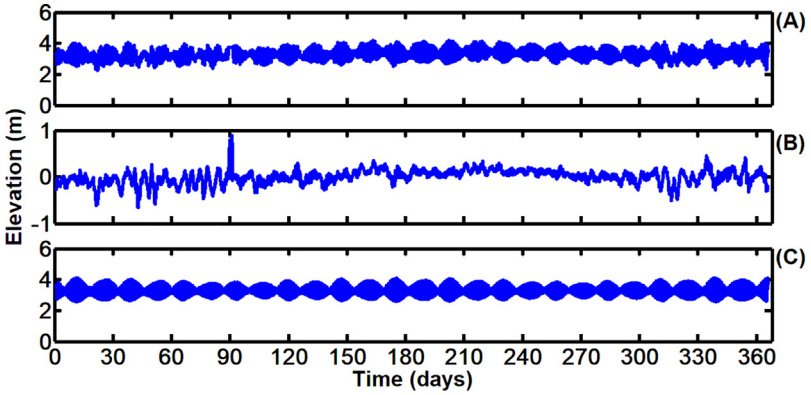

Figure 3 One-year time series of hourly tide gauge data (A), residual sea level (B) and the astronomical tide prediction at Murjan Island (C).

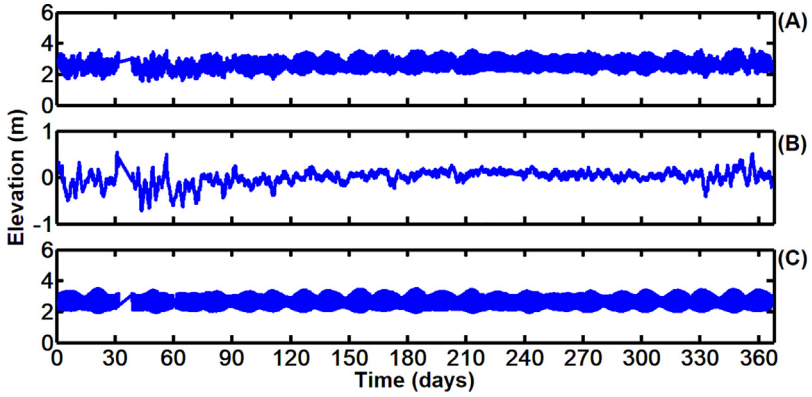

Figure 4 One-year time series of hourly tide gauge data (A), residual sea level (B) and the astronomical tide prediction at Arrabiyah Island station.

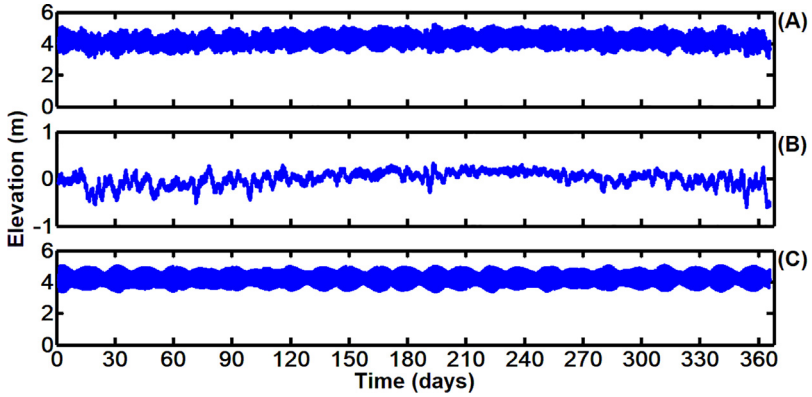

Figure 5 One-year time series of hourly tide gauge data (A), residual sea level (B) and the astronomical tide prediction at Abu Ali Pier station.

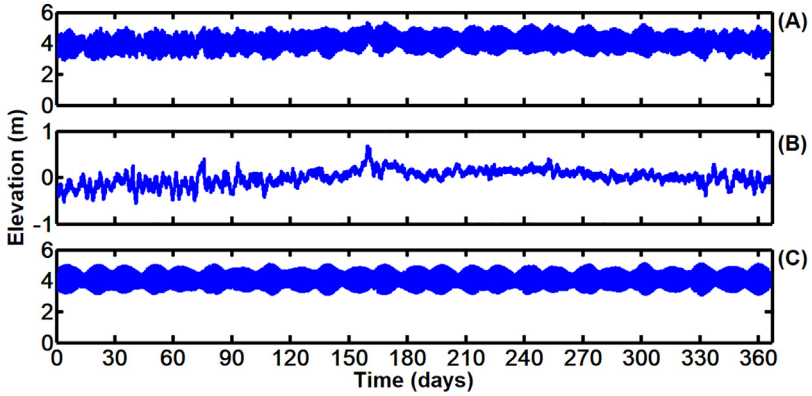

Figure 6 One-year time series of hourly tide gauge data (A), residual sea level (B) and the astronomical tide prediction at Jubail station.

Fig. 3 shows the time series of one-year raw tide gauge data, the residual sea level and the predicted astronomical tide at Murjan Island. The astronomical tide is dominant in the sea level variability with a range of ~1.00 m. Out of the eight major tidal constituents S2, M2, N2, K2, K1, P1, O1 and Q1, the amplitudes of diurnal constituents K1 and O1 show clear dominance (Fig. 10). It is also evident in the F-ratio ($F \approx 6.62$). At Arrabiyah, the tidal range is 1.60 m (Fig. 4) and the tide is mixed semidiurnal with clear dominance of semidiurnal component M2 (Fig. 10), where the F-ratio is ≈0.7. The tidal range at Abu Ali Pier is 1.27 m (Fig. 5). Here, the tide is mixed semidiurnal and the semidiurnal component M2 shows the highest amplitudes compared to the other tidal components (Fig. 10) with an F-ratio of ≈0.52. Previous studies also reported mixed semidiurnal tide in this station (John, 1992) and near the station (Najafi, 1997; Pous et al., 2012).

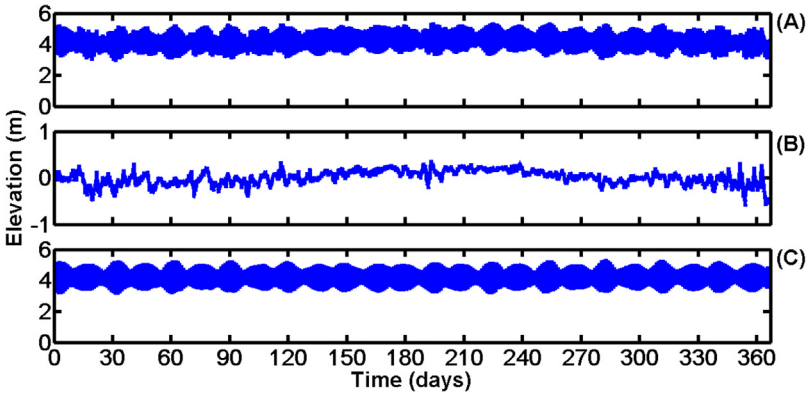

Figure 7 One-year time series of hourly tide gauge data (A), residual sea level (B) and the astronomical tide prediction at Ras Tanura station.

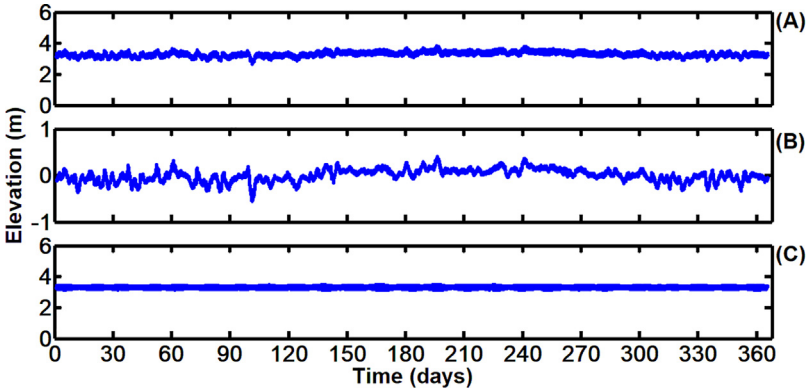

Figure 8 One-year time series of hourly tide gauge data (A), residual sea level (B) and the astronomical tide prediction at Qurayyah Pier station.

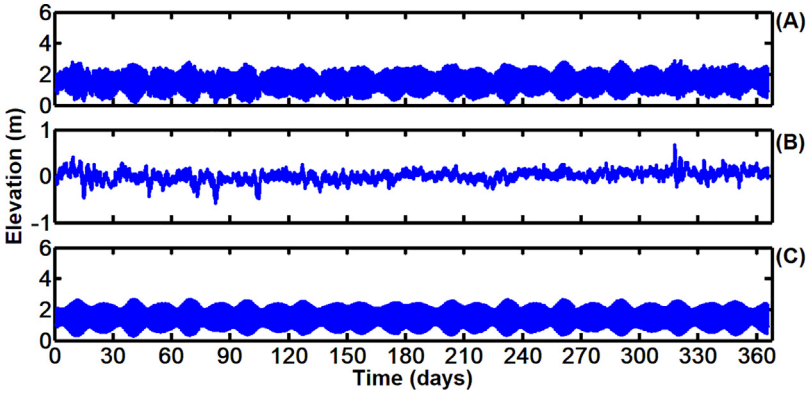

Figure 9 One-year time series of hourly tide gauge data (A), residual sea level (B) and the astronomical tide prediction at Mina Salman station.

The tidal range at Jubail is one among the highest in the AG, which is about 2.00 m (Fig. 6). The tide is mixed semidiurnal with the clear dominance of semidiurnal component M2, where the *F*-ratio is ≈0.42. This is consistent with other studies conducted in stations close to Jubail (Al-Subhi, 2010; John, 1992; Najafi, 1997; Pous et al., 2012). The maximum tidal range reported in this study is at Ras Tanura station, which is about 2.26 m (Fig. 7). Here, the semidiurnal constituents are dominant, with the clear dominance of M2 over the other major tidal components (Fig. 10). Hence, this is also of mixed semidiurnal (dominant) and the *F* ratio is ≈0.3. Several studies have been conducted to study the tide in this region, due to the economic importance of the area (John, 1992; Pous et al., 2012; Sultan et al., 1995).

The lowest tidal range is observed at Qurayyah Pier, which is around 0.34 m (Fig. 8). The tidal analysis shows that the highest amplitude among the 8 major tidal components was M_2 (Fig. 10). This station shows the same value of the F-ratio as that of Ras Tanura with mixed mainly semidiurnal, even though the two stations represent the two extreme ranges among all stations. Najafi (1997) results showed mixed semidiurnal tides at this station. The seventh station is Mina Salman with tidal range among the highest in the AG with 2.12 m (Fig. 9). The semidiurnal constituents M2 and S2 are dominant with highest amplitudes among the 8 major tidal components (Fig. 10). This station is the only station with semidiurnal tide with $F \approx 0.2$ which shows a similar tidal type to that reported by Sharaf El Din (1988) and El-Sabh and Murty (1988).

In general, the tide at Murjan Island is dominated by diurnal components, since this station is close to the semidiurnal amphidromic points in the northern AG. Similarly, the Mina Salman station is near to the diurnal amphidromic points, and hence the tide is dominated by semidiurnal constituents. The remaining five stations show the mixed tidal type. There are no previous studies available on tide analysis at Murjan Island, Arrabiyah Island and Jubail stations. Thus the results obtained in this study will significantly contribute to the scientific knowledge of the region.

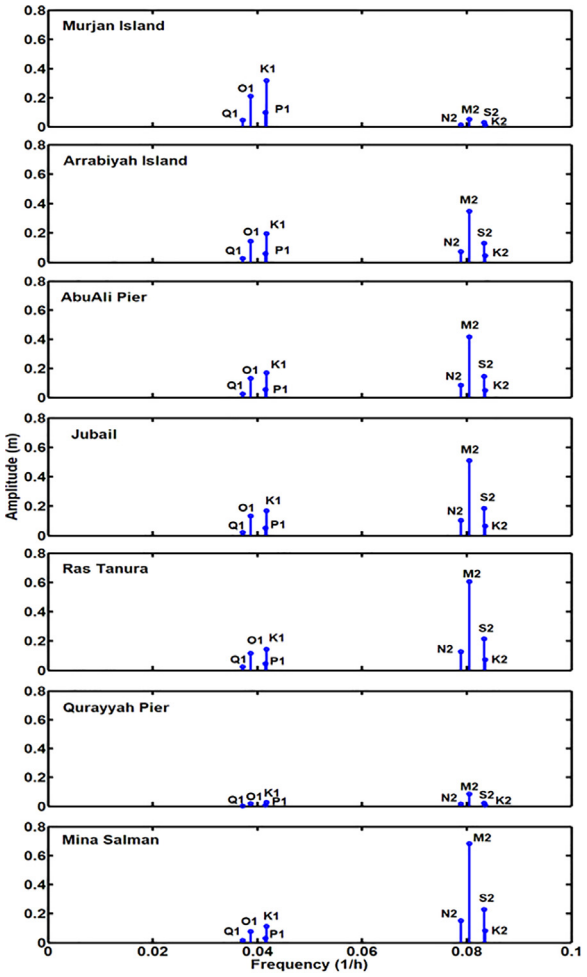

Figure 10 Tidal amplitudes of the major 8 constituents for all the stations.

5. Trend analysis

The monthly averaged residual sea level was used to estimate the linear trend. The sea levels from all the tide stations and those estimated from satellites show significant positive trends with P-value < 0.05, except at Mina Salman and Arrabiyah Island. The inconsistencies in these two stations are due to large data gaps in the time series. Mina Salman has discontinuity in data string from the available source about six years as shown in Fig. 2 (panel 7). However, the trend analysis for the uninterrupted period (1982–1997) show

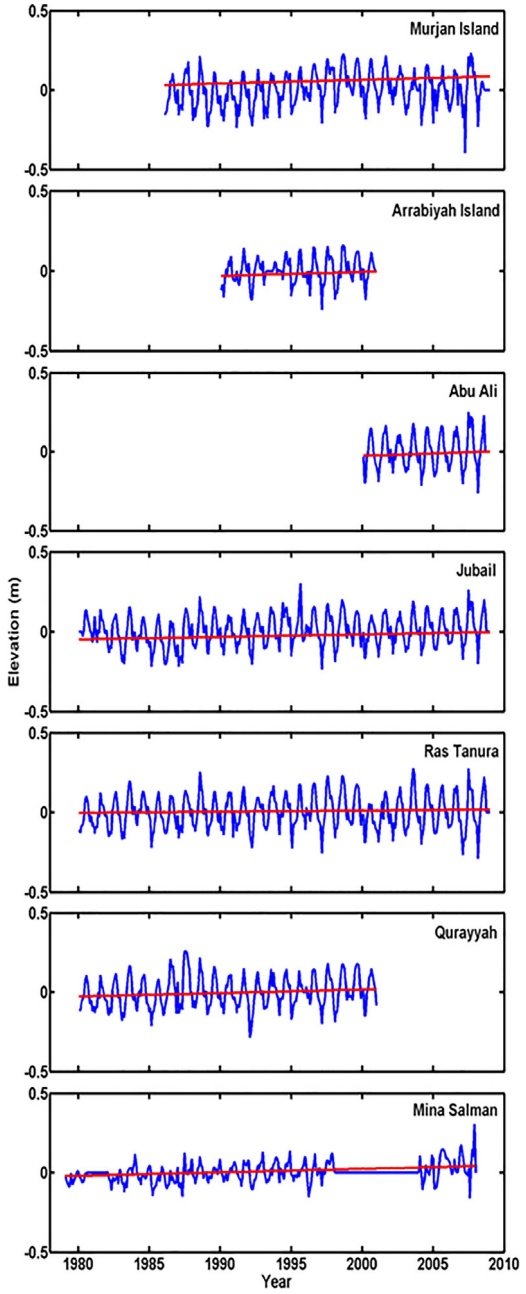

Figure 11 Estimated linear trend for TG stations.

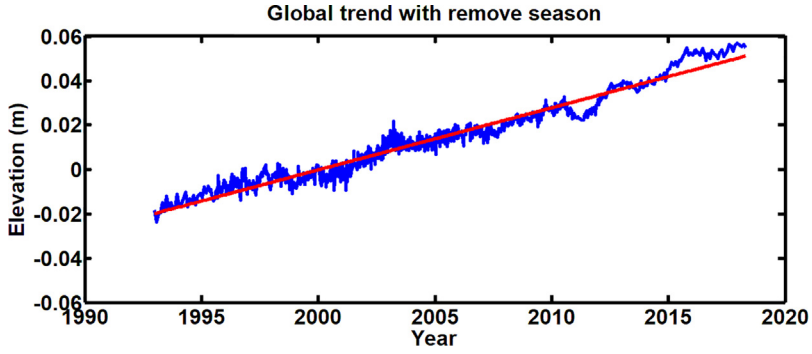

Figure 12 Global oceans mean sea level trend 2.8 mm/year, from multi-mission satellite altimetry.

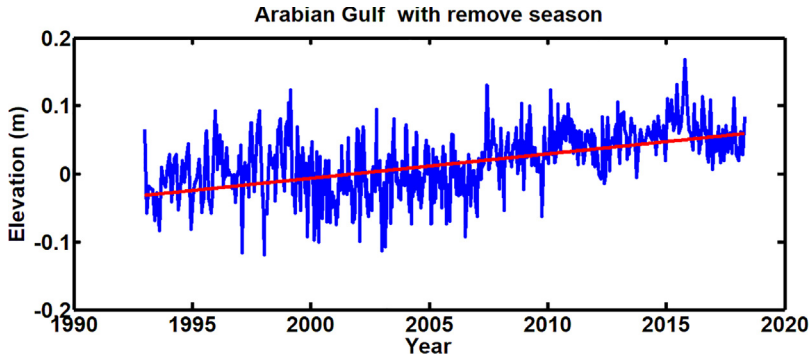

Figure 13 Arabian Gulf mean sea level trend 3.6 mm/year, from multi-mission satellite altimetry.

Table 5 Estimated mean sea level trend rates for the northwestern Arabian Gulf area as compared with the previous estimates.

Stations	The present study			Hosseinibalam et al. (2007)		Alothman and Ayhan (2010)		Alothman et al. (2014)	
	Estimated trend [mm/year]	*P*-value	Period	Estimated trend [mm/year]	Period	Estimated trend [mm/year]	Period	Estimated trend [mm/year]	Period
Murjan Island	2.4 ± 0.94	0.0001	1986–2008	9.75 ± 0.15	1990–2000	9.37 ± 2.02	1986–2001	7.05 ± 1.17	1986–2001
Arrabiyah Island	2.4 ± 0.66	0.032	1990–2000			−4.15 ± 3.52	1985–1998	−0.33 ± 0.18	1985–1998
Abu Ali Pier	3.1 ± 0.70	0.000	2000–2008	4.5 ± 0.04	1990–2000	1.74 ± 1.14	1980–2001	1.18 ± 0.63	1980–2001
Jubail	1.6 ± 0.71	0.002	1980–2008						
Ras Tanura	0.7 ± 0.31	0.015	1980–2008	0.84 ± 0.03	1990–2000	1.85 ± 1.05	1980–2001	0.74 ± 1.11	1980–2001
Qurayyah Pier	2.2 ± 0.84	0.001	1980–2000			3.29 ± 1.35	1980–1998	2 ± 0.99	1980–1998
Mina Salman	3.4 ± 0.98	0.0001	1979–2007			3.22 ± 0.58	1979–2007	2.97 ± 0.51	1979–2007

significant trend with *P*-value = 0.0001. Similarly at Arrabiyah Island, after removing the periods with severe gaps, the trend analysis (during 1990–2000) shows significant positive trend. Fig. 11 shows the monthly sea level with fitted trend at all the stations. The highest trend is seen at Mina Salman and Abu Ali Pier stations (3.4 ± 0.98 and 3.1 ± 0.7 mm/year, respectively). The lowest trend is found in Jubail (1.6 ± 0.71 mm/year) and Ras Tanura (0.7 ± 0.31 mm/year), while the trend at the remaining stations are as follows: at Murjan Island 2.4 ± 0.94 mm/year, Qurayyah Pier 2.2 ± 0.84 mm/year and at Arrabiyah Island 2.4 ± 0.66 mm/year. The monthly average of the Multi-Missions Satellite Altimetry data from 1993 to 2018 has been used to estimate the linear trend for global oceans and the AG. The estimated trends are 2.8 ± 0.4 mm/year (Fig. 12) and about 3.6 ± 0.4 mm/year (Fig. 13) respectively. They are significant with *P*-value = 0.0001. Table 5 lists all the trends estimated in this study as well as in the previous studies for an inter-comparison of values, however, the data duration may vary among the studies.

Even though, the estimated trend at Murjan Island station is in a good agreement with that of other stations in the AG, it

is much less than the previous estimates (Alothman and Ayhan, 2010; Alothman et al., 2014; Hosseinibalam et al., 2007). The main reason for the inconsistency is the shorter duration in the previous studies (11–15 years). There are clear decadal signals in our estimates with 23 years of data (Fig. 11). We re-estimated the trends in same periods of the previous studies and the results show similar high values, which confirms the influence of decadal cycle in the analysis (figure not shown). At Abu Ali Pier, the estimated trend is 3.1 mm/year, which is lower than the estimate by Hosseinibalam et al. (2007) and higher than the estimated by Alothman and Ayhan (2010) and Alothman et al. (2014) (Table 5). At Qurayyah Pier, the estimated trend is similar to that of Alothman et al. (2014), while that at Ras Tanura agrees with the estimates of both Hosseinibalam et al. (2007) and Alothman et al. (2014). At Mina Salman, the estimated trend agrees with that estimated by Alothman and Ayhan (2010) and Alothman et al. (2014). At Arrabiyah Island, the estimated trend show contradictory results compared to previous studies; they found a decreasing trend (Alothman and Ayhan, 2010; Alothman et al., 2014). Alothman et al. (2014) related that decrease to human activities in that area and the existence of oil platforms near the station. We find that the data gaps in our records significantly affect the estimated trends. A rough estimate by incorporating the previous trends at the time of data gaps leads to a decreasing trend in this region. In the present study that period is excluded and only the data of minimal discontinuity is used (1990–2000) in the trend estimation. The mean trend value for all the stations is ≈2.3 mm/year in the AG.

6. Conclusion

In this paper, seven tide gauge stations on the west coast of the AG have been analyzed. The observed tide data show a pure diurnal tide at Murjan Island, semidiurnal at Mina Salman and a mixed type of tide with semidiurnal dominance at Arrabiyah Island, Abu Ali Pier, Jubail, Ras Tanura and Qurayyah Pier station. The highest tidal range is recorded at Ras Tanura with 2.26 m and the minimum tidal range is seen at southern coastal station (Qurayyah Pier) with 0.34 m (Table 3).

The linear trend has been estimated using monthly mean residual sea level for all stations. The highest trend values is at Mina Salman about 3.4 ± 0.98 mm/year and Abu Ali Pier about 3.1 ± 0.7 mm/year. At Arrabiyah Island and Murjan Island station the trend is about 2.4 ± 0.66 mm/year and 2.4 ± 0.94 mm/year, respectively. The trend estimate for Qurayyah Pier station is almost similar, with an estimate of 2.2 ± 0.84 mm/year. Lower trends have been estimated at Jubail and Ras Tanura stations with about 1.6 ± 0.71 mm/year and 0.7 ± 0.31 mm/year respectively. The average linear trend for all seven stations is about 2.3 mm/year.

The trend for global oceans based on satellite data for the period from 1993 to 2018 was estimated as 2.8 + 0.4 mm/year, while trend in the AG is about 3. 6 ± 0.4 mm/year.

The present study shows the tidal analysis and trend estimates for Jubail station from 29 years (1980–2008) for the first time. Similarly, at Arrabiyah Island the present study shows positive trend, which agrees with all other stations, while all previous studies show negative trend at the same station. The main reason for the negative trends in the previous studies was due to inclusion of high variability data (the period from 1985 to 1989) having lots of gaps. At Murjan Island, the longer duration data (23 years) produced good trend estimates, which agrees with that of the other stations. The previous studies show very high trend at this station, which is mainly due to shorter data record they analyzed.

Acknowledgments

N.A. Siddig would like to thank ARAMCO for providing the data. Also, Recognitions are due to Permanent Service for Mean Sea Level (PSMSL) data, available at URL: http://www.psmsl.org/data/obtaining/map.html, and (NOAA) National Oceanic and Atmospheric Administration data, available at URL: https://www.star.nesdis.noaa.gov/sod/lsa/SeaLevelRise/LSA_SLR_maps.php.

References

Ahmad, F., Sultan, S.A.R., 1991. Annual mean surface heat fluxes in the Arabian Gulf and the net heat transport through the Strait of Hormuz. Atmos. Ocean 29 (1), 54–61, http://dx.doi.org/10.1080/07055900.1991.9649392.

Akbari, P., Sadrinasab, M., Chegini, V., Siadatmousavi, M., 2016. Tidal constituents in the Persian Gulf, Gulf of Oman and Arabian Sea: a numerical study. Indian J. Geo-Mar. Sci. 45 (8), 1010–1016.

Al-Mahdi, A., Abdullah, S.S., Hussian, N.A., 2007. Some features of the physical oceanography in Iraqi marine waters. Mesopot. J. Mar. Sci. 22 (2), 209–222.

Al-Subhi, A.M., 2010. Tide and sea level characteristics at Juaymah, west coast of the Arabian Gulf. JKAU: Mar. Sci. 21 (1), 133–149, http://dx.doi.org/10.4197/Mar.21-1.8.

Alothman, A.O., Ayhan, M.E., 2010. Detection of sea level rise within the Arabian Gulf using space based GNSS measurements and insitu tide gauge data: preliminary results. In: 38th COSPAR Scientific Assembly, Bremen, p. 3.

Alothman, A.O., Bos, M.S., Fernandes, R.M.S., Ayhan, M.E., 2014. Sea level rise in the north-western part of the Arabian Gulf. J. Geodyn. 81, 105–110, http://dx.doi.org/10.1016/j.jog.2014.09.002.

Antonov, J.I., Levitus, S., Boyer, T.P., 2005. Thermosteric sea level rise, 1955–2003. Geophys. Res. Lett. 32 (12), 1–4, http://dx.doi.org/10.1029/2005GL023112.

Bindoff, N.L., Willebrand, J., Artale, V., Cazenave, A., Gregory, J.M., Gulev, S., Hanawa, K., Le Quéré, C., Levitus, S., Nojiri, Y., Shum, C.K., Talley, L.D., Unnikrishnan, A.S., 2007. Observations: oceanic climate change and sea level. In: Solomon, S., Qin, D., Manning, M., Chen, Z., Marquis, M., Averyt, K., Tignor, M.M.B., Miller, Jr., H.L., Chen, Z. (Eds.), Climate Change 2007: The Physical Science Basis: Contribution of Working Group I to the Fourth Assessment Report of the Intergovernmental Panel on Climate Change. Cambridge Univ. Press., Cambridge, 996 pp.

Boon, J., 2004. Secrets of the Tide: Tide and Tidal Current Analysis and Applications, Storm Surges and Sea Level Trends. Horwood Publ., Chichester, UK, 224 pp., http://dx.doi.org/10.1016/C2013-0-18114-7.

Church, J.A., White, N.J., Aarup, T., Wilson, W.S., Philip, L., Domingues, C.M., Hunter, J.R., Lambeck, K., 2008. Understanding global sea levels: past, present and future. Sustain. Sci. 3 (1), 9–22, http://dx.doi.org/10.1007/s11625-008-0042-4.

Crum, W.L., 1925. The least squares criterion for trend lines. J. Am. Stat. Assoc. 20 (150), 211–222, http://dx.doi.org/10.1080/01621459.1925.10502142.

Defant, A., 1961. Physical Oceanography, vol. 1. Pergamon Press, London, 729 pp., http://dx.doi.org/10.1017/S0025315400070089.

El-Sabh, M.I., Murty, T.S., 1988. Simulation of the movement and dispersion of oil slicks in the Arabian Gulf. Nat. Hazards 1 (2), 197—219, http://dx.doi.org/10.1007/BF00126615.

Emery, K.O., 1956. Sediments and water of Persian Gulf. Am. Assoc. Pet. Geol. Bull. 40 (10), 2354—2383.

Gornitz, V., 1995. Monitoring sea level changes. Clim. Change 31 (2—4), 515—544, http://dx.doi.org/10.1007/BF01095160.

Hastenrath, S., Lamb, P.J., 1979. Climatic Atlas of the Indian Ocean. Part II: The Oceanic Heat Budget. University of Wisconsin Press, Madison, Wisconsin, 119 pp.

Hoshmand, R., 1997. Statistical Methods for Environmental and Agricultural Sciences. CRC Press, New York, 464 pp.

Hosseinibalam, F., Hassanzadeh, S., Kiasatpour, A., 2007. Interannual variability and seasonal contribution of thermal expansion to sea level in the Persian Gulf. Deep Sea Res. Oceanogr. Res. Paper. 54 (9), 1474—1485, http://dx.doi.org/10.1016/J.DSR.2007.05.005.

John, V.C., 1992. Harmonic tidal current constituents of the western Arabian Gulf from moored current measurements. Coastal Eng. J. 17 (1—2), 145—151, http://dx.doi.org/10.1016/0378-3839(92)90016-N.

Johns, W.E., Yao, F., Olson, D.B., Josey, S.A., Grist, J.P., Smeed, D. A., 2003. Observations of seasonal exchange through the Straits of Hormuz and the inferred heat and freshwater budgets of the Persian Gulf. J. Geophys. Res. 108 (12), 12—21, http://dx.doi.org/10.1029/2003JC001881.

Kämpf, J., Sadrinasab, M., 2006. The circulation of the Persian Gulf: a numerical study. Ocean Sci. 2 (1), 27—41, http://dx.doi.org/10.5194/os-2-27-2006.

Khalilabadi, M.R., 2016. Tide—surge interaction in the Persian Gulf, Strait of Hormuz and the Gulf of Oman. J. Weather 71 (10), 256—261, http://dx.doi.org/10.1002/wea.2773.

Khalilabadi, M.R., Dariush, M., 2013. Effect of super cyclone "GONU" on sea level variation along Iranian coastlines. Indian J. Geo-Mar. Sci. 42 (4), 470—475.

Lardner, R.W., Belen, M.S., Cekirge, H.M., 1982. Finite difference model for tidal flows in the Arabian Gulf. Comput. Math. Appl. 8 (6), 425—444, http://dx.doi.org/10.1016/0898-1221(82)90018-9.

Le-Provost, C., 1984. Models for tides in the KAP region. Oceanographic modelling of the Kuwait Action Plan (KAP) region. UNESCO Rep. Mar. Sci. 28, 25—36.

Meshal, A.H., Hassan, H.M., 1986. Evaporation from the coastal water of the central part of the Gulf. Arabian Gulf Sci. Res. 4 (2), 649—655.

Najafi, H.S., 1997. Modelling tides in the Persian Gulf using dynamic nesting. Ph.D. thesis. Univ. Adelaide, South Australia, 145 pp.

Perrone, T.J., 1979. Winter shamal in the Persian Gulf. Tech. Rep., Naval Environ. Predict. Res. Facil., Monterey, Calif., 79—106.

Poul, H.M., 2016. Modelling tidal processes in the Persian Gulf: with a view on renewable energy. Ph.D. dissertation. Univ. Hamburg, Germany, 115 pp.

Pous, S., Carton, X., Pascal, L., 2012. A process study of the tidal circulation in the Persian Gulf. Open J. Mar. Sci. 2 (4), 131—140, http://dx.doi.org/10.4236/ojms.2012.24016.

Privett, D.W., 1959. Monthly charts of evaporation from the N. Indian Ocean (including the Red Sea and the Persian Gulf). Q. J. R. Meteorolog. Soc. 85 (366), 424—428, http://dx.doi.org/10.1002/qj.49708536614.

Reynolds, R.M., 1993. Physical oceanography of the Gulf, Strait of Hormuz, and the Gulf of Oman—Results from the *Mt Mitchell* expedition. Mar. Pollut. Bull. 27, 35—59, http://dx.doi.org/10.1016/0025-326X(93)90007-7.

Sharaf El Din, S.H., 1988. Sea Level Variation along the Saudi Coast of the Arabian Gulf and their Relation to Meteorological Parameters. Special Report 1409 H. King Fahad Naval Academy, Jubail, Saudi Arabia, 101 pp.

Sultan, S.A.R., Ahmad, F., Elghribi, N.M., Al-Subhi, A.M., 1995. An analysis of Arabian Gulf monthly mean sea level. Cont. Shelf Res. 15 (11—12), 1471—1482, http://dx.doi.org/10.1016/0278-4343(94)00081-W.

Sultan, S.A.R., Moamar, M.O., El-Ghribi, N.M., Williams, R., 2000. Sea level changes along the Saudi coast of the Arabian Gulf. Indian J. Geo-Mar. Sci. 29 (3), 191—200.

Thompson, E.F., Demirbilek, Z., Hadley, L.L., Rivers, P., Huff, K.E., 1994. Water Level and Current Simulation for LOTS Operations — Persian Gulf and Gulf of Oman. Miscellaneous Report CERC-94-XX. U.S. Army Engineer Waterways Experiment Station, Vicksburg, MS, 52 pp.

Xue, P., Eltahir, E.A.B., 2015. Estimation of the heat and water budgets of the Persian (Arabian) gulf using a regional climate model. J. Clim. 28 (13), 5041—5062, http://dx.doi.org/10.1175/JCLI-D-14-00189.1.

Oceanologia (2019) 61, 412—426

Available online at www.sciencedirect.com

ScienceDirect

journal homepage: www.journals.elsevier.com/oceanologia/

ORIGINAL RESEARCH ARTICLE

Assessment of coastal vulnerability in Chabahar Bay due to climate change scenarios

Mahmoudreza Armanfar [a], **Hamid Goharnejad** [a,c,d,*], **Mahmoud Zakeri Niri** [b], **Will Perrie** [c]

[a] *Environmental Sciences Research Center, IslamShahr Branch, Islamic Azad University, IslamShahr, Iran*
[b] *Young Researchers and Elite Club, IslamShahr Branch, Islamic Azad University, IslamShahr, Iran*
[c] *Fisheries and Oceans Canada, Bedford Institute of Oceanography, Dartmouth, Nova Scotia, Canada*
[d] *Engineering Mathematics and Internetworking, Dalhousie University, Halifax, Nova Scotia, Canada*

Received 2 October 2018; accepted 7 March 2019
Available online 21 March 2019

KEYWORDS
Climate change;
Sea level rise;
Wave regime prediction;
Coastal vulnerability;
MIKE21 model

Summary A substantial body of research has shown that two key factors of global sea level rise are thermal expansion and melting of land-based ice, glaciers and ice sheets. Moreover, climate change may result in changes to wind speeds and directions, consequently resulting in contributions to variations in wind-wave components, wave heights and directions. In this research, climate change scenarios were used to assess the coastal vulnerability to the Chabahar port area due to global sea level rise, significant wave height changes and tidal regime effects. These three items were calculated separately using numerical models and the impacts of possible climate change scenarios were applied to estimate possible changes to these items by 2100. Significant wave heights for 25, 50 and 100-year return periods were evaluated. Based on statistical analysis, the maximum significant wave heights for the A2 and A1B scenarios were estimated at approximately 13.7 and 7.6, respectively. Since the main aim of this research was to assess the coastal zones at higher flood risk, therefore the mean global sea level rise, extreme values of significant wave heights and tidal heights were investigated. The height of sea during sea storms and for the most extreme case was calculated as 17.3 m and 11.2 m for A2 and the A1B scenarios, respectively. According to output maps of inundation areas, large coastal zones in the Chabahar port area are at risk due to the sea storms and possible climate change.

* Corresponding author at: Department of Civil Engineering, Environmental Sciences Research Center, IslamShahr Branch, Islamic Azad University, IslamShahr, Iran. Tel.: +98 9127144265.
E-mail address: Hgn1982@gmail.com (H. Goharnejad).
Peer review under the responsibility of Institute of Oceanology of the Polish Academy of Sciences.

Production and hosting by Elsevier

https://doi.org/10.1016/j.oceano.2019.03.001

1. Introduction

During the past two decades, scientists and politicians from developed and developing countries have become increasingly interested in global warming and climate change. Although climate change, as a natural phenomenon, occurs on a variety of scales, some as long as a thousand years or more, changes due to human activities have resulted in increasing volumes of greenhouse gases in the atmosphere. The recent climate changes have perhaps been more intense than the earlier ones, happening some two million years ago (IPCC, 2001; Stone et al., 2003). According to the IPCC report, a global warming of 0.89°C has occurred in the global ocean temperature over the period 1901—2012, whereas this figure was 0.74°C within 1951—2003 (IPCC, 2007). Recent studies have shown that in the 20th century the mean sea level and average wind speed increased by as much as 30 cm and 1 m/s, respectively (WCRP, 2018). Related changes, such as stronger hurricanes suggest that coastal areas are becoming more vulnerable. Furthermore, due to specific topography, population density, as well as economic parameters, coastal zones are recognized as sensitive climate areas in the world (Tragaki et al., 2018). For example, in the United States, approximately 25 million people live in areas vulnerable to coastal flooding.

Climate change can affect coastal areas in a variety of ways. The effects of climate change include a rise of mean sea level, significant wave height changes due to wind speed and direction changes, and the severity of oceanic storms. These factors can seriously endanger coastal structures, tourism, fisheries, transportation systems, and even offshore energy farms. As a result, it is necessary to carry out studies to analyze the impact of climate change on coastal zones. In previous studies, global mean sea level rise due to the increased water temperature, ocean internal expansions, as well as melting glaciers have captured the interest of several investigations (Bindoff et al., 2007; Houghton et al., 2001; Pfeffer et al., 2008).

On the other hand, research conducted over the past decade has suggested that wind characteristics including speed and direction are influenced by climate changes, and hence can result in changes in wind-wave heights. Over a 100-year period to 2100, Chini et al. (2010) projected that wind-wave heights may increase up to 12 percent because of the climate change impacts on wind speed over the eastern coast of England. Kamranzad et al. (2013) used three emission scenarios, A1B, A2 and B1, to investigate the impact of climate change on wind speed and direction in the area around Chabahar. Vanem et al. (2012) considered the impact of climate change on the wave climate of the global ocean. They investigated 12 specific zones including the North, South, and middle Atlantic, North East, North West, and South Pacific, Gulf of Mexico, Indian Ocean, Tasmanian Sea, Mediterranean Sea, and West Australia ocean areas, and found a correlation between CO_2 changes and significant wave heights under A2 and B1 emission scenarios. At 90% confidence level, the results showed that the maximum and minimum changes in the significant wave heights occurred in the A2 and B1 climate change scenarios, respectively.

Dastgheib et al. (2016) analyzed the effect of climate change in waters off the Vietnamese coastline. Two periods of 1981—2000 and 2081—2100 were considered to represent the present and the future climate periods, respectively. They found that for northern Vietnam coastal areas, the mean significant wave heights decreased by some 8 cm compared to the present climate, and the wave periods increased by 0.2 s; whereas, for central and southern coastal areas, the mean significant wave heights and wave periods showed 5—7 cm and 0.08 and 0.16 s increases, respectively. In the meanwhile, Duan et al. (2014) studied the effects of climate change on wave characteristics in 10 zones around the Japanese coasts using observed buoy data from 1988—2012. They used sea surface temperature (SST), Multivariate ENSO Index (MEI), Southern Oscillation Index (SOI), Arctic Oscillation Index (AOI), Pacific Decade Oscillation Index (PDOI), and North Pacific Index (NPI) to calculate correlations between the meteorological indexes and the wave parameters, significant wave height, and wave period. They finally concluded that mean significant wave heights and wave periods at all zones increased 49.65 cm and 0.25 s, respectively.

In the North Atlantic during the fall hurricane season, Guo et al. (2015) studied the impacts of climate changes on surface waves. They used WAVEWATCHIII wave model and winds from the Canadian global climate model, CGCM3.1, dynamically downscaled using a regional climate model, and A1B and B1 climate change scenarios to elucidate the changes that might occur during 2040—2069 in wave regimes. They suggest that compared to the present climate represented as 1970—1999 in their study, wave heights may increase in the northeast North Atlantic, whereas in other areas such as mid-latitudes, decreases are expected, with associated changes in winds. Mitchell et al. (2015) simulated waves using WAVEWATCHIII under the A1B scenario to study the effect of climate change on potential wave energy off the coasts of England. They found a small reduction in mean significant wave heights during 2040—2069; however, the reduction was so trivial that no reductions are expected in potential wave power levels. Wave power is directly related to the squared significant wave height and the period.

Wandres and Pattiaratchi (2017) studied the possible changes of the wave climate off the southwestern Australian coast under two atmospheric greenhouse gas concentration pathways using SWAN wave model for RCP4.5 and RCP8.5 climate change scenarios. They used wind data over the period of 1986—2005 to model wave characteristics and then they used the calibrated model to simulate the wave regime during 2081—2100. Results suggest a 2—4% increase in mean significant wave heights in nearshore areas and a small change in the dominant wave directions. Moreover, in winter months, the longshore wave energy flux, which is responsible for littoral drift, is expected to increase by up to 39% and 62% under the RCP4.5 and RCP8.5 greenhouse gas concentration pathway with SLR, respectively. Karymbalis et al. (2012) assessed the vulnerability of the southern coast of the Gulf of Corinth due to the sea level rise. They concurred that 57.0 km of coastline (corresponding to 38.7% of the whole coastline), is highly vulnerable because of low topography.

Likewise, Pantusa et al. (2018) investigated vulnerable areas of Apulian coastline of southern Italy using the coastal vulnerability index (CVI), which is described as follows. They used 10 parameters (relative sea-level change, mean significant wave height and mean tide range, etc.) to assess CVI in the study area. Their results confirmed the importance of CVI

to assess coastal vulnerability with respect to climate change. Pendleton et al. (2005) also studied the vulnerability of Cape Hatteras using this approach. CVI ranks the following in terms of their physical contribution to sea-level rise-related coastal change: geomorphology, regional coastal slope, rate of relative sea-level rise, historical shoreline change rates, mean tidal range, and mean significant wave height.

Regarding mean sea level rise, many studies have been carried out worldwide and on local scales (Horton et al., 2008; Jevrejeva et al., 2010; Pfeffer et al., 2008; Rahmstorf, 2007). Mean sea level rise in the study area has been discussed by Goharnejad et al. (2013). They used A1B and A2 scenarios to study sea level changes to 2100 and reported that the maximum expected sea level rise is 60 cm. The current study continues the previous work by Goharnejad et al. (2013).

In this study, we modeled tidal flows and wind-waves regimes in the Chabahar port area. Since tidal currents are not directly affected by climate change, hence wind-waves have been calculated due to climate change under two scenarios, namely A1B and A2, to 2100. The A2 and A1B scenarios represent the possibly extreme and mean climate changes, respectively. Thus, significant wave height extreme values are estimated for return periods of 25, 50 and 100 years using three probability distribution functions. The mean global sea level rise has been extracted from the previous study by Goharnejad et al. (2013). Finally, in order to assess the vulnerability of the Chabahar coastal zone, the three above-mentioned parameters have been summarized.

2. Study area

Chabahar with a total area of 17,155 km^2 is located on the southeastern part of Iran along the Oman Sea and close to the Indian Ocean. As seen in Fig. 1, Chabahar port area is more than 11 km^2 with the altitude of 7 m above sea level and is located between 60°20′ to 60°32′E longitudes, and 25°17′ to 25°27′N latitudes. Chabahar Bay with the geometry of Ω shape and without any considerable rivers has moderate tropical weather. The summer monsoon winds from the Indian subcontinent make Chabahar the coolest southern port in the summer and the warmest port of Iran in the winter. It has an average maximum temperature of 34°C and an average minimum temperature of 21.5°C.

3. Methodology and data collection

3.1. Spectral wave model setting and data used

In order to study the wave regimes in coastal areas off Chabahar, it is necessary to have geographic data (boundaries and bathymetry data), wind data (speed and direction), Buoy wave data, and sea level pressure data. In this study, the Spectral Wave analysis (SW) and Flow Model (FM) modules of MIKE21 were used with the aim of hindcasting offshore wave characteristics using available wind data. Waves were numerically modeled in the study area using the SW model, which is a dynamic modeling system based on the spectral wave model and implemented on an irregular unstructured grid often used in coastal areas, estuaries, and rivers. Danish Hydraulic Institute initially prepared this wave model in the version 2005 of DHI software (DHI, 2005). The model can solve the energy transfer equation with wave source and sink terms to predict the developing wave field.

The governing equation of MIKE21 wave model is the spectral action balance equation, which for Cartesian coordinates is:

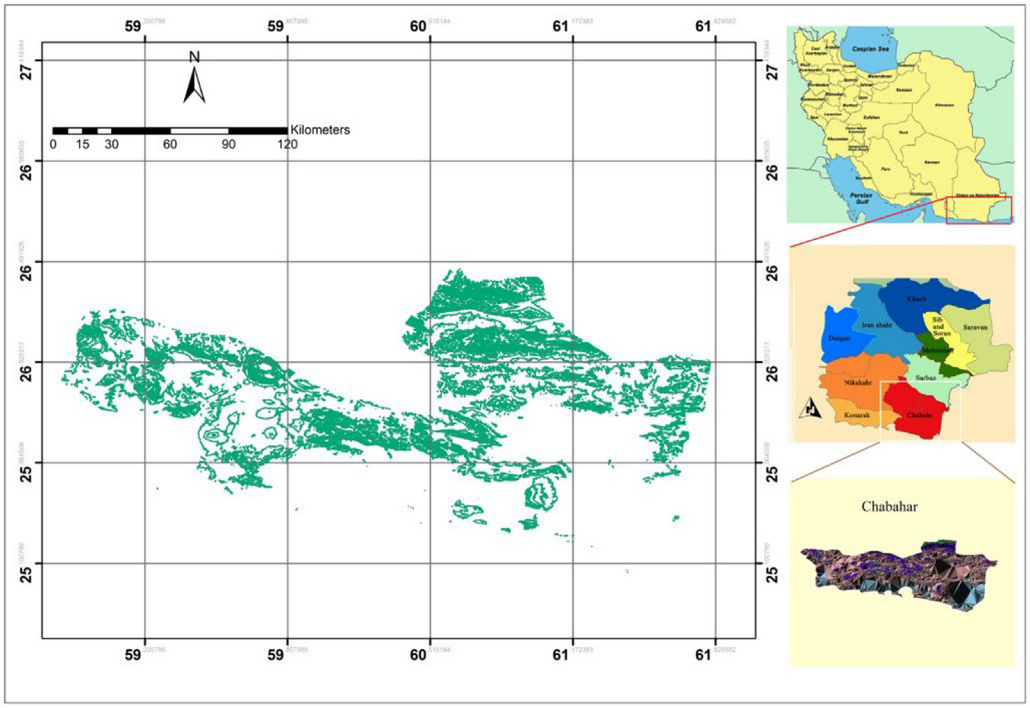

Figure 1 General view of the study area.

$$\frac{\partial}{\partial t}N+\frac{\partial}{\partial x}C_{g,x}N+\frac{\partial}{\partial y}C_{g,y}N+\frac{\partial}{\partial \sigma}C_{g,\sigma}N+\frac{\partial}{\partial \theta}C_{g,\theta}N=\frac{S}{\sigma}, \quad (1)$$

where σ is the relative frequency, θ is wave direction, N is wave action density, which is equal to the energy density divided by the relative frequency ($N(\sigma, \theta) = E(\sigma, \theta)/\sigma$) and C_g is the propagation velocity of wave action in (x, y, σ, θ) space. The last term on the left side of the equation denotes the effects of refraction and shoaling. The source term on the right of the wave transfer equation is defined as follows:

$$S = S_{in} + S_{nl} + S_{dis} + S_{ot} + S_{surf}, \quad (2)$$

where S_{in} represents energy transfer from wind to the waves, S_{nl} represents energy transfer from one frequency to another by nonlinear wave-wave interactions, S_{dis} is wave energy dissipation under the effect of the white-capping, S_{ot} is the wave dissipation due to bottom friction, and S_{surf} represents wave dissipation resulting from the wave breaking in a shallow area.

Bathymetry data at 1-min resolution (about 1.7 km) were collected from National Centers for Environmental Information, NOAA (https://www.ngdc.noaa.gov/mgg/bathymetry/relief.html).

Because there were no comprehensive observed data of the wind and waves in the study area at the beginning of the study, a large scale model that covered the Oman Sea and a small part of Indian Ocean with the eastern longitudes extending from 56° to 66° and the northern latitudes extending from 21° to 27°, was deployed (see Fig. 2). Moreover, wind data were extracted from ERA-Interim reanalysis data (Jan. 1979–present) with 0.25° spatial and 6-h temporal resolutions at 10 m reference height above sea level as wave model inputs (https://www.ecmwf.int/en/forecasts). In the numerical wave model, wind data were used for two periods within 1971–2000 and 2006–2016, as calibration and verification periods, respectively.

Fig. 3 shows the average wind rose along the Chabahar coastline based on ECMWF data.

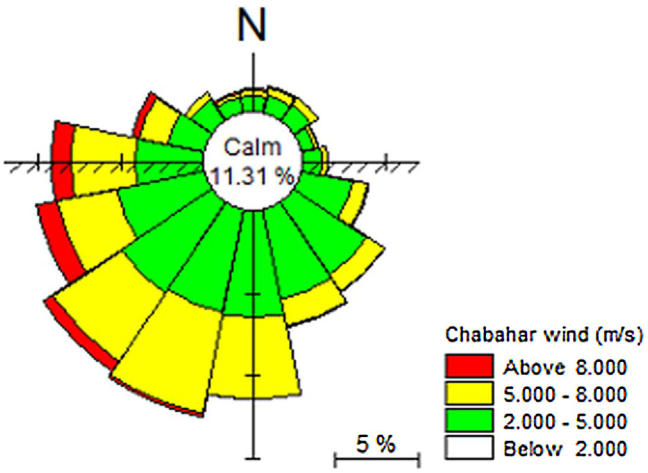

Figure 3 Chabahar local wind rose based on ECMWF data (2006–2016).

As seen, the dominant winds blow from south and southwest. Table 1 also represents the monthly minimum and maximum wind speed, as well as the dominant direction of the Chabahar local winds.

Determining the time step is one of the most important parts of a wave model set up. Large time steps, on one hand, require fewer integration steps and higher execution of model computation. However, excessively large time steps may decrease model accuracy. In this regard, with suitable numerical experimentation, the appropriate time steps were obtained in both large and local scales for the current and wave models of MIKE21 (see Table 2).

Moreover, five other parameters are needed to calibrate the model. The default and calibrated values are shown in Table 3. As seen in this table, the bottom friction is a sensitive factor in the wave model, whereas other parameters showed no significant effects on the results.

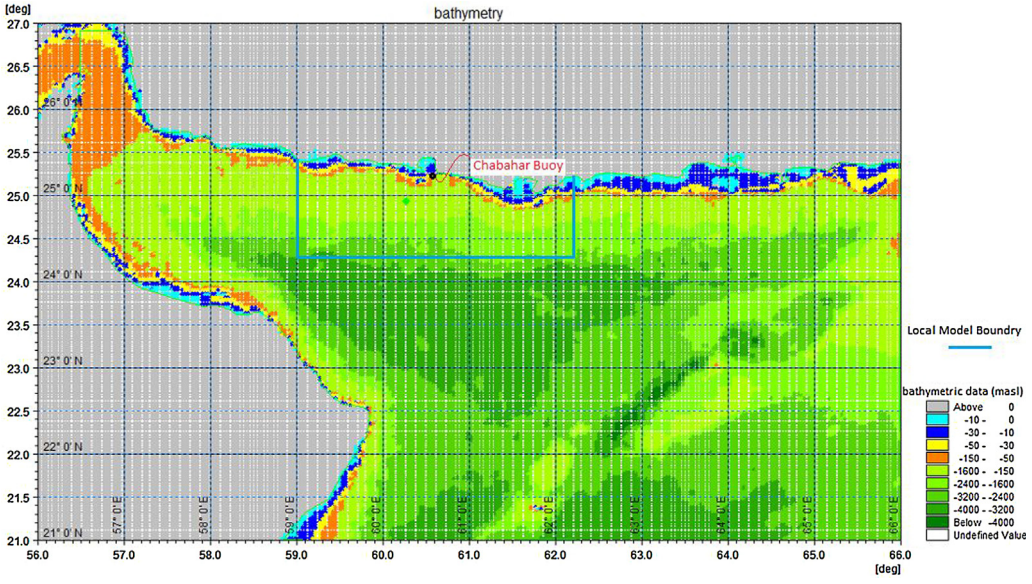

Figure 2 Large scale model bathymetry, Chabahar buoy, and local model boundary in the Oman Sea and the Indian Ocean.

Table 1 Wind characteristics in the study area based on ECMWF wind data (2006–2016).

Month	Wind speed (m/s)		Dominant wind direction
	Minimum	Maximum	
January	0.08	10.71	WSW-SW
February	0.10	11.98	SW- WSW
March	0.09	11.50	WSW-SW
April	0.02	12.37	WSW-SW
May	0.21	11.51	SW-SSW
June	0.21	18.4	S-SSW
July	0.36	10.65	S-SSE
August	0.40	10.37	S-SSE
September	0.16	8.6	S-SE-SW
October	0.11	7.57	SSW-WSW
November	0.16	8.81	SW-SSW
December	0.04	11.45	N-W

Table 2 Time steps for large and local scales for ocean current and wave models.

Scale	Current model time step (s)			Wave model time step (s)		
	Appropriate	Maximum	Minimum	Appropriate	Maximum	Minimum
Large	60	600	60	600	3600	300
Local	30	300	30	60	600	30

Table 3 Appropriate values for parameters in the wave model.

Parameter	White capping (C_{dis})	White capping (δ)	Wave breaking (γ)	Wave breaking (α)	Bottom friction
Default	4.5	0.5	0.8	1	0.04
Calibrated	4	0.5	0.8	1	0.13

Once the effective parameter values were determined, the model was used to simulate a one-month period and the results were compared with buoy data. The buoy wave data were obtained from the Chabahar Buoy station. It was established in 1996 and the completeness percentage is 97% (see https://www.psmsl.org/data/obtaining/stations/1881.php). These data were used to calibrate and validate the wave model results (see http://marinedata.pmo.ir). Buoy characteristics are presented in Table 4. Thereafter, the wind-wave model was verified for an additional three one-month periods. The calibration and verification results for these periods are shown in Table 5.

3.1.1. Spectral wave model performance

In order to evaluate the model performance, statistical parameters between observed and modeled data were calculated as follows:

bias $\quad \mathrm{Bias} = (S-O),$

root mean squared errors $\quad \mathrm{RMSE} = \sqrt{\frac{1}{N}\sum(S_i-O_i)^2},$

correlation coefficient $\quad \mathrm{CC} = \frac{\sum(S_i-S)(O_i-O)}{\sqrt{\sum(S_i-S)^2\sum(O_i-O)^2}},$

Table 4 Chabahar buoy properties.

Station	Type	Coordinate		Depth (m)	Available parameters
		Latitude	Longitude		
Chabahar	Datawell	25.283	60.616	17	• Mean wave direction • Wave period • Significant wave height

Table 5 Calibration and verification periods for the wave model.

Calibration period	Verification period 1	Verification period 2	Verification period 3
July 2016 31 days	October 2015 31 days	January 2012 31 days	April 2011 30 days

Table 6 Results of model performance indices for the Chabahar buoy (2006–2016).

Parameter	Normal range	Ideal range	Calibration	Validation 1	Validation 2	Validation 3
Bias (m)	0.2–0.5	<0.3	0.150	0.008	0.015	0.003
CC	0.75–0.90	>0.8	0.830	0.930	0.870	0.910
RMSE (m)	0.1–0.7	<0.5	0.189	0.048	0.118	0.140
SI	0.15–0.35	<0.3	0.291	0.095	0.181	0.080

dispersion coefficient $\mathrm{SI} = \frac{\sqrt{\frac{1}{N}\sum(S_i - O_i)^2}}{O}$,

where O_i is the observed value at the ith time step, S_i is a forecast value at the same moment of time, N is the number of time steps and O and S are the mean values of the observed data and forecast results, respectively. Table 6 depicts the results of the model performance indices. Columns 2 and 3 show the normal and ideal ranges of each index, implying that the wave model is sufficiently accurate to estimate wave climate features. Meanwhile, Fig. 4 illustrates the modeled and observed significant wave heights.

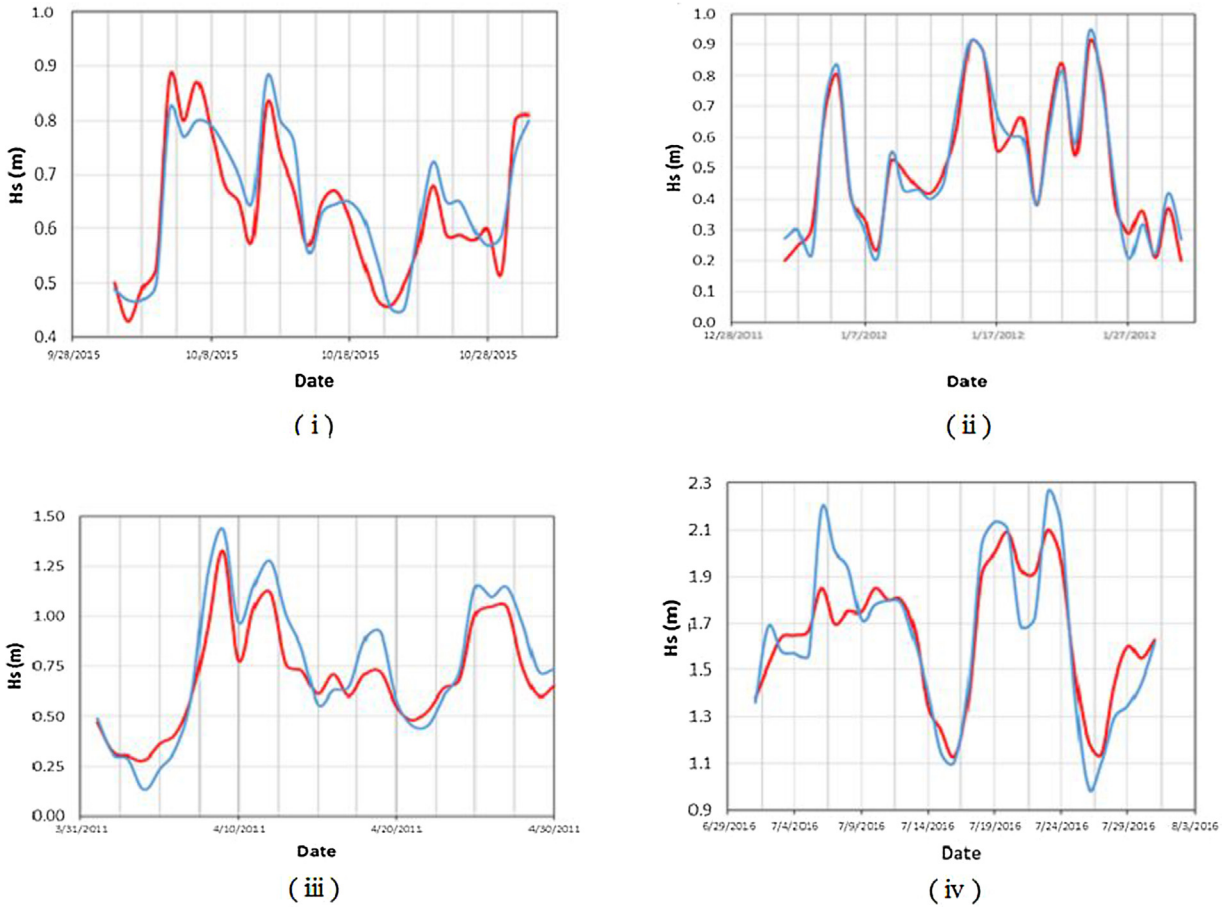

Figure 4 Time series of the modeled and observed significant wave heights at Chabahar station. (i) Calibration period (July 2016); (ii) Verification period 1 (October 2015); (iii) Verification period 2 (January 2012); (iv) Verification period 3 (April 2011); red line: observed significant wave height; blue line: modeled significant wave height. (For interpretation of the references to color in this figure legend, the reader is referred to the web version of this article.)

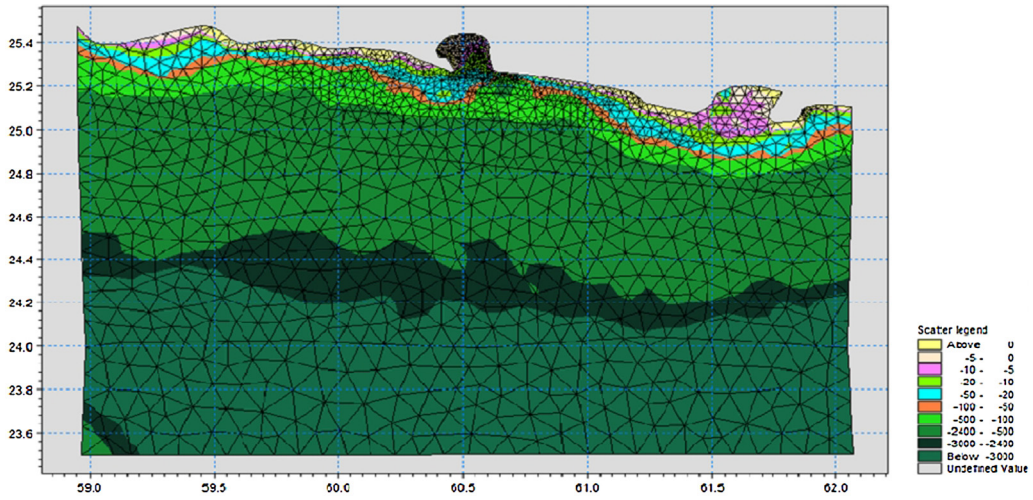

Figure 5 The local model with triangular meshes in the study area.

In the next step, boundary conditions including time series of wave parameters were extracted from the large area model and were used as boundary conditions for the local model. The local model with triangular meshes is shown in Fig. 5. The optimization of the number of nodes and elements is an important part of wave modeling. Thence, numerical experimentation with several model-runs with different meshes were executed and eventually, the number of elements and nodes were determined as 2484 and 1453, respectively. As shown in Fig. 5, the mesh sizes in deeper water areas are bigger than those of shallow water areas, which are closer to the coastline.

3.1.2. Spectral wave model outputs

Once the accuracy of the wind-wave model performance was confirmed by statistical parameters, the model was run for 11 years, from 2006 to 2016. Significant wave height, wave period, wave direction and the frequency of occurrence (%) for these parameters are shown in Figs. 6 and 7.

3.2. Flow model setting and data used

In order to calculate the sea surface tidal currents and to consider the tidal effects on coastal areas, the current model was run over the local model domain. The wave breaking and tidal currents are among the most important parameters needed to determine the dominant wave regime in the study area (Rahimipouri et al., 2006). Thus, to set up a flow model, radiation stress data (S_{xx}, S_{xy}, and S_{yy}), local tidal parameters, as well as wind data are required. A further point of interest is that the number of elements and nodes were the same as those used for the spectral wave model, and the radiation stress data were taken from the spectral wave model and used as input parameters in the flow model. Model calibration was conducted during 3.15.2012 to 5.15.2012, and the verification period was from 11.19.2014 to 3.19.2015. The calibration and verification periods are different from those of the SW wave model because we used a different source of observed tidal data, and our recorded data

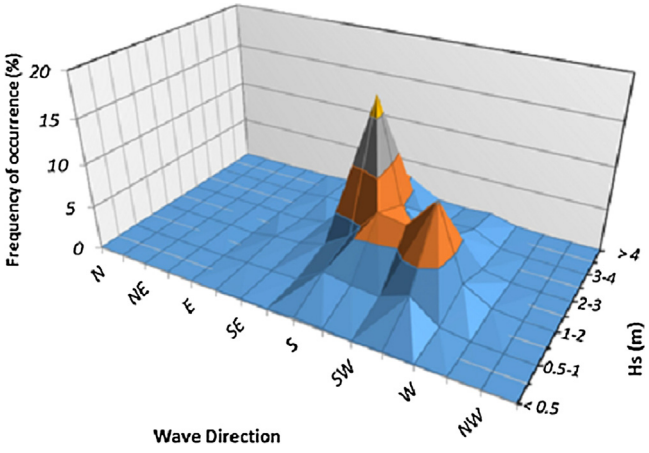

Figure 6 Frequency of occurrence (%) for significant wave height and wave direction at the Chabahar buoy location (2006—2016).

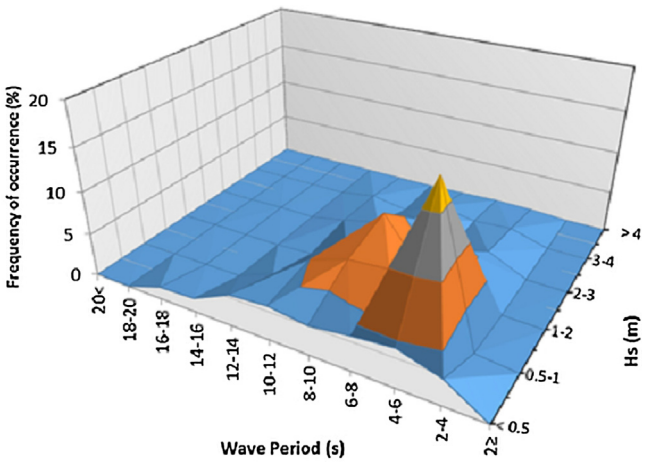

Figure 7 Frequency of occurrence (%) for significant wave height and wave period at the Chabahar buoy (2006—2016).

Table 7 The harmonic parameter values at Chabahar (Shirinmanesh and Chegini, 2014).

M2		S2		K1		O1	
Phase	Amplitude	Phase	Amplitude	Phase	Amplitude	Phase	Amplitude
267.3	0.62	299.6	0.24	34.5	0.4	35.8	0.2

have better quality during these selected periods. The main harmonic tidal parameters at Chabahar are extracted as recorded in Table 7 (http://www.tidetablechart.com/tides/hightide_lowtide/64110/Chabahar and http://marinedata.pmo.ir/).

Time series of tidal data were extracted from the flow model as shown in Fig. 8. In order to assess the flow model performance, the mentioned statistical indices were calculated and the results are presented in Fig. 9 and Table 8. Our results suggest that the flow model performance is acceptable and the output parameter series can be used with high reliability. Using the flow model outputs, the minimum and maximum sea level due to tidal flows are shown in Table 9. The results indicate that the minimum and maximum water levels during these 11 years are 1.69 and 2.96 m, respectively.

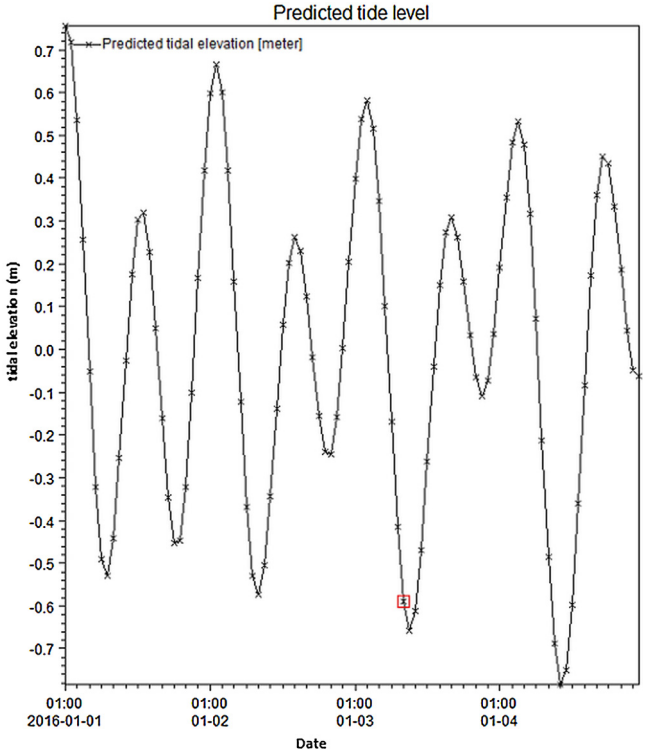

Figure 8 Predicted tidal level at Chabahar.

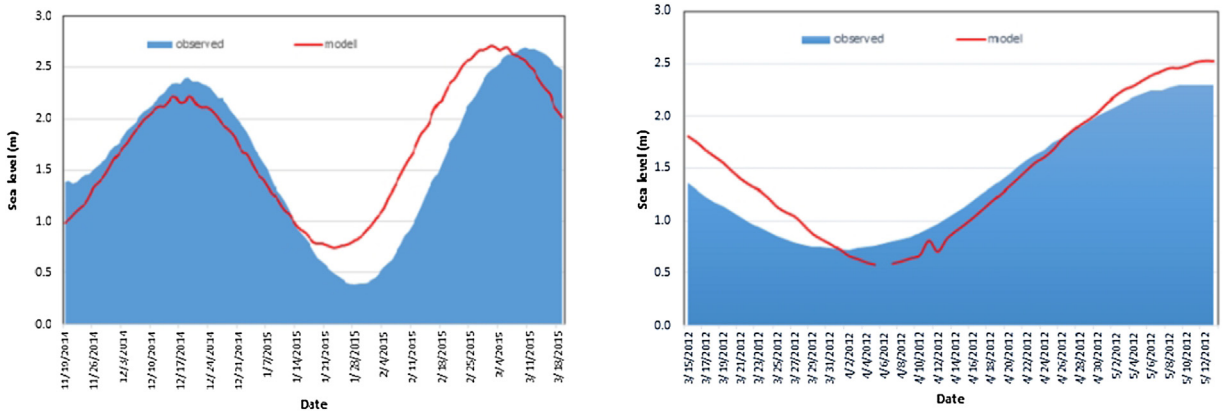

Figure 9 Time series of modeled and observed sea level due to tidal flows during two different periods.

Table 8 Error parameters between observed and modeled data during calibration and verification time periods.

Parameter	Bias (m)	CC	RMSE (m)	SI
Calibration	0.09	0.81	0.16	0.20
Verification	0.17	0.80	0.23	0.28

Table 9 Minimum and maximum sea level (2006–2016).

Year	Minimum sea level (m)	Maximum sea level (m)
2006	1.69	2.96
2007	1.76	2.70
2008	1.77	2.68
2009	1.76	2.93
2010	1.80	2.70
2011	1.72	2.85
2012	1.77	2.84
2013	1.80	2.70
2014	1.79	2.79
2015	1.86	2.61
2016	1.85	2.79

3.3. Impact of climate change

There are several global climate models that attempt to estimate the effects of climate change. In this research study, the Coupled Global Climate Model (CGCM3) was used and two emission scenarios, A2 and A1B, were selected (see http://climate-scenarios.canada.ca). Because of the large spatial and temporal scales of these data, downscaling is needed to describe climate model outputs. Downscaling is the process by which coarse-resolution GCM outputs are translated into finer resolution climate information, so that they can better account for regional climatic influences, such as local topography. The resolution of CGCM3.1 data is inappropriate for fine-resolution modeling of wave regimes. On the other hand, output time steps in GCM models are often monthly whereas modeling of local wave parameters needs hourly data. Hence, downscaling is an essential procedure for preparing input data. Generally, three main downscaling methods are available, including dynamical, statistical and combination of dynamical and statistical methods (Gutmann et al., 2012).

In this study, a Change Factor Methodology (CFM) has been applied, which is a combined method of dynamical and statistical approaches for spatial downscaling of GCM data (Trzaska and Schnarr, 2014). This method is consistent with the methods used by Kamranzad (2014) in the Persian Gulf to estimate wave power, and Breslow and Sailor (2002), in the U.S. for approximating wind power. In order to confirm the reliability of climate models outputs, it was necessary to initially compare observed and climate data. In this regard, a period was determined as a control period and the collocated data were examined. Comparing the ECMWF and CGCM3.1 wind data revealed that CGCM3.1 wind data were often underestimated. Hence, equations 3 and 4 were used to re-calibrate the CGCM3.1 wind data. The modification of CGCM3.1 wind data for monthly averages of absolute wind components is calculated by:

$$\beta_u = \frac{|u|_{\text{ECMWF(monthly average)}}}{|u|_{\text{CGCM3.1(monthly average)}}}, \tag{3}$$

$$\beta_v = \frac{|v|_{\text{ECMWF(monthly average)}}}{|v|_{\text{CGCM3.1(monthly average)}}}, \tag{4}$$

in which, β_u and β_v represent the modification factors for u and v components of the wind speed, respectively.

Figs. 10–13 depict ECMWF data ratio to A1B and A2 data in the 4 periods (July, January, October, and April) of calibration and verification.

Wind speed data taken from GCM climate change scenarios and ECMWF were compared with each other and results are depicted in Fig. 14. It is clear that the wind speed ratios between ECMWF data and A2 scenario are higher than those of the A1B scenario, which implies that A1B data and ECMWF data are more similar.

Once CGCM3.1 wind data were downscaled for A1B and A2 scenarios, the spectral wave model was run with modified

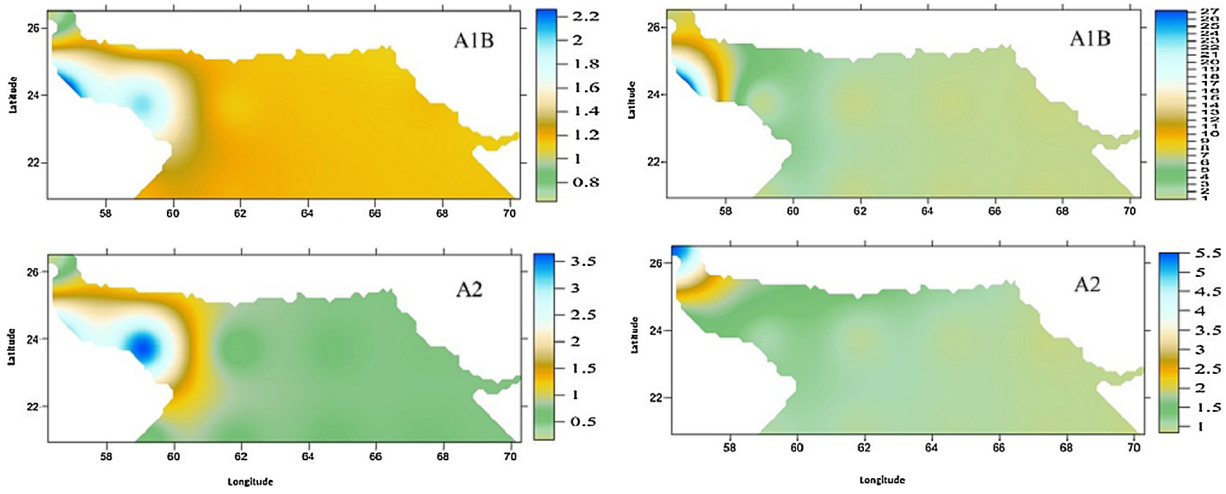

Figure 10 β_u (left) and β_v (right) for A1B and A2 scenarios in July (1981–2010).

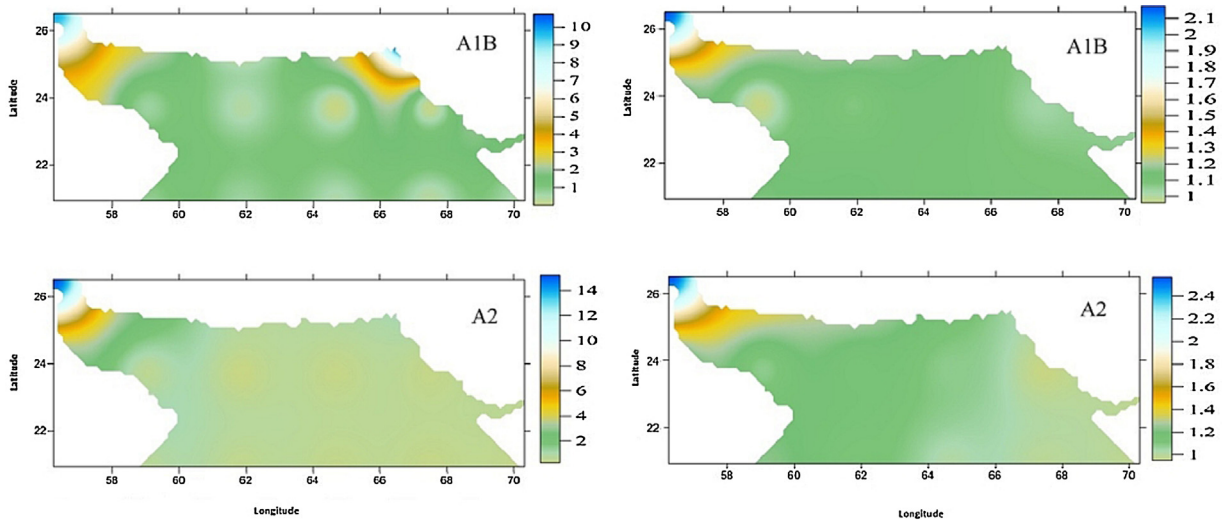

Figure 11 β_u (left) and β_v (right) for A1B and A2 scenarios in January (1981–2010).

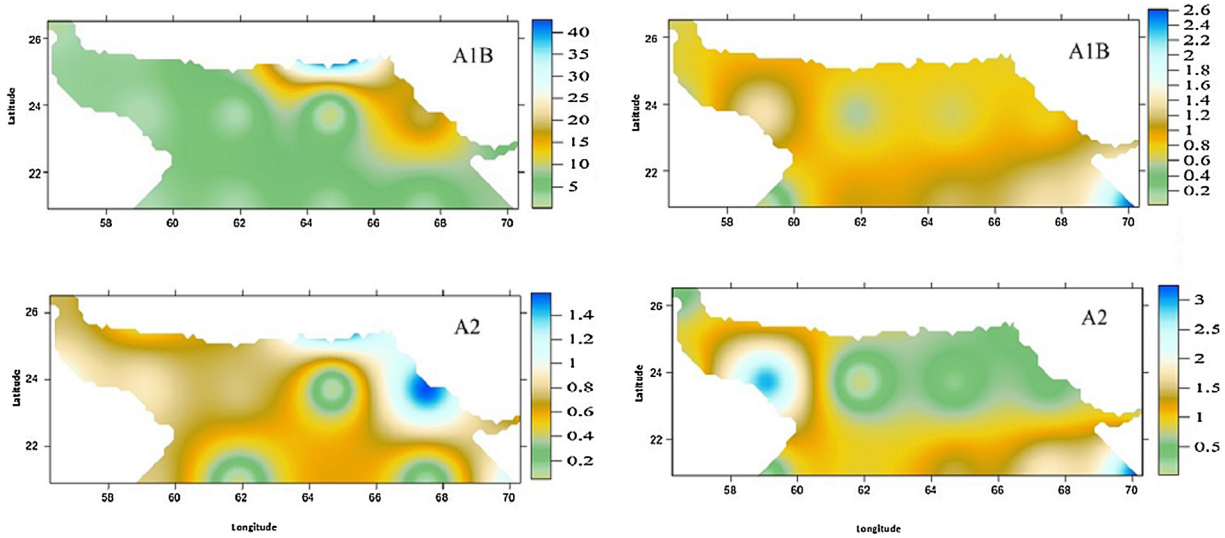

Figure 12 β_u (left) and β_v (right) for A1B and A2 scenarios in October (1981–2010).

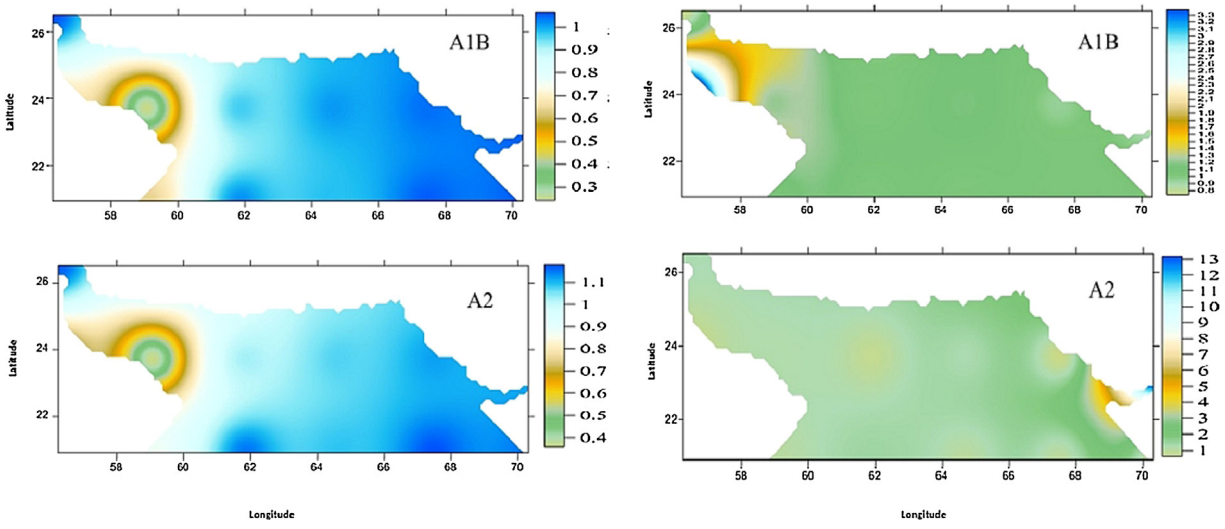

Figure 13 β_u (left) and β_v (right) for A1B and A2 scenarios in April (1981–2010).

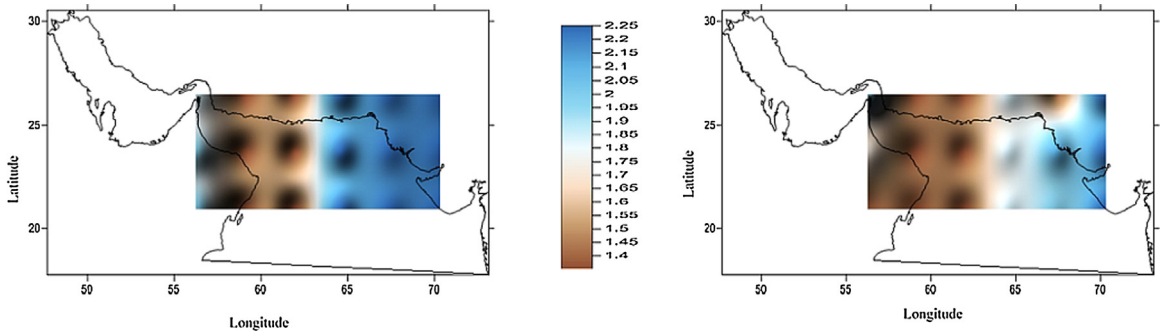

Figure 14 Comparison of wind speed ratios for (i) A2 climate change scenario and (ii) A1B climate change scenario to the ECMWF wind speed data for the present climate (1981—2010).

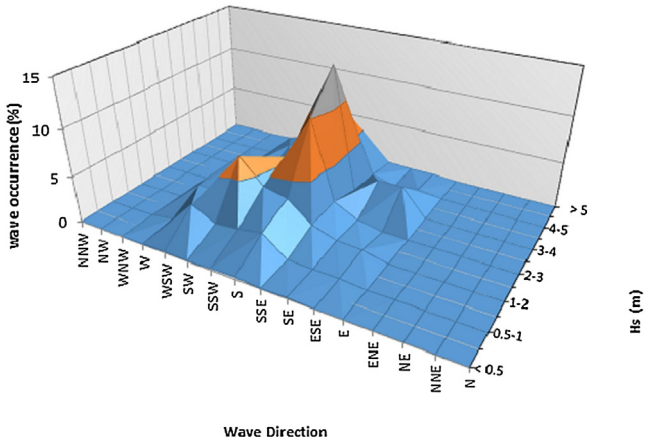

Figure 15 Frequency of occurrence (%) for significant wave height (Hs) and wave direction at Chabahar for A1B scenario (2071—2100).

climate change wind data for 30 years, 2071—2100. Wind model implementation results using A1B and A2 scenarios for climate data of years 2071—2100 are provided in Figs. 15—18, respectively.

Furthermore, as we should consider the global mean sea levels in our study, we used the results from Goharnejad et al. (2013). Their study showed that sea levels in southern seas of Iran are increasing because of thermal expansion and melting glaciers. According to their results for Chabahar, the mean sea level rise by 2100 for A1B and A2 are estimated to be 48 and 60 cm, respectively.

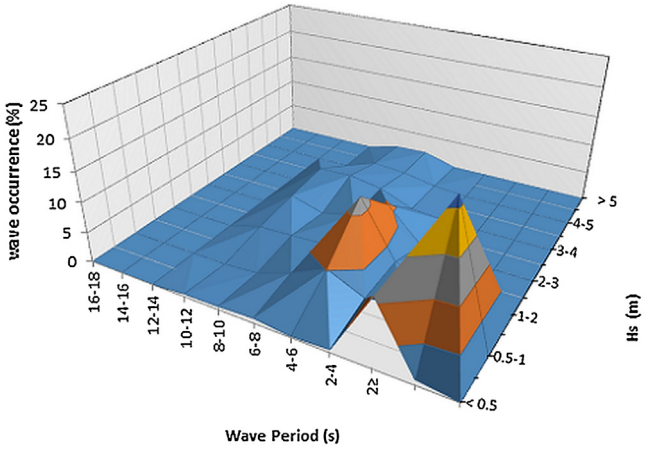

Figure 16 Frequency of occurrence (%) for significant wave height (Hs) and wave period at Chabahar for A1B scenario (2071—2100).

4. Discussion and results

We have calculated the wave characteristics for an 11-year period (2006—2016) representing the present time and a 30-year period (2071—2100) representing the future; the results are shown in Figs. 6 and 7. Accordingly, over 65% of the mean significant wave heights are smaller than 1 m, the majority of the waves have a period of less than 8 s, and travel from the south. The waves in the Oman Sea are influenced by several phenomena including monsoon fronts, local winds, and tropical typhoons. Since Chabahar is an oceanic port, it is influenced by swells coming from the Indian Ocean and the Arabian Sea; thus wind roses in this area are different from other parts of the Oman Sea. Moreover, due to the Arabian Peninsula, warm regional winds blow, in some months, from the southwest causing southwesterly waves to emerge. In general, mean significant wave heights of more than one meter often occur in June to September during summer monsoon phenomena. The maximum wave height for the 11-year period is 7 m with about 10 s wave period and direction toward the south, which are seen essentially every year in July. The mean wave height is 0.8 m and the mean wave period is calculated as 3.5 s. With respect to 11-year occurrences, the mean significant wave height is 2.5 m with a period of 5.7 s. Wave heights between 0.5—1.0 m have the maximum frequency of occurrence.

The ocean current flow direction is often from east to west turning towards the north at about Chabahar Bay. Sea level for the east-west current flow is between 1.7—2.8 m (Fig. 19i). Sometimes, additional weak flows travel from south-west and west directions into the study area, especially in the winter. In such cases, the maximum change in water level is less than 1.5 m (Fig. 19ii).

4.1. The effects of climate change

Studies have revealed that climate change influences the wave climate (Wojtysiak et al., 2018). The results of wave modeling for years 2006—2016 indicate that about 65% of the

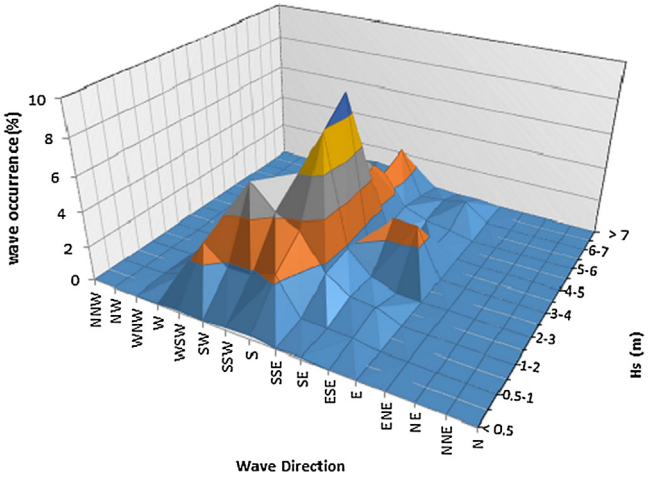

Figure 17 Wave occurrence (%) based on significant wave height (Hs) and wave direction in Chabahar for A2 scenario (2071—2100).

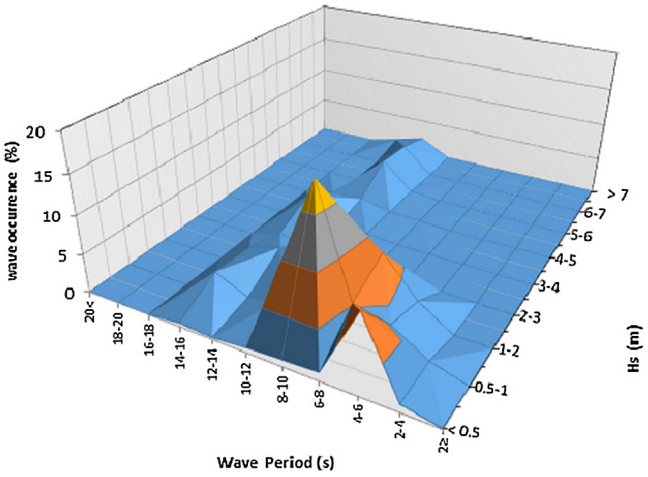

Figure 18 Wave occurrence (%) based on significant wave height (Hs) and wave period in Chabahar for A2 scenario (2071—2100).

wave heights are less than 1 m, of which 48% and 17% of these waves have wave periods less than, and more than, 10 s, respectively. In both climate change scenarios, approximately 50 percent of mean significant wave heights are 1 m or less. According to the wind-wave model results for A1B and A2 scenarios, it is suggested that although there is no considerable difference between wind speeds under A1B and A2 scenarios in Chabahar bay, wind speeds for A2 scenario in other areas of the integration, especially along the eastern boundary longitudes towards the Indian Ocean are much more than corresponding wind speeds under A1B scenario. In current climate conditions, most mean significant wave heights more than 1 m are observed during monsoon conditions between 1—2 m, and during hurricane conditions, wave heights with more than 4 m height have been observed in numerical results. According to these results, mean significant wave heights of 1 m or more during 2071—2100 would be expected in approximately 50% of the total distribution of waves where wave frequency is 2—4. Therefore, according to the A2 scenario, it is projected that longer waves will be developed during this climate scenario. On the other hand, more swells are expected to travel into Chabahar harbor in the future.

4.2. Wave characteristics in current conditions and climate change scenarios

As depicted in Fig. 6, in current conditions, more than 50% of the recorded waves travel from south and southwest directions relative to Chabahar Bay. Moreover, 4.19% of the mean significant wave heights are more than 4 m, 13.51% are between 3—4 m, 32.14% between 2—3 m, 39.38% between 1—2 m, 9.94% between 0.5—1 m, and only 0.83% are less than 0.5 m. According to Fig. 7, most wave periods were seen in the range 4—6 s with the mean significant wave heights 0.5—1 m, whereas wave periods with 8—10 s periods have 23.54% frequency of occurrence. In addition, the wave periods with over 14 s have a relatively rare frequency of occurrence.

Regarding A1B scenario, the majority of waves travel from the south with a frequency of occurrence of 38.3% followed by those from the south-southwest with a frequency of occurrence of 17.6%. Under this scenario, more than 70% of the waves travel from south and southwest. Around 25% of the mean significant wave heights of 2—3 m also come from the south. Furthermore, 24.1% and 21.5% of waves have

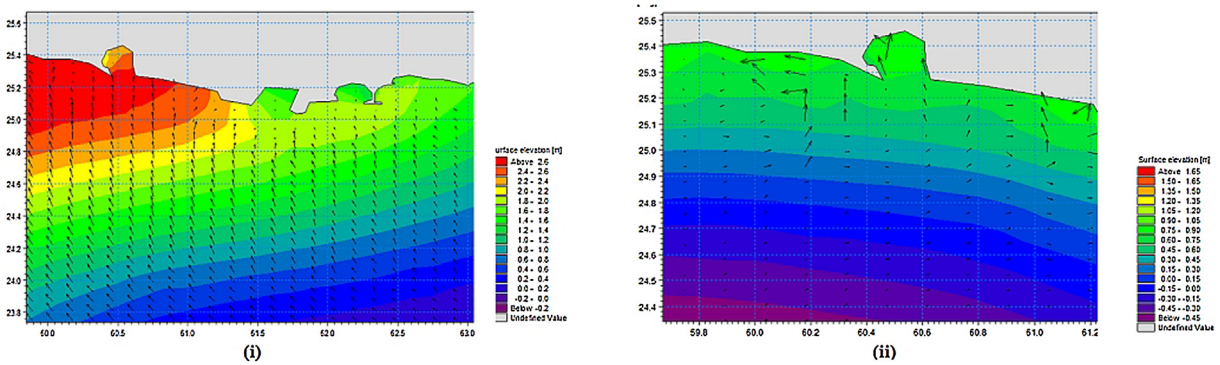

Figure 19 The current flow direction in Chabahar Bay: (i) the dominant flows in the study area and (ii) weak winter current flows.

periods of 8—10 and 2—4 s, respectively, which show that wave periods will decrease in the A1B scenario in comparison with present climate conditions. In addition, approximately 21.59% of the waves with periods of 2—4 s have the height of 0.5—1 m.

Concerning A2 scenario, 35.31% of the waves travel from the south, 18.3% from the south-southwest, 14.1% from the southwest, and 11.5% of the waves come from the west-southwest. This implies that around 80% of the waves move from south and west to the coast with mean significant wave heights of 2—4 m. Moreover, in 25.6% of the waves, the wave periods occur in the range 8—10 s. In general, wave periods for this scenario will increase by end-of-the-century, where 18.3% of the wave periods with 8—10 s are in the range between 0.5—1 m in height.

4.3. Climate change and extreme values of mean significant wave heights

To evaluate the Chabahar coastal vulnerability, it is necessary to calculate mean significant wave heights with 25, 50, and 100-year return periods. Additionally, one of the most important parameters in determining vulnerable areas with respect to coastal floods is significant wave heights. Thus, once climate change impacts were modeled for the time 2071—2100 (30 years) under A1B and A2 scenarios, statistical computations were completed to estimate wave heights for the 25, 50, and 100-year return periods and at-risk coastal areas were determined based on statistical analysis. Fig. 20 shows wave heights under the two A1B and A2 climate change scenarios for the three 25, 50, and 100-year return periods. For these calculations, three distribution functions were considered, namely log-normal, Weibull, and Gumbel. Finally, based on an evaluation of chi-squared test, the Weibull distribution function was selected.

According to Fig. 20 and under the A1B scenario, the mean significant wave heights for 25, 50, and 100-year return periods were 6.1, 6.7, and 7.6 m, respectively; and for the A2 scenario, the mean significant wave heights for 25, 50, and 100-year return periods were calculated as 8.4, 11.0, and 13.7 m, respectively. The results show that the mean significant wave heights under the A2 scenario is considerably higher than those under the A1B scenario; and according to these estimates, the areas influenced by such waves are also augmenting.

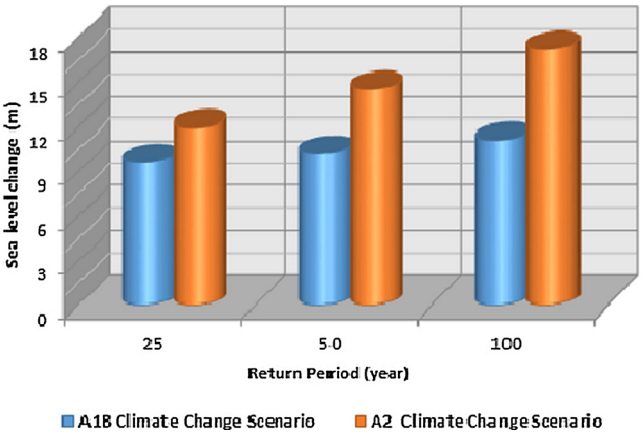

Figure 21 Sea level changes for A1B and A2 climate change scenarios for the three 25, 50, and 100-year return periods.

4.4. Extreme values of sea levels for climate change scenarios

The purpose of the present study is to investigate the coastal vulnerability in Chabahar Bay; thus, the maximum sea levels under both scenarios were calculated. In order to calculate maximum sea levels, three parameters are considered, including global mean sea level, maximum tidal wave height, and significant wave heights. Thus, we assess vulnerability for this region based on possibly severe climate change scenarios to 2100.

According to Fig. 21, the results indicate that under A1B scenario, the sea level change with 25, 50, and 100-year return periods will increase by 9.7, 10.3, and 11.2 m, respectively, and for A2 scenario, will increase by 11.9, 14.6, and 17.3 m for 25, 50, and 100-year return periods, respectively.

4.5. Zoning of water level in Chabahar

In the study area, after determining wave heights for the 25, 50, and 100-year return periods, inundation should be estimated. A flood inundation map was created in order to estimate vulnerable areas, as shown in Fig. 22, taking into account significant wave heights, mean sea level rise, and tidal heights. Clearly, the potential impact might be large,

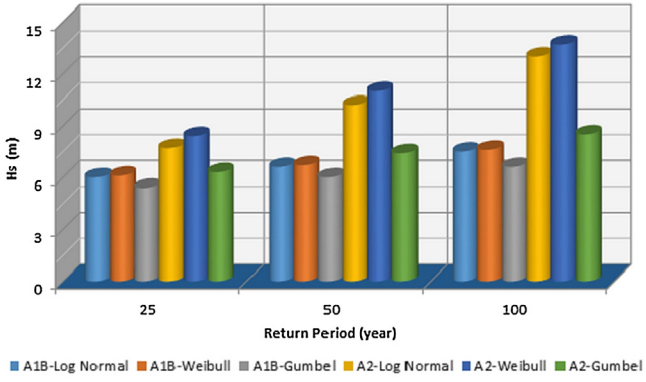

Figure 20 Mean significant wave heights for A1B and A2 climate change scenarios for the three 25, 50, and 100-year return periods.

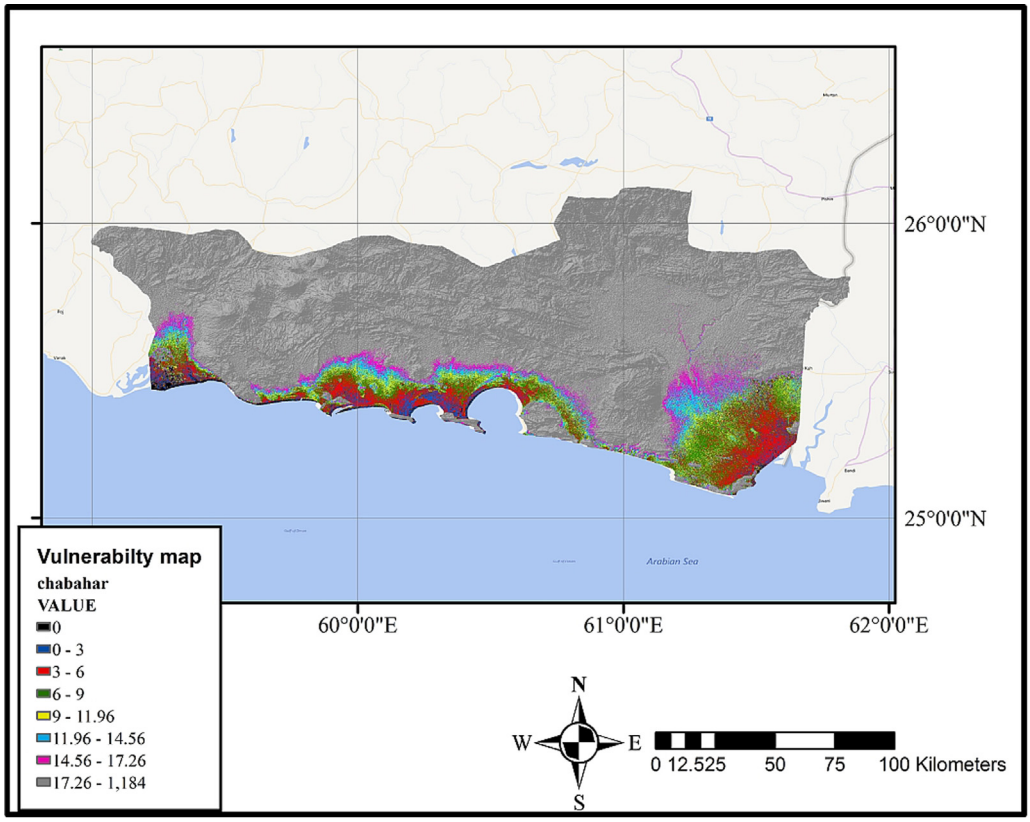

Figure 22 Potential inundation map for end-of-the-century taking into account possible climate change impacts on significant wave heights, mean sea level rise, and tidal heights.

implying that mitigation measures may need to be implemented.

5. Conclusions

To have sustainable development in coastal areas, attention should be drawn to present climate conditions as well as possible future climate scenarios. The present study focuses on the possible effects of climate changes on wind-wave characteristics in Chabahar Bay. In this regard, using wind data as well as bathymetric data of the study area, the wind-wave model was implemented as part of the MIKE21 model system. Next, the model outputs were compared and calibrated with data from buoy located in Chabahar Bay, using statistical methods. Once a model performance was shown reliable, it was run for an 11-year calibration period. Then, using the flow model of MIKE21, the sea level was simulated.

To predict the effect of climate change, global climate model data (CGCM3.1) was downscaled for A1B and A2 scenarios. Results suggest that in comparison to the current climate regimes, there is a notable potential for coastal inundation in the future climate, 2071—2100, and increased Hs wave climate, particularly in regard to the A2 climatic change scenario. Clearly, additional studies are needed, including ensembles of simulations, and additional climate scenarios, such as the more recent RCP4.5 and RCP8.5. When a consensus is reached of these additional studies, with some level of reliability, society may need to re-examine policies and protocols guiding offshore and coastal infrastructure and activities, for sure concerns as design criteria and operational procedures, for example in routine situations as well as in emergencies and severe storm events. These considerations might affect a wide range of activities such as offshore and coastal oil and gas developments, marine transport, fisheries, recreational coastal touring, search and rescue, and coastal security.

References

Bindoff, N.L., Willebrand, J., Artale, V., Cazenave, A., Gregory, J., Gulev, S., Hanawa, K., Le Quere, C., Levitus, S., Nojiri, Y., Shum, C.K., Talley, L.D., Unnikrishnan, A.S., 2007. Observations: oceanic climate change and sea level. In: Solomon, S., Qin, D., Manning, M., Chen, Z., Marquis, M., Averyt, K.B., Tignor, M., Miller, H.L. (Eds.), Climate Change 2007: The Physical Science Basis. Contribution of Working Group I to the Fourth Assessment Report of the Intergovernmental Panel on Climate Change. Cambridge Univ. Press, Cambridge, New York, 387—429.

Breslow, P.B., Sailor, D.J., 2002. Vulnerability of wind power resources to climate change in the continental United States. Renew. Energ. 27 (4), 585—598, http://dx.doi.org/10.1016/S0960-1481(01)00110-0.

Chini, N., Stansby, P., Leake, J., Wolf, J., Roberts-Jones, J., Lowe, J., 2010. The impact of sea level rise and climate change on inshore wave climate: A case study for East Anglia (UK). Coast. Eng. 57 (11—12), 973—984, http://dx.doi.org/10.1016/j.coastaleng.2010.05.009.

Dastgheib, A., Reyns, J., Thammasittirong, S., Weesakul, S., Thatcher, M., Ranasinghe, R., 2016. Variations in the wave climate and sediment transport due to climate change along the coast of Vietnam. J. Marine Sci. Eng. 4 (4), 86, http://dx.doi.org/10.3390/jmse4040086.

DHI, 2005. Mike21 spectral wave module. Sci. Document. Danish Hydraulic Institute (DHI).

Duan, W., He, B., Takara, K., Luo, P., Hu, M., Alias, N.E., Ishihara, M., Wang, Y., 2014. Climate change impacts on wave characteristics along the coast of Japan from 1986 to 2012. J. Coast. Res. 86 (Special Issue 1), 97—104, http://dx.doi.org/10.2112/SI68-013.1.

Goharnejad, H., Shamsai, A., Hosseini, S.A., 2013. Vulnerability assessment of southern coastal areas of Iran to sea level rise: evaluation of climate change impact. Oceanologia 55 (3), 611—637, http://dx.doi.org/10.5697/oc.55-3.611.

Guo, L., Perrie, W., Long, Z., Toulany, B., Sheng, J., 2015. The impacts of climate change on the North Atlantic wave climate. Atmos. Ocean 53 (5), 1—19, http://dx.doi.org/10.1080/07055900.2015.1103697.

Gutmann, E.D., Rasmussen, R.M., Liu, C., Ikeda, K., Gochis, D.J., Clark, M.P., Dudhia, J., Thompson, G., 2012. A comparison of statistical and dynamical downscaling of winter precipitation over complex terrain. J. Climate 25, 262—281, http://dx.doi.org/10.1175/2011JCLI4109.1.

Horton, R., Herweijer, C., Rosenzweig, C., Liu, J., Gornitz, V., Ruane, A.C., 2008. Sea level rise projections for current generation CGCMs based on the semiempirical method. Geophys. Res. Lett. 35 (2), L02715, http://dx.doi.org/10.1029/2007GL032486.

Houghton, J.T., Ding, Y., Griggs, D.J., Noguer, M., van der Linden, P.J., Xiaosu, D. (Eds.), 2001. Climate Change 2001: The Scientific Basis. Contribution of Working Group I to the Third Assessment Report of the Intergovernmental Panel on Climate Change. Cambridge Univ. Press, Cambridge, New York, 639—693.

Intergovernmental Panel on Climate Change (IPCC), 2001. In: Houghton, J.T., Ding, Y., Griggs, D.J., Noguer, M., van der Linden, P.J., Dai, X., Maskell, K., Johnson, C.A. (Eds.), Climate Change 2001: The Scientific Basis. Contribution of Working Group I to the Third Assessment Report of the Intergovernmental Panel on Climate Change. Cambridge Univ. Press, Cambridge, New York, 881 pp.

Intergovernmental Panel on Climate Change (IPCC), 2007. In: Solomon, S., Qin, D., Manning, M., Chen, Z., Marquis, M., Averyt, K.B., Tignor, M., Miller, H.L. (Eds.), Climate Change 2007: The Physical Science Basis. Contribution of Working Group I to the Fourth Assessment Report of the Intergovernmental Panel on Climate Change. Cambridge Univ. Press, Cambridge, New York, 996 pp.

Jevrejeva, S., Moore, J.C., Grinsted, A., 2010. How will sea level respond to changes in natural and anthropogenic forcings by 2100? Geophys. Res. Lett. 37 (7), L07703, http://dx.doi.org/10.1029/2010GL042947.

Kamranzad, B., 2014. Assessment of the changes in average wind speed in Chabahar, Gulf of Oman, due to climate change. Int. J. Maritime Tech. 19, 13—20, (in Persian).

Kamranzad, B., Etemad-Shahidi, A., Chegini, V., Hadadpour, S., 2013. Assessment of CGCM 3.1 wind field in the Persian Gulf. J. Coast. Res. 65, 249—253, http://dx.doi.org/10.2112/SI65-043.1.

Karymbalis, E., Chalkias, C., Chalkias, G., Grigoropoulou, E., Manthos, G., Ferentinou, M., 2012. Assessment of the sensitivity of the southern coast of the Gulf of Corinth (Peloponnese, Greece) to sea-level rise. Cent. Eur. J. Geosci. 4 (4), 561—577.

Mitchell, J.A., Bett, P.E., Hanlon, H.M., Saulter, A., 2015. Investigating the impact of climate change on the UK wave power climate. Meteorol. Z. 26 (3), 291—306, http://dx.doi.org/10.1127/metz/2016/0757.

Pantusa, D., D'Alessandro, F., Riefolo, L., Principato, F., Tomasicchio, G., 2018. Application of a Coastal Vulnerability Index. A case study along the Apulian coastline, Italy. Water 10 (9), 1218, http://dx.doi.org/10.3390/w10091218.

Pendleton, E.A., Thieler, E.R., Williams, S.J., 2005. Coastal vulnerability assessment of Cape Hatteras National Seashore (CAHA) to sea-level rise. Open-file Rep., http://dx.doi.org/10.3133/ofr20041064 20 pp.

Pfeffer, W.T., Harper, J.T., O'Neel, S., 2008. Kinematic constraints on glacier contributions to 21st-century sea-level rise. Science 321 (5894), 1340—1343, http://dx.doi.org/10.1126/science.1159099.

Rahimipouri, H., Gharibreza, M., Isaee, H., Dolatshahi, M., 2006. Hydrodynamic of Currents and Prediction of Erosion and Sedimentation Pattern of the GB. Soil Conservation and Watershed Management Res. Inst., Tehran, 246 pp.

Rahmstorf, 2007. A semi-empirical approach to projecting future sea level rise. Science 315 (5810), 368—370, http://dx.doi.org/10.1126/science.1135456.

Shirinmanesh, S., Chegini, V., 2014. Tidal energy extraction in Chabahar Bay. Geosciences 24 (93) (in Persian).

Stone, M.C., Hotchkiss, R.H., Mearns, L.O., 2003. Water yield responses to high and low spatial resolution climate change scenarios in the Missouri River Basin. Geophys. Res. Lett. 30 (4), 1186, http://dx.doi.org/10.1029/2002GL016122.

Tragaki, A., Gallousi, C., Karymbalis, E., 2018. Coastal hazard vulnerability assessment based on geomorphic, oceanographic and demographic parameters: the case of the Peloponnese (Southern Greece). Land 7 (2), 56, http://dx.doi.org/10.3390/land7020056.

Trzaska, S., Schnarr, E., 2014. A review of downscaling methods for climate change projections. US Agency Internat. Develop., Tetra Tech ARD, 1—42.

Vanem, E., Natvig, B., Huseby, A.B., 2012. Modelling the effect of climate change on the wave climate of the world's oceans. Ocean Sci. J. 47 (2), 123—145, http://dx.doi.org/10.1007/s12601-012-0013-7.

Wandres, M., Pattiaratchi, C., 2017. Projected changes of the southwest Australian wave climate under two atmospheric greenhouse gas concentration pathways. Ocean Model. 117, 70—87.

WCRP Global Sea Level Budget Group, 2018. Global sea-level budget 1993—present. Earth System Sci. Data 10, 1551—1590, http://dx.doi.org/10.5194/essd-10-1551-2018.

Wojtysiak, K., Herman, A., Moskalik, M., 2018. Wind wave climate of west Spitsbergen: seasonal variability and extreme events. Oceanologia 60 (3), 331—343, http://dx.doi.org/10.1016/j.oceano.2018.01.002.

Oceanologia (2019) 61, 427—444

Available online at www.sciencedirect.com

ScienceDirect

journal homepage: www.journals.elsevier.com/oceanologia/

ORIGINAL RESEARCH ARTICLE

Spatio-temporal variations in sulfur-oxidizing and sulfate-reducing bacterial activities during upwelling, off south-west coast of India

A. Sam Kamaleson [a], Maria-Judith Gonsalves [a,*], Swatantar Kumar [b], V.K. Jineesh [c], P.A. LokaBharathi [a]

[a] *CSIR-National Institute of Oceanography, Dona Paula, Goa, India*
[b] *International Max Planck Research School of Global Biogeochemical Cycles, Friedrich Schiller University, Jena, Germany*
[c] *Academy of Climate Change, Education and Research, Agricultural University, Kerala, India*

Received 15 October 2018; accepted 13 March 2019
Available online 8 April 2019

KEYWORDS
Sulfate-reduction;
Sulfur-oxidation;
Environmental parameters;
Upwelling phases;
South-west coast of India;
Arabian Sea

Summary The Arabian Sea, off SW India, is becoming more anoxic in recent years. Poor ventilation affects microbial degradation of organic matter in the oxygen minimum zone ($\leq$2.85 ml l^{-1} O_2, $\leq$0.02 μM NO_2) and the anoxic marine zone ($\leq$0.09 ml l^{-1} O_2, $\geq$0.5 μM NO_2). We posit that one of the reasons at the microbial level could be due to a more prominent increase in sulfate-reducing activity (SRA), than sulfur-oxidizing activity (SOA). Hence, the objective was to measure the extent to which SOA can counter the effect of SRA. We, therefore examined these activities along with relevant environmental variables from 2009 to 2011 off Kochi (9.55°N—75.33°E) and Trivandrum (8.26°N—76.50°E), covering the three phases of upwelling. SRA was measured radiometrically using ^{35}S, and SOA by iodometry. Off Kochi, the SOA of the water column increased 6× (194—1151 μM d^{-1}) and SRA 4× (13—54 nM d^{-1}) from phase I to III. Off Trivandrum, the increase in SOA was 1.7× (339—560 μM d^{-1}) and SRA 7× (24—165 nM d^{-1}) contributing to the build-up of reducing/oxidizing conditions. This increase in SOA moderates the effect of increase in SRA. Besides, the average concentrations of dissolved oxygen and nitrite off Trivandrum were 1.80 ± 1.66, 1.48 ± 1.55, 1.93 ± 1.86 ml l^{-1} and 0.14 ± 0.14, 1.69 ± 0.67, 0.34 ± 0.42 μM during the three phases respectively. Hence, it is suggested that the coastal

* Corresponding author at: CSIR-National Institute of Oceanography, Dona Paula, Goa, 403004, India. Tel.: +918322450624; fax: +91(0)832-2450602.
E-mail address: mjudith@nio.org (M.-J. Gonsalves).
Peer review under the responsibility of Institute of Oceanology of the Polish Academy of Sciences.

Production and hosting by Elsevier

https://doi.org/10.1016/j.oceano.2019.03.002

waters examined in this study could probably be between oxygen minimum zone (OMZ) and anoxic minimum zone (AMZ) in patches temporarily. The present paper highlights the interactions between sulfate-reducing and sulfur-oxidizing activities, during upwelling for the first time in these waters. These observations give an important and timely insight into the implications.

1. Introduction

In the North Indian Ocean, off the south-west coast of India, the Arabian Sea water experiences seasonal upwelling during the summer monsoon (May—September). This upwelling phenomenon initiates from Trivandrum (TVM) in the south, and its strength decreases northward (Shetye et al., 1990). The process generally comprises of three different phases, i.e., the initial (May to June: phase I), middle (July to August: phase II) and final (August to September: phase III). During the first phase, primary productivity is at a relatively higher rate triggered by the nutrients brought to the surface. In the second phase, the primary production increases, along with an increase in secondary production. In the third phase, the processes decline, accompanied by plankton degradation by microbes mediating different biogeochemical cycles (Walsh et al., 1999).

While a number of researchers have covered the physical and chemical aspects influencing the biological parameters like primary, secondary and tertiary production (Kumar et al., 2001; Madhupratap et al., 2003; Naqvi, 1991; Shetye et al., 2015), the important aspect of bacterial contribution linking different trophic levels and different parameters have been few. Lately, off TVM and off Kochi, Malik et al. (2015), observed strong relationships between the variables mediated by the microbes.

The maintenance of redox conditions of such coastal systems could depend upon the capacity to oxidize or reduce a certain amount of organic material without significantly changing the redox potential. This net condition could result from several oxidizing and reducing activities prevailing in the system. The relative increase in the sulfate-reducing activity over sulfur-oxidizing activity could be one such important redox cycle that could play a major role in contributing to the lowering of dissolved oxygen and other electron acceptors like nitrate and the "build-up of reducing conditions". It is this accumulation of these reducing conditions/regions coupled with the weak ventilation that could add to the spread of the oxygen minimum zone (OMZ) in space and time. During monsoon/upwelling, intense winds tend to weaken the OMZ in the upper layers by the supply of oxygen through enhanced ventilation which is greater than oxygen consumed by remineralization. However, below thermocline layers (>100 m, Banse et al., 2017), the biological consumption of oxygen exceeds the supply of oxygen by ventilation which causes intensification and expansion of OMZ on a decadal scale (Lachkar et al., 2018). In line with these observations, we have noticed such intensification at the micro-aerophilic to anaerobic level, which particularly revolves around the activities of colourless sulfur-oxidizing (CSOB) and sulfate-reducing bacteria (SRB) and the interactions between them.

Previous studies by Canfield et al. (2010) in the OMZ of Chilean coast have used the metagenomic approach to study the cryptic sulfur cycle. Nevertheless, in our studies, the abundance and activity of pertinent microbial groups were used to understand the spatiotemporal spread in oxidizing/reducing conditions in upwelling waters. However, Banse et al. (2014) stated that 8—12°N of Arabian Sea was outside the suboxic OMZ. Moreover, till 2004, the borders of the OMZ in the Arabian Sea, extended from 18°N to 11°N at a depth of 150—400 m (Banse et al., 2017). More importantly, it has been reported that the Arabian Sea OMZ is weakly dictated by the seasonal cycle of ocean dynamics and the biogeochemistry influenced by the Asian monsoon system of the region. Also, OMZ of this region is "spatially decorrelated" from the coastal upwelling systems where biological productivity is the highest (Resplandy et al., 2012).

However, the participation of microbes and the processes they mediate need to be quantified to appreciate their relative influence from the oxic to the sub-oxic state of the waters. Sulfate-reduction could be an important process in the anaerobic marine environment (Canfield et al., 2005) perhaps even in the OMZ. Organic mineralization by SRA in the marine ecosystem is one of the important terminal degradative processes in low ambient oxygen concentration. It is able to degrade >50% organic matter, accumulating sulfide in the process (Jørgensen and Boetius, 2007). SRB are ubiquitous and are prevalent under both anaerobic and aerobic conditions (Bottrell et al., 1991; Fortin et al., 2002; Gibson, 1990; Winch et al., 2009). Besides, a relatively wide number of sulfate-reducing bacterial genera have been identified from the water column of stratified fjords (Teske et al., 1996). Generally, oxic degradation of organic matter is followed by micro-aerobic to anaerobic breakdown. The predominance of anaerobic bacterial community and their activity over the aerobic counterparts could contribute to the intensification of the reducing conditions in the eastern Arabian Sea (Gonsalves et al., 2011). Besides, SRB and their activity have been known to propagate in regions rich in electron donors like sediments and even in surface layers of euphotic waters (Teske et al., 1996). This is particularly true for upwelling waters where electron donors are supplied both physically due to upwelling and biologically by primary and secondary production.

The colourless sulfur-oxidizing bacteria (CSOB) and their activity could play a major role in oxidizing reduced sulfur and restoring the redox balance in the ecosystem (Jørgensen and Gallardo, 1999; Lavik et al., 2009). SOA could be prominent even in the absence of oxygen, where nitrate could act as an alternate electron acceptor (Fossing et al., 1995). Such interactions between sulfate-reducing and sulfur-oxidizing bacteria have been elucidated but restricted to the sediments of upwelling regions off Namibia, Peru and

Chile using lipid biomarkers (Arning et al., 2008; Canfield, 2001). The present study aims to understand the extent of SRA and SOA in the upwelling waters of the south-west coast of India. Here, the term reducing activity has been used, in the context where the rate of increase in sulfate-reducing activity is more than the rate of increase in sulfur-oxidizing activity during the three phases of the study.

We posit that one of the explanations for the restoration of redox balance could be a higher "increase" in sulfur-oxidizing activity (SOA) when compared to "increase" in sulfate-reducing activity (SRA). However, a significantly large imbalance in which SRA exceeds SOA could lead to the spread of reducing conditions in time and space. Hence, the activity and the distribution patterns of bacteria responsible for these processes were examined along the transects off Kochi and Trivandrum during the initial, middle and final phases of upwelling. The present paper highlights the interactions between sulfate-reducing and sulfur-oxidizing bacterial abundance and their activities, along with the related environmental parameters during upwelling.

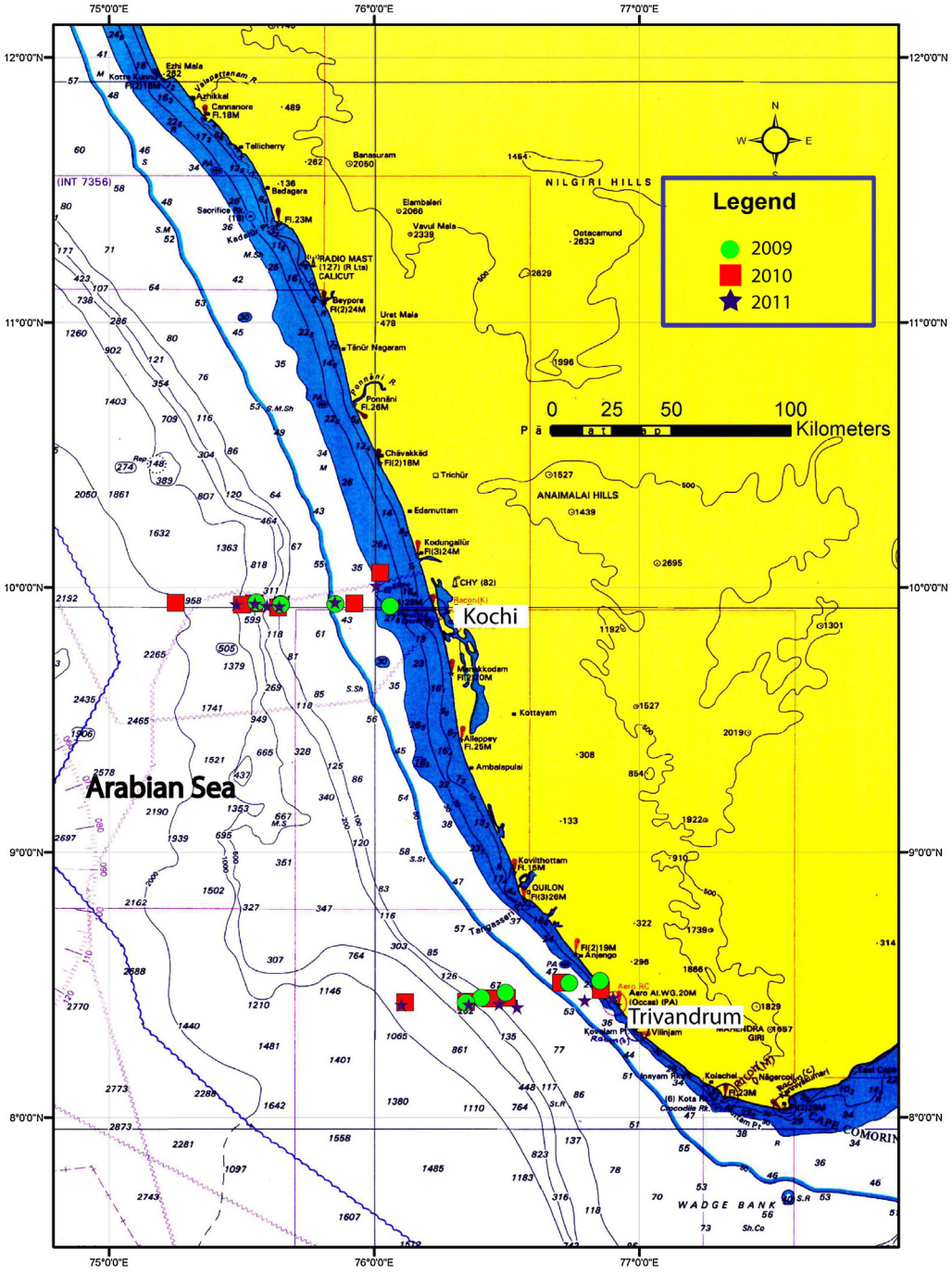

Figure 1 Details of sampling locations off Kochi and Trivandrum, southwest coast of India during phase I (2009), phase II (2010) and phase III (2011) of upwelling.

Table 1 Details of sampling depths in the southwest coast of India during phase I (2009), phase II (2010) and phase III (2011) of upwelling.

Station no.	Water depth [m]	Sampling depth [m] Kochi and Trivandrum
1	30	5, 15, 25
2	50[a]	5, 10, 25, 45
3	100	5, 20, 60, 80, 90
4	200	5, 20, 60, 80, 150, 175
5	500[b]	5, 20, 60, 80, 150, 300, 450

Total number of samples, *n*: Phase I (2009) = 25; Phase II (2010) = 28; Phase III (2011) = 32.
[a] No sampling during Phase II.
[b] No sampling during Phase I.

2. Material and methods

2.1. Description of the study sites

Water samples were collected onboard FORV *Sagar Sampada*, during cruises #267 (2009), #276 (2010), #289 (2011), along the transect off Trivandrum and Kochi in the south-eastern Arabian Sea at 8.26°N–76.50°E & 9.55°N–75.33°E (Fig. 1), during the three phases of upwelling – end-May to end-June 2009, initial phase (phase I), July to mid-August 2010, middle phase (phase II) and mid-August to mid-September 2011, final phase (phase III). Hereafter, these samplings would be referred to as phase I, II and III respectively. Samples were collected at different depths from six different stations in each transect (Table 1).

2.2. Sample collection

Water samples were collected using 10 L Niskin bottles fixed to CTD-rosette system. Bottles were rinsed twice with sample water before sub-sampling for parameters like dissolved oxygen (DO), nutrients (nitrate, nitrite, phosphate and silicate), chlorophyll *a* (Chl *a*), phaeopigments, total counts (TC) and total viable counts (TVC) of bacteria, sulfate-reducing bacteria (SRB) and colourless sulfur-oxidizing bacteria (CSOB). Experiments were conducted for SRA and SOA and were incubated onboard.

2.3. Chemical parameters

Dissolved oxygen was measured by Winkler's titrimetric method (Strickland and Parsons, 1977). Samples were collected in 125 ml glass stoppered bottles without air bubbles and were immediately fixed with Winkler's reagents. Fixed samples were stored in the dark for further analyses. DO samples were analyzed onboard using a dosimeter (Metrohms785 DMP Titrino). Analyses of nutrients were carried out onboard using a SKALAR auto analyzer (Wurl, 2009). Chlorophyll *a* (Chl *a*) concentrations were determined (Yentsch and Menzel, 1963) fluorometrically (Turner Designs, USA). Samples were filtered on GF/F filters (0.7 μm) and the extraction was done by adding 10 ml of 90% acetone to the filter and incubating for 24 h in the dark under refrigerated condition. For phaeopigments, the Chl *a*, samples were acidified with 10% HCl just before fluorometric measurement (Yentsch and Menzel, 1963). Ammonium was estimated manually by spectrophotometric method (Grasshoff et al., 1983).

2.4. Bacteriological parameters

The TC of bacteria was determined by acridine orange direct count (AODC) method using epifluorescence microscopy and expressed as numbers per litre. Aliquots of 5 ml water sample in triplicate were each fixed with 250 μL of buffered formalin (2% final concentration) as described by Hobbie et al. (1977). TVC was done quantitatively as outlined by Kogure et al. (1984). In brief, the yeast extract in the incubating medium allows for an increase in size but the cocktail of antibiotics used prevented the cell division, thus enabling the enumeration of enlarged cells. The fixed water samples of TVC were stained for 5 min with acridine orange (final concentration 2%) and filtered through 0.22 μm Millipore black nucleopore membrane filters. The bacterial cells were counted by epifluorescence microscope (Nikon Epifluorescence Microscope, Model A 80i) and expressed as numbers per litre.

SRB were enumerated using the most probable number (MPN) method, with the liquid media supplemented with 0.5 mM lactate and 0.5 mM acetate as carbon sources (Hatchikian's medium (1972) modified by LokaBharathi and Chandramohan (1990)). The samples were inoculated in screw-capped tubes and incubated at 27 ± 2°C and were enumerated after 15–20 days.

Modified Leiske's medium with 10% of the recommended thiosulfate concentration (0.5 g l^{-1}) was used for the enumeration of CSOB by MPN technique (LokaBharathi, 1989 and references therein). The samples were incubated at 27 ± 2°C for 5–7 days and the numbers were expressed as cells l^{-1}.

MPN method used as the target organisms were less in numbers and difficult to grow on medium containing agar. This method also helps to measure the number and activity simultaneously. Though the method selected is used for fast-growing bacteria on liquid medium, it is also useful for comparing trends in the distribution of numbers and activity across samples (LokaBharathi et al., 1988).

2.5. Sulfate-reducing activity

SRA was measured in the terms of rate (SRR) expressed in nM d^{-1}. The method was described earlier by King (2001) and was adopted for coastal waters by Lavik et al. (2009). Radioactive sodium sulfate 300 μl ($^{35}SO_4^{-2}$, specific activity, 37 kBq from BARC, Mumbai) was injected into a known volume of sample in gas-tight vials and the activity was arrested at the end of 72 h by adding 5 ml (5% w/v) zinc acetate and maintained at 4°C until further analysis. At each station, zinc acetate was added to each tube before the tracer addition to determine a blank. Radioactivity was measured using a liquid scintillation counter (Perkin Elmer Wallace 1409 DSA). SRA was calculated using the equation:

$$\mathrm{SRA(dpm)} = \left(\frac{H_2{}^{35}S}{{}^{35}SO_4{}^{2-}}\right) \times {}^{32}SO_4{}^{2-} \times \frac{IDF}{T},$$

where SRA is the sulfate-reducing activity, $H_2{}^{35}S$ the radioactivity of reduced sulfur in DPM (disintegration per minute), $^{35}SO_4{}^{2-}$ the radioactivity of sulfate at the beginning of incubation, $^{32}SO_4{}^{2-}$ the sea water sulfate concentration in mM $SO_4{}^{2-}$, IDF the isotopic discrimination factor = 1.06, and T is the time of incubation in hours.

The SRA was calculated from the amount of radioactive sulfate used and was expressed in nM $SO_4{}^{2-}$ d^{-1}. The SRB medium contained both lactate and acetate in order to assess the SRA at the expense of both the major substrates.

2.6. Sulfur-oxidizing activity

The water samples were tested for their ability to oxidize thiosulfate by measuring the residual concentration of thiosulfate, iodimetrically (Hansen, 1973). To 200 ml of sample, 50 ml of diluted sulfuric acid (3 N), and 25 ml of 0.0125 N iodine solution were added and titrated immediately with standardized 0.0125 N $Na_2S_2O_3{\cdot}5H_2O$ until most of the iodine was consumed. A few drops of freshly prepared starch solution (1%) was added and titrated until the blue colour disappeared. Blanks were estimated as mentioned below. The method was suitably adopted to estimate MPN and to measure the sulfur-oxidizing activity. The experimental tubes were incubated at $27 \pm 2^{\circ}C$ for 5–7 days. Uptake of thiosulfate was expressed as $\mu M\ S_2O_3\ d^{-1}$.

Titre value of sea water blank (Avg): A
Titre value of un-inoculated media (Avg): B
Average titre value of sample: S

$$\frac{A-B\times 1400}{\text{Volume of sea water used for titration (100 ml)}} = B1\ (\text{thiosulfate measured in medium}),$$

$$\frac{A-S\times 1400}{\text{Volume of sea water used for titration (100 ml)}} = S1\ (\text{thiosulfate measured in sample}),$$

where 1400 = mol. wt. of S_2O_3 ($112 \times 0.0125\ N \times 1000$),

$$B1-S1 = D\ (\text{amount of thiosulfate utilized [mg]}) = D/112\ (\text{mol. wt. of } S_2O_3) \times 1000\ (\text{mg to } \mu g)/\text{incubation in days} = D\ \mu M d^{-1}.$$

The rates of these processes are generally measured in nM for sulfate reduction (Albert et al., 1995) and μM for thiosulfate oxidation (Tuttle and Jannasch, 1976; Visscher et al., 1992). This difference in the activity is attributable to ecological and technical reasons. While the product of the former (sulfide) is environmentally toxic to fauna even in low concentrations from nM to μM, the latter, is relatively benign. Therefore, there is a 3–4 order difference between the two activities. Technically the methodology for sulfate reduction based on radiometry is much more sensitive to lower concentrations than the iodometric method for thiosulfate oxidation.

It is, therefore, suggested that the spread of reducing activity may not be directly based on the stoichiometry but on the 'actual changes in the rates' of these two activities over the three different phases of upwelling. It should be noted that the main focus is on measuring the "relative increase" in these activities over the three phases.

2.7. Statistical analysis

Biological data was $\log(x+1)$ transformed for statistical analysis. Correlations between biological and environmental parameters were determined using Statistica version 6.0. One-way analysis of variance (ANOVA) was performed on data to find the significant variation between SRA, SOA from phase I to phase III. The analysis was carried out using Statistica 6.0 software package.

3. Results

Comparison of transects, parameter wise, off Kochi and TVM, was performed to reveal how microbial variables especially SRA/SRB and SOA/CSOB responded to differences in the physical, chemical and biological forcings. The vertical variations in these parameters were more off Kochi than off TVM.

3.1. Physico-chemical parameters

Off Kochi, from phase I to phase III, the average values of physico-chemical parameters like temperature (23.58–20.31°C), pH (7.97–7.56), salinity (35.05–34.77) and DO concentrations (2.03–1.82 ml l^{-1}) showed decreasing trends (Table 2) with a dip in the DO concentration in the second phase of 1.75 ml l^{-1}. The average values of parameters for the three different phases showed decreasing trends. This decrease is not statistically significant. However, the water column averages of some chemical parameters like nitrate, nitrite and phosphate showed little variation over the study period. Other chemical parameters like silicate concentrations decreased from 7.64 to 5.08 μM with a dip in the second phase (0.32 μM), and ammonium concentration showed a definite increase from 0.07 to 1.51 μM (Table 2, Fig. 2a).

Off TVM, the average values of the parameters from phase I to phase III, like temperature (21.56–20.69°C), pH (7.98–7.50) and salinity (34.97–34.84), also showed decreasing trends with little or no statistical significance. The nutrient distribution was different off TVM, from that off Kochi. Off TVM, nitrite, phosphate, and silicate did not show any definite trend, whereas nitrate and ammonium increased 1.3× (15.55–20.22 μM) and ~7× (0.19–1.31 μM) respectively (Fig. 2b). In the first phase, the range in the concentration of phosphate (0.18–2.96 μM), silicate (0.47–28.15 μM), and nitrate (0.02–37.78 μM) levels were higher off TVM than off Kochi.

Off Kochi, the SRA was not depth dependent, while off TVM, SRA decreased with depth, i.e. about 10% of the variation in SRA was negatively influenced by depth ($r = -0.315$; $r^2 \times 100 = 10\%$) in phase I and 13% in phase III. Off Kochi and TVM the SRB was depth dependent in phase I and phase III. However, the temperature had a positive influence of 36% on the distribution of SRB ($p < 0.05$) in phase I off Kochi.

Off TVM, nutrients affect the distribution of CSOB in phase I, phase III and that of SRB in phase II. Relationship of SRB with

Table 2 Range (bold), average and standard deviation (±) of physico-chemical and biological parameters during the three phases of upwelling (2009–2011).

Parameters	Phase I		Phase II		Phase III	
	Kochi	Trivandrum	Kochi	Trivandrum	Kochi	Trivandrum
Temperature (°C)	[a]**13.46–28.88**	**10.90–29.18**	**11.30–26.90**	**11.25–28.30**	**7.26–27.03**	**7.13–28.04**
	[b]23.58 ± 4.97	21.56 ± 4.94	23.06 ± 4.03	20.07 ± 5.80	20.31 ± 5.79	20.69 ± 6.17
Salinity (%)	**34.88–35.61**	**34.80–35.30**	**34.30–35.60**	**34.30–35.20**	**33.53–35.21**	**34.15–35.15**
	35.05 ± 0.20	34.97 ± 0.13	35.07 ± 0.29	34.97 ± 0.21	34.77 ± 0.43	34.84 ± 0.29
pH	**7.68–8.30**	**7.69–8.50**	**7.76–7.93**	**7.70–8.26**	**7.32–7.85**	**7.25–7.78**
	7.97 ± 0.23	7.98 ± 0.24	7.92 ± 0.23	7.90 ± 0.17	7.56 ± 0.18	7.50 ± 0.18
Phosphate (μM)	**0.16–2.42**	**0.18–2.96**	**0.35–4.51**	**0.85–1.56**	**0.23–2.16**	**0.30–5.16**
	1.44 ± 0.74	1.21 ± 0.81	1.49 ± 1.57	1.06 ± 0.25	1.25 ± 0.58	1.70 ± 0.94
Silicate (μM)	**0.29–19.45**	**0.47–28.15**	**ndl–1.74**	**0.07–4.75**	**1.07–12.40**	**0.71–18.76**
	7.64 ± 5.71	7.75 ± 7.48	0.32 ± 0.50	1.65 ± 1.12	5.08 ± 2.96	5.80 ± 4.30
Nitrate (μM)	**0.64–33.17**	**0.02–37.78**	**ndl–15.40**	**0.51–17.39**	**0.06–36.50**	**ndl–40.84**
	18.20 ± 11.26	15.55 ± 12.62	11.36 ± 7.37	12.56 ± 6.14	17.55 ± 13.37	20.22 ± 11.99
Nitrite (μM)	**0.04–1.96**	**ndl–0.68**	**0.13–7.0**	**1.24–4.25**	**ndl–2.15**	**ndl–1.39**
	0.34 ± 0.51	0.14 ± 0.14	1.92 ± 4.47	1.69 ± 0.67	0.28 ± 0.46	0.34 ± 0.42
Ammonium (μM)	**ndl–0.14**	**ndl–1.23**	**0.03–4.59**	**0.13–4.59**	**0.63–4.79**	**0.57–2.75**
	0.07 ± 0.06	0.19 ± 0.27	0.47 ± 1.06	0.79 ± 1.25	1.51 ± 0.80	1.31 ± 0.55
Chl *a* (μg l^{-1})	**ndl–2.18**	**ndl–1.04**	**0.35–17.45**	**ndl–3.49**	**0.07–15.31**	**0.02–1.90**
	0.67 ± 0.70	0.34 ± 0.33	4.97 ± 6.28	0.63 ± 1.03	1.96 ± 3.19	0.65 ± 0.58
Phaeopig* (μg l^{-1})	**ndl–0.76**	**ndl–0.87**	**0.80–2.17**	**0.02–2.67**	**ndl–10.72**	**ndl–2.98**
	0.28 ± 0.22	0.23 ± 0.21	1.29 ± 0.44	0.49 ± 0.68	1.06 ± 2.24	0.57 ± 0.58
Phaeopig/Chl *a*	**0.01–2.50**	**0.15–4.64**	**0.05–3.16**	**0.44–9.50**	**0.01–4.66**	**0.12–9.17**
	1.01 ± 0.80	1.38 ± 1.23	2.67 ± 9.25	2.65 ± 2.52	1.23 ± 1.36	1.85 ± 2.08
DO (ml l^{-1})	**0.29–4.88**	**0.03–4.40**	**0.54–4.50**	**0.23–4.57**	**0.40–5.24**	**0.33–5.17**
	2.03 ± 1.70	1.80 ± 1.66	1.75 ± 1.73	1.48 ± 1.55	1.82 ± 1.73	1.93 ± 1.86
TC × 10^8 l^{-1}	**8.21–8.73**	**8.32–8.91**	**8.11–10.58**	**8.83–10.17**	**0.50–7.12**	**0.94–9.56**
	8.39 ± 0.13	8.59 ± 0.14	9.48 ± 0.77	9.09 ± 0.27	3.20 ± 1.67	4.36 ± 2.13
TVC × 10^7 l^{-1}	**7.82–8.18**	**7.70–8.0**	**7.84–9.07**	**7.09–8.83**	**0.23–4.43**	**0.21–6.05**
	7.97 ± 0.11	7.84 ± 0.09	8.50 ± 0.32	8.44 ± 0.41	1.72 ± 1.03	1.98 ± 1.51
SRA (nM d^{-1})	**1.37–54.98**	**5.87–90.65**	**21.08–28.79**	**19.24–28.43**	**12.76–290.15**	**0.71–398.35**
	13.72 ± 14.55	23.90 ± 30.83	26.19 ± 2.15	22.89 ± 2.32	54.04 ± 71.90	165.17 ± 155.45
SRB × 10^4 l^{-1}	**0.05–0.91**	**0.18–1.50**	**0.04–2.20**	**0.20–4.0**	**0.01–0.90**	**0.01–0.96**
	0.46 ± 0.31	0.52 ± 0.34	0.33 ± 0.51	1.40 ± 1.17	0.25 ± 0.27	0.36 ± 0.30
SOA (μM d^{-1})	**18.74–568.62**	**9.39–601.71**	**33.85–729.58**	**3.76–793.51**	**348.46–1747.44**	**6.45–1728.10**
	194.25 ± 205.84	339.29 ± 195.37	360.19 ± 213.43	215.10 ± 232.67	1151.06 ± 365.16	560.93 ± 388.60
CSOB × 10^6 l^{-1}	**0.26–1.56**	**0.28–1.71**	**0.12–1.08**	**0.06–0.66**	**0.01–0.20**	**0.01–0.37**
	0.72 ± 0.45	0.83 ± 0.34	0.46 ± 0.23	0.34 ± 0.19	0.10 ± 0.05	0.15 ± 0.09

* *Note*: ndl, non-detectable limits; DO, dissolved oxygen; Chl *a*, chlorophyll *a*; phaeopig, phaeopigment; TC, total counts; TVC, total viable counts; SRB, sulfate-reducing bacteria; SRA, sulfate-reducing activity; SOA, sulfur-oxidizing activity; CSOB, colourless sulfur-oxidizing bacteria.

[a] Range.

[b] Average and standard deviation.

ammonium evolved from negative ($r = -0.394$, $p < 0.05$) to positive ($r = 0.424$, $p < 0.05$) from phase I to phase III and synchronized with an increase in phaeopigment from 0.23 μg l^{-1} in phase I to 0.57 μg l^{-1} in phase III. The SOA negatively influenced ambient phosphate (26%, $p < 0.01$), silicate (24%, $p < 0.01$) and nitrate concentrations (18%, $p < 0.05$) in phase I. In phase II, SOA positively correlated with nitrite ($r = 0.430$, $p < 0.05$) (Table 3).

Both groups of bacteria were influenced differently with phosphate. In phase I, off TVM, SOA related negatively with phosphate ($r = -0.506$, $p < 0.01$), while in phase II, SRB related positively ($r = 0.615$, $p < 0.01$). Silicate was influenced positively by SRB ($r = 0.446$, $p < 0.05$) in phase II and negatively by SOA ($r = -0.490$, $p < 0.01$) in phase I. However, SRB showed positive relation with phosphate ($r = 0.615$, $p < 0.01$) and silicate ($r = 0.446$, $p < 0.05$) in phase II.

3.2. Biological parameters

Off Kochi, the average Chl *a* values increased from 0.67 to 1.96 μg l^{-1} from phase I to phase III. High Chl *a* values

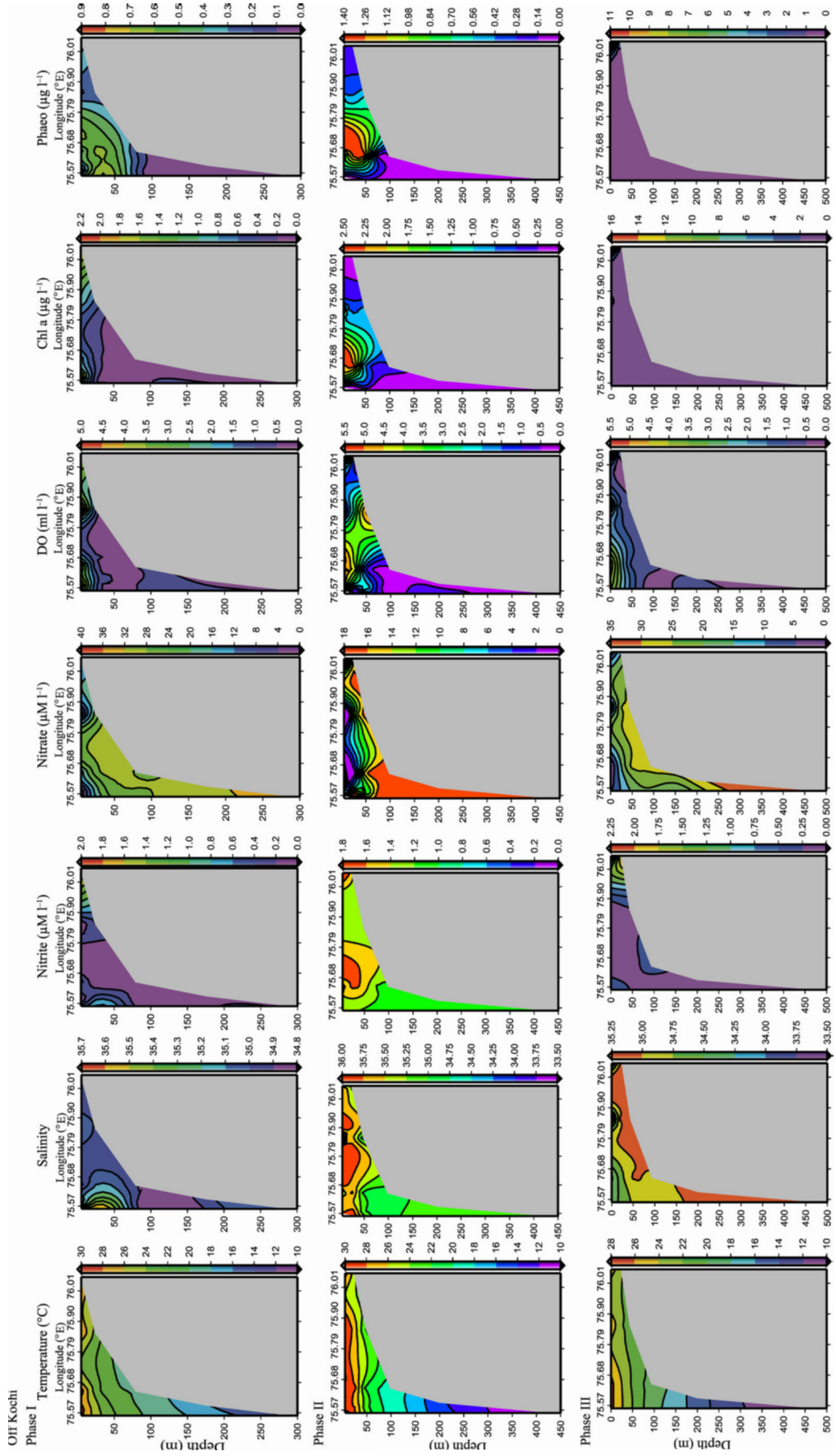

Figure 2 Distributory pattern of environmental parameters off (a) Kochi and (b) Trivandrum (TVM), showing depth wise variation on *y*-axis and distance from the shore on *x*-axis.

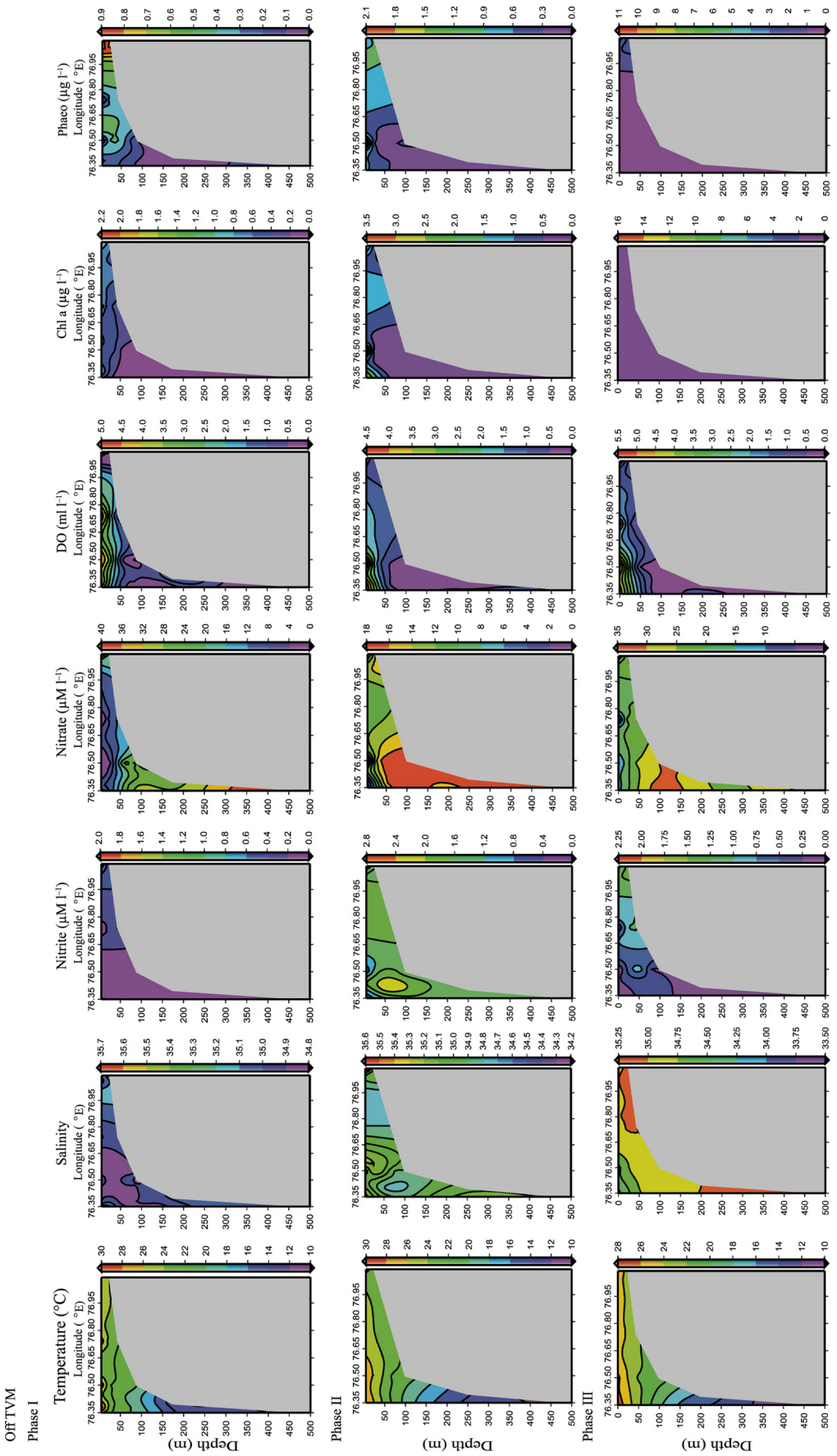

Figure 2 (*Continued*).

Table 3 Significant correlation of sulfate-reducing bacteria (SRB), sulfate-reducing activity (SRA), colourless sulfur-oxidizing bacteria (CSOB) and sulfur-oxidizing activity (SOA) with various environmental parameters.

Parameters	Kochi			Trivandrum		
	Phase I	Phase II	Phase III	Phase I	Phase II	Phase III
Depth	SRB (−0.545*)	CSOB (0.589**)		SOA (0.524*)	SRB (0.782***)	SRA (−0.359*)
Temperature	SRB (0.593*)	–	SRB (0.396*)	SRB (0.394*), SRA (0.396*), SOA (0.524*)	–	–
Nutrients	–	CSOB (NO_2^- 0.530*)	–	CSOB (NH_4^+ −0.394*), SOA (PO_4^{3-} −0.506**, SiO_4^{4-} −0.490**, NO_3^- −0.420*)	SRB (PO_4^{3-} 0.615**, SiO_4^{4-} 0.446*, NO_3^- 0.435*), SOA (NO_2^- 0.430*)	CSOB (NH_4^+ 0.424*, NO_2^- 0.417*), SOA (NO_3^- 0.364*)
Chlorophyll *a*	–	–	SOA (−0.523*)	SRB (0.572**), SRA (0.595**)	SRB (−0.451*)	SRA (0.382*)
Phaeopigments	–	CSOB (0.538*)	SOA (−0.549*)	SRB (0.539**), SRA (0.652***)	SRB (−0.442*)	–

Note: Values in parenthesis indicate *r* values (correlation coefficient). Chl *a*, chlorophyll *a*; phaeo, phaeopigments; PO_4^{3-}, phosphate; SiO_4^{4-}, silicate; NH_4^+, ammonium; NO_2^-, nitrite; NO_3^-, nitrate.
* $p < 0.05$.
** $p < 0.01$.
*** $p < 0.001$.

(4.97 μg l^{-1}) off Kochi in phase II was matched by low silicate (non-detectable levels (ndl) to 1.74 μM) and nitrate concentrations (ndl to 15.4 μM). Consequently, like Chl *a*, phaeopigments and phaeo/Chl *a* ratio also showed increasing trends over the phases from 0.28 to 1.06 μg l^{-1} and 1.01 to 1.23 μg l^{-1} respectively (Table 2).

Off TVM, the average Chl *a* increased from 0.34 μg l^{-1} in phase I, to 0.63 μg l^{-1} in phase II, and to 0.65 μg l^{-1} in phase III (Table 2). Like the transect off Kochi, the average phaeopigment concentrations off TVM showed a definite increasing trend from 0.23 μg l^{-1} to 0.57 μg l^{-1} from phase I to phase III. The phaeopigment/Chl *a* ratio ranged from 0.15–4.64 in phase I, 0.44–9.50 in phase II and 0.12–9.17 in phase III. The whole water column average of phaeo-pigment/Chl *a* ratio was 1.38 in phase I, 2.65 in phase II and 1.85 at phase III.

Off TVM, in phase I, SRB and SRA varied positively with Chl *a* ($r = 0.572$, $r = 0.595$, $p < 0.01$ respectively). In phase II, SRB varied negatively with Chl *a* ($r = -0.451$, $p < 0.05$) and in phase III, it was not influenced. However, in phase III, SRA varied positively with Chl *a* ($r = 0.382$, $p < 0.05$). In phase I, SRB and SRA varied positively with phaeopigment ($r = 0.539$, $p < 0.01$, $r = 0.652$, $p < 0.001$ respectively). In phase II, SRB varied negatively with phaeopigment ($r = -0.442$, $p < 0.05$), whereas in phase III, no such relationship was observed with SRB and SRA. Such relationships were not observed off Kochi (Table 3).

3.3. Microbiological parameters — abundance

Off Kochi, total bacterial counts were in the order of 10^8 l^{-1} and did not show significant variation over the period examined. Similarly, there was no appreciable change in the direct viable count which was one order less. Off TVM, the total bacterial abundance and viability was 4.36–8.59 × 10^8 l^{-1} and 1.98–7.84 × 10^7 l^{-1} respectively.

Off Kochi, the average SRB population showed low variation from 0.25 × 10^4 l^{-1}–0.46 × 10^4 l^{-1}. Off TVM, the range in SRB abundance was from 10^2 to 10^4 l^{-1}. Generally, higher SRB population was observed in the upwelling waters off TVM. Off Kochi, CSOB did not show any logarithmic variation and was in the range of 0.1 × 10^6 l^{-1} to 0.72 × 10^6 l^{-1}. Off TVM, CSOB populations varied from 0.15 × 10^6 l^{-1} to 0.83 × 10^6 l^{-1} (Fig. 3a and b, Table 2).

Spearman's correlation analysis showed TC to correlate with environmental parameters at phase I only off TVM (depth: $r = -0.473$, $p < 0.05$, temperature: $r = 0.631$, phosphate: $r = -0.664$, silicate: $r = 0.609$, nitrate: $r = -0.696$, ammonium: $r = 0.606$, Chl *a*: $r = 0.577$, phaeo/Chl *a*: $r = -0.502$, $p < 0.001$).

3.4. Microbiological parameter — activity

There was a general increase in reduction processes over the phases. Off Kochi, the average SRA increased from 13.72 nM d^{-1} in phase I, to 26.19 nM d^{-1} in phase II, and 54.04 nM d^{-1} during phase III. Off TVM, the average SRA increased from 23.90 to 165 nM d^{-1} from phase I to phase III, with a lower rate of 22.89 nM d^{-1} in phase II.

Off Kochi, SOA values were 194, 360, 1151 μM d^{-1}, for the three phases respectively. Comparatively, off TVM low SOA of 339, 215 and 560 μM d^{-1} was noticed during the three phases respectively.

Off Kochi, the average water column SRA increased 4 times, and SOA 6× from phase I to III. The increase in offshore SRA was 5.9× (10.09 nM d^{-1} to 59.58 nM d^{-1}) over these phases. Off TVM, the increase in column SRA was 7× (24 nM d^{-1} to 165 nM d^{-1}) and SOA was 1.7×. The increase in offshore SRA was 9× (13.94 nM d^{-1} to 126.65 nM d^{-1}) over the phases (Fig. 4).

Analysis of variance (ANOVA) of the whole column of SRA and SOA off Kochi and TVM further support our observation on the differences in the 2 processes between the transects. The increase in SRA from phase I to phase III is more significant off TVM ($p < 0.001$) than Kochi ($p < 0.03$). SOA, on the other hand, is more significant off Kochi ($p < 0.001$) than off TVM ($p < 0.04$) (Table 4).

4. Discussion

The results are discussed in the context of physicochemical parameters off Kochi, and TVM, followed by biological and microbial parameters. The interaction of geochemical variables of sulfur bacteria and their activities highlight for the first time, the contribution of this group to the ecology of the upwelling system in these waters.

The physical oceanographic processes influence the input of nutrients to the nutrient-impoverished waters of Arabian Sea (Goes et al., 2005; Wiggert et al., 2002) thus making it one of the most productive areas (Madhupratap et al., 1996). The decreasing trends of temperature, pH, DO in both the transects could be attributed to the different phases of upwelling which were associated with the different stages of monsoon. The upwelling is discernible by the presence of cooler more saline and denser water containing less DO than the normal waters of the surface layers (Fig. 2a and b).

The differences in the parameters off the two transects could be attributed to the difference in the upwelling intensity due to the differences in the strength of physical forcing of upwelling (Shetye et al., 1990).

Off Kochi, the increase in Chl *a* and phaeopigments at phase II has been noticed (Fig. 2a). The increase in the range of phaeopigments, and phaeo/Chl *a* ratio from phase I to

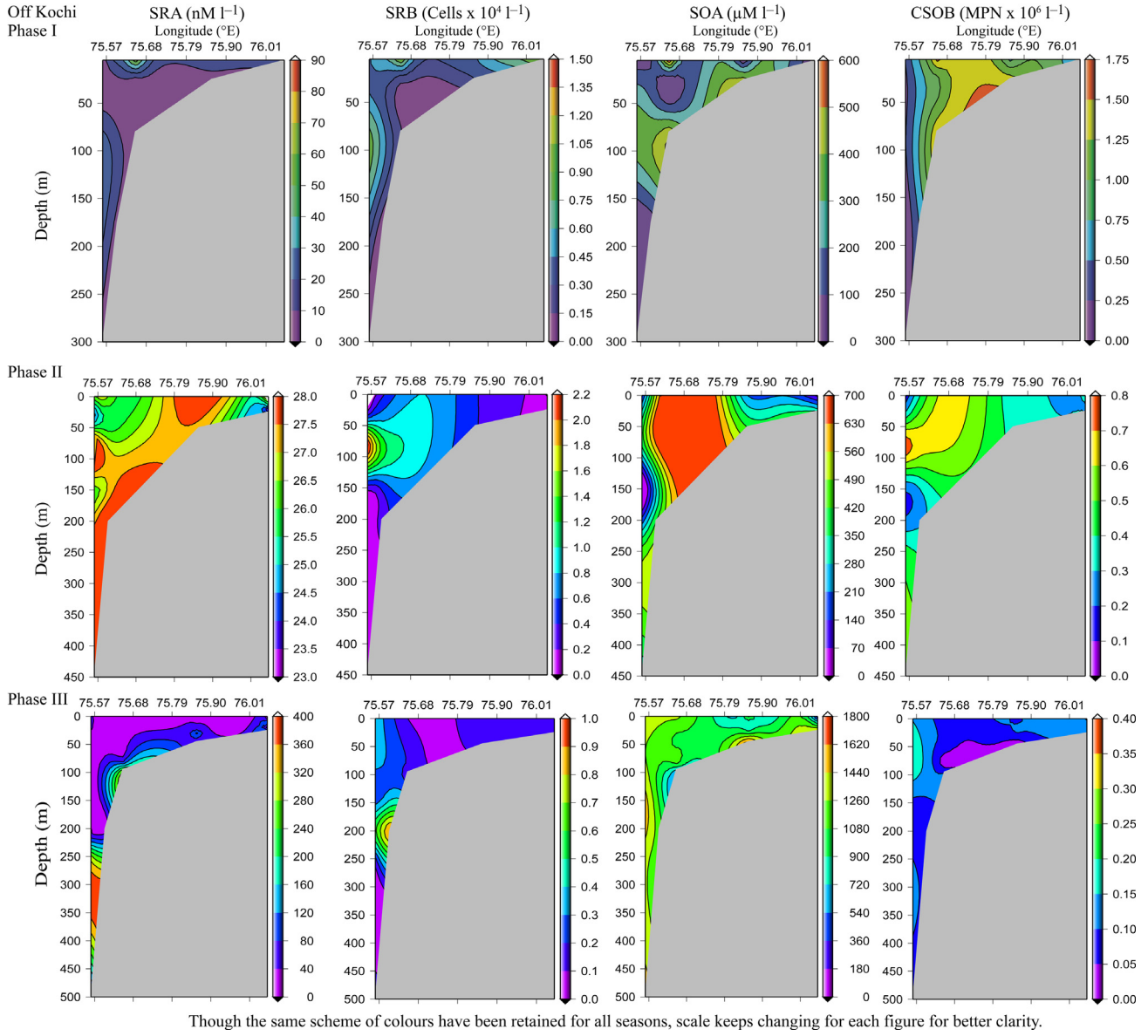

Figure 3 Distributory pattern of sulfate-reducing activity (SRA), sulfate-reducing bacteria (SRB), sulfur-oxidizing activity (SOA) and colourless sulfur-oxidizing bacteria (CSOB) off (a) Kochi and (b) Trivandrum (TVM) in southwest coast of India during phase I (2009), phase II (2010) and phase III (2011).

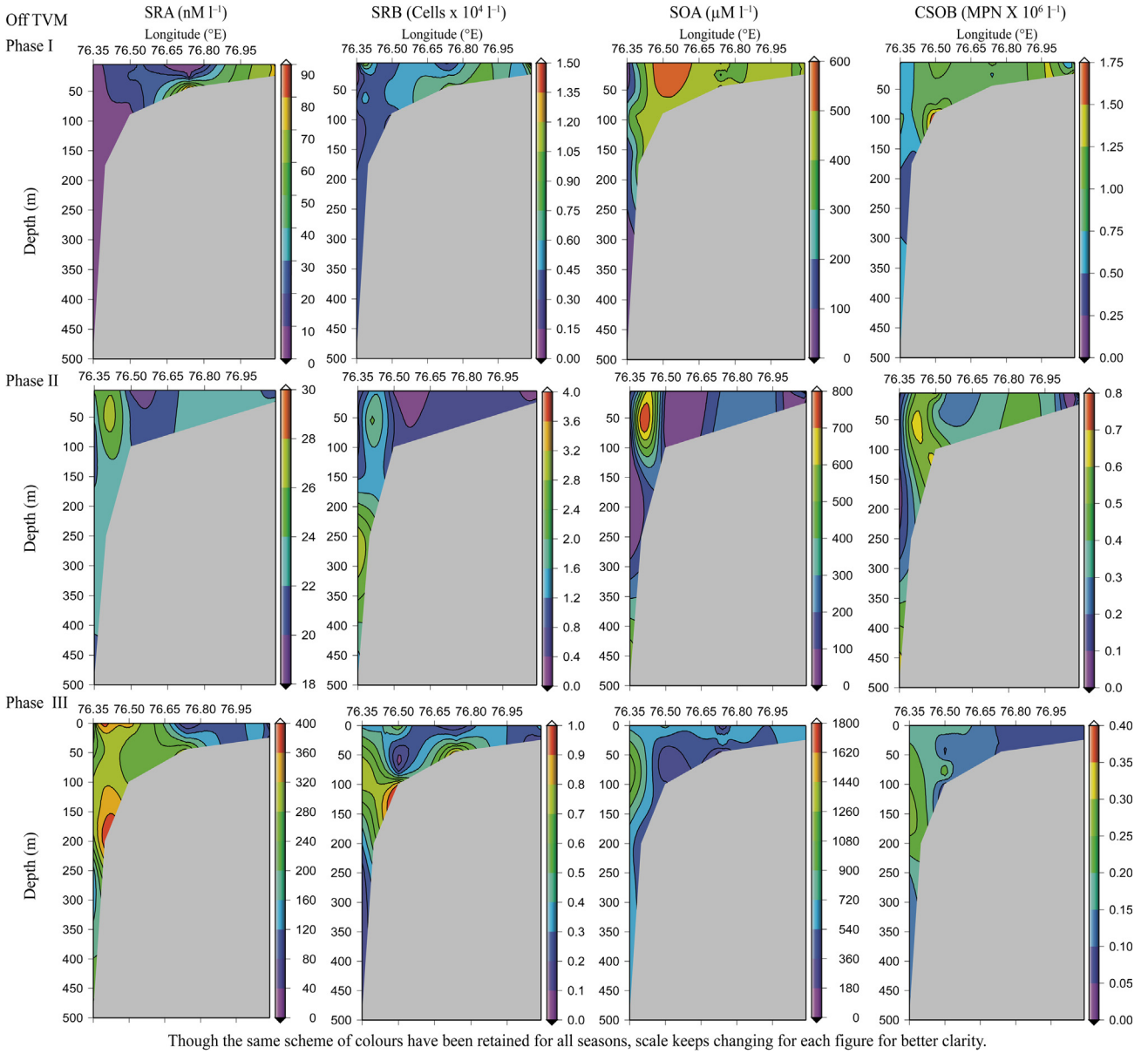

Figure 3 (*Continued*).

phase III suggest that the three phases follow the general paradigm, where the phytoplankton and zooplankton increase in succession. The phytoplankton then get intensely grazed and degraded.

Although TVM is known to be more productive (Gerson et al., 2014), the Chl *a* concentration was generally lower than that off Kochi due to higher grazing activity by mesozooplankton. Consequently, the phaeopigment concentration off TVM was highest (2.98 µg l^{-1}) during phase III and was distributed throughout the water column. However, the water column phaeopigment/Chl *a* ratio, suggest that the degradation processes were more active in phase II.

4.1. Microbiological parameters — abundance

The abundance of TC and TVC are in the range reported earlier by Ducklow et al. (2001). The abundance of SRB ranged from 10^2 to 10^4 l^{-1}. Of late, they have been encountered in the aerobic regions hosting anaerobic microniches (Colin et al., 2017; Jørgensen and Parkes, 2010; LokaBharathi and Chandramohan, 1990; Shanks and Reeder, 1993). In the solar lake, the higher abundance of SRB at 10^{6-7} l^{-1} was reported in the oxic surface waters (Teske et al., 1998). Similarly, Neretin et al. (2007) stated that, the proportion of SRB to total bacteria was 0.1% in the oxic, 0.8–1.9% in the suboxic and 1.2–4.7% in the anoxic zone, where SRB population ranged from 5×10^5 l^{-1}–6.3×10^5 l^{-1} in sub-oxic to anoxic water column of Black Sea. The peak MPN SRB of 2.5×10^9 cells l^{-1} was estimated in the water column of the alpine meromictic Gek-Gel Lake at 33 m depth (Karnachuk et al., 2006). In the present study, the higher abundance of SRB was in the sub-surface waters and accounted for 0.01% of total bacterioplankton. Colin et al. (2017) also stated that SRB thriving in the anoxic sediments may be re-suspended in the oxic water column and transported through oxic

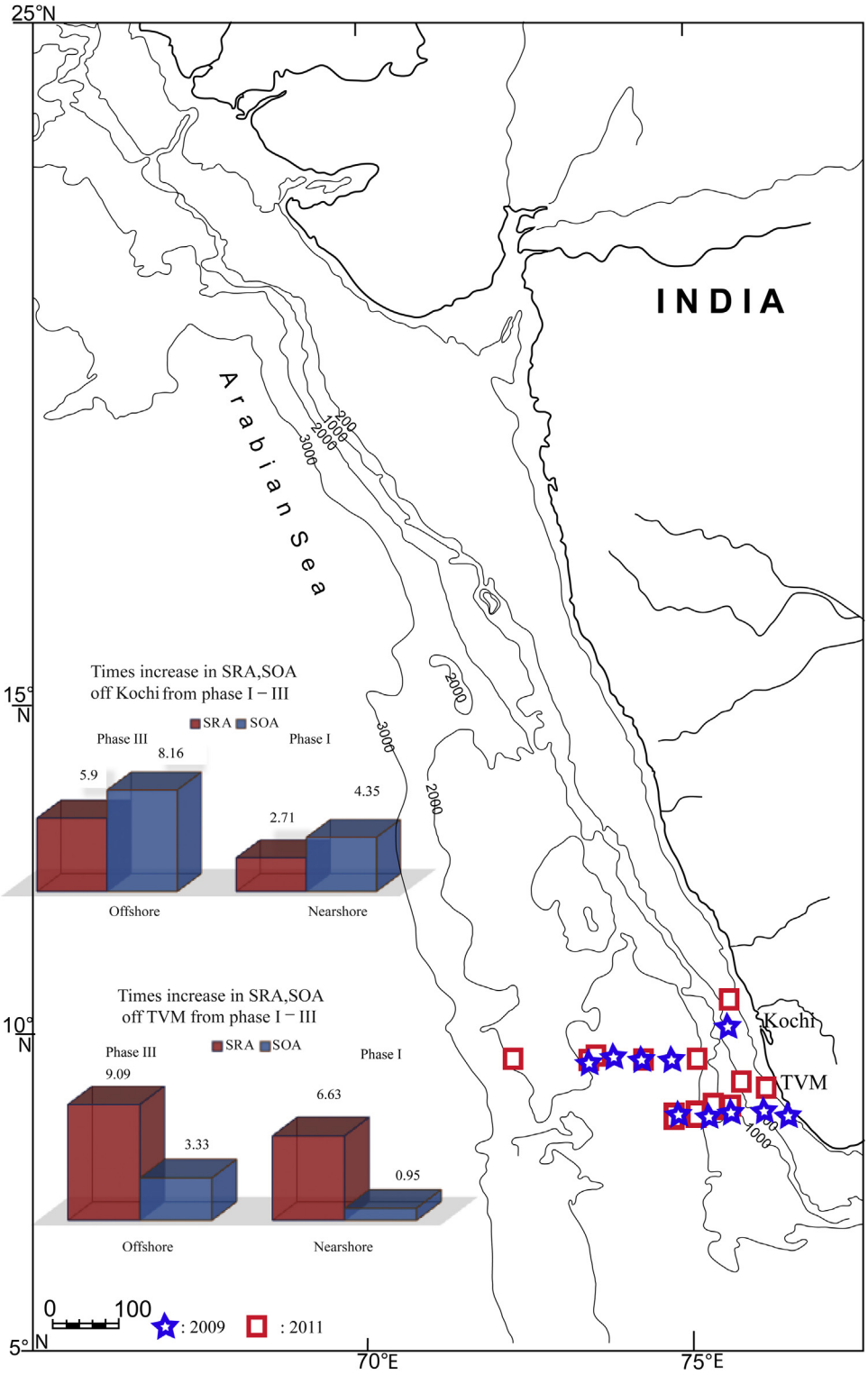

Figure 4 Times increase in sulfate-reducing activity (SRA) and sulfur-oxidizing activity (SOA) from phase I (2009) to phase III (2011) of upwelling at nearshore and offshore of Kochi and Trivandrum (TVM).

marine-influenced waters. Intense interactions among physical, chemical, and biological processes forming strong gradients of the waters may help re-suspend anaerobes to survive in the water column and even maintain their metabolism within anoxic micro-niches. More importantly, SRB can be found in water column either because they have the enzyme superoxide dismutase (Wu et al., 2017) or they have anti-oxidative defense systems (Brioukhanov et al., 2010) or they have the ability to respire oxygen (Cypionka, 2000). Dolla et al. (2006) also stated that SRB can develop molecular strategies to remove oxygen or they use oxygen temporarily for respiration to reduce toxicity.

Table 4 Analysis of variance of sulfate-reducing activity (SRA) and sulfur-oxidizing activity (SOA) during the three phases of upwelling off Kochi and Trivandrum (TVM).

Station	Parameters	Source of variation	SS	df	MS	*F*	*P*-value	*F* crit
Kochi	SRA: Phase I to Phase III	Between groups	13,487.59	1	13,487.59	5.37	**0.0286**	4.22
		Within groups	65,302.40	26	2511.63			
	SOA: Phase I to Phase III	Between groups	6,484,745.00	1	6,484,745.00	66.23	**0.0000**	4.22
		Within groups	2,545,819.00	26	97,916.12			
TVM	SRA: Phase I to Phase III	Between groups	409,652.70	1	409,652.70	39.52	**0.0000**	4.07
		Within groups	435,257.90	42	10,363.28			
	SOA: Phase I to Phase III	Between groups	488,047.70	1	488,047.70	4.55	**0.0387**	4.07
		Within groups	4,501,256.00	42	107,172.80			

While SRB produces sulfide, CSOB can oxidize this toxic end product to polythionates/thiosulfate and sulfate, both aerobically in the presence of oxygen or anaerobically in presence of nitrate (Nelson et al., 2004). Off Kochi and TVM, CSOB did not show any logarithmic variation and ranged from 0.1×10^6 l^{-1} to 0.72×10^6 l^{-1} and 0.15×10^6 l^{-1} to 0.83×10^6 l^{-1} respectively (Fig. 3a and b, Table 2). The free-living marine sulfur oxidizers are abundant in diverse seawater samples including in dark ocean (Swan et al., 2011) and they accounted for 45% of the 16S rRNA gene clones recovered from an OMZ in the South Atlantic and 37% from an anoxic fjord in British Columbia (Lavik et al., 2009; Walsh et al., 2009). They are especially abundant in coastal seawater. Some of the thiosulfate oxidizers oxidize thiosulfate as an auxiliary electron donor to tetrathionate. This allows them to use a greater portion of available organic carbon for biosynthesis rather than for respiration (Jannasch et al., 1991). However, knowledge regarding their abundance, distribution, and ecological role is scarce. Lavik et al. (2009) also identified groups of sulfur oxidizers in the upwelling coastal waters of Namibian shelf and reported chemoautotrophic bacteria to account for ~20% of the bacterioplankton in the sulfidic waters. Their abundance in the non-sulfidic and sulfidic bottom waters was in the range of 10^6 cells l^{-1} to 10^7 cells l^{-1}. Other authors (Arning et al., 2008; Goldhammer et al., 2010; Sievert et al., 2007) noticed the presence of chemolithotrophic sulfur-oxidizing bacteria in the upwelling areas. The present study shows that the culturable sulfur oxidizers are widely present in upwelling waters, accounting for 1% of the bacterio-plankton.

A culturable approach was used for the analysis because the high organic loading in the coastal waters permits relatively high recovery (De Souza et al., 2007). Despite the inherent caveats, the culturable approach retrieves the dominant culturable bacterio-plankton communities as coastal waters have considerable dissolved organic carbon levels (Simu et al., 2005). Besides, new isolates could add to the existing bacterial database which is an important requirement.

4.2. Microbiological parameters — activity

Off Kochi, the SRA values increased over the phases. Off TVM, SRA increased from phase I to phase III with the dip in phase II (Table 2). This decrease was associated with high Chl *a* and phaeopigment concentrations. The SRA off Kochi and TVM are comparable to 13 nM d^{-1} reported by Jørgensen et al. (1991), and 3.5 nM d^{-1} by Albert et al. (1995) in the Black Sea water column and 12 nM d^{-1} in the OMZ waters of Chilean coast by Canfield et al. (2010). However, much higher values of 1569 nM d^{-1} have been reported by Pimenov and Neretin (2006) in these waters.

SOA values were 194, 360, 1151 μM d^{-1} off Kochi and 339, 215 and 560 μM d^{-1} off TVM for the three phases respectively suggesting more dominant oxidation processes off Kochi. The sulfur-oxidizing activity was comparable to the north Atlantic water where 358 μM d^{-1} was reported by Tuttle and Jannasch (1976). High values could be due to the contribution from organic loading from inshore waters that promote both SRA and SOA. Thomas et al. (2013) stated that coastal waters off Kochi receive inshore waters and organic load from backwaters along with more fresh water and nutrients. Perhaps higher inputs of electron donors could account for higher SOA off Kochi, especially, in the presence of nitrate (LokaBharathi et al., 1997).

4.3. Inter-relationship of parameters driving SRA/SRB and SOA/CSOB

4.3.1. Depth

The SRA off Kochi is not depth dependent, while off TVM, SRA is negatively influenced by depth in phase I ($r = -0.315$; $r^2 \times 100 = 10\%$) and phase III (13%). These observations suggest that the signature of upwelling had just begun in phase I and it had dissipated by phase III. However, the SRB off Kochi and TVM are depth dependent in phase I and phase III. These observations suggest that the activity gets relatively more influenced by upwelling than the bacterial abundance. At these stages, the availability of organic matter (PON: $r = 0.820$, $p < 0.001$ and POC: $r = 0.633$, $p < 0.01$ unpublished data by Sam Kamaleson et al., under review) released during phytoplankton growth and degradation at the surface waters facilitates the distribution and intensity of SRA than the abundance of SRB. Moreover, Aluwihare et al. (1997) stated that DOM available in the ocean's surface was at least twice that in the deep sea. Besides, a high abundance of SRB has been noticed earlier by other researchers at the surface in non-upwelling regions (Cypionka, 2000; LokaBharathi and Chandramohan, 1990; Teske et al., 1998).

4.3.2. Temperature

The temperature, on the other hand, influenced SRB distribution positively, being responsible for 36% ($p < 0.05$) of the variation in phase I off Kochi. SRA and SOA are also positively influenced by temperature ($p < 0.05$) in phase I off TVM accounting for 16% and 27% of their variation respectively. Sokolova (2010) suggested that the optimum temperature for SRB was in the range of 27°C–35°C. They also found that the SRA was 6× higher at mesophilic condition than at psychrophilic condition.

4.3.3. Nutrients

Off TVM, nutrients affect the distribution of CSOB in phase I and in phase III and, SRB in phase II. Relationship of ammonium with CSOB evolves from negative to positive from phase I to phase III. The pigment degradation to form phaeopigments increased from 0.23 μM in phase I to 0.57 μM in phase III and is accompanied by more ammonium production in phase III. Perhaps CSOB increases due to the higher rate of nitrification that could provide nitrate as an electron acceptor (Sorokin et al., 2006). The SOA negatively influences ambient phosphate, silicate and nitrate concentrations in phase I (Table 3). In phase II, CSOB positively correlated with nitrite suggesting that the community is capable of nitrate reduction. Krishnan et al. (2008) have shown that intrinsic nitrification can feed denitrification in the coastal waters. Such release has also been noticed by Schutte et al. (2018) along with nitrate accumulation.

Off TVM, both the groups of bacteria act differently with phosphate. In phase I, SOA related negatively with phosphate, while in phase II, SRB related positively (Table 3). Anaerobic oxidation of phosphite to phosphate during sulfate reduction increases soluble phosphate (Schink and Friedrich, 2000). The SRB produce sulfide through SRA which binds with ambient iron thus releasing the iron-bound phosphate (Howarth et al., 2011). However, phosphate could be taken up by CSOB through SOA directly for later use (Glaubitz et al., 2013).

Off TVM, the significant correlation of silicate with SRB and negative correlation with SOA suggests its oxidation to the insoluble state. SRA increases pH during the process and silica solubility also increases with alkalinity (Meier et al., 2012).

Sulfur oxidizers are also known to store phosphate intracellularly and use phosphate for sulfide/thiosulfate oxidation (Goldhammer et al., 2010). In this study also, SRB correlated with phosphate and silicate, indicating its role in releasing these nutrients, which CSOB utilize, thus confirming the synergistic relationship between these two groups.

4.3.4. Chl *a* and phaeopigments

Off Kochi, high Chl *a* values are matched by low concentrations of silicate and nitrate ($r = -0.709$, $p < 0.001$ and $r = -0.521$, $p < 0.05$) suggesting the uptake of these nutrients for chlorophyll build-up and primary productivity. Moreover, iron limited diatom communities that multiply generally deplete silicate long before nitrate (Capone and Hutchins, 2013). The limitation of bio-available iron could be attributed to the increase in SRA over the three phases. Sulfide the product of sulfate reduction is known to readily bind with iron.

The relationships of SRA/SRB with Chl *a*/phaeopigments could be incidental and attributed to the effects of upwelling which could have facilitated the interactions between SRB and the surface-produced chlorophyll. In phase II, the relation between SRB and Chl *a*, phaeopigment was negative due to limited availability or due to faster uptake of break down products of the pigments. The influence of Chl *a* on SRA, changes from negative to positive from phase II to phase III. The observation suggests that when upwelling peaks, it increases the production of pigments and DOC which is turn stimulates SRA at the surface. It should be also noted that SRA and SRB are not deterred by the presence of oxygen (Cypionka, 2000; Sass et al., 2002) especially under DOC/POC replete conditions in upwelling waters.

Both SRA and SRB relate to Chl *a* off TVM due to upwelling linked productivity. Further, anaerobic niches in TSM could support these bacteria and their activity better. Such an observation was however restricted to TVM. Further, phaeopigment which covaries with Chl *a* could also contribute to this association. Up to 43% of the variation in SRA was due to phaeopigment off TVM. Phaeopigments form a part of TSM as evidenced by their inter-relationships. Besides, phaeopigment is a degradative product of Chl *a*, and is a rich source of secondary metabolites for SRB and its activity. Hence both TSM ($r = 0.624$, $p < 0.001$) and phaeopigments ($r = 0.652$, $p < 0.001$) influence SRA positively.

On the contrary, the influence of these parameters is negative to CSOB and its activity as these forms are less heterotrophic and more autotrophic to mixotrophic (Nelson et al., 2004). Incidentally, phase I off Kochi was an exception. Thus, on the whole, chlorophyll *a* and phaeopigments have a positive influence on SRB (32%) and SRA (43%) respectively while, nutrients like nitrate, phosphate and silicate responded and interacted with CSOB and SOA.

4.4. Microbial interaction — abundance

The interaction of TC with environmental parameters was obvious off TVM in the initial phase of upwelling, disappeared in the subsequent phases suggesting disruption of connectivity over the phases. These interactions of TC show that they decrease with depth, and covary with phosphate, nitrate and phaeo/Chl *a* ratio. However, silicate and ammonium interacted positively being responsible for 36% variation of TC. Intriguingly, such interactions were not observed in all phases off Kochi perhaps attributed to higher riverine forcing than upwelling.

4.5. Reducing activity

In coastal areas, the reducing activity due to hypoxia (oxygen concentration $\leq$ 2.8 ml l^{-1} or 63 μM) has been increasing (Banse et al., 2014; Middelburg and Levin, 2009). Naqvi et al. (2010) also stated that the coastal hypoxia has been developing in the most productive part of the Indian Ocean (Arabian Sea). Moreover, recent studies on the Gulf of Arabian Sea proved that the dead zone (OMZ) has expanded more than expected, raising a serious threat on local fisheries and ecosystems (Queste et al., 2018). As low as 10 μM of oxygen (0.23 ml l^{-1}) was detected in phase II and 15 μM (0.33 ml l^{-1}) in phase III off TVM. Understanding how the sulfur cycle

operates in such an environment is important to predict how these expanding areas will impact organic matter degradation. It should be noted that the borders of the OMZ in the Arabian Sea, south-west coast of India have extended from 18°N to 11°N as on 2004 (Banse et al., 2017) and have not yet been known to impinge the waters off Kochi (10°N) and Trivandrum (08°N). However, to distinguish low oxygen zones from true anoxic zones, which are rich in nitrite, the latter are often referred to as anoxic marine zones (AMZs) by Ulloa et al. (2012). OMZ waters are characterized by $\leq$63 μM of oxygen and $\leq$0.02 μM of nitrite (Banse et al., 2014) and AMZs are characterized by $\leq$2 μM oxygen and $\geq$0.5 μM of nitrite (Ulloa et al., 2012). In the current study, the average oxygen concentration off TVM was 1.48 ± 1.55 ml l^{-1} and 1.93 ± 1.86 ml l^{-1} in phase II and III respectively. The corresponding minimum oxygen concentrations were 10 μM and 15 μM respectively. The average nitrite concentrations were 1.69 ± 0.67 μM and 0.34 ± 0.42 μM in phase II and III respectively. The minimum nitrite concentration was 1.24 μM in phase II and it was non-detectable in phase III. Hence, it is suggested that the coastal waters examined in this study could probably have a status between OMZ and AMZ in patches intermittently. Noticeably, some pockets of hypoxic conditions defined by oxygen concentration ~45 μM have also been encountered off Kochi. However, physicochemical and microbiological processes perhaps prevent the spread of hypoxic pockets over time and space.

The spread of reducing activity off Kochi could be mostly due to the riverine influence and anthropogenic effects (Thomas et al., 2013), while off TVM could be more a consequence of upwelling. Here, the SRA gets mitigated both by stronger physical forcing that carries the water offshore and by SOA which counters the effect of SRA partially.

Thus, the coastal waters off TVM and Kochi are influenced by sulfate-reducing and sulfur-oxidizing activities. Prevalence of both SRB and CSOB has also been documented in the Chilean coast by Canfield et al. (2010) and Aldunate et al. (2018). Though they state that the sulfur cycle was cryptic with no obvious *in situ* chemical expression, the metagenomic results suggest an active sulfur cycle. Perhaps SOA counters SRA so effectively with a quick turn over of sulfide that the sulfur cycle appeared cryptic in those waters (Crowe et al., 2018).

4.6. Relation between SRA and SOA

Sulfur oxidation is one of the important processes which occur in most productive upwelling areas (Arning et al., 2008). Generally, SRA and SOA increase over the three phases of observation. Wherever the sulfate reduction is prominent, it is accompanied by sulfur-oxidizing activity (Alsenz et al., 2015; Arning et al., 2008). Ulloa et al. (2012) also identified sulfide (dsr), thiosulfate oxidation (sox) and sulfate-reducing (aprA) genes by metagenomics of Arabian Sea waters. Similarly, in the present study SRA and SOA have been shown to occur simultaneously except that, the increase in rates are different in different phases and transects. The increase ~7× in SRA and 1.7× in SOA, return the redox of the ecosystem only partially off TVM. Off Kochi, ~6× increase in SOA is more than the ~4× increase in SRA thus mitigating an increased effect of SRA (Fig. 4). Further, ANOVA of whole column SRA and SOA emphasizes that the increase in SRA is more statistically significant ($p < 0.001$) off TVM than off Kochi ($p < 0.02$) and the increase in SOA is more significant off Kochi ($p < 0.001$) than off TVM ($p < 0.03$). Thus, the present study highlights the importance of SOA. Besides, it is imperative that sulfide/thiosulfate-oxidation proceeds at much faster rates than sulfate-reduction, as the end product sulfide could be detrimental to biotic variables even at low concentrations. Our studies show that bacterial communities responsible for sulfur-cycle, shift over the course of the upwelling season from a sulfate-reduction dominated regime to a more sulfur-oxidation-dominated system in the later stage.

5. Conclusion

The self-organization of a system runs through several layers mainly, primary, secondary and tertiary levels, which have been well documented. However, the layer below the primary level that is the microbial layer which is responsible for the important processes of mineralization and rejuvenation is hardly chronicled. This is a first attempt to elucidate the contribution of bacteria of the sulfur cycle at the activity level in these waters. Thus we have been able to detect a general temporal increase in oxidizing activity over three different phases accompanied by general spatial spread towards offshore. However, due to eutrophication, these couplings could weaken, and there is a tendency for the increase and spread of reducing activity. Future observations beyond upwelling seasons including transects south of 10°N could further enlighten our inference. Our studies reiterate the ecological rebound and recovery that happens after upwelling due to bacterial processes.

Acknowledgements

Authors express their gratitude to the Director of CSIR-NIO, for the encouragement and the facilities provided. The financial support by the Ministry of Earth Sciences is acknowledged. This work was carried out under the Project number GAP 2033 funded by CMLRE (MoES), and 'Supra Institutional project' SIP 1301 of Council of Scientific and Industrial Research (CSIR)-NIO, Goa, India. CMLRE, Kochi, is acknowledged for the cooperation extended by the participants and crew of FORV Sagar Sampada (#267, #276, #282). Dr. Gauns MU is kindly acknowledged for Chl *a* values. The contributions of anonymous reviewers and editor of *Oceanologia* have considerably improved the manuscript. Sam Kamaleson acknowledges CSIR for Senior Research Fellowship. This is NIO contribution No. 6368.

References

Albert, D.B., Taylor, C., Martens, C.S., 1995. Sulfate reduction rates and low molecular weight fatty acid concentrations in the water column and surficial sediments of the Black Sea. Deep Sea Res. Pt. I 42 (7), 1239–1260, http://dx.doi.org/10.1016/0967-0637(95)00042-5.

Aldunate, M., De la Iglesia, R., Bertagnolli, A.D., Ulloa, O., 2018. Oxygen modulates bacterial community composition in the

coastal upwelling waters off central Chile. Deep Sea Res. Pt. II 156, 68—79, http://dx.doi.org/10.1016/j.dsr2.2018.02.001.

Alsenz, H., Illner, P., Ashckenazi-Polivoda, S., Meilijson, A., Abramovich, S., Feinstein, S., Almogi-Labin, A., Berner, Z., Püttmann, W., 2015. Geochemical evidence for the link between sulfate reduction, sulfide oxidation and phosphate accumulation in a Late Cretaceous upwelling system. Geochem. Trans. 16, 1—13, http://dx.doi.org/10.1186/s12932-015-0017-1.

Aluwihare, L.I., Repeta, D.J., Chen, R.F., 1997. A major biopolymeric component to dissolved organic carbon in surface sea water. Nature 387, 166—169, http://dx.doi.org/10.1038/387166a0.

Arning, E.T., Birgel, D., Schulz-Vogt, H.N., Holmkvist, L., Jørgensen, B.B., Larson, A., Peckmann, J., 2008. Lipid biomarker patterns of phosphogenic sediments from upwelling regions. Geomicrobiol. J. 25, 69—82, http://dx.doi.org/10.1080/01490450801934854.

Banse, K., Naqvi, S.W.A., Narvekar, P.V., Postel, J.R., Jayakumar, D. A., 2014. Oxygen minimum zone of the open Arabian Sea: variability of oxygen and nitrite from daily to decadal time scales. Biogeosci. Discuss. 11 (8), 2237, http://dx.doi.org/10.5194/bg-11-2237-2014.

Banse, K., Naqvi, S.W.A., Postel, J.R., 2017. A zona incognita surrounds the secondary nitrite maximum in open-ocean oxygen minimum zones. Deep Sea Res. Pt. I 127, 111—113, http://dx.doi.org/10.1016/j.dsr.2017.07.004.

Bottrell, S.H., Smart, P.L., Whitaker, F., Raiswell, R., 1991. Geochemistry and isotope systematics of sulfur in the mixing zone of Bahamian blue holes. Appl. Geochem. 6 (1), 97—103, http://dx.doi.org/10.1016/0883-2927(91)90066-x.

Brioukhanov, A.L., Pieulle, L., Dolla, A., 2010. Antioxidative defense systems of anaerobic sulfate reducing microorganisms. In: Mendez Vilas, A. (Ed.), Current Research, Technology and Education Topics in Applied Microbiology and Microbial Biotechnology. Microbiology Book Series, volume 1. Formatex Research Center, Badajoz, Spain, 148—159.

Canfield, D.E., 2001. Isotope fractionation by natural populations of sulfate-reducing bacteria. Geochim. Cosmochim. Acta 65 (7), 1117—1124, http://dx.doi.org/10.1016/s0016-7037(00)00584-6.

Canfield, D.E., Kristensen, E., Thamdrup, B., 2005. Aquatic geomicrobiology. Adv. Mar. Biol. 48, 1—599, http://dx.doi.org/10.1016/s0065-2881(05)48015-3.

Canfield, D.E., Stewart, F.J., Thamdrup, B., Brabandere, L.D., Dalsgaard, T., Delong, E.F., Revsbech, N.P., Ulloa, O., 2010. A cryptic sulfur cycle in oxygen-minimum zone waters off the Chilean Coast. Science 330, 1375—1378, http://dx.doi.org/10.1126/science.1196889.

Capone, D.G., Hutchins, D.A., 2013. Microbial biogeochemistry of coastal upwelling regimes in a changing ocean. Nat. Geosci. 6, 711—717, http://dx.doi.org/10.1038/ngeo1916.

Colin, Y., Goñi-Urriza, M., Gassie, C., Carlier, E., Monperrus, M., Guyoneaud, R., 2017. Distribution of sulfate-reducing communities from estuarine to Marine Bay Waters. Microb. Ecol. 73, 39—49, http://dx.doi.org/10.1007/s00248-016-0842-5.

Crowe, S.A., Cox, R.P., Jones, C., Fowle, D.A., Santibañez-Bustos, J. F., Ulloa, O., Canfield, D.E., 2018. Decrypting the sulfur cycle in oceanic oxygen minimum zones. ISME J. 12, 2322—2329, http://dx.doi.org/10.1038/s41396-018-0149-2.

Cypionka, H., 2000. Oxygen respiration by desulfovibrio species. Annu. Rev. Microbiol. 54, 827—848, http://dx.doi.org/10.1146/annurev.micro.54.1.827.

De Souza, M.J., LokaBharathi, P.A., Shanta, N., Chandramohan, D., 2007. "Trade-off" in Antarctic bacteria: limnetic psychrotrophs concede multiple enzyme expressions for multiple metal resistance. Biometals 20 (6), 821—828, http://dx.doi.org/10.1007/s10534-006-9045-8.

Dolla, A., Fournier, M., Dermoun, Z., 2006. Oxygen defense in sulfate reducing bacteria. J. Biotechnol. 126, 87—100, http://dx.doi.org/10.1016/j.jbiotec.2006.03.041.

Ducklow, H.W., Smith, D.C., Campbell, L., Landry, M.R., Quinby, H. L., Steward, G.F., Azam, F., 2001. Heterotrophic bacterioplankton in the Arabian Sea: basinwide response to year-round high primary productivity. Deep Sea Res. Pt. II 48 (6—7), 1303—1323, http://dx.doi.org/10.1016/s0967-0645(00)00140-5.

Fortin, D., Rioux, J.P., Roy, M., 2002. Geochemistry of iron and sulfur in the zone of microbial sulfate reduction in mine tailings. Water Air Soil Poll. 2 (3), 37—56, http://dx.doi.org/10.1023/a:1019983024680.

Fossing, H., Gallardo, V.A., Jørgensen, B.B., Hüttel, M., Nielsen, L.P., Schulz, H., Canfield, D.E., Forster, S., Glud, R.N., Gundersen, J. K., Küver, J., Ramsing, N.B., Teske, A., Thamdrup, B., Ulloa, O., 1995. Concentration and transport of nitrate by the mat-forming sulphur bacterium *Thioploca*. Nature 374, 713—715, http://dx.doi.org/10.1038/374713a0.

Gerson, V.J., Madhu, N., Jyothibabu, R., Balachandran, K., Nair, M., Revichandran, C., 2014. Oscillating environmental responses of the eastern Arabian Sea. Indian J. Geo-Mar. Sci. 43, 67—75.

Gibson, G.R., 1990. Physiology and ecology of the sulphate-reducing bacteria. J. Appl. Microbiol. 69, 769—797, http://dx.doi.org/10.1111/j.1365-2672.1990.tb01575.x.

Glaubitz, S., Kießlich, K., Meeske, C., Labrenz, M., Jürgens, K., 2013. SUP05 dominates the gamma proteobacterial sulfur oxidizer assemblages in pelagic redoxclines of the Central Baltic and Black Seas. J. Appl. Microbiol. 79 (8), 2767—2776, http://dx.doi.org/10.1111/j.1365-2672.1990.tb01575.x.

Goes, J.I., Thoppil, P.G., Gomes, H., Fasullo, J.T., 2005. Warming of the Eurasian landmass is making the Arabian Sea more productive. Science 308 (5721), 545—547, http://dx.doi.org/10.1126/science.1106610.

Goldhammer, T., Brüchert, V., Ferdelman, T.G., Zabel, M., 2010. Microbial sequestration of phosphorus in anoxic upwelling sediments. Nat. Geosci. 3 (8), 557—561, http://dx.doi.org/10.1038/ngeo913.

Gonsalves, M.J., Paropkari, A.L., Fernandes, C.E.G., LokaBharathi, P. A., Krishnakumari, L., Fernando, V., Nampoothiri, G.E., 2011. Predominance of anaerobic bacterial community over aerobic community contribute to intensify 'oxygen minimum zone' in the eastern Arabian Sea. Cont. Shelf Res. 31, 1224—1235, http://dx.doi.org/10.1016/j.csr.2011.04.011.

Grasshoff, K., Ehrhardt, M., Kremling, K., 1983. Methods of Seawater Analysis. Verlag Chemie, Weinheim, 125 pp.

Hansen, N.W., 1973. Official Standardized and Recommended Methods of Analysis. The Society of Analytical Chemistry, London, 897 pp.

Hobbie, J.E., Daley, R.J., Jasper, S., 1977. Use of nuclepore filters for counting bacteria by fluorescence microscopy. Appl. Environ. Microbiol. 33, 1225—1226.

Howarth, R., Chan, F., Conley, D.J., Garnier, J., Doney, S.C., Marino, R., Billen, G., 2011. Coupled biogeochemical cycles: eutrophication and hypoxia in temperate estuaries and coastal marine ecosystems. Front. Ecol. Environ. 9 (1), 18—26, http://dx.doi.org/10.1890/100008.

Jannasch, H.W., Wirsen, C.O., Molyneaux, S.J., 1991. Chemoautotrophic sulfur-oxidizing bacteria from the Black Sea. Deep Sea Res. Pt. I 38 (2), S1105—S1120, http://dx.doi.org/10.1016/S0198-0149(10)80026-3.

Jørgensen, B.B., Boetius, A., 2007. Feast and famine-microbial life in the deep-sea bed. Nat. Rev. Microbiol. 5 (10), 770—781, http://dx.doi.org/10.1038/nrmicro1745.

Jørgensen, B.B., Fossing, H., Wirscn, C.O., Jannasch, H.W., 1991. Sulfide oxidation in the anoxic Black Sea chemocline. Deep-Sea Res. 38 (2), S1083—S1103, http://dx.doi.org/10.1016/s0198-0149(10)80025-1.

Jørgensen, B.B., Gallardo, V.A., 1999. *Thioploca* spp.: filamentous sulfur bacteria with nitrate vacuoles. FEMS Microbiol. Ecol. 28 (4), 301—313, http://dx.doi.org/10.1016/s0168-6496(98)00122-6.

Jørgensen, B.B., Parkes, R.J., 2010. Role of sulfate reduction and methane for anaerobic carbon cycling in eutrophic fjord

sediments (Limfjorden, Denmark). Limnol. Oceanogr. 55, 1338–1352, http://dx.doi.org/10.4319/lo.2010.55.3.1338.

Karnachuk, O.V., Pimenov, N.V., Iusupov, S.K., Frank, I., Puhakka, J. A., Ivanov, M.V., 2006. Distribution, diversity, and activity of sulfate-reducing bacteria in the water column in Gek-Gel Lake, Azerbaijan. Microbiology 75 (1), 82–89, http://dx.doi.org/10.1134/s0026261706010152.

King, G.M., 2001. Radiotracer assays (35S) of sulfate reduction rates in marine and freshwater sediments. Method. Microbiol. 30, 489–500, http://dx.doi.org/10.1016/s0580-9517(01)30059-4.

Kogure, K.U., Simidu Taga, N., 1984. An improved direct viable count method for aquatic bacteria. Archives of Hydrobiol 102, 117–122.

Krishnan, K.P., Fernandes, S., LokaBharathi, P.A., Krishna Kumari, L., Shanta, N., Pratihari, A.K., Rao, B.R., 2008. Anoxia over the western continental shelf of India: bacterial indications of intrinsic nitrification feeding denitrification. Marine Environ. Res. 65 (5), 445–455, http://dx.doi.org/10.1016/j.marenvres.2008.02.003.

Kumar, S.P., Ramaiah, N., Gauns, M., Sarma, V.V.S.S., Muraleedharan, P.M., Raghukumar, S., Kumar, M.D., Madhupratap, M., 2001. Physical forcing of biological productivity in the Northern Arabian Sea during the Northeast Monsoon. Deep Sea Res. Pt. II 48 (6), 1115–1126, http://dx.doi.org/10.1016/S0967-0645(00)00133-8.

Lachkar, Z., Lévy, M., Smith, S., 2018. Intensification and deepening of the Arabian Sea Oxygen Minimum Zone in response to increase in Indian monsoon wind intensity. Biogeosciences 15 (1), 159–186, http://dx.doi.org/10.5194/bg-15-159-2018.

Lavik, G., Stuhrmann, T., Brüchert, V., Van der Plas, A., Mohrholz, V., Lam, P., Mussmann, M., Fuchs, B.M., Amann, R., Lass, U., Kuypers, M.M., 2009. Detoxification of sulphidic African shelf waters by blooming chemolithotrophs. Nature 457, 581–586, http://dx.doi.org/10.1038/nature07588.

LokaBharathi, P.A., 1989. The occurrence of denitrifying colourless sulfur-oxidizing bacteria in marine waters and sediments as shown by the agar shake technique. FEMS Microbiol. Ecol. 62, 335–342, http://dx.doi.org/10.1111/j.1574-6968.1989.tb03388.x.

LokaBharathi, P.A., Chandramohan, D., 1990. Sulfate-reducing bacteria from the Arabian Sea – their distribution in relation to thiosulfate-oxidizing and heterotrophic bacteria. Bull. Mar. Sci. 47, 622–630.

LokaBharathi, P.A., Chandramohan, D., Nair, S., 1988. A preliminary study of anaerobic thiosulfate-oxidizing bacteria as denitrifiers in the Arabian Sea. Geomicrobiol. J. 6, 195–207, http://dx.doi.org/10.1080/01490458809377839.

LokaBharathi, P.A., Nair, S., Chandramohan, D., 1997. Anaerobic sulfide-oxidation in marine colorless sulfur-oxidizing bacteria. J. Mar. Biotechnol. 5, 172–177.

Madhupratap, M., Gauns, M., Ramaiah, N., Kumar, S.P., Muraleedharan, P.M., De Sousa, S.N., Sardessai, S., Muraleedharan, U., 2003. Biogeochemistry of the Bay of Bengal: physical, chemical and primary productivity characteristics of the central and western Bay of Bengal during summer monsoon 2001. Deep Sea Res. Pt. II 50 (5), 881–896, http://dx.doi.org/10.1016/s0967-0645(02)00611-2.

Madhupratap, M., Kumar, S.P., Bhattathiri, P.M.A., Kumar, M.D., Raghukumar, S., Nair, K.K.C., Ramaiah, N., 1996. Mechanism of the biological response to winter cooling in the northeastern Arabian Sea. Nature 384, 549–552, http://dx.doi.org/10.1038/384549a0.

Malik, A., Fernandes, C.E.G., Gonsalves, M.J.B.D., Subina, N.S., Mamatha, S.S., Krishna, K., Varik, S., Kumari, R., Gauns, M., Cejoice, R.P., Pandey, S.S., Jineesh, V.K., Kamaleson, A.S., Vijayan, V., Mukherjee, I., Subramanyan, S., Nair, S., Ingole, B., LokaBharathi, P.A., 2015. Interactions between trophic levels in upwelling and non-upwelling regions during summer monsoon. J. Sea Res. 95, 56–69, http://dx.doi.org/10.1016/j.seares.2014.10.012.

Meier, J., Piva, A., Fortin, D., 2012. Enrichment of sulfate-reducing bacteria and resulting mineral formation in media mimicking pore water metal ion concentrations and pH conditions of acidic pit lakes. FEMS Microbiol. Ecol. 79 (1), 69–84, http://dx.doi.org/10.1111/j.1574-6941.2011.01199.x.

Middelburg, J.J., Levin, L.A., 2009. Coastal hypoxia and sediment biogeochemistry. Biogeosciences 6, 1273–1293, http://dx.doi.org/10.5194/bg-6-1273-2009.

Naqvi, S.W.A., 1991. Geographical extent of denitrification in the Arabian Sea in relation to some physical processes. Oceanologica Acta 14 (3), 281–290.https://archimer.ifremer.fr/doc/00101/21257.

Naqvi, S.W.A., Bange, H.W., Farías, L., Monteiro, P.M.S., Scranton, M.I., Zhang, J., 2010. Marine hypoxia/anoxia as a source of CH_4 and N_2O. Biogeosciences 7, 2159–2190, http://dx.doi.org/10.5194/bg-7-2159-2010.

Nelson, D.C., Amend, J.P., Edwards, K.J., Lyons, T.W., 2004. Sulfide oxidation in marine sediments: geochemistry meets microbiology. Sulfur Biogeochem. 379, 63–81, http://dx.doi.org/10.1130/0-8137-2379-5.63.

Neretin, L.N., Abed, R.M., Schippers, A., Schubert, C.J., Kohls, K., Kuypers, M.M., 2007. Inorganic carbon fixation by sulfate-reducing bacteria in the Black Sea water column. Environ. Microbiol. 9 (12), 3019–3024, http://dx.doi.org/10.1111/j.1462-2920.2007.01413.x.

Pimenov, N.V., Neretin, L.N., 2006. Compositions and activities of microbial communities involved in carbon, sulfur, nitrogen and manganese cycling in the oxic/anoxic interface of the Black Sea. In: Neretin, L.N. (Ed.), Past and Present Water Column Anoxia. Springer, Dordrecht, 501–521, http://dx.doi.org/10.1007/1-4020-4297-3_19.

Queste, B.Y., Vic, C., Heywood, K.J., Piontkovski, S.A., 2018. Physical controls on oxygen distribution and denitrification potential in the north west Arabian Sea. Geophys. Res. Lett. 45 (9), 4143–4152, http://dx.doi.org/10.1029/2017GL076666.

Resplandy, L., Lévy, M., Bopp, L., Echevin, V., Pous, S., Sarma, V.V.S.S., Kumar, D., 2012. Controlling factors of the oxygen balance in the Arabian Sea's OMZ. Biogeosciences 9 (12), 5095–5109, http://dx.doi.org/10.5194/bgd-9-5509-2012.

Sass, A.M., Eschemann, A., Kühl, M., Thar, R., Sass, H., Cypionka, H., 2002. Growth and chemosensory behavior of sulfate-reducing bacteria in oxygen-sulfide gradients. Microbiol. Ecol. 40 (1), 47–54, http://dx.doi.org/10.1111/j.1574-6941.2002.tb00935.x.

Schink, B., Friedrich, M., 2000. Bacterial metabolism: phosphite oxidation by sulphate reduction. Nature 406 (6791), 37, http://dx.doi.org/10.1038/35017644.

Schutte, C.A., Wilson, A.M., Evans, T., Moore, W.S., Joye, S.B., 2018. Deep oxygen penetration drives nitrification in intertidal beach sands. Limnol. Oceanogr. 63 (S1), S193–S208, http://dx.doi.org/10.1002/lno.10731.

Shanks, A.L., Reeder, M.L., 1993. Reducing microzones and sulfide production in marine snow. Mar. Ecol. Prog. Ser. 96, 43–47, http://dx.doi.org/10.3354/meps096043.

Shetye, S.R., Gouveia, A.D., Shenoi, S.S.C., Sundar, D., Michael, G. S., Almeida, A.M., Santanam, K., 1990. Hydrography and circulation off the west coast of India during the southwest monsoon 1987. J. Mar. Res. 48, 359–378, http://dx.doi.org/10.1357/002224090784988809.

Shetye, S.S., Mohan, R., Patil, S., Jena, B., Chacko, R., George, J.V., Noronha, S., Singh, N., Priya, L., Sudhakar, M., 2015. Oceanic pCO_2 in the Indian sector of the Southern Ocean during the austral summer–winter transition phase. Deep Sea Res. Pt. II 118, 250–260, http://dx.doi.org/10.1016/j.dsr2.2015.05.017.

Sievert, S.M., Wierings, E.B.A., Wirsen, C.O., Taylor, C.D., 2007. Growth and mechanism of filamentous-sulfur formation by *Candidatus* Arcobacter sulfidicus in opposing oxygen-sulfide gradients. Environ. Microbiol. 9, 271–276, http://dx.doi.org/10.1111/j.1462-2920.2006.01156.x.

Simu, K., Holmfeldt, K., Zweifel, U.L., Hagström, A., 2005. Culturability and coexistence of colony-forming and single-cell marine bacterioplankton. Appl. Environ. Microbiol. 71, 4793–4800, http://dx.doi.org/10.1128/aem.71.8.4793-4800.2005.

Sokolova, E.A., 2010. Influence of temperature on development of sulfate-reducing bacteria in the laboratory and field in winter. Contemp. Probl. Ecol. 3 (6), 631—634, http://dx.doi.org/10.1134/s1995425510060032.

Sorokin, D.Y., Tourova, T.P., Lysenko, A.M., Muyzer, G., 2006. Diversity of culturable halophilic sulfur-oxidizing bacteria in hypersaline habitats. Microbiology 152, 3013—3023, http://dx.doi.org/10.1099/mic.0.29106-0.

Strickland, J.D.H., Parsons, T.R., 1977. A Practical Handbook of Seawater Analysis, 2nd ed. Fisheries Research Board of Canada, Ottawa, 21 pp., http://publications.gc.ca/pub?id=9.581564&sl=0.

Swan, B.K., Martinez-Garcia, M., Preston, C.M., Sczyrba, A., Woyke, T., Lamy, D., Reinthaler, T., Poulton, N.J., Masland, E.D., Gomez, M.L., Sieracki, M.E., DeLong, E.F., Herndl, G.J., Stepanauskas, R., 2011. Potential for chemolithoautotrophy among ubiquitous bacteria lineages in the dark ocean. Science 333 (6047), 1296—1300, http://dx.doi.org/10.1126/science.1203690.

Teske, A., Ramsing, N.B., Habicht, K., Fukui, M., Küver, J., Jørgensen, B.B., Cohen, Y., 1998. Sulfate-reducing bacteria and their activities in cyanobacterial mats of Solar Lake (Sinai, Egypt). Appl. Environ. Microbiol. 64 (8), 2943—2951, PMID: 9687455.

Teske, A., Wawer, C., Muyzer, G., Ramsing, N.B., 1996. Distribution of sulfate-reducing bacteria in a stratified fjord (Mariager Fjord, Denmark) as evaluated by most-probable-number counts and denaturing gradient gel electrophoresis of PCR-amplified ribosomal DNA fragments. Appl. Environ. Microbiol. 62 (4), 1405—1415, PMID: 8919802.

Thomas, L.C., Padmakumar, K.B., Smitha, B.R., Asha Devi, C.R., Bijoy Nandan, S., Sanjeevan, V.N., 2013. Spatio-temporal variation of microphytoplankton in the upwelling system of the southeastern Arabian Sea during the summer monsoon of 2009. Oceanologia 55 (1), 185—204, http://dx.doi.org/10.5697/oc.55-1.185.

Tuttle, J.H., Jannasch, H.W., 1976. Microbial utilization of thiosulfate in the deep sea. Limnol. Oceanogr. 21 (5), 697—701, http://dx.doi.org/10.4319/lo.1976.21.5.0697.

Ulloa, O., Canfield, D.E., DeLong, E.F., Letelier, R.M., Stewart, F.J., 2012. Microbial oceanography of anoxic oxygen minimum zones. PNAS 109 (40), 15996—16003, http://dx.doi.org/10.1073/pnas.1205009109.

Visscher, P.T., Prins, R.A., Gemerden, H., 1992. Rates of sulfate reduction and thiosulfate consumption in a marine microbial mat. FEMS Microbiol. Ecol. 9 (4), 283—294, http://dx.doi.org/10.1111/j.1574-6941.1992.tb01763.x.

Walsh, D.A., Zaikova, E., Howes, C.G., Song, Y.C., Wright, J.J., Tringe, S.G., Tortell, P.D., Hallam, S.J., 2009. Metagenome of a versatile chemolithoautotroph from expanding oceanic dead zones. Science 326, 578—582, http://dx.doi.org/10.1126/science.1175309.

Walsh, J.J., Dieterle, D.A., Müller-Karger, F.E., Bohrer, R., Bissett, W.P., Varela, R.J., Aparicio, R., Díaz, R., Thunell, R., Taylor, G.T., Scranton, M.I., Fanning, K.A., Peltzer, E.T., 1999. Simulation of carbon/nitrogen cycling during spring upwelling in the Cariaco Basin. J. Geophys. Res. 104, 7807—7825, http://dx.doi.org/10.1029/1998jc900120.

Wiggert, J.D., Murtugudde, R.G., McClain, C.R., 2002. Processes controlling interannual variations in wintertime (Northeast Monsoon) primary productivity in the central Arabian Sea. Deep Sea Res. Pt. II: Top. Stud. Oceanogr. 49 (12), 2319—2343, http://dx.doi.org/10.1016/s0967-0645(02)00039-5.

Winch, S., Mills, H.J., Kostka, J.E., Fortin, D., Lean, D.R.S., 2009. Identification of sulfate-reducing bacteria in methylmercury-contaminated mine tailings by analysis of SSU rRNA genes. FEMS Microbiol. Ecol. 68 (1), 94—107, http://dx.doi.org/10.1111/j.1574-6941.2009.00658.x.

Wu, J., Liu, H., Wang, P., Zhang, D., Sun, Y., Li, E., 2017. Oxygen reduction reaction affected by sulfate-reducing bacteria: different roles of bacterial cells and metabolites. Indian J. Microbiol. 57 (3), 344—350, http://dx.doi.org/10.1007/s1208.

Wurl, O., 2009. Practical Guidelines for the Analysis of Seawater. CRC Press, Ottawa, 408 pp.

Yentsch, C.D., Menzel, D.W., 1963. A method for determination of chlorophyll *a*nd phaeophytin by fluorescence. Deep Sea Res. 10, 221—231, http://dx.doi.org/10.1016/0011-7471(63)90358-9.

Oceanologia (2019) 61, 321—330

Available online at www.sciencedirect.com

ScienceDirect

journal homepage: www.journals.elsevier.com/oceanologia/

ORIGINAL RESEARCH ARTICLE

Linking sea level dynamic and exceptional events to large-scale atmospheric circulation variability: A case of the Seine Bay, France

Imen Turki*, **Nicolas Massei**, **Benoit Laignel**

Continental and Coastal Morphodynamic Laboratory, Normandy University, Rouen, France

Received 16 September 2018; accepted 15 January 2019
Available online 1 February 2019

KEYWORDS
Sea level dynamic;
Envelope approach;
Demodulated surges;
Storm events;
Climate patterns

Summary In this study, the multi-time-scale variability of the South English Channel (case of the Seine Bay, North France) sea level and its exceptional events have been investigated in relation with the global climate patterns by the use of wavelet multi-resolution decomposition techniques. The analysis has been focused on surges demodulating by an envelope approach. The low-frequency components of the interannual (2.1-yr, 4-yr, 7.8-yr) and the interdecadal (15.6-yr and 21.2-yr) time-scales, extracted from 46-years demodulated surges, have been correlated to 36 exceptional stormy events according to their intensity. Results have revealed five categories of storms function on their correlation with the interannual and the interdecadal demodulated surges: events with high energy are manifested at the full scales while moderate events are only observed at the interannual scales. The succession of storms is mainly carried by the last positive oscillations of the interannual and the interdecadal scales. A statistical downscaling approach integrating the discrete wavelet multi-resolution analysis for each time-scale has been used to investigate the connection between the local dynamic of surges and the global atmospheric circulation from SLP composites. This relation illustrates dipolar patterns of high-low pressures suggesting positive anomalies at the interdecadal scales of 15.6-yr and 21.3-yr and the interannual scales of 4-yr while negative anomalies at 7.8-yr should be related to a series of physical mechanisms linked to the North-Atlantic and ocean/atmospheric circulation oscillating at the same time-scales. The increasing storm frequency is probably related to the Gulf Stream variation and its weakening trend in the last years.

* Corresponding author at: Continental and Coastal Morphodynamic Laboratory, Normandy University, Rouen 76821, France. Tel. +0033 235146952; fax: +0033 235140019.
E-mail addresses: imen.turki@univ-rouen.fr (I. Turki), nicolas.massei@univ-rouen.fr (N. Massei), benoit.laignel@univ-rouen.fr (B. Laignel).
Peer review under the responsibility of Institute of Oceanology of the Polish Academy of Sciences.

Production and hosting by Elsevier

https://doi.org/10.1016/j.oceano.2019.01.003

1. Introduction

During the last decades and in relation with the global evolution induced by climate change, the oceanographic scientific community have devoted their efforts to improve our understanding of the impacts of climate fluctuations on coastal hydrodynamic variability, in particular during stormy events. Several approaches have been extensively employed to investigate the extreme physical dynamic of the sea level and simulate the impact of the global climate oscillations for providing different coastal projections. For this reason, determining how and to what extent the large-scale climate oscillations can be identified in the oceanographic parameters and storm surges is required.

In the present context of global changes, the combined effects of the sea level rise and the land loss are commonly mentioned as a consequence of climate variability (e.g., Devoy, 2008; Nicholls et al., 2010). In the same context, the land loss itself is often a result of an increasing storminess responsible for coastal erosion (Stive et al., 2002) or flooding areas whose repeated restoration might be inefficient and the land is abandoned.

The acceleration of the sea level rise along the coastal mid-Atlantic in recent decades, where the climate is strongly influenced by the Gulf Stream (GS), is possibly caused by the Atlantic Meridional Overturning Circulation (AMOC) and its upper branch, the GS. Consequently, coastal communities have observed a significant increase in flooding frequency in the last years (Mitchell et al., 2013).

By the hypothesis that the variation in the GS location and strength is responsible on changes in the sea surface height gradient across the GS and, consequently, the sea level variability on both sides of the stream, the elevation of the sea surface gradient is proportional to the surface velocity of the GS. Then, the weakening of the GS strength will raise the sea level northwest of the GS; which is suggested by several recent studies (e.g., Ezer and Corlett, 2012; Ezer et al., 2013; Levermann et al., 2005; Sallenger et al., 2012). The impact of the GS variation on coastal sea level has been demonstrated by many observations (Sweet et al., 2009) and circulations models (Ezer, 2001) of the Atlantic Oceans and, also, by Global Climate models (Yin et al., 2009).

The effects of continuous changes in atmospheric patterns on sea level dynamic and stormy events have been investigated through a series of probabilistic approaches based on of climate indices by the use of nonstationary analyses of extremes (e.g. Minguez et al., 2012). Marcos et al. (2012) have related changes in the median and the higher-order percentiles of observed water levels in the Mediterranean Sea by the large-scale atmospheric circulation of winter North Atlantic Oscillation (NAO). Moreover, Menendez and Woodworth (2010) have demonstrated that changes in extreme events are due to changes in mean sea levels; they have reported the important role of the NAO and the Arctic Oscillation (AO) indices on the extreme sea level variability along the European coasts. Then, Masina et al. (2015) have shown a similar behavior between the regional and global scales at Venice and Porto Corsini (Adriatic Sea) from a detailed analysis of the annual mean sea level evolution. They have evidenced a relation between increasing extreme water levels since the 1990s and changes in wind regime, in particular, the intensification of Bora and Sirocco winds events whose intensity and frequency have been increased after the second half of the 20th century.

One of the challenges in investigating the sea level dynamic with global patterns related to Climate circulation is how to identify the multi-scale variability associated with the different physical processes involved.

In the framework of the further altimetry mission of Surface Water and Ocean Topography (SWOT), planned for launch in 2021, Turki et al. (2015) have investigated the low-frequencies of the sea level variability in the eastern English Channel (NW France) at annual and inter-monthly scales. Such changes result from the combining effect of meteorological and oceanography forces with an important contribution of the hydrological signal coming from the Seine river; the climate signature of the NAO circulation is also observed at the annual scales. Massei et al. (2017) have focused on the relation of the local Seine hydrological variability with the global climate patterns, and the time-scale dependence of this connection by developing a downscaling modeling basing on an empirical statistical approach. Their works have shown that the multi-scale links between the sea level pressure (SLP) and the regional hydrological variations are statistically significant for frequencies greater than 2 years (3.2-yr, 7.2-yr and 19.3-yr); they should be caused by coupling effects of North-Atlantic oceanic paths and atmospheric circulation.

In this context, the present research has been carried out to investigate the multi-time-scale variability of the sea level in the Seine Bay (South English Channel) and its exceptional events in relation with the global climate patterns by the use of high-resolution spectral techniques. A special focus is devoted to the connection of stormy events and their occurrence with the atmospheric circulation. The paper is organized as follow. After the introduction, the second section presents the data and the methodological approach used. Section 3 provides all results and discussions of the multi-scale sea level variability in relation to the exceptional events and the teleconnections of the atmospheric circulation. Finally, some concluding remarks and further researches are presented in Section 4.

2. Data and methodological approach

2.1. Sea level and climatological data set

Hourly sea level measurements, extracted from Le Havre tide gauge between 1964 and 2010, have been provided by the National Navy Hydrographic Service (http://refmar.shom.fr/en/home); see Fig. 1. Climatological data in the North Atlantic zone have been extracted from the National Center for Environmental Prediction and National Center for Atmospheric Research-1 (NCEP/NCAR-1) reanalysis (Kalnay et al., 1996) with a time resolution of a month. This dataset represents the North Atlantic atmospheric dynamics over the North Atlantic region (75°W–35°E and 15°E–75°N) with a horizontal spatial resolution of 2.5*2.5 (i.e., 1125 grid-points). As suggested by previous researches, SLP field is considered as a good indicator for the local hydro-climatic conditions (e.g., Massei et al., 2017; Ruigar and Golian, 2015); it has been used in the present analysis and will be

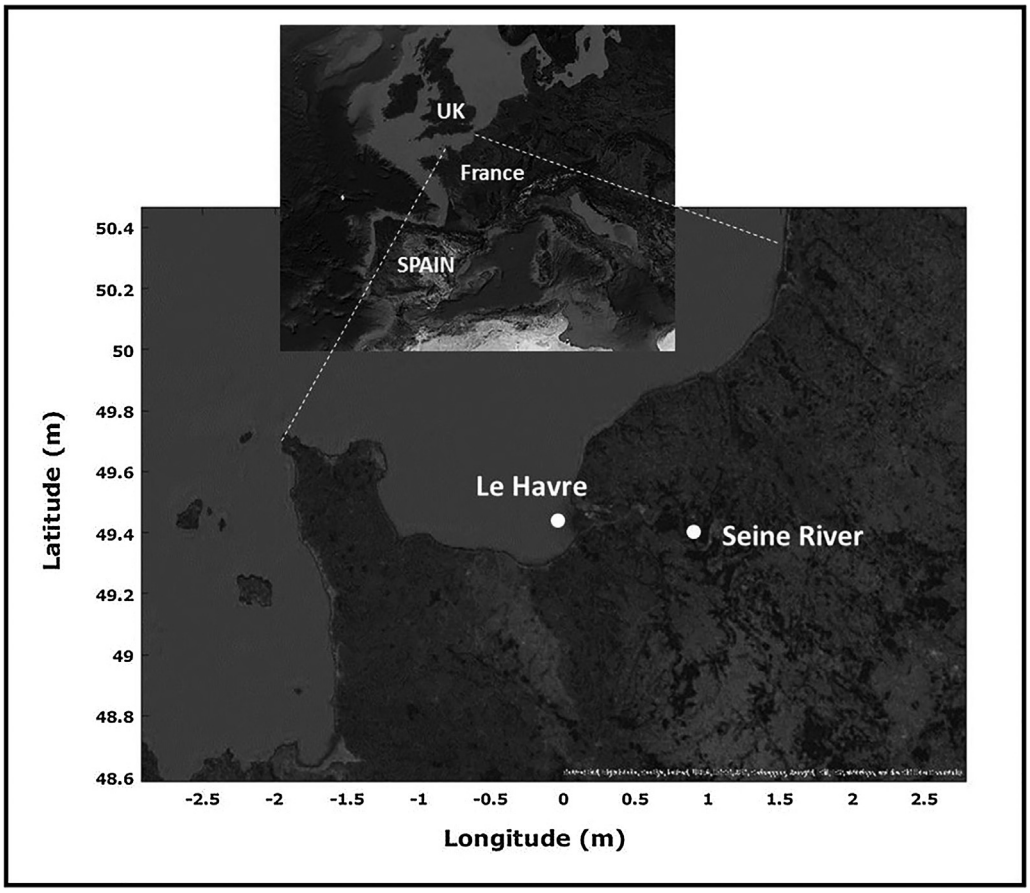

Figure 1 Study area: the Seine Bay located in the south-eastern English Channel (NW France).

referred to "large scale" in the subsequent parts of the analysis while local scale" refers to the sea level.

2.2. Tidal modulation and residual sea level

The total sea level height, resulting from the astronomical and the meteorological processes, exhibits a temporal non-stationarity explained by the combining effects of the long-term trend in the mean sea level, the modulation by the deterministic tidal component and the stochastic signal of surges, and the interactions between tides and surges. The occurrence of extreme sea levels is controlled by periods of high astronomically generated tides, in particular at inter-annual scales when two phenomena of precession cause systematic variation of high tides. The modulation of tides contributes to the enhanced risk of coastal flooding.

The separation between tidal and non-tidal signals is an important task in any analysis of sea level timeseries. The stochastic component associated with the non-tidal variation in the Seine Bay, extracted from Le Havre tide gauge, is mainly explained by the meteorological and the hydrological effects of the Seine river reaching the bay during flood events. By the hypothesis of independence between the astronomical and the stochastic effects, the non-linear relationship between both components is not considered to separate the tidal modulation from the total sea level.

Using the classical harmonic analysis, the tidal component has been modeled as the sum of a finite set of sinusoids at specific frequencies to determine the determinist phase/amplitude of each sinusoid and predict the astronomical component of tides. In order to obtain a quantitative assessment of the non-tidal contribution in storminess changes, technical methods basing on MATLAB t-tide package have been used to estimate year-by-tear tidal constituents. The sea level measurements present strong tidal modulations which have long been recognized by their significant effects on long-term changes (e.g., Gratiot et al., 2008); in particular, those produced at inter-annual scales. These processes result from 18.61-year lunar nodal cycle and the 8.85-year cycle of lunar perigee and influence the sea level as a quasi 4.4-year cycle (Menendez and Woodworth, 2010; Wood, 2001; Woodworth and Blackman, 2004).

A year-by-year tidal simulation (Shaw and Tsimplis, 2010) has been applied to the sea level timeseries to determine the amplitude and the phase of tidal modulations using harmonic analysis fitted to 18.61, 9.305, 8.85, and 4.425-year sinusoidal signals (Pugh, 1987).

2.3. Demodulated surges by the use of envelope technique

Once the annual sea level trend and the tidal components have been removed, the residual signal has been used as 'surges' to be demodulated by an envelope approach, a preliminary step before the frequency decomposition by the multi-resolution wavelet.

Determining envelopes of a statistical signal is generally used for detecting the amplitude modulation. In the present research, the objective is to detect if any (and what) underlying low- frequency component controls the variations of the sea level signal amplitude. The most known envelope is the analytic one based on the Hilbert transform. However and in practice, calculating envelopes of real signals in environmental contexts is different from analytic ones, although these uniquely define envelopes (Yang, 2017). The most methods for envelope identification depend on extrema detection followed by a low-pass filter. The envelopes of real signals are obtained using a spline interpolation from extrema sequences, as used for instance in the empirical mode decomposition (EMD) (Massei and Fournier, 2012; Massei et al., 2017). Here, the present work is more particularly interested in high surges with extreme values from considering only the upper envelope of a real-valued surge signal by identifying all the local maxima and interpolating between them using a cubic spline.

2.4. Atmospheric composite maps

The relationship between the local sea level variability and the global atmospheric patterns has been investigated to identify the physical links at different time-scales by the use of the Sea Level Pressure (SLP) field. The procedure for investigating this global/local scale connection consists in decomposing both the SLP field and the surge signal across the different time-scales into a series of wavelet details (WD) using a multiresolution analysis.

Then, for each wavelet time-scale, an associated SLP composite map is constructed by: (1) calculating the point-wise (i.e. at each grid-point) positive temporal mean of the SLP field WD at this scale for high values of the corresponding surge WD, (2) similarly, calculate the point-wise negative temporal mean of SLP field WD for low values of surge WD, (3) computing the difference positive mean-negative mean SLP value at each grid point (Massei et al., 2017). Here, "high" and "low" values of sea level WD have been chosen such as they exceed +0.5 or fall below −0.5 standard deviation (SD). Statistically significant regions have been estimated for each wavelet scale from the highest to the lowest frequencies; the degrees of freedom has been adjusted according to the wavelet scale and the "effective" sample size N from the actual sample size N has been calculated according to the first order autocorrelation coefficient AR[1] of each of the two positive and negative mean SLP WD (Mitchell et al., 1966).

3. Results and discussions

3.1. Sea level dynamic and exceptional events in the Seine Bay

The sea level variability in the Seine Bay has been investigated from the 46-year record. Once the tidal components and the regressive trend of the sea level rise were removed, the signal of surges has been demodulated by an envelope approach; then, the upper envelope has been calculated by joining local extrema and using a spline function (Fig. 2a).

Taking the Fourier transform of the original and the demodulated surges, the spectrums S_S and S_{SM} have been simulated in Fig. 2b with the aim to illustrate the different frequency components characterizing each signal. Compar-

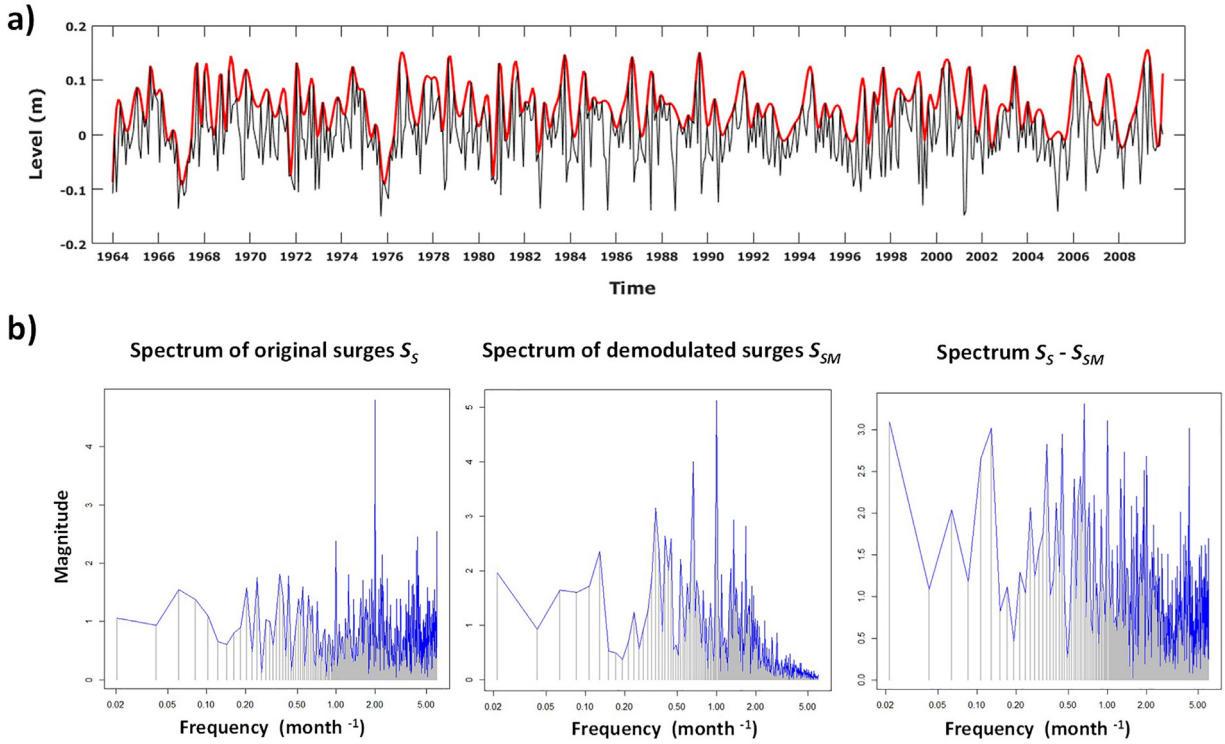

Figure 2 (a) The maxima envelope (thick line) of the mean monthly surges (thin line) between 1961 and 2010; (b) spectrum of the original S_S, demodulated S_{SM} surges, and the difference $S_S - S_{SM}$.

ing both spectrums shows that the interpolative envelope contains the message signal of the original surges: similarities of the main components with the most vibration of the high-frequency components in the original signal vs a clear illustration of low-frequency components in the demodulated signal. Hence, the simulated upper envelope can be used to modulate the main information of nonstationary surges.

The interpolative envelope, used for demodulating nonstationary surges, contains the lower chirp signal component with the fault characteristic frequency and its harmonic interferences. The demodulated surges cover a series of frequencies with different time-periods able to reconstruct the most variability of the original signal. This result confirms the last investigations reported by Yang (2017); they have concluded that the envelopes of real-valued stationary and nonstationary signals contain some low-frequency components of the original signal and some new components generated by the new-Nyquist extrema sampling.

Fig. 3 displays the continuous wavelet spectrum of the total sea level (a), surges (b) and the demodulated surges (c). The first spectrum (Fig. 3a) shows that most of the energy is homogenously located around 1-yr with more than 90% of the total variance. By removing the astronomical components, the signal of surges reveals the existence of frequencies lower than 1-yr, differently distributed at 2-yr and 4-yr scales; it illustrates a non-homogenous repartition during the period 1964–2010 (Fig. 3b) with two peaks of energy in both periods 1970–1980 and 2000–2001. The 2-yr and 4-yr frequencies are even more pronounced in the spectrum of the demodulated surges where the interannual and the interdecadal frequencies of 8-yr and 15-yr, respectively, are clearly structured with a high concentration of energy (Fig. 3c).

A multiresolution analysis has been applied to the demodulated surges with the aim to extract the different components explaining the total variability of the envelope. The process has resulted in the separation of 9 components, the so-called wavelet details numbered from D1 to D9.

The different wavelet details have been associated to the following time-scales: intermonthly (D1, D2 and D3), annual (D4), interannual (D5, D6 and D7) and interdecadal (D8 and D9) scales. The most part of these frequencies has been illustrated as peaks of energy in the continuous wavelet spectrum (Fig. 3c).

The focus of the present research is to investigate the key role of the low-frequency components (higher than 2-yr) with a mean explaining variance of 82.7% from the total demodulated signal (Table 1): ∼2.1-yr, ∼4-yr, ∼7.8-yr, ∼15.6-yr and ∼21.3-yr. This distribution of variance between 2-yr and 21-yr implies the importance of the large-scale variability in surges of the Seine Bay.

Similar scales, reported by Massei et al. (2017) from Seine watershed precipitations, have only presented a mean explained variance of 30% showing a low contribution of the large-scales in the total energy of the signal and highlighting the eventual weak dependence between high and low frequencies. In the case of high discrepancies between the different frequencies composing some statistical signals and with the aim to extract their low-frequency components, demodulating their evolution by the use of the envelope technique should be a useful way to investigate more deeply their large-scale behavior.

A total of 36 exceptional stormy events (from E_1 to E_{36}) produced in the Seine bay during the period 1964–2010 and with surges higher than 2-yr return period level has been extracted from REFMAR data base (Table 2). The different storms have been reported to the low-frequency components of the demodulated surges by vertical color bars (Fig. 4).

Five categories have been defined and attributed to the different storms according to their surge return period (Re): "A" with Re = 2-yr, "B" 2-yr <Re<5-yr, "C" with 5-yr <Re<10-yr, "D" with 10-yr <Re<20-yr and "E" with Re > 20-y using gray, yellow, red, purple and dark purple colors, respectively. The closing events succeeding in time within a given period (days to months) are represented in Fig. 4 by only one vertical bar whose color is attributed to the higher category of storms produced during this period.

The first two categories of storms with a moderate surge return period are related to higher frequencies and can be observed at scales smaller than ∼4-yr. For example, stormy events E_8, E_{16} and $E_{17\text{-}19}$ of the category "A" (gray box in Fig. 4) are mainly manifested at 2.1-yr and seem to be not expressed at higher scales. $E_{3\text{-}7}$, $E_{9\text{-}10}$ and $E_{32\text{-}34}$ of the category "B" (yellow box in Fig. 4) are well observed at the interannual scales 2.1-yr and 4-yr. The events E1, E_{11}, $E_{20\text{-}21}$, E_{35} and E_{36} of the category "C" (red box in Fig. 4) are manifested at the three scales 2.1-yr, 4-yr and 7.8-yr. The category "E", E_{13}, $E_{28\text{-}29}$ and $E_{30\text{-}31}$ (dark purple box in Fig. 4),

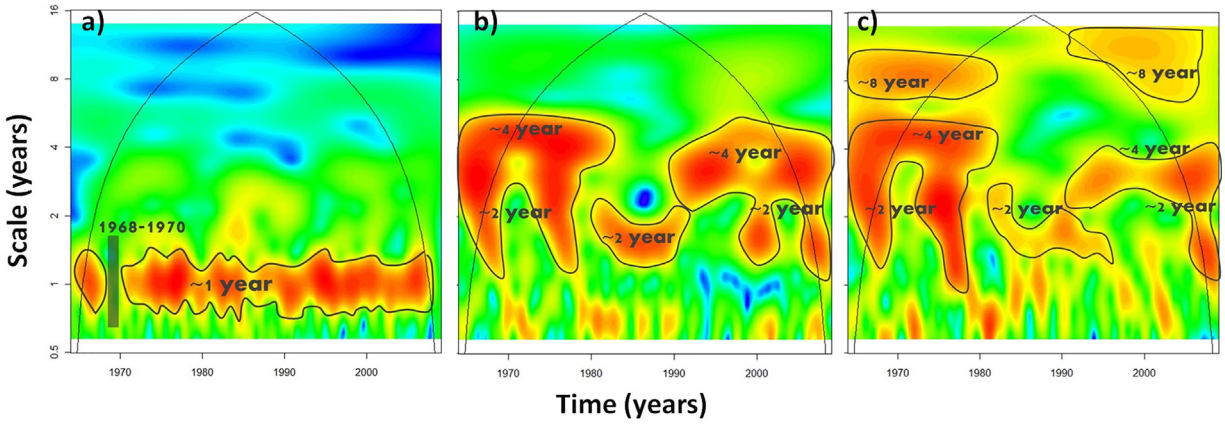

Figure 3 Continuous wavelet diagram of the monthly mean sea level: (a) the total sea level, (b) the surges and (c) the demodulated surges (maxima envelope) between 1964 and 2010.

Table 1 Equivalent Fourier period, standard deviation and energy, expressed as the percentage of total standard deviation of the maxima envelope, associated with each component (i.e. wavelet details and smooth) of Seine surges between 1964 and 2010.

Surges	D1–D4	D5	D6	D7	D8	D9	Total
Fourier period (yr)	$\leq\sim1$	~2.1	~4	~7.8	~15.6	~21.3	–
Standard deviation (m)	0.01	0.009	0.005	0.0035	0.003	0.005	–
Energy (%)	17.3	32	26	11	8	5.7	100

is fully manifested at the different time-scales while E_2, $E_{14\text{-}15}$ and $E_{23\text{-}27}$ of the category "D" (purple box in Fig. 4) pass away the lowest frequency of 21.1-yr.

According to this analysis, 36 high stormy events (Re > 2-yr) have been identified during a period of 46 years; they are of different categories depending on the surge return period and the time-scale associated with the spectral period: 19 events of category "A" with 2.1-yr, 6 events of category "B" with 4-yr, 5 events of category "C" with 7.8-yr, 3 events of each category "D" and "E" with 15.6-yr and 21.3-yr, respectively.

The distribution of storms is not homogeneous in time and their occurrence according to the different categories takes a nonstationary behavior since the number of events in a window of one-year changes in time. Results have shown that 24 among 46 years do not display any significant event (Re > 2-yr) emphasizing alternating phases of moderate energy and storminess. Moderate phases with non-significant

Table 2 List of stormy events produced between 1964 and 2010; only storms with surge return period (Re) higher than 2 years.

Number of event	Date of event	Return period of surges (Re)	Tidal cycle
E_1	20 January 1965	5–10 years	Spring tide (coefficient 102)
E_2	27 November 1965	10–20 years	Neap tide (coefficient 68)
E_3	11 March 1967	2 years	Neap tide (coefficient 86)
E_4	04 October 1967	2–5 years	Spring tide (coefficient 113)
E_5	13 November 1967	2 years	Neap tide (coefficient 63)
E_6	02 November 1967	2–5 years	Spring tide (coefficient 111)
E_7	07 January 1968	2 years	Neap tide (coefficient 50)
E_8	06 July 1969	2 years	Neap tide (coefficient 67)
E_9	06 February 1974	2 years	Spring tide (coefficient)
E_{10}	09 February 1974	2–5 years	Spring tide (coefficient 112)
E_{11}	25 December 1976	2–5 years	Neap tide (coefficient 70)
E_{12}	15 December 1979	2 years	Neap tide (coefficient 66)
E_{13}	13 December 1981	>20 years	Spring tide (coefficient 104)
E_{14}	25 October 1984	2 years	Spring tide (coefficient 100)
E_{15}	22 November 1984	10–20 years	Spring tide (coefficient 102)
E_{16}	15 October 1987	2 years	Neap tide (coefficient 28)
E_{17}	20 December 1989	2 years	Neap tide (coefficient 90)
E_{18}	03 January 1990	2 years	Spring tide (coefficient 103)
E_{19}	26 February 1990	2 years	Spring tide (coefficient 106)
E_{20}	20 January 1994	2–5 years	Neap tide (coefficient 50)
E_{21}	15 April 1994	5–10 years	Spring tide (coefficient 100)
E_{22}	19 February 1996	2 years	Spring tide (coefficient 113)
E_{23}	25 December 1999	10–20 years	Spring tide (coefficient 104)
E_{24}	22 January 2000	5–10 years	Spring tide (coefficient 106)
E_{25}	08 February 2000	2 years	Neap tide (coefficient 88)
E_{26}	04 April 2000	2 years	Spring tide (coefficient 98)
E_{27}	02 September 2000	2 years	Spring tide (coefficient 94)
E_{28}	10 October 2000	>20 years	Spring tide (coefficient 101)
E_{29}	29 October 2000	2 years	Spring tide (coefficient 95)
E_{30}	17 September 2001	>20 years	Spring tide (coefficient 115)
E_{31}	28 December 2001	2 years	Neap tide (coefficient 74)
E_{32}	08 February 2004	2 years	Spring tide (coefficient 90)
E_{33}	10 December 2004	2 years	Neap tide (coefficient 79)
E_{34}	08 April 2005	2–5 years	Spring tide (coefficient 104)
E_{35}	11 March 2008	5–10 years	Spring tide (coefficient 106)
E_{36}	09 January 2009	5–10 years	Spring tide (coefficient 108)

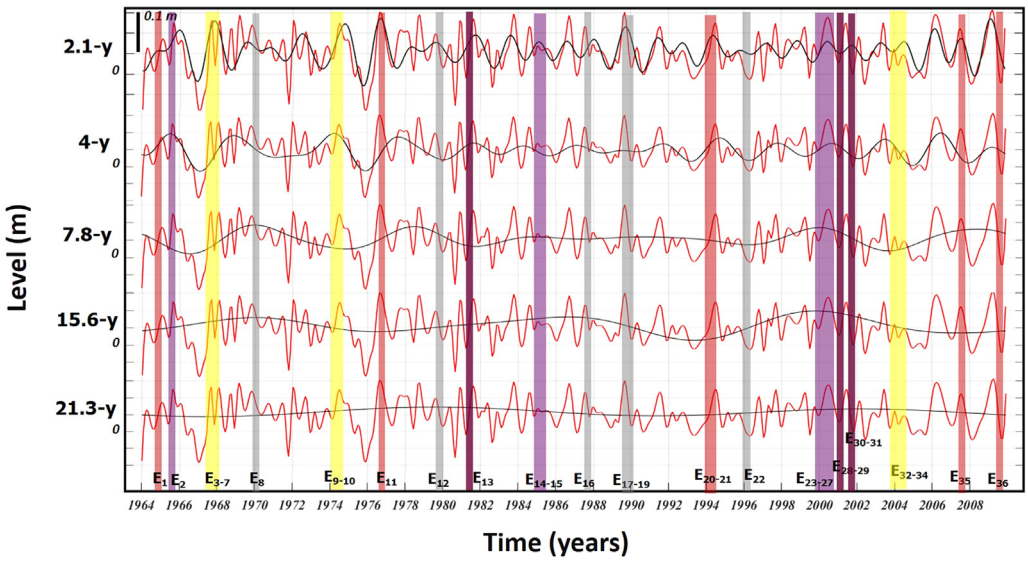

Figure 4 Multiresolution decomposition of the monthly surges, using the so-called, redundant, maximum-overlap discrete wavelet transform. Wavelet detail at scales higher than 1 year: 2.1-yr, 4-yr, 7.8-yr, 15.6-yr and 21.3-yr. The 36 exceptional stormy events with different categories function of their return period (Re), occurred during the period 1964–2010, are illustrated by colored boxes: "A" (gray line) Re = 2-yr, "B" (yellow line) 2-yr $<$ Re $<$ 5-yr, "C" (red line) 5-yr $<$ Re $<$ 10-yr, "D" (purple line) 10-yr $<$ Re $<$ 20-yr and "E" (dark purple line) $>$ 20-yr.

storms are longer with 3–4 successive years during the first 35 years (1964–2000) and decrease to 2 years in the beginning of the last decade when the succession of events seems to be more important. Stormy phases display different categories of events mainly distributed between November and February with only 11% of storms observed in October. Some events for each of September (2000, 2001), April (1994 and 2000) and March (1967 and 2008), July (1967) have been associated with the category "A".

This connection between the low-frequency components and the historical record of the exceptional events suggests that storms would occur differently according to a series of physical processes oscillating at multi-time-scales; these processes control their frequency and their intensity.

The seasonal dependence between stormy events and the extreme sea levels, already observed in previous works (e.g., Tsimplis and Woodworth, 1994), is mainly caused by astronomical forces of spring tides and meteorological conditions of seasonal storms. This dependence explains the distribution of storms and their organization in time; which is strongly related to the large-scale variability of surges. For example, the four storms of 1967 (E_3 to E_6) and the five storms of 2000 (E_{25} to E_{29}) show a seasonal dependence in their succession, tidal phase and intensity (return period).

The combining effect of local driven forces with meteorological, oceanographic and hydrological origins explains the most significant of the stochastic signal of surges in the Seine Bay where the fluvial activity plays an important role in changes of water elevations. This activity is largely observed during flooding periods; an example is produced in December 2001 (e.g., Massei and Fournier, 2012) when E_{31} of the category A has occurred.

The origin of physical processes responsible for storm surges exhibits a temporal nonstationary behavior due to a combination between the seasonal, the interannual and the interdecadal variability, and a non-linear interaction between the different time-scales. The assessment of the nonstationary effect on the estimation of extreme surges should be largely considered in the methods of extreme analysis by the use of the nonstationary models. For example, a time-dependent Generalized Extreme Value (GEV) distribution has been used by Masina and Lamberti (2013) to model the nonstationary features contained in the sea level time series by introducing the seasonality effect of GEV parameters (location, scale and shape) in order to improve the fitting of extreme values and reduce the uncertainty on the estimation of the return levels.

3.2. Relationship between storm surge dynamics and the atmospheric patterns

This section is focused on the connection between the local large-scale variability of surges and the global climate changes induced by the atmospheric circulation.

The climate patterns, extensively studied over the last two decades, have been mainly described by the NAO mechanisms (e.g. Hurrell et al., 2003). The SLP fields covering the English Channel, between 1964 and 2010, have been used with their different structures to characterize the climate patterns from the wavelet multiresolution decomposition into different time-scales.

Five composite maps have been calculated from the SLP field and the large-scale components of demodulated surges (Fig. 5). Provided maps are focused only on low frequencies ranging between 2.1-yr (D5) and 21.3-yr (D9) whose fluctuations correspond to oscillations periods less than half the length of the time series, and with the high-energy contribution on the variance of the total signal. As suggested by these

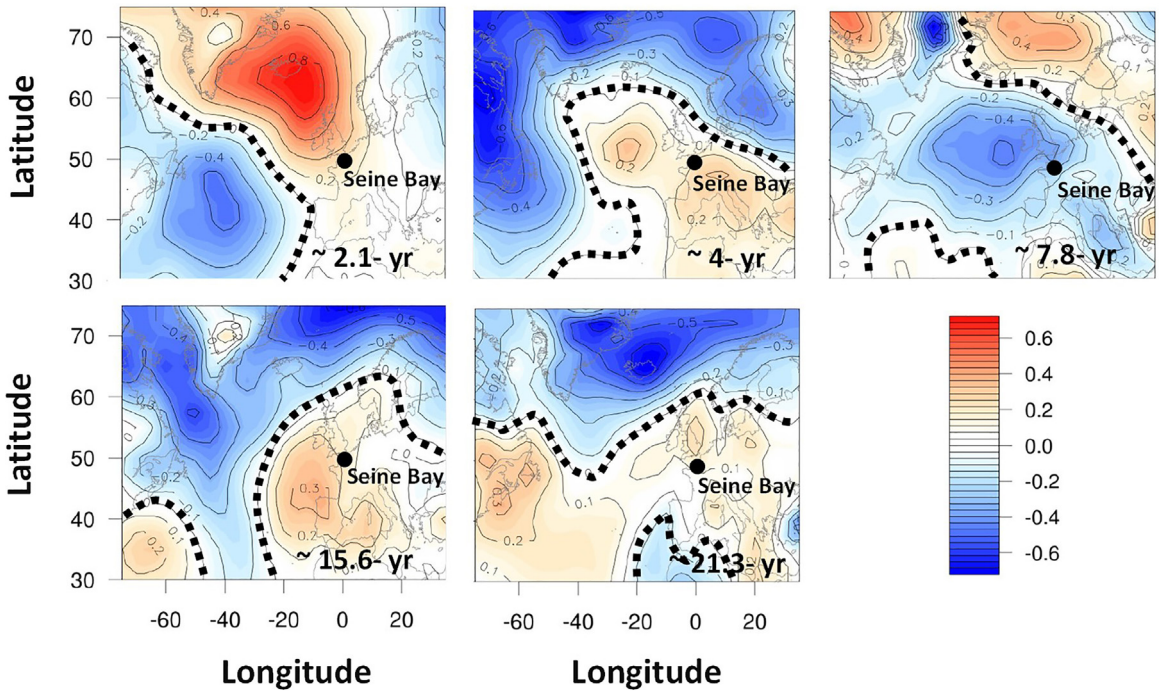

Figure 5 Composite maps of SLP generated for each scale based on surge variability. Black dashed lines indicate statistically significant regions (Student *t*-test with a 95% confidence limit).

composite maps, the relationship between the demodulated surges and the SLP fields is statistically significant and varies spatially in magnitude and phase. The spatial extent and the location of high-low pressure regions displayed by the atmospheric patterns are organized differently according to the time-scales of variability. Both 2.1-yr and 7.8-yr time-scales have shown dipolar structures with high-pressure anomalies located over the northern North Atlantic/sub-Arctic regions and low-pressure anomalies across the Atlantic (2.1-yr time-scale) and developing toward the English Channel and the North Sea (7.8-yr time-scale). Such dipolar structures can be associated with the typical western circulation, reminiscent of the negative NAO regime, more particularly for the 7.8-yr time-scale. This distribution should be attributed to the cyclonic circulation over northwestern Europe (50°N) with an alternating increase and decrease of West moisture fluxes from the Atlantic Ocean to the southern side of the English Channel and the Seine Bay.

On the contrary, 4-yr (D6), 15.6-yr (D8) and 21.3-yr (D9) time-scales have pointed North-South structures that could not be related to western circulation. Trough-shaped SLP anomalies in the center of the North-Atlantic basin would suggest weakened western circulation dynamics that would not be preeminent at these time-scales. In their analysis of multi-time-scale hydroclimate dynamics over the Seine river watersheds in Northern France, Massei et al. (2017) have found similar pattern shapes of SLP composites calculated from the Seine rainfall at the same time-scales.

Similar low-frequency oscillations have also been outlined by Feliks et al., 2011 in relation with NAO patterns of the simulated marine atmospheric boundary layer (MABL) forced with SST from a simple Ocean Data Analysis. Such relations to NAO index have been also observed by Turki et al. (2015) from the sea level fluctuations for scales between 1-yr and 3-yr, while the origin of higher frequencies, smaller than 1-yr, is related to the seasonal cycle of alternating high-low energy and changes in river discharges and temperature.

The different time-scales of the local variability of surges is not linearly related to the atmospheric circulation processes since their spatial extent, highlighted by the wavelet-based composite analysis, seems to be not fully similar according to the different scales of the hydro-climatic variability; each time-scale is associated with a determined physical mechanism explaining the oscillation period of changes.

The “switch on” and “off” of the influence of climate patterns on the variability of surges have an important application for many predictability issues. In this way, if SLP structures and surges anomalies are of similar patterns, the use of surges for predicting its variability from the SLP patterns at different time-scales could increase the accuracy of statistical predictions. At these scales, the atmospheric teleconnections explained by a series of physical mechanisms show a nonstationary behavior with a focus in the stochastic variability of surges.

This behavior is still under debate (Martin-Rey et al., 2012; Polo et al., 2008; Rodriguez-Fonseca et al., 2009).

According to their works related to the nonstationarities of the Atlantic influence on the Pacific in the 20th century, Lopez-parages et al. (2013) have shown that the statistical predictability of the rainfall variability can be improved by selecting the most suitable predictors depending on the period on which the prediction is carried out. They have also suggested that the nonstationary link between rainfall and SST takes place when the dipolar patterns of rainfall is

reinforced and coincides with negative phases of the AMO (Atlantic Multidecadal Oscillation) index along the 20th century.

Hence, the results obtained here point out a nonstationary behavior of the teleconnections between the local surges and the global SLP field, in particular for the interannual oscillations modulated by the interdecadal scales. The physical coherent modulation at a multi-scale variability is mainly related to the atmospheric circulation influenced generally by ocean currents and the Gulf Stream (GS). Several questions behind the reasons for this nonstationary teleconnections remain open, as the origin of the modulating factors.

In fact, the sea level pressure (SLP) and the baroclinic instability of wind stress are related to the GS path as given by NCEP reanalysis. In fact, the dominant signal is a northward (southward) displacement of the GS after the NAO reaches positive (negative) extrema (Frankignoul et al., 2001).

In the present context of global changes, the underlying issue of rising sea levels is combined to more stormy events and extremes. The increasing trend of stormy events in the Seine Bay, probably induced by the sea level rise scenarios of the English Channel, should be highly correlated with large variations in the GS transport (Ezer et al., 2013). The hypothesis of the GS transport reduction resulting in slower surface geostrophic currents, smaller gradients across the GS, and higher variations in the coastal sea level in the north GS has been supported by global climate models and satellite observations. Ezer et al. (2013) have demonstrated a strong relation between the coastal sea level changes and the GS variations on time-scales ranging from a few months to many decades with an increasing explained variance. The shift of the GS from 6—8 year oscillation cycle to a continuous weakening trend since the beginning the last century; which corresponds to the period of changes in storm organization and an increase in their frequency in time.

4. Conclusions

This research is focused on investigating the nonstationary dynamic of surges in the Seine Bay (southern side of the English Channel, NW France) and its nonlinear relationship with the global atmospheric circulation basing on a spectral approach of wavelet multi-resolution decomposition. By the use a new technique of envelope for demodulating surges, the large-scale variability has been quantified during 46 years (1964—2010). A total of 36 exceptional stormy events has been reported to the interannual (2.1-yr, 4-yr and 7.8-yr) and interdecadal (15.6-yr and 21.3-yr) time-scales of surges. Results have suggested a strong connection between the categories of storms, their intensity (return period 'Re') and their organization in time with the large-scale variability of surges. In fact, the interannual scales of 15.6-yr and 21.3-yr have been linked to stormy events with Re higher than 10 years; storms with Re of 2 years are only manifested at 2.1-yr scales, while events with Re between 2 and 10 years have been reported to 4-yr and 7.8-yr scales. Dipolar patterns of high-low pressures have been detected at 2.1-yr and 7.8-yr scales and should be related to the western circulation having an impact on the sea surge maxima, while the variability of 4-yr, 15.6-yr and 21.3-yr should obey to different mechanisms related to the pronounced North-South circulation processes and NAO, as interpreted from the distribution of SLP anomalies.

The present investigation brings some interesting results about the nonstationary behavior the teleconnections between the local surges and the global climate circulation at large-time scales. By simulating the low-frequency components of demodulated surges and SLP fields, results have highlighted the important role of the interdecadal frequencies in the modulation of interannual variability. Deeper investigations related to the physical mechanisms responsible for this nonstationary dynamic are required in order to improve our understanding of the system climate-ocean changes.

The conclusion of this research suggests that wind—stress variations driven by energetic currents such as the GS may play a key role in coastal sea level changes. Establishing a strong connection between large-scale sea level changes with flooding risks and the GS gradients could improve our understanding of the relation between the global climate patterns and the local sea level changes; also allow us to infer the future projections of sea level change and extreme events.

This finding can represent a step forward in the understanding of the role of the sea level surges and should be useful to improve the downscaling models of sea surges, therefore allowing a better assessment of flood risks. Further works will be focused on developing the large-scale/local-scale nonstationary models by the use of different large-scale variables related to the atmospheric circulation. This may allow proposing the improved statistical downscaling models and exploring the capabilities of such models to produce forecasts of the probability of extreme sea level trends by considering the interannual and the interdecadal variability of global climate patterns.

Acknowledgments

The authors are grateful to ANR funded project “RICCOCHET” of French national program as well as the international project COTEST funded by CNES-TOSCA and related to the future mission of Surface Water and Ocean Topography (SWOT). Authors thank also National Navy Hydrographic Service and National Center for Environmental Prediction for providing sea level and atmospheric data. Also, the authors greatly thank the reviewers and the editors of the journal Oceanologia for their useful suggestions to improve the manuscript.

References

Devoy, R.J.N., 2008. Coastal vulnerability and the implications of sea level rise for Ireland. J. Coast. Res. 24 (2), 325—341, http://dx.doi.org/10.2112/07A-0007.1.

Ezer, T., 2001. Can long-term variability in the Gulf Stream transport be inferred from sea level? Geophys. Res. Lett. 28 (6), 1031—1034, http://dx.doi.org/10.1029/2000GL011640.

Ezer, T., Atkinson, L.P., Corlett, W.B., Blanco, J.L., 2013. Gulf Stream's induced sea level rise and variability along the U.S. mid-Atlantic coast. J. Geophys. Res. 118, 685—697, http://dx.doi.org/10.1002/jgrc.20091.

Ezer, T., Corlett, W.B., 2012. Analysis of relative sea level variations and trends in the Chesapeake Bay: is there evidence for acceler-

ation in sea level rise? In: Proc Oceans'12 MTS/IEEE, October 14–19, IEEE Xplore, http://dx.doi.org/10.1109/OCEANS.2012.6404794.

Feliks, Y., Ghil, M., Robertson, A.W., 2011. The atmospheric circulation over the North Atlantic as induced by the SST field. J. Clim. 24 (2), 522–542, http://dx.doi.org/10.1175/2010JCLI3859.1.

Frankignoul, C., Coëtlogon, G., Joyce, T.M., Dong, S., 2001. Gulf Stream variability and ocean–atmosphere interactions. J. Phys. Oceanogr. 31 (12), 3516–3529, http://dx.doi.org/10.1175/1520-0485(2002)031<3516:GSVAOA>2.0.CO;2.

Gratiot, N., Anthony, E.J., Gardel, A., Gaucherel, C., Proisy, C., Wells, J.T., 2008. Significant contribution of the 18.6 year tidal cycle to regional coastal changes. Nat. Geosci. 1 (3), 169–172, http://dx.doi.org/10.1038/ngeo127.

Hurrell, J.W., Kushnir, Y., Ottersen, G., Visbeck, M., 2003. An Overview of the North Atlantic Oscillation. Geophys. Monog. Ser. 134, AGU, http://dx.doi.org/10.1029/134GM01.

Kalnay, E., Kanamitsu, M., Kistler, R., Collins, W., Deaven, D., Gandin, L., Joseph, D., 1996. The NCEP/NCAR 40-year reanalysis project. Bull. Am. Meteorol. Soc. 77 (3), 437–472, http://dx.doi.org/10.1175/1520-0477(1996) 077<0437:TNYRP>2.0.CO;2.

Levermann, A., Griesel, A., Hofmann, M., Montoya, M., Rahmstorf, S., 2005. Dynamic sea level changes following changes in the thermohaline circulation. Clim. Dynam. 24 (4), 347–354, http://dx.doi.org/10.1007/s00382-004-0505-y.

Lopez-parages, J., Villamayor, J., Gomaeai, I., Losada, T., Martinrey, M., Mohino, E., Polo, I., Rodriguez-Fonseca, B., Suarezi, R., 2013. Nonstationary interannual teleconnections modulated by multidecadal variability. Física de la Tierra 25, 11–39, http://dx.doi.org/10.5209/rev_FITE.2013.v25.43433.

Marcos, M., Chust, G., Jordá, G., Caballero, A., 2012. Effect of sea level extremes on the western Basque coast during the 21st century. Clim. Res. 51 (3), 237–248, http://dx.doi.org/10.3354/cr01069.

Martin-Rey, M., Polo, I., Rodriguez-Fonseca, B., Kucharski, F., 2012. Changes in the interannual variability of the tropical Pacific as a response to an equatorial Atlantic forcing. Sci. Mar. 76 (S1), 105–116, http://dx.doi.org/10.3989/scimar.03610.19A.

Masina, M., Lamberti, A., 2013. A nonstationary analysis for the Northern Adriatic extreme sea levels. J. Geophys. Res. 118, 3999–4016, http://dx.doi.org/10.1002/jgrc.20313.

Masina, M., Lamberti, A., Archetti, R., 2015. Coastal flooding: a copula based approach for estimating the joint probability of water levels and waves. Coast. Eng. 97, 37–52, http://dx.doi.org/10.1016/j.coastaleng.2014.12.010.

Massei, N., Dieppois, B., Hannah, D.M., Lavers, D.A., Fossa, M., Laignel, B., Debret, M., 2017. Multi time-scale hydroclimate dynamics of a regional watershed and links to large-scale atmospheric circulation: Application to the Seine river catchment, France. J. Hydrol. 546, 262–275, http://dx.doi.org/10.1016/j.jhydrol.2017.01.008.

Massei, N., Fournier, M., 2012. Assessing the expression of large-scale climatic fluctuations in the hydrological variability of daily Seine river flow (France) between 1950 and 2008 using Hilbert-Huang Transform. J. Hydrol. 448–449, 119–128, http://dx.doi.org/10.1016/j.jhydrol.2012.04.052.

Menendez, M., Woodworth, P.L., 2010. Changes in extreme high water levels based on a quasi-global tide-gauge data set. J. Geophys. Res. 115, C10011, http://dx.doi.org/10.1029/2009JC005997.

Minguez, R., Tomas, A., Mendez, F.J., Medina, R., 2012. Mixed extreme wave climate model for reanalysis databases. Stoch. Environ. Res. Risk. Assess. 27, 757–768, http://dx.doi.org/10.1007/s00477-012-0604-y.

Mitchell, J.M., Dzerdzeevskii Jr., Flohn, B., Hofmeyr, H., Lamb, W.L., Rao, H.H., Wallén, C.C., 1966. Climatic change: Technical Note No. 79, report of a working group of the Commission for Climatology. WMO No. 195 TP 100. World Meteorological Organization, Geneva, Switzerland, 81 pp.

Mitchell, M., Hershner, C., Herman, J., Schatt, D., Eggington, E., Stiles, S., 2013. Recurrent flooding study for Tidewater Virginia, Report SJR 76, 2012. Virginia Instit. Marine Sci., Gloucester Point, VA, 141 pp.

Nicholls, R., Brown, S., Hanson, S., Hinkel, J., 2010. Economics of coastal zone adaptation to climate change, Discussion Paper 10. World Bank, Washington, DC.

Polo, I., Rodriguez-Fonseca, B., Losada, T., Garcia-Serrano, J., 2008. Tropical Atlantic variability modes (1979–2002). Part I: Time evolving SST modes related to West African rainfall. J. Clim. 21, 6457–6475, http://dx.doi.org/10.1175/2008JCLI2607.1.

Pugh, D.J., 1987. Tides, Surges and Mean Sea-Level: A Handbook for Engineers and Scientists. John Wiley, Chichester, 472 pp.

Rodriguez-Fonseca, B., Polo, I., Garcia-Serrano, J., Losada, T., Mohino, E., Mechosos, C.R., Kucharski, F., 2009. Are Atlantic Niños enhancing Pacific ENSO events in recent decades? Geophys. Res. Lett. 36, L20705, http://dx.doi.org/10.1029/2009GL040048.

Ruigar, H., Golian, S., 2015. Prediction of precipitation in Golestan dam watershed using climate signals. Theor. Appl. Climatol. 123 (3–4), 671–682, http://dx.doi.org/10.1007/s00704-015-1377-2.

Sallenger, A.H., Doran, K.S., Howd, P., 2012. Hotspot of accelerated sea-level rise on the Atlantic coast of North America. Nat. Clim. Change 2, 884–888, http://dx.doi.org/10.1038/NCILMATE1597.

Shaw, A.G.P., Tsimplis, M.N., 2010. The 18.6 yr nodal modulation in the tides of Southern European Coasts. Cont. Shelf Res. 30 (2), 138–151, http://dx.doi.org/10.1016/j.csr.2009.10.006.

Stive, M.J.F., Aarninkhof, S.G.J., Hamm, L., Hanson, H., Larson, M., Wijnberg, K.M., Nicholls, R.J., Capobianco, M., 2002. Variability of shore and shoreline evolution. Coast. Eng. 47 (2), 211–235, http://dx.doi.org/10.1016/S0378-3839(02)00126-6.

Sweet, W., Zervas, C., Gill, S., 2009. Elevated east coast sea level anomaly: June-July 2009, NOAA Tech. Rep. No. NOS CO-OPS 051. NOAA NOS, Silver Spring, MD, 40 pp.

Tsimplis, M.N., Woodworth, P.L., 1994. The global distribution of the seasonal sea level cycle calculated from coastal tide gauge data. J. Geophys. Res. 99 (C8), 16031–16039.

Turki, I., Laignel, B., Chevalier, L., Costa, S., Massei, N., 2015. Coastal sea level changes in the southeastern side of the English channel: potentialities for future SWOT applicability. IEEE J. Sel. Top. Appl. Earth Obs. Remote Sens. 8 (4), 1564–1569, http://dx.doi.org/10.1109/JSTARS.2015.2419693.

Wood, F., 2001. Tidal dynamics. Volume 1: theory and analysis of tidal forces. J. Coast. Res. 259–326, https://www.jstor.org/stable/25736216.

Woodworth, P.L., Blackman, D.L., 2004. Evidence for systematic changes in extreme high waters since the mid-1970s. J. Clim. 17 (6), 1190–1197, http://dx.doi.org/10.1175/1520-0477(1996) 077<0437:TNYRP>2.0.CO;2.

Yang, Y., 2017. A signal theoretic approach for envelope analysis of real-valued signals. IEEE Access 5, 5623–5630, http://dx.doi.org/10.1109/ACCESS.2017.2688467.

Yin, J., Schlesinger, M.E., Stouffer, R.J., 2009. Model projections of rapid sea-level rise on the northeast coast of the United States. Nat. Geosci. 2, 262–266, http://dx.doi.org/10.1038/NGEO462.

Oceanologia (2019) 61, 460—470

Available online at www.sciencedirect.com

ScienceDirect

journal homepage: www.journals.elsevier.com/oceanologia/

ORIGINAL RESEARCH ARTICLE

Gas transfer velocities in Norwegian fjords and the adjacent North Atlantic waters

Hanne M. Banko-Kubis, Oliver Wurl, Nur Ili Hamizah Mustaffa, Mariana Ribas-Ribas *

Center for Marine Sensors, Institute for Chemistry and Biology of the Marine Environment, Carl von Ossietzky University of Oldenburg, Wilhelmshaven, Germany

Received 17 December 2018; accepted 12 April 2019
Available online 1 May 2019

KEYWORDS
Air-sea CO_2 flux;
Gas transfer velocity;
Gas exchange;
Parameterization;
Fjord

Summary We investigated air-sea carbon dioxide (CO_2) transfer in situ to determine the role of wind and turbulence in forcing gas transfer. In situ gas transfer velocities of CO_2 were measured with a floating chamber technique along the Norwegian coast and inside the Sogne- and Trondheimsfjord. Gas transfer velocities were related to wind speed and turbulence, but neither wind speed nor turbulence can satisfactorily predict gas transfer velocity. However, comparison to existing wind-based parameterizations showed that the data from this study have a similar trend. Generally, we measured higher transfer velocities than the parameterizations predict. In the North Atlantic, we measured transfer velocities of up to 54.9 cm h^{-1} versus predicted transfer velocities of 6.3 cm h^{-1} at a wind speed of 3.7 m s^{-1}. In addition, we observed that measurements of transfer velocities at wind speeds below 4 m s^{-1} are higher than predictions. Wind-based parameterizations are lacking data in the low wind regime for validation, and we provide 25 data points for this critical wind speed range. Overall, results indicate that Norwegian fjords and the adjacent North Atlantic are sinks for atmospheric CO_2 during summer, with uptake rates of -9.6 ± 7.6 μmol m^{-2} min^{-1} and -4.1 ± 1.7 μmol m^{-2} min^{-1}, respectively. Due to the low partial pressure of CO_2 in the upper water layer of the stratified fjords (down to 150.7 μatm), the Sogne- and Trondheimsfjord absorb 196 tons of carbon per day during the summer.

* Corresponding author at: Center for Marine Sensors, Institute for Chemistry and Biology of the Marine Environment, Carl von Ossietzky University of Oldenburg, 26382, Wilhelmshaven, Germany. Tel.: +494421944164; fax: +494421944140.
E-mail address: mariana.ribas.ribas@uol.de (M. Ribas-Ribas).
Peer review under the responsibility of Institute of Oceanology of the Polish Academy of Sciences.

ELSEVIER Production and hosting by Elsevier

https://doi.org/10.1016/j.oceano.2019.04.002

1. Introduction

Since the beginning of the Industrial Era, the atmospheric concentration of carbon dioxide (CO_2) has increased by 128 ppm, to approximately 405 ppm in 2017 (Le Quéré et al., 2018). Due to the continuous increase of anthropogenic CO_2 emission and its property as a greenhouse gas, understanding how the ocean absorbs CO_2 is crucial in climate research. For example, about 25% of anthropogenically released CO_2 is taken up by the oceans (Takahashi et al., 2009). It is therefore essential to determine exchange rates of CO_2 between the atmosphere and the ocean for reliable estimation of the global carbon budget.

The CO_2 uptake by the oceans influences water chemistry and leads to ocean acidification because aqueous CO_2 reacts to carbonic acid, bicarbonate, and carbonate ions (Fabry et al., 2008). Ocean acidification, also known as "the other CO_2 problem" (Doney et al., 2009), has become an important field of study to obtain a better understanding of its effect on marine ecosystems (e.g., Hong et al., 2017; Kroeker et al., 2013). With global warming and ocean acidification, two highly debated environmental issues are directly related to the concentration of CO_2 in the atmosphere and the role of the oceans regarding the uptake of CO_2 from the atmosphere.

Whether the ocean acts as a source or a sink for CO_2 depends on the partial pressures of CO_2 in the ocean ($pCO_{2,ocean}$) and the atmosphere ($pCO_{2,atm}$). These partial pressures try to reach an equilibrium; e.g., CO_2 gets dissolved in the ocean if pCO_2 is lower in the water than in the atmosphere, until $pCO_{2,ocean}$ is equal to $pCO_{2,atm}$. The air-sea flux rate of CO_2 depends on the difference of the partial pressures and the gas transfer velocity, also represented by the letter *k*. However, field measurements of gas transfer velocities (k) are challenging (Vachon et al., 2010). For this reason, it is common that k are estimated from parameterizations, solely based on wind speed (Wanninkhof, 2014), to compute fluxes and the global ocean budget (Takahashi et al., 2009). The gas transfer velocity is often parameterized to wind speed because it is well-known that wind-driven near-surface turbulence has a major influence on *k* (Ho et al., 2011; Vachon et al., 2010; Zappa et al., 2003). However, the wide span of wind-based parameterizations indicate that other parameters affect the velocity, such as surfactants, microscale wave breaking, bubbles, rain and biological and chemical enhancement (Garbe et al., 2014). For this reason, field-based measurements of *k* are important to gain a mechanistic understanding of gas exchange processes and to validate parameterizations. Indeed, few studies report the agreement of parameterizations between field studies (Ho et al., 2006; McGillis et al., 2001; Wanninkhof, 1992). While data for moderate wind speeds exist (reviewed by Johnson, 2010), data for low (<4 m s^{-1}) and high (>15 m s^{-1}) wind speeds are lacking (Johnson, 2010; Ribas-Ribas et al., 2018a).

The aim of this study is to contribute to advanced knowledge of air-sea CO_2 exchange velocities under different field conditions. We compared measurements from two Norwegian fjords with transects from the inner parts to the adjacent North Atlantic. A drifting buoy with a floating chamber was deployed to measure in situ *k* and relate them to coherent measurements on turbulence and wind speed. Moreover, we compared the field measurements to existing parameterizations and provide new data to the low wind regime.

2. Material and methods

2.1. Study area

The data were collected during cruise HE491 onboard the r/v *Heincke* from July 8 to 25, 2017. Stations were located in the Sognefjord, the Trondheimsfjord, and along the Norwegian coast, as shown in Fig. 1. The Sognefjord is the world's second-longest (205 km) and deepest (up to 1308 m) fjord (Manzetti and Stenersen, 2010). With a length of 130 km, Trondheimsfjord is the third-largest Norwegian fjord. Fjords are high-latitude estuaries that were formed by glaciers (Syvitski et al., 1987). They typically have deep basins that are separated from the shallower coastal ocean through a sill. The depths of the sill in the Sognefjord and the Trondheimsfjord are 155 m and 195 m, respectively (Mascarenhas et al., 2017). Due to large freshwater inputs, water masses of fjords are commonly stratified (Stigebrandt, 2012). However, only the upper 5 to 15 m of the water column in the Sogne- and Trondheimsfjord show a strong salinity gradient, and the lower water masses are well-mixed. The Sognefjord shows a strong salinity gradient in the surface layers from the inner to the outer fjord due to large freshwater inputs from glacial meltwater (Mascarenhas et al., 2017). Both the Sogne- and Trondheimsfjord are influenced by semi-diurnal tides. The Norwegian coastal current consists of water from the Atlantic Ocean and the North Sea, which mixes with less-saline water masses from the Baltic Sea and the runoff from the Norwegian coast (Sætre et al., 2003). The Norwegian Coastal Current

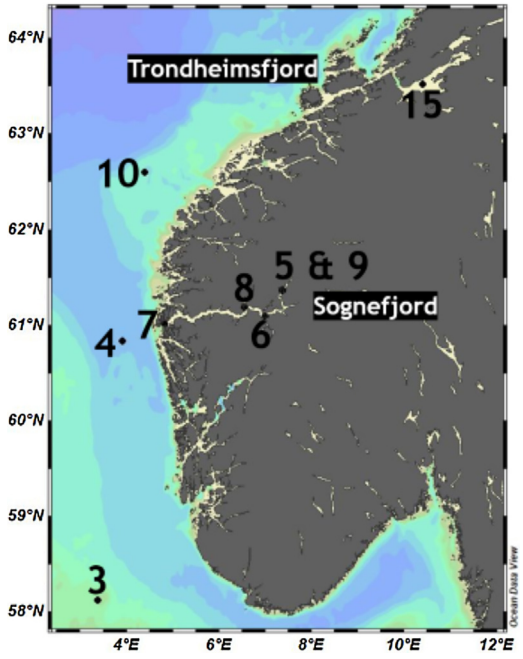

Figure 1 Map of the sampling region during cruise HE491 (southwestern Norway), with all stations that are analyzed in this study. The map was produced using Ocean Data View (Schlitzer, 2017, Ocean Data View, https://odv.awi.de/).

transports heat and less-saline water northwards (Skagseth et al., 2011).

2.2. Field sampling

We deployed an autonomous drifting buoy (*Sniffle*) to measure in situ data on gas transfer velocities (k), which is described in detail by Ribas-Ribas et al. (2018b). To measure the k of CO_2, we used the floating chamber (FC) technique (Kremer et al., 2003) by monitoring pCO_2 over time inside the chamber, floating upside-down within the perimeter of *Sniffle*. *Sniffle* measured pCO_2 in the air ($pCO_{2,atm}$), in the water ($pCO_{2,ocean}$), and in the FC ($pCO_{2,FC}$) with an integrated infrared gas analyzer (IIRGA) (SubCtech OceanPack™, LI-COR LI-840×, range: 0 to 3000 μatm ± 1.5%). $pCO_{2,ocean}$ was measured for 40 min through a 1–2-μm flat-silicone-membrane-equilibrator at a depth of 1.2 m. The upside-down floating chamber had a volume of six liters (diameter: 0.33 m). It was connected to the IIRGA via gas-tight tubing (Swagelok, inner diameter: 6.4 mm). $pCO_{2,FC}$ was measured twice in a sequence, each time over 15 min. From station 5 to station 15, only data from the last 9 min were used due to nonlinearity in the beginning of the cycles. Before recording pCO_2 inside the chamber, air in the floating chamber was exchanged completely by four air pumps (NMP 830 KNDC-B, KNF, flow rate = 2.5 L min^{-1}). $pCO_{2,atm}$ was measured before and after each deployment for one hour on the deck of the r/v *Heincke* while on the station. For later calculations, the mean of all stable $pCO_{2,atm}$ measurements taken on the cruise was used.

Temperature, air pressure, and humidity inside the floating chamber were recorded with a UNI-T UT330C USB data logger at 30-s intervals. The drift of *Sniffle* was monitored by a GPS logger (GT-730FL-S, Canmore, Taiwan) every 10 s. Additionally, *Sniffle* was equipped with two acoustic doppler velocimeters (ADVs) (Nortek) to measure the turbulent kinetic energy (TKE) at approximately 0.1 m depth. The first ADV is located underneath the floating chamber, and the second ADV approximately 0.55 m outside the chamber's perimeter. The inner ADV was equipped with an inertial motion sensor (IMU) (Microstain 3DM-GX3-25-OEM) to correct TKE for the movement of *Sniffle*. A correction was performed according to Kilcher et al. (2016), and data treatment of TKE is described by Ribas-Ribas et al. (2018b).

Conductivity (±0.2%) and temperature (±0.1°C) at 1 m depth were measured from the research catamaran *Sea Surface Scanner* (S^3) (as described in Ribas-Ribas et al. (2017)). Wind speed and air temperature were measured at 3 m height by a weather station mounted on S^3 (Davis Instruments, Vantage Pro2, range wind speed: 0.5 to 89 ± 1 m s^{-1}; range air temperature: −40.0 to 65.0 ± 0.3°C). Wind speed was converted to u_{10} according to Kleemann and Meliß (1993): $u_{10} = (10/H)^{g^*} \times u_H$ (H = 3 m, u_H = wind speed at H, g^* = 0.16 for open water). The wind speed data taken by S^3 were compared to the wind speed measurements on the research vessel (Thies Clima, Windgeber Classic, 0.3 to 50 m s^{-1} ± 2% or 0.3 m s^{-1}) at 23 m height (converted to u_{10} as described above). During deployment, *Sniffle* and S^3 were drifting together with a distance of approximately 20 m to collect data from the same water mass. *Sniffle* and S^3 drifted at a distance of >50 m, but typically >100 m from the research vessel. Air pressure was continuously measured on the research vessel.

2.3. Gas transfer velocities

Gas transfer velocities were calculated according to Ribas-Ribas et al. (2018b). Fluxes in CO_2 (F_{CO_2}) were obtained using the following equation (1):

$$F_{CO_2} = \frac{dp\,CO_2}{dt}\,\frac{V}{S\,T\,R_g}, \tag{1}$$

where $dpCO_2/dt$ is the slope of pCO_2 increase or decrease inside the floating chamber, V is the volume of the floating chamber, S is its surface area, T is the water temperature at 1 m depth, and R_g is the gas constant. Negative fluxes indicate an oceanic uptake of CO_2, while positive fluxes show a release to the atmosphere.

Measurements of $dpCO_2/dt$ were rejected with regression coefficients $R^2 < 0.90$ for the slope. To calculate the gas transfer velocity k_{CO_2}, the following equation (2) was used:

$$k_{CO_2} = \frac{F_{CO_2}}{K(pCO_{2,ocean} - pCO_{2,atm})}. \tag{2}$$

The solubility coefficient K depends on the temperature and salinity (computed from the conductivity) of the seawater and was calculated according to Weiss (1974).

Finally, k_{CO_2} was standardized to k_{660} with the following formula (3):

$$k_{660} = k_{CO_2}\left(\frac{660}{Sc_{CO_2}}\right)^{-n0.5}, \tag{3}$$

Sc_{CO_2} is the temperature-depending Schmidt number (Wanninkhof, 1992) and n the Schmidt number exponent (n = 1/2) (Guérin et al., 2007).

In this study, we obtained 66 accepted k values from 88 measured values in total; i.e., 75% were valid measurements. The error associated with k_{660} and CO_2 fluxes are 13.7% and 10.8%, respectively (Ribas-Ribas et al., 2018b).

2.4. Statistics

Data from the fjords and the North Atlantic were divided into two groups. All stations inside a fjord as well those located at the fjord's mouth were assigned to the group “fjord” due to their direct influence by the characteristics of the fjord system. Stations in the North Atlantic were assigned to the group “oceanic” with a distance of >20 km from the coast (Wurl et al., 2011).

Statistical analysis was performed using R (R Core Team, 2017). Two putative outliers of k_{660} were excluded from further statistical analyses. Correlations between two variables were analyzed using Spearman's correlation analysis. Deming regression was used to find the best fit for two independent variables. Comparison of means was performed using the non-parametric Wilcoxon rank sum test. Analysis of covariance (ANCOVA) was used to compare the means and intercept of the regressions for k with TKE_{ins} and TKE_{out}. A null hypothesis was assumed to be significant when $p < 0.05$.

To parameterize k_{660}'s dependency on u_{10}, quadratic regression analysis was performed. As recommended in

Table 1 Main variables (mean ± standard deviation) measured at each station (abbreviations: station (st.), number (no.), temperature (temp.)).

St.	Day [2017-07-]	Deployment coordinates [start]	Region	Sampling duration [min]	$pCO_{2,ocean}$ [μatm]	No. of k	k_{660} [cm h^{-1}]	Flux [μmol m^{-2} min^{-1}]	u_{10} [m s^{-1}]	TKE_{out} [m^2 s^{-2}]
3	10	58°07′01.286″N 03°22′33.766″E	Oceanic	446	370.9 ± 5.7	11	35.6 ± 9.4	−5.5 ± 0.4	4.7 ± 0.7	0.051 ± 0.010
4	11	60°49′51.938″N 03°55′37.412″E	Oceanic	300	383.7 ± 1.6	7	25.8 ± 3.8	−2.3 ± 0.5	7.0 ± 1.0	0.077 ± 0.013
5	12	61°21′24.455″N 07°22′01.528″E	Inner Sognefjord	397	195.3 ± 15.6	11	10.4 ± 7.5	−11.7 ± 6.3	3.1 ± 1.3	0.017 ± 0.012
6	13	61°05′20.717″N 06°59′56.663″E	Middle-Inner Sognefjord	436	192.0 ± 5.9	11	10.9 ± 3.4	−14.1 ± 4.3	4.9 ± 1.6	0.018 ± 0.011
7	15	61°00′49.630″N 04°49′36.919″E	Outer Sognefjord	144	365.4 ± 3.6	3	24.6 ± 6.0	−4.6 ± 0.7	7.1 ± 0.6	0.050 ± 0.017
8	16	61°11′02.342″N 06°33′36.058″E	Middle-Outer Sognefjord	372	211.1 ± 5.2	2	13.0 ± 1.4	−15.6 ± 1.6	7.8 ± 0.9	0.026 ± 0.004
9	17	61°21′58.579″N 07°22′31.199″E	Inner Sognefjord	376	150.7 ± 21.9	5	10.0 ± 5.6	−16.3 ± 9.9	8.5 ± 1.7	0.031 ± 0.025
10	19	62°35′58.596″N 04°23′27.938″E	Oceanic	388	385.6 ± 3.8	2	45.2 ± 3.2	−2.6 ± 0.5	7.3 ± 0.7	0.066 ± 0.005
15	25	63°31′27.300″N 10°24′39.798″E	Middle Trondheimsfjord	415	336.1 ± 2.7	12	3.2 ± 1.2	−1.1 ± 0.4	1.2 ± 1.0	0.005 ± 0.002

Spiess and Neumeyer (2010), the Bayesian Information Criterion (BIC) was used to compare nonlinear models. Basically, the lower the BIC, the better the fit. The relationship between k_{660}, u_{10}, and TKE was examined with a multiple linear regression (MLR), and the goodness of fit was also evaluated with the BIC (Quinn and Keough, 2009).

3. Results

3.1. Description of general observations

Mean $pCO_{2,atm}$ during the cruise was 398.3 ± 5.3 μatm (N = 1800). Mean $pCO_{2,ocean}$ ranged from 150.7 ± 21.9 μatm (N = 5) in the inner Sognefjord to 385.6 ± 3.8 μatm (N = 2) in the North Atlantic (Table 1). Salinity ranged from 1.32 in the inner Sognefjord (station 5) to 35.14 in the North Atlantic (station 3). $pCO_{2,ocean}$ and salinity show a significant correlation (Spearman correlation, $R \approx 0.83$, $p < 0.0005$). The water temperature in the North Atlantic (14.0 ± 0.3°C) was in general lower than inside fjords (15.5 ± 0.8°C).

Meteorological records are presented in Table S1. The range of u_{10} during the chamber cycles was from 0.43 m s^{-1} (station 15) to 9.65 m s^{-1} (station 9). Wind speed from S^3 and the research vessel are comparable, as shown by correlation analysis (Spearman correlation: $R \approx 0.93$, $p < 0.0001$). For further data analysis, we used wind speeds from the catamaran S^3 due to close proximity to *Sniffle*—i.e., < 20 m.

3.2. *k* parameterizations

Fig. 2 shows k_{660} without error bars for better clarity. The same data with error bars are shown in Figure S1. Mean k_{660} values from all oceanic North Atlantic measurements are, at 33.1 ± 9.5 cm h^{-1}, significantly higher than those from fjords at 9.6 ± 7.0 cm h^{-1} (Wilcoxon rank sum test, $p < 0.005$). The highest mean k_{660} value was measured at station 10 in the North Atlantic (45.2 ± 3.2 cm h^{-1}, N = 2), while lowest mean k_{660} was found at station 15 in the Trondheimsfjord (3.2 ± 1.2 cm h^{-1}, N = 12), associated with the lowest mean wind speed of 1.2 ± 1.0 m s^{-1}.

Fig. 2 shows that k_{660} values from this study generally fit to existing parameterizations, but values measured in the fjords show a better fit than the values from the North Atlantic. However, scattering of the values does not allow choosing a single parameterization for the best fit. Therefore, we performed quadratic regression for our data (Fig. 2), as recommended in Wanninkhof (2014). Regression of all our data ($k_{660} \approx 0.176 \times u_{10}^2 + 12.21$, N = 64, BIC ≈ 532.3), and the data from fjords ($k_{660} \approx 0.138 \times u_{10}^2 + 3.60$, N = 44, BIC ≈ 293.9) lie in the range of the existing parameterizations (McGillis et al., 2001; Raymond and Cole, 2001; Wanninkhof, 2014), although they predict higher k_{660} values at low wind speeds but a smaller slope. Regression for oceanic data ($k_{660} \approx -0.240 \times u_{10}^2 + 41.09$, N = 20, BIC ≈ 151.8) has a negative slope which does not accord to what is known from the literature. Therefore, we assume that the regression shows a wrong trend due to the limited amount of data in a small range of wind speed and other factors than wind affecting k_{660} in the North Atlantic. It is noticeable that nearly all North Atlantic measurements revealed higher k_{660} values than predicted from the wind-based parameterizations. Donelan and Drennan (1995) measured k_{660} in a similar high range in Lake Ontario (see Fig. 3 in Donelan and Drennan, 1995). Though several k_{660} values fit best to the curve of Raymond and Cole (2001), probably because data used in Raymond and Cole (2001) were taken in rivers and estuaries and about 33% of their data were measured with the floating chamber technique similar to this study. However, our study provides

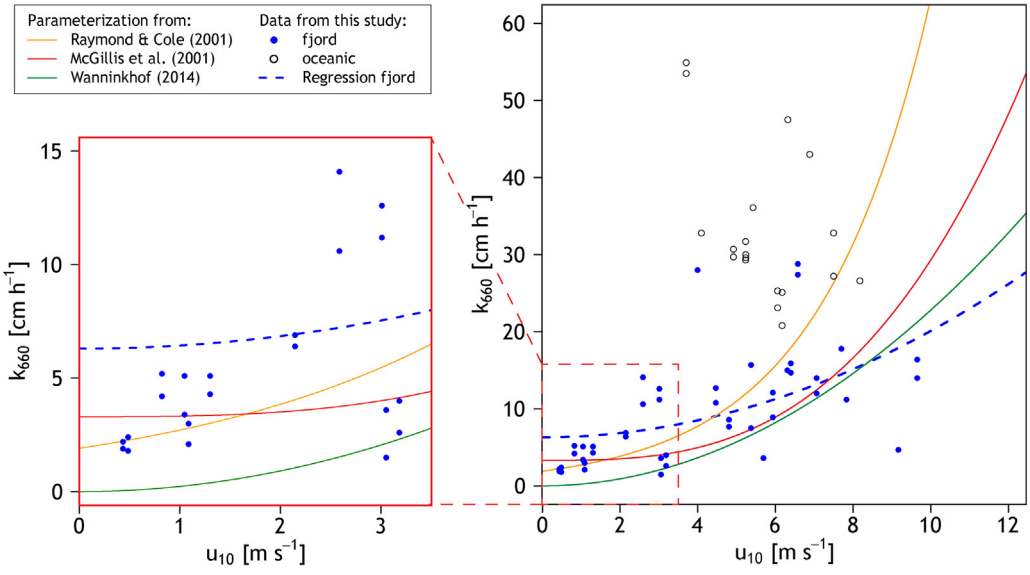

Figure 2 Gas transfer velocities scaled to a Schmidt number of 660 (k_{660}) and a Schmidt number exponent of −0.5 for the fjord (solid blue circles) and the oceanic stations (open data points) vs. a wind speed (u_{10}) scatterplot in comparison to other parameterizations (McGillis et al., 2001; Raymond and Cole, 2001; Wanninkhof, 2014). The data in the red box are the empirical data added in the lower wind speeds, where known parameterizations fall short. (For interpretation of the references to color in this figure legend, the reader is referred to the web version of this article.)

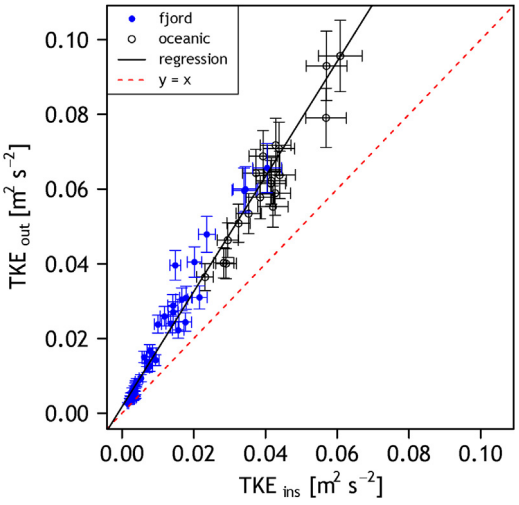

Figure 3 Relationship between Turbulent Kinetic Energy (TKE) inside (TKE_{ins}) and outside (TKE_{out}) the floating chamber for the fjord stations (solid blue circles) and oceanic stations (open data points). The black line represents the Deming regression ($TKE_{out} \approx 1.54 \times TKE_{ins} + 0.0018$). The line of perfect agreement (1:1 line) is shown in red. (For interpretation of the references to color in this figure legend, the reader is referred to the web version of this article.)

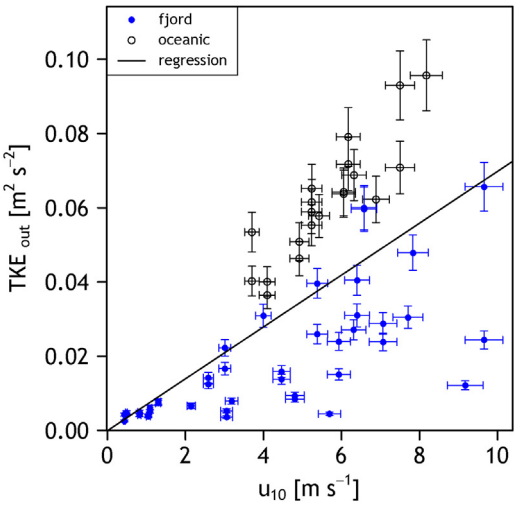

Figure 4 Relationship between wind speed at 10 m (u_{10}) and TKE_{out} for the fjord stations (solid blue circles) and oceanic stations (open data points). The black line represents the Deming regression ($TKE_{out} \approx 0.007 \times u_{10}$). (For interpretation of the references to color in this figure legend, the reader is referred to the web version of this article.)

k_{660} values ($N = 25$) for the low wind regime (0 to 4 m s^{-1}), while wind-based parameterizations typically lack empirical data for low wind speeds. Our data show that the gas transfer velocity is not as close to zero as predicted by parameterizations for the low wind regimes (<4 m s^{-1}), as shown in Fig. 2.

3.3. TKE measurements

Fig. 3 shows that TKE outside *Sniffle's* structure (TKE_{out}) was higher for nearly all measurements. On average, TKE_{out} was approximately 1.5 times higher than TKE below the floating chamber (TKE_{ins}) (Deming regression: $TKE_{out} \approx 1.54 \times TKE_{ins} + 0.0018$, $N = 64$). TKE measurements from the two different measuring points (TKE_{ins} and TKE_{out}) have a significant dissimilarity (Wilcoxon rank sum test; $p < 0.005$). Additionally, TKE measured in the fjords was significantly lower compared to the TKE measured in the North Atlantic (Wilcoxon rank sum test; $p < 0.005$).

ANCOVA showed that the slopes between k_{660} and both TKE measurements were similar (F-test of slopes, $p \approx 0.59$, $F \approx 0.29$), and thus any interference of the chamber on near-surface turbulence was minimal and did not interfere with the CO_2 flux. Because TKE_{ins} and TKE_{out} have a similar slope, only TKE_{out} will be shown in the further analysis for simplicity.

Although there is a significant correlation between wind speed and turbulence (Spearman correlation, TKE_{ins}: $r \approx 0.72$, TKE_{out}: $r \approx 0.74$, $p < 0.001$), higher turbulence did not always result in higher wind speeds (Fig. 4). For example, in the fjords, TKE does not reach high values at higher wind speeds (e.g., >8 m s^{-1} at station 9), probably due to the lower fetch. On the other hand, at low wind speeds, TKE tended to be in its lowest range. The relationship between k_{660} and TKE_{out} is shown in Fig. 5. We observe two clear data groups, one for measurements in the fjords with

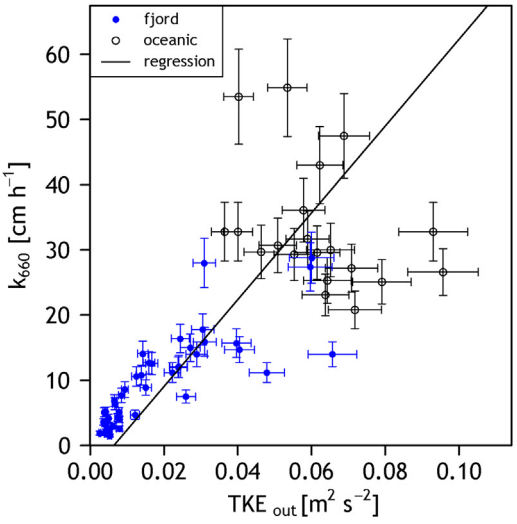

Figure 5 Relationship between TKE_{out} and k_{660} for the fjord stations (solid blue circles) and oceanic stations (open data points). The black line represents the Deming regression ($k_{660} \approx 665.95 \times TKE_{out} - 4.26$). (For interpretation of the references to color in this figure legend, the reader is referred to the web version of this article.)

TKE lower than 0.04 m^2 s^{-2} and another with higher TKE and k_{660} observed in the North Atlantic.

3.4. Combined impact of wind speed and turbulence

To investigate the combined effect of u_{10} and TKE on k_{660}, MLR was performed with u_{10} and TKE_{out}: $\log(k_{660}) \approx 1.35$ (± 0.13)

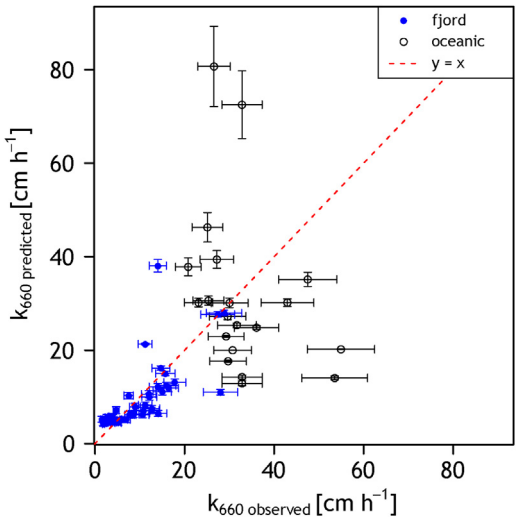

Figure 6 Relationship between observed k_{660} and predicted k_{660} from the multiple linear regression for the fjord stations (solid blue circles) and oceanic stations (open data points). The line of perfect agreement (1:1 line) is shown in red. (For interpretation of the references to color in this figure legend, the reader is referred to the web version of this article.)

+ 0.05 (±0) × u_{10} + 27.51(±2.53) × TKE_{out}; BIC ≈ 121.45. Due to the lower BIC values, MLR explains the relationships between k, u_{10}, and TKE better than the quadratic regression between k_{660} and u_{10} (see Section 3.2). Fig. 6 shows the relationship between observed and predicted k_{660} values from multiple linear regression with TKE_{out} and TKE_{ins}. It is clear that there is a bilateral trend and that there is less scattering in the area of low k_{660} values.

3.5. Revisiting a single station

We deployed *Sniffle* twice in the inner part of the Sognefjord; i.e., on the 12th and 17th of July 2017 (stations 5 and 9) (Table 1). The k were insignificantly different (*t* test, *p* value ≈ 0.91) at station 5 (10.4 ± 7.5 cm h^{-1}) and station 9 (10.0 ± 5.6 cm h^{-1}), although the wind speed was significantly higher (Wilcoxon rank sum test, p value < 0.005) at station 9 (8.5 ± 1.7 m s^{-1}) compared to station 5 (3.1 ± 1.3 m s^{-1}). The dominating wind direction on both days was west-northwest. Mean TKE under the chamber was 0.06 m^2 s^{-2} (station 5) and 0.11 m^2 s^{-2} (station 9). Salinity was low on both days and ranged from 1.7 to 4.0 (station 5: 5.88 ± 4.75; station 9: 3.37 ± 0.29) (Table S1). $pCO_{2,ocean}$ was *significantly higher (test,p* at station 5 (195.3 ± 15.6) compared to station 9 (150.7 ± 21.9). Ancillary data, like surfactants reported in Mustaffa et al. (submitted) and chlorophyll-*a* (data not shown), were similar at both stations, not explaining similar k_{660} values of the two wind regimes.

4. Discussion

4.1. Aqueous pCO_2

This study shows that the Norwegian fjords might play an important role as sinks for atmospheric CO_2. Due to the high inflow of cold, fresh glacial meltwater, they have low pCO_2 values. Even though estuaries are known to be a source of CO_2 (Cai, 2011), other studies concluded that fjords may play an important role in global carbon cycling (Meire et al., 2015; Smith et al., 2015). For example, Meire et al. (2015), who investigated an Arctic fjord, calculated CO_2 fluxes and reported that the fjord act as sink for CO_2 throughout the year. Our correlation of aqueous pCO_2 with salinity agrees with Torres et al. (2011), who found a correlation between aqueous pCO_2 and salinity, as well as aqueous pCO_2 and water temperature. In addition, surface CO_2 saturation changes with the season due to differences in biological activity or the frequency of storm events. For example, Torres et al. (2011) observed a maximum saturation of CO_2 in winter, while aqueous pCO_2 was lower in spring and summer. In our study, photosynthetic efficiency was low (data not presented), suggesting that we conducted our measurements after summer bloom.

4.2. Modification of k parameterization

In this study, it was inappropriate to parameterize k solely by wind speed. Existing wind-based parameterizations do not fully explain k in the fjords or in the North Atlantic. The fact that we measured similar k values at the same location under different wind and turbulence regimes (Section 3.5) clearly indicates that the wind speed or turbulence alone could not explain the variability in k. Interestingly, k values for stations 5 and 9 were close to 10 cm h^{-1} and consistent with a reported non-zero intercept (Ribas-Ribas et al., 2018a; Zhang and Cai, 2007) suggesting a background k in certain conditions.

For example, multiple linear regression of our data with wind and turbulence explained the variations better but with some remaining discrepancies. As Jeffery et al. (2010) already suggested, other influencing parameters, such as surfactants and rising bubbles, should be taken into account to develop a complete model for k. For example, the effect of surfactants was recently investigated in a wind-wave tunnel with a reduction of k by up to 60% with increasing surfactant concentrations (Ribas-Ribas et al., 2018b). However, this has not been achieved yet due to challenges in field measurements and the high complexity of air-sea gas transfer and its description in models. Hence, parameterizations with one variable, for example, wind or turbulence, have been used as an approximation. Nevertheless, it should be considered if parameterizations are valid in general terms and how good such approximations are. For example, the data from our study show that there are differences between estuaries and oceanic CO_2 transfer velocities. Therefore, we agree with Raymond and Cole (2001) that parameterizations of k should be distinguished for estuaries and open ocean environments.

Although there are still some discrepancies, our data show that a parameterization with TKE explains more variance of k compared to parameterizations with wind speed alone. That is illustrated in Fig. 5, showing that higher turbulence is not always related to higher wind speeds. This is in agreement with Zappa et al. (2007) and Esters et al. (2017), suggesting that near-surface turbulence is the primary driving mechanism for k at low to moderate wind speeds (u_{10} < 10 m s^{-1}). Therefore, we propose to use TKE instead of the dissipation rate (ε) because the calculation of ε is a parameter in a

spectral fit and not straightforward to determine. A good fit is critical for ε to be a good proxy for k. TKEs are easier to calculate for scientists from a wider range of research backgrounds, as determination of TKE does not require the computation of the fit and can be directly calculated from the dolfyn routine (https://lkilcher.github.io/dolfyn/). Moreover, TKE and ε show a similar trend (e.g., Figures 14B and D in Kilcher et al. (2017)).

Regarding parameterizations with wind speed, Wanninkhof (2014) highlighted the strong agreement between existing quadratic parameterizations. In terms of the data collected in this study, we suggest adding an intercept to the parameterization because we observed higher k at low wind speeds than the quadratic parameterizations predict (see Fig. 3). Our statement agrees with other studies (McGillis et al., 2001; Raymond and Cole, 2001; Ribas-Ribas et al., 2018a) who also detected higher k in the range of 0 to 4 m s^{-1}, based on direct covariance, gas tracer measurements and the floating chamber.

4.3. Other factors and processes potentially affecting gas transfer velocities

There are several other factors apart from wind speed or turbulence, that have an impact on the CO_2 transfer velocity as described by Wanninkhof et al. (2009). These additional factors might explain the high values for k we detected in the North Atlantic: values which are higher than other in situ data from the literature (Ho et al., 2006; McGillis et al., 2001). Such a discrepancy can have various reasons:

(a) *Fetch*: In the fjord systems, correlations between turbulence and wind speed are less significant (Fig. 4) than the open ocean, which could be due to the different wind fetch in the narrow fjords. On the open surface at the oceanic stations, high wind speeds have a more pronounced effect on near-surface turbulence as well as the formation of waves and therefore the presence of bubbles and sea spray.

(b) *Surfactants*: The occurrence of surface slicks, a sea surface phenomenon of wave-damping areas visible as lighter patches (Romano, 1996) can reduce near-surface turbulence and thus have a profound effect on the reduction of k (Frew et al., 2002). In different experiments, the suppression of k due to surfactants was investigated. In in situ measurements, k was found to decrease by 62% in the presence of surface films (Mustaffa et al., in preparation), which is in agreement with Pereira et al. (2016), who found 14–51% k suppression (ex-situ) and Bock et al. (1999), who performed lab experiments (k reduction up to 60%).

(c) *Water-side convection*: Water-side convection can greatly increase gas transfer velocity (Rutgersson and Smedman, 2010), such as surface cooling and resulting convective mixing enhancing the oceanic uptake of CO_2. Andersson et al. (2017) found strong enhancement of CO_2 exchange in Arctic fjords and highlight the importance of this observation for Arctic fjords and coastal waters. In the case of this study, high k values were found at the oceanic stations but not inside the fjords. That can have several reasons. In contrast to Andersson et al. (2017) who conducted their measurements in the high Arctic in March, we sampled in temperate fjords in summer. Furthermore, a deep mixed layer depth is important for high water-side convection. The observed fjords have a highly stratified water column during summer, while high turbulence might have caused a deep mixed layer depth in the North Atlantic.

(d) *Temporal and spatial variability*: Sampling for this study took place in summer, while other parameterizations include measurements at other seasons or over a complete seasonal cycle. Biogeochemistry of the sampled water can largely differ depending on the sampling time and region. For example, McGillis et al. (2001) reported gas fluxes for the open North Atlantic during June, with the potential presence of a phytoplankton bloom.

(e) *Technology*: The use of different techniques to measure k may further explain discrepancies between different data sets as we further explain in Section 4.5.

Clearly, the bilateral trend of our data indicates that more research is needed in the future to identify the impact of factors that might affect k.

4.4. CO_2 air-sea fluxes in fjords and adjacent oceans

As mentioned above, the results show that fjords have a large CO_2 absorption capacity: Mean flux for fjords was -9.6 ± 7.6 μmol m^{-2} min^{-1} ($N = 44$) and -4.1 ± 1.7 μmol m^{-2} min^{-1} ($N = 20$) for the North Atlantic. Overall, our study reveals that the Sogne- and Trondheimsfjord absorb 196 tons of carbon per day (C d^{-1}) during summer, based on the fjords' area and assuming that our measured fluxes are representative across the whole area. Chilean fjords also act as a CO_2 sink during warm weather in a similar range (-9.5 μmol m^{-2} min^{-1}) (Torres et al., 2011). The sampling locations in the North Atlantic are located north of 54°N, which Bozec et al. (2005) defined as the northern North Atlantic. Bozec et al. (2005) reported that the northern North Atlantic acts as a sink for atmospheric CO_2 within a similar range to our observation — i.e., -1.7 to -2.6 μmol m^{-2} d^{-1} — during late summer.

Turbulence inside the two fjords was lower than in the North Atlantic, with averaged TKE inside the fjords of 0.010 ± 0.009 ($n = 44$) and 0.040 ± 0.009 ($n = 20$) in the North Atlantic, consequently causing lower k in the fjords. Large absorption with low k could only happen with very large ΔpCO_2, which drives the large uptake of CO_2 inside the fjords (Table 1).

Regarding the difference in k between estuarine and open-ocean measurements, we observed the reverse trend of Raymond and Cole (2001). They detected higher k values in estuaries than in the open ocean at the same wind speed. A possible reason could be that they investigated estuaries from North American rivers that already run great distances, whereas the glacial meltwater in the fjords has not been exposed to the atmosphere for long and was less influenced by humans.

4.5. Possible limitations of the floating chamber technique

Measuring k remains a challenging task of today's ocean scientists. Three techniques are widely used: the floating

chamber technique (as in this paper), eddy covariance, and the dual tracer technique (Wanninkhof et al., 2009). The floating chamber technique is a direct measurement and offers a high spatial and temporal resolution, which is needed to understand high ocean variability. Eddy covariance and dual-tracer gases have a much larger spatial footprint (>1 km^2) and temporal scales (>12 h). Furthermore, their data analysis requires more expertise, and they are challenging to apply from research vessels due to the ship's movement (eddy covariance) and need to track the plumes of injected tracer gases (dual tracer gases). The floating chamber technique has been criticized because it covers the water surface and thus has a direct impact on the flux measurement (Borges et al., 2004). The wind is eliminated from the chamber's interior, and the chamber can cause mass boundary perturbations (Vachon et al., 2010). Our data showed that the chamber did not create artificial turbulence as is assumed in Tokoro et al. (2007), as the measurements inside the floating chamber (TKE_{ins}) were not higher than outside (see Fig. 4). To the contrary, turbulence outside the chamber was 1.5 times higher than inside. It could be that the chamber was dampening the movement of the inner ADV or that the outer ADV moved more due to leverage and we only corrected for *Sniffle*'s movement with the inner ADV, where the IMU is located. In our case, we did not correct for different turbulence because the two regressions did not intersect; i.e., they had similar slopes (Ribas-Ribas et al., 2018b). Additionally, no light penetrates the chamber's walls. This might shift the dominant metabolism under the chamber from photo- to heterotrophy and thereby change the gas transfer. However, the switch from photo- to heterotrophy requires more time on a scale of hours (Pringault et al., 2007) than the measuring cycle from *Sniffle* (15 min). Another critique is that the temperature and pressure inside the chamber might also change during one measuring cycle. In our case, both factors slightly changed by a maximum of 31 and 0.6%, respectively (Table S1), but not always in the same direction, making it challenging to determine their influence on k measurements. Moreover, the partial pressure inside the chamber is measured over a period of time (in our case 15 min), so the value for pCO_2 in the air inside the chamber changes over that time. We achieved good slopes to calculate k with a strict quality control scheme, but changing partial pressure may also shift the slopes during deployment. Another source of error, shared with the eddy covariance and dual-tracer techniques is, that *Sniffle* measures $pCO_{2,ocean}$ at 1.2 m depth (due to the size of the pCO_2 sensor) and not close to the sea surface, where the exchange occurs. This could be a possible explanation of why we observed occasionally negative k with higher $pCO_{2,ocean}$ than $pCO_{2,atm}$. Due to the stratification of the water, the gradient from 1.2 m water depth to the surface could have been significant with much lower $pCO_{2,ocean}$ at the sea surface, and therefore the surface layer may act as a source of CO_2 with negative k values. For future measurements, we recommend measuring aqueous pCO_2 closer to the water surface and comparing the floating chamber measurements in situ to another method (e.g., the eddy covariance and dual gas tracer techniques).

5. Conclusion

Overall, our study provides a better understanding of k, especially at low wind speeds. The data from this study show that there are differences between estuaries and oceanic CO_2 transfer velocities. Therefore, we agree with Raymond and Cole (2001) that parameterizations should be distinguished for estuaries, coastal areas, and open ocean. Our data from two marine environments show that wind-based parameterizations of k cannot fully explain both regimes. Our data suggest that a parameterization with TKE would explain more variance of k than parameterizations with wind speed. Additionally, we conclude that fjords might play an important role as a sink for CO_2 due to low aqueous pCO_2 values driving flux. Measurements in the North Atlantic revealed lower uptake rates of CO_2 but higher transfer velocities due to closer conditions to equilibrium. Therefore, new in situ approaches to parameterize k with multiple parameters (e.g., turbulence) should be developed to verify or modify existing parameterizations.

Acknowledgements

This work was funded by the European Research Council's (ERC) PASSME project (grant no. GA336408). The authors would like to thank the captain and crew of the r/v *Heincke* for their supportive work on board. We also thank the scientific crew onboard r/v *Heincke* for their help in the deployments. We thank Marcus Plath and Tiera-Brandy Robinson for editorial assistance.

Appendix A. Supplementary data

Supplementary data associated with this article can be found, in the online version, at doi:10.1016/j.oceano.2019.04.002.

References

Andersson, A., Falck, E., Sjöblom, A., Kljun, N., Sahlée, E., Omar, A. M., Rutgersson, A., 2017. Air-sea gas transfer in high Arctic fjords. Geophys. Res. Lett. 44 (5), 2519–2526, http://dx.doi.org/10.1002/2016GL072373.

Bock, E.J., Hara, T., Frew, N.M., McGillis, W.R., 1999. Relationship between air-sea gas transfer and short wind waves. J. Geophys. Res.-Oceans 104 (C11), 25821–25831, http://dx.doi.org/10.1029/1999jc900200.

Borges, A.V., Delille, B., Schiettecatte, L.S., Gazeau, F., Abril, G., Frankignoulle, M., 2004. Gas transfer velocities of CO_2 in three European estuaries (Randers Fjord, Scheldt, and Thames). Limnol. Oceanogr. 49 (5), 1630–1641, http://dx.doi.org/10.4319/lo.2004.49.5.1630.

Bozec, Y., Thomas, H., Elkalay, K., de Baar, H.J.W., 2005. The continental shelf pump for CO_2 in the North Sea – evidence from summer observation. Mar. Chem. 93 (2–4), 131–147, http://dx.doi.org/10.1016/j.marchem.2004.07.006.

Cai, W.-J., 2011. Estuarine and coastal ocean carbon paradox: CO_2 sinks or sites of terrestrial carbon incineration? Annu. Rev. Mar. Sci. 3, 123–145, http://dx.doi.org/10.1146/annurev-marine-120709-142723.

Donelan, M., Drennan, W., 1995. Direct field measurements of the flux of carbon dioxide. In: Jähne, B., Monahan, E.C. (Eds.), Air-water Gas Transfer. Aeon Ver., Hanau, 677–683.

Doney, S.C., Fabry, V.J., Feely, R.A., Kleypas, J.A., 2009. Ocean acidification: the other CO_2 problem. Annu. Rev. Mar. Sci. 1, 169–192, http://dx.doi.org/10.1146/annurev.marine.010908.163834.

Esters, L., Landwehr, S., Sutherland, G., Bell, T.G., Christensen, K. H., Saltzman, E.S., Miller, S.D., Ward, B., 2017. Parameterizing air-sea gas transfer velocity with dissipation. J. Geophys. Res. 122 (4), 3041–3056, http://dx.doi.org/10.1002/2016JC012088.

Fabry, V.J., Seibel, B.A., Feely, R.A., Orr, J.C., 2008. Impacts of ocean acidification on marine fauna and ecosystem processes. ICES J. Mar. Sci. 65 (3), 414–432, http://dx.doi.org/10.1093/icesjms/fsn048.

Frew, N.M., Nelson, R.K., McGillis, W.R., Edson, J.B., Bock, E.J., Hara, T., 2002. Spatial variations in surface microlayer surfactants and their role in modulating air-sea exchange. In: Gas Transfer at Water Surfaces. American Geophys Union, Washington, DC, 153–159.

Garbe, C.S., Rutgersson, A., Boutin, J., de Leeuw, G., Delille, B., Fairall, C.W., Gruber, N., Hare, J., Ho, D.T., Johnson, M.T., Nightingale, P.D., Pettersson, H., Piskozub, J., Sahlée, E., Tsai, W.-T., Ward, B., Woolf, D.K., Zappa, C.J., 2014. Transfer-across the air-sea interface. In: Liss, P.S., Johnson, M.T. (Eds.), Ocean-Atmosphere Interactions of Gases and Particles. Springer, Heidelberg, 55–112.

Guérin, F., Abril, G., Serça, D., Delon, C., Richard, S., Delmas, R., Tremblay, A., Varfalvy, L., 2007. Gas transfer velocities of CO_2 and CH_4 in a tropical reservoir and its river downstream. J. Mar. Syst. 66 (1–4), 161–172, http://dx.doi.org/10.1016/j.jmarsys.2006.03.019.

Ho, D.T., Law, C.S., Smith, M.J., Schlosser, P., Harvey, M., Hill, P., 2006. Measurements of air-sea gas exchange at high wind speeds in the Southern Ocean: implications for global parameterizations. Geophys. Res. Lett. 33 (16), L16611, http://dx.doi.org/10.1029/2006GL026817.

Ho, D.T., Wanninkhof, R., Schlosser, P., Ullman, D.S., Hebert, D., Sullivan, K.F., 2011. Toward a universal relationship between wind speed and gas exchange: gas transfer velocities measured with $^3He/SF_6$ during the Southern Ocean Gas Exchange Experiment. J. Geophys. Res. 116 (C4), C004F04, http://dx.doi.org/10.1029/2010JC006854.

Hong, H., Shen, R., Zhang, F., Wen, Z., Chang, S., Lin, W., Kranz, S. A., Luo, Y.-W., Kao, S.-J., Morel, F.M., 2017. The complex effects of ocean acidification on the prominent N_2-fixing cyanobacterium *Trichodesmium*. Science 356 (6337), 527–531, http://dx.doi.org/10.1126/science.aal2981.

Jeffery, C.D., Robinson, I.S., Woolf, D.K., 2010. Tuning a physically-based model of the air–sea gas transfer velocity. Ocean Model. 31 (1–2), 28–35, http://dx.doi.org/10.1016/j.ocemod.2009.09.001.

Johnson, M., 2010. A numerical scheme to calculate temperature and salinity dependent air-water transfer velocities for any gas. Ocean Sci. 6 (4), 913–932, http://dx.doi.org/10.5194/os-6-913-2010.

Kilcher, L.F., Thomson, J., Harding, S., Nylund, S., 2017. Turbulence measurements from compliant moorings. Part II: Motion correction. J. Atmos. Ocean Technol. 34, 1249–1266, http://dx.doi.org/10.1175/jtech-d-16-0213.1.

Kilcher, L., Thomson, J., Talbert, J., DeKlerk, A., 2016. Measuring Turbulence from Moored Acoustic Doppler Velocimeters. A Manual to Quantifying Inflow at Tidal Energy Sites. National Renewable Energy Lab., http://dx.doi.org/10.2172/1244672.

Kleemann, M., Meliß, M., 1993. Regenerative Energiequellen: mit 75 Tabellen, 2nd edn. Springer, Berlin.

Kremer, J.N., Nixon, S.W., Buckley, B., Roques, P., 2003. Technical note: Conditions for using the floating chamber method to estimate air-water gas exchange. Estuaries 26, 985–990, http://dx.doi.org/10.1007/BF02803357.

Kroeker, K.J., Kordas, R.L., Crim, R., Hendriks, I.E., Ramajo, L., Singh, G.S., Duarte, C.M., Gattuso, J.P., 2013. Impacts of ocean acidification on marine organisms: quantifying sensitivities and interaction with warming. Glob. Change Biol. 19 (6), 1884–1896, http://dx.doi.org/10.1111/gcb.12179.

Le Quéré, C., Andrew, R.M., Friedlingstein, P., Sitch, S., Hauck, J., Pongratz, J., Pickers, P.A., Korsbakken, J.I., Peters, G.P., Canadell, J.G., Arneth, A., Arora, V.K., Barbero, L., Bastos, A., Bopp, L., Chevallier, F., Chini, L.P., Ciais, P., Doney, S.C., Gkritzalis, T., Goll, D.S., Harris, I., Haverd, V., Hoffman, F.M., Hoppema, M., Houghton, R.A., Hurtt, G., Ilyina, T., Jain, A.K., Johannessen, T., Jones, C.D., Kato, E., Keeling, R.F., Goldewijk, K.K., Landschützer, P., Lefèvre, N., Lienert, S., Liu, Z., Lombardozzi, D., Metzl, N., Munro, D.R., Nabel, J.E.M.S., Nakaoka, S.I., Neill, C., Olsen, A., Ono, T., Patra, P., Peregon, A., Peters, W., Peylin, P., Pfeil, B., Pierrot, D., Poulter, B., Rehder, G., Resplandy, L., Robertson, E., Rocher, M., Rödenbeck, C., Schuster, U., Schwinger, J., Séférian, R., Skjelvan, I., Steinhoff, T., Sutton, A., Tans, P.P., Tian, H., Tilbrook, B., Tubiello, F.N., van der Laan-Luijkx, I.T., van der Werf, G.R., Viovy, N., Walker, A.P., Wiltshire, A.J., Wright, R., Zaehle, S., Zheng, B., 2018. Global Carbon Budget 2018. Earth Syst. Sci. Data 10 (4), 2141–2194, http://dx.doi.org/10.5194/essd-10-2141-2018.

Manzetti, S., Stenersen, J.H.V., 2010. A critical view of the environmental condition of the Sognefjord. Mar. Poll. Bull. 60 (12), 2167–2174, http://dx.doi.org/10.1016/j.marpolbul.2010.09.019.

Mascarenhas, V.J., Voß, D., Wollschlaeger, J., Zielinski, O., 2017. Fjord light regime: bio-optical variability, absorption budget, and hyperspectral light availability in Sognefjord and Trondheimsfjord, Norway. J. Geophys. Res. 122, 3828–3847, http://dx.doi.org/10.1002/2016JC012610.

McGillis, W.R., Edson, J.B., Ware, J.D., Dacey, J.W., Hare, J.E., Fairall, C.W., Wanninkhof, R., 2001. Carbon dioxide flux techniques performed during GasEx-98. Mar. Chem. 75 (4), 267–280, http://dx.doi.org/10.1016/S0304-4203(01)00042-1.

Meire, L., Søgaard, D., Mortensen, J., Meysman, F., Soetaert, K., Arendt, K., Juul-Pedersen, T., Blicher, M., Rysgaard, S., 2015. Glacial meltwater and primary production are drivers of strong CO_2 uptake in fjord and coastal waters adjacent to the Greenland Ice Sheet. Biogeosciences 12 (8), 2347–2363, http://dx.doi.org/10.5194/bg-12-2347-2015.

Mustaffa, N.I.H., Ribas-Ribas, M., Banko-Kubis, H.M., Wurl, O., in preparation. In situ CO_2 transfer velocity reduction by natural surfactants in the sea surface microlayer. Nat. Commun.

Pereira, R., Schneider-Zapp, K., Upstill-Goddard, R.C., 2016. Surfactant control of gas transfer velocity along an offshore coastal transect: results from a laboratory gas exchange tank. Biogeosciences 13 (13), 3981–3989, http://dx.doi.org/10.5194/bg-13-3981-2016.

Pringault, O., Tassas, V., Rochelle-Newall, E., 2007. Consequences of respiration in the light on the determination of production in pelagic systems. Biogeosciences 4 (1), 105–114, http://dx.doi.org/10.5194/bg-4-105-2007.

Quinn, G.P., Keough, M.J., 2009. Experimental Design and Data Analysis for Biologists. Cambridge Univ. Press, New York, 537 pp.

R Core Team, 2017. R: A Language and Environment for Statistical Computing. R Foundation for Statistical Computing, Vienna, Austria.

Raymond, P.A., Cole, J.J., 2001. Gas exchange in rivers and estuaries: choosing a gas transfer velocity. Estuaries 24 (2), 312–317, http://dx.doi.org/10.2307/1352954.

Ribas-Ribas, M., Helleis, F., Rahlff, J., Wurl, O., 2018a. Air-sea CO_2-exchange in a large annular wind-wave tank and the effects of surfactants. Front. Mar. Sci. 5, 457, http://dx.doi.org/10.3389/fmars.2018.00457.

Ribas-Ribas, M., Kilcher, L., Wurl, O., 2018b. Sniffle: A step forward to measure in situ CO_2 fluxes with the floating chamber tech-

nique. Elementa 6 (1), 14, http://dx.doi.org/10.1525/elementa.275.

Ribas-Ribas, M., Mustaffa, N.I.H., Rahlff, J., Stolle, C., Wurl, O., 2017. Sea Surface Scanner (S3): A catamaran for high-resolution measurements of biogeochemical properties of the sea surface microlayer. J. Atmos. Oceanic Technol. 34 (7), 1433—1448, http://dx.doi.org/10.1175/jtech-d-17-0017.1.

Romano, J.-C., 1996. Sea-surface slick occurrence in the open sea (Mediterranean, Red Sea, Indian Ocean) in relation to wind speed. Deep-Sea Res. Pt. I 43 (4), 411—423, http://dx.doi.org/10.1016/0967-0637(96)00024-6.

Rutgersson, A., Smedman, A., 2010. Enhanced air—sea CO_2 transfer due to water-side convection. J. Mar. Syst. 80 (1—2), 125—134, http://dx.doi.org/10.1016/j.jmarsys.2009.11.004.

Sætre, R., Aure, J., Danielssen, D., 2003. Long-term hydrographic variability patterns off the Norwegian coast and in the Skagerrak. ICES Marine Sci. Sym. 150—159.

Schlitzer, R., 2017. Ocean Data View. Ver 5.0.0., https://odv.awi.de/.

Skagseth, Ø., Drinkwater, K.F., Terrile, E., 2011. Wind- and buoyancy-induced transport of the Norwegian Coastal Current in the Barents Sea. J. Geophys. Res.-Oceans 116 (C8), C08007, http://dx.doi.org/10.1029/2011JC006996.

Smith, R.W., Bianchi, T.S., Allison, M., Savage, C., Galy, V., 2015. High rates of organic carbon burial in fjord sediments globally. Nat. Geosci. 8, 450—453, http://dx.doi.org/10.1038/NGEO2421.

Spiess, A.-N., Neumeyer, N., 2010. An evaluation of R^2 as an inadequate measure for nonlinear models in pharmacological and biochemical research: a Monte Carlo approach. BMC Pharmacology 10 (1), 6, http://dx.doi.org/10.1186/1471-2210-10-6.

Stigebrandt, A., 2012. Hydrodynamics and circulation of fjords. I. In: Bengtsson, L., Herschy, R.W., Fairbridge, R.W. (Eds.), Encyclopedia of Lakes and Reservoirs. Springer Netherlands, Dordrecht, 327—344.

Syvitski, J.P.M., Burrell, D.C., Skei, J.M., 1987. Fjords. Processes and Products. Springer, New York, 215 pp.

Takahashi, T., Sutherland, S.C., Wanninkhof, R., Sweeney, C., Feely, R.A., Chipman, D.W., Hales, B., Friederich, G., Chavez, F., Sabine, C., 2009. Climatological mean and decadal change in surface ocean pCO_2, and net sea—air CO_2 flux over the global oceans. Deep-Sea Res. Pt. II 56 (8—10), 554—577, http://dx.doi.org/10.1016/j.dsr2.2008.12.009.

Tokoro, T., Watanabe, A., Kayanne, H., Nadaoka, K., Tamura, H., Nozaki, K., Kato, K., Negishi, A., 2007. Measurement of air—water CO_2 transfer at four coastal sites using a chamber method. J. Mar. Syst. 66 (1—4), 140—149, http://dx.doi.org/10.1016/j.jmarsys.2006.04.010.

Torres, R., Pantoja, S., Harada, N., González, H.E., Daneri, G., Frangopulos, M., Rutllant, J.A., Duarte, C.M., Rúiz-Halpern, S., Mayol, E., Fukasawa, M., 2011. Air-sea CO_2 fluxes along the coast of Chile: from CO_2 outgassing in central northern upwelling waters to CO_2 uptake in southern Patagonian fjords. J. Geophys. Res.-Oceans 116 (C9), C09006, http://dx.doi.org/10.1029/2010JC006344.

Vachon, D., Prairie, Y.T., Cole, J.J., 2010. The relationship between near-surface turbulence and gas transfer velocity in freshwater systems and its implications for floating chamber measurements of gas exchange. Limnol. Oceanogr. 55 (4), 1723—1732, http://dx.doi.org/10.4319/lo.2010.55.4.1723.

Wanninkhof, R., 1992. Relationship between wind speed and gas exchange over the ocean. J. Geophys. Res. 97, 7373—7382.

Wanninkhof, R., 2014. Relationship between wind speed and gas exchange over the ocean revisited. Limnol. Oceanogr 12 (6), 351—362, http://dx.doi.org/10.4319/lom.2014.12.351.

Wanninkhof, R., Asher, W.E., Ho, D.T., Sweeney, C., McGillis, W.R., 2009. Advances in quantifying air-sea gas exchange and environmental forcing. Annu. Rev. Mar. Sci. 1, 213—244, http://dx.doi.org/10.1146/annurev.marine.010908.163742.

Weiss, R.F., 1974. Carbon dioxide in water and seawater: the solubility of a non-ideal gas. Mar. Chem. 2 (3), 203—215, http://dx.doi.org/10.1016/0304-4203(74)90015-2.

Wurl, O., Wurl, E., Miller, L., Johnson, K., Vagle, S., 2011. Formation and global distribution of sea-surface microlayers. Biogeosciences 8 (1), 121—135, http://dx.doi.org/10.5194/bg-8-121-2011.

Zappa, C.J., McGillis, W.R., Raymond, P.A., Edson, J.B., Hintsa, E.J., Zemmelink, H.J., Dacey, J.W.H., Ho, D.T., 2007. Environmental turbulent mixing controls on air-water gas exchange in marine and aquatic systems. Geophys. Res. Lett. 34 (10), L01601, http://dx.doi.org/10.1029/2006GL028790.

Zappa, C.J., Raymond, P.A., Terray, E.A., McGillis, W.R., 2003. Variation in surface turbulence and the gas transfer velocity over a tidal cycle in a macro-tidal estuary. Estuaries 26 (6), 1401-1415, http://dx.doi.org/10.1007/BF02803649.

Zhang, X., Cai, W.-J., 2007. On some biases of estimating the global distribution of air-sea CO_2 flux by bulk parameterizations. Geophys. Res. Lett. 34 (1), L01608, http://dx.doi.org/10.1029/2006GL027337.

Oceanologia (2019) 61, 471—483

Available online at www.sciencedirect.com

ScienceDirect

journal homepage: www.journals.elsevier.com/oceanologia/

ORIGINAL RESEARCH ARTICLE

Chamelea gallina in the coastal waters of the Anapa bay bar (the Black Sea) as a carbonate sediment producer

Alisa R. Kosyan [a,*], **Boris V. Divinsky** [b]

[a] *A.N. Severtsov Institute of Ecology and Evolution, Russian Academy of Sciences, Moscow, Russia*
[b] *P.P. Shirshov Institute of Oceanology, Russian Academy of Sciences, Moscow, Russia*

Received 22 October 2018; accepted 26 April 2019
Available online 16 May 2019

KEYWORDS
Population;
Biomass;
Shell length;
Age;
Rapana venosa;
Black Sea

Summary The paper presents preliminary results of monitoring the population of the bivalve *Chamelea gallina*, which is the main source of biogenic carbonates for the Anapa bay bar beaches (the Black Sea). It is shown that by 2017, the biomass of the clams decreased more than twice compared to 2010, but began to increase in 2018. The average sizes of *C. gallina* are clearly divided in terms "year" — "section" — "age". At the same time, interannual variations of the average size are very strong in all age groups. The average shell length of *C. gallina* significantly increased in 2018 compared to 2016, and especially — to 2017. This may be caused by the population decline of the predator *Rapana venosa* feeding on clams. Geographic differences in the shell length between sections are not directly related to the distribution of biogenic elements (nitrogen and phosphorus). The differences in longevity and shell size between *C. gallina* from the Anapa region and distant populations from the other parts of the distribution area are likely related to its significant negative correlation with the growth rate, which in turn negatively correlates with latitude.

* Corresponding author at: A.N. Severtsov Institute of Ecology and Evolution, Russian Academy of Sciences, 33 Leninsky prospect, 119071 Moscow, Russia. Tel.: +7 9154113558; fax: +74959545534.
E-mail addresses: kosalisa@yandex.ru (A.R. Kosyan), divin@ocean.ru (B.V. Divinsky).
Peer review under the responsibility of Institute of Oceanology of the Polish Academy of Sciences.

Production and hosting by Elsevier

https://doi.org/10.1016/j.oceano.2019.04.003

1. Introduction

The accumulative shores of the World Ocean are unique natural formations of great recreational, economic, and historical value. According to the geological time scales, the modern coasts are of the same age as the Holocene transgression, estimated at 7000—9000 years BP (before present). Immediately after the Holocene transgression, intense changes in the coastal slopes began to occur along the entire coastline of the oceans causing the destruction of abrasion areas and simultaneous formation of accumulative bodies. As the rate of abrasion decreased, the transport of new sediments to accumulative forms declined, and in many cases, the accumulation process was replaced by erosion. The action of some factors, primarily solid river runoff and the entry of biogenic material (shells of benthic mollusks) reduced the erosion rate, but erosion generally increases during the deficit of sediments or during the periods of the ocean level rise (Kosyan and Krylenko, 2014). Flooding of coastal areas, erosion of sandy beaches, and the destruction of harbor constructions became typical on the global and regional scales (Kont et al., 2003; Mimura, 1999; Nicholls and Cazenave, 2010; Nicholls and Mimura, 1998; Peltier, 1999; Zerbini et al., 1996). Biogenic material (shells, supplied by coastal mollusks) is becoming increasingly important. In some areas of the Black Sea, the proportion of shell residues that makes up the beaches reaches 98% (Kosyan, 2018).

During several years, we have been studying the lithodynamics of the Black Sea accumulative shores, the main of which are situated near the Anapa city (Anapa bay bar) (Kosyan et al., 2018, 2011; Kosyan and Krylenko, 2014; Krylenko et al., 2011). According to our data, mass bivalve mollusks *Chamelea gallina* and *Donax trunculus* are the main suppliers of carbonates in the sediments of sandy beaches (Fedorova et al., 2018). The main quantitative contribution belongs to *C. gallina* population whose mass development zone is located at depths of 6—10 m (Kosyan et al., 2012).

Chamelea gallina (Linnaeus, 1758) is a common infaunal bivalve of the Veneridae family inhabiting shallow water sand or mud along the European coasts. It is distributed throughout the Mediterranean and Black Seas as well as in a few localities in the Atlantic, along the southern coast of the Iberian Peninsula as far west as Faro, Algarve (Backeljau et al., 1994). The species is commercially used in the Mediterranean and Atlantic (Froglia, 1975a; Gaspar et al., 2004; Özden et al., 2009). There are a number of papers focused on its population studies in the Mediterranean countries and Portugal (Delgado et al., 2013; Froglia, 1975b; Romanelli et al., 2009), but only fragmentary information exists about its ecology in the Black Sea (Boltacheva and Mazlumyan, 2003; Chikina, 2009; Kiseleva, 1981; Koluchkina et al., 2017a,b,c; Revkov et al., 2014).

To determine the volume of shell material (biogenic carbonates) entering the Anapa bay bar beach and to predict its changes in the coming years it is necessary to know the number and biomass, size and age structure of mollusk populations in the coastal waters, as well as the threats and factors influencing their dynamics such as biogenic nutrients concentration, environmental conditions, and predators. In order to fill the data gap, monitoring of the bivalve *C. gallina* and its predator, the gastropod *Rapana venosa* has been conducted in 2016—2018. The goal of this work is to study the spatial characteristics of the distribution and interannual dynamics of the *C. gallina* populations on the Anapa bay bar coast of the Black Sea. The main question of the data analysis is as follows: are there statistically significant differences between the average shell sizes (in terms of length) depending on the year of observation, age, geographic location, and habitat depth.

2. Material and methods

Samples of mollusks were taken in the area of the Anapa bay bar located in the northeastern part of the Black Sea; this is an open part of the coast with a total length of about 40 km (Fig. 1). The bottom is flat in the offshore part with a pronounced system of underwater bars at depths of up to 6 m. The sampling was carried out along four sections (7, 18, 24, 29) in June 2016, 2017, and May 2018, with stations at depths of 6 and 10 m (Fig. 1 and Table 1). Two samples were taken at each station. The location of sections was determined by the characteristics of the granulometric composition of the sediments. High content of coarse fractions in the sands was previously identified over sections 18, 24, and 29 (Fedorova et al., 2018); it was low on section 7. Samples were taken by divers by means of the bottom frame with a size of 32 cm × 32 cm; the thickness of the sand layer collected under the frame was about 3 cm. Subsequently, the samples were sieved through a sieve with 1 mm mesh. The following characteristics of the collected mollusks were determined: number, weight, length of the shell (maximum distance along the anterior-posterior axis), and age. The age was determined

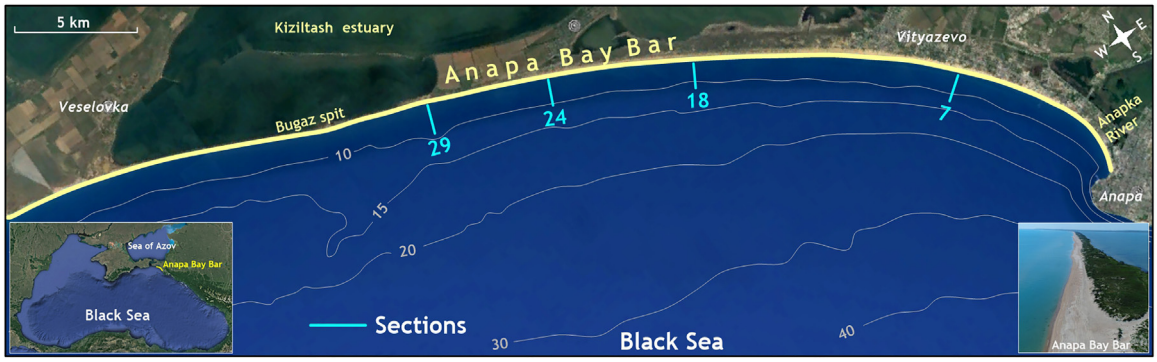

Figure 1 Map of sampling sites.

Table 1 Salinity and N, P and Si concentration in the sea water of Anapa bay bar, May 2018.

Section	Coordinates		Depth [m]	Salinity [‰]	PO_4 [μM/l]	Si [μM/l]	NO_3 [μM/l]	NO_2 [μM/l]	NH_4 [μM/l]
7	37°16′12″	44°57′16″	10[a]	18.20	0.16	3.04	0.21	0.05	1.65
	37°16′12″	44°57′16″	10	17.93	0.09	3.28	0.45	0.07	1.75
	37°16′27″	44°57′27″	6	18.44	0.06	3.04	0.15	0.04	1.33
	37°16′44″	44°57′36″	2	19.59	0.37	3.70	0.75	0.13	2.46
18	37°09′44″	45°00′49″	10[a]	19.06	0.05	2.86	0.17	0.07	1.26
	37°09′44″	45°00′49″	10	18.57	0.41	3.46	0.13	0.18	2.33
	37°09′56″	45°01′02″	6	18.52	0.41	3.52	0.00	0.11	1.45
	37°10′07″	45°01′12″	2	19.82	0.19	2.62	0.11	0.12	1.60
24	37°05′51″	45°02′14″	10[a]	18.52	0.12	2.86	0.33	0.00	1.92
	37°05′51″	45°02′14″	10	18.99	0.44	3.76	0.12	0.14	3.04
	37°05′59″	45°02′31″	6	18.60	0.21	3.28	0.28	0.17	2.18
	37°06′06″	45°02′43″	2	19.59	0.19	3.10	0.00	0.17	1.77
29	37°02′19″	45°03′12″	10[a]	18.23	0.13	2.27	0.08	0.00	2.20
	37°02′19″	45°03′12″	10	19.23	0.12	3.58	1.22	0.08	3.69
	37°02′30″	45°03′35″	6	18.40	0.13	3.52	0.00	0.05	1.32
	37°02′34″	45°03′47″	2	19.11	0.24	3.40	0.00	0.08	2.18

[a] Samples taken in near-bottom layer.

by counting external shell rings (Deval, 2001; Ramon and Richardson, 1992); this method is considered as appropriate for quick estimates of the age (Gaspar et al., 2004).

In addition to *C. gallina*, we sampled *R. venosa*, a carnivorous gastropod predating on bivalves, at the same sections and dates (sampling methods and some results are published in Kosyan (2017)).

Samples of seawater for determining the hydrochemical parameters were taken on all sections at 2, 6, and 10 m depths. At depths of 2, 6, and 10 m, the samples were taken from the boat in the surface layer of the sea into clean polystirol 1 l bottles; additional samples of near-bottom water were taken at a depth of 10 m. The sampling and processing of nitrates, nitrites, ammonium, silicates, and phosphates were performed by standard methods (Grashoff et al., 1999). The measurements were carried out in the Laboratory of Chemistry of the Southern Branch of the Shirshov Institute of Oceanology. Phosphates ($P\text{-}PO_4$) were determined by the modified Murphy and Riley method (Hansen and Koroleff, 1999). Absorbance was measured at 885 nm in a 50-mm cell, the precision of the technique was 0.03 μM. Silicates (Si) were determined colorimetrically according to the blue silicon–molybdenum complex (Koroleff, 1983). Absorbance was measured at 810 nm with a 10-mm cuvette; the precision of the technique was 0.06 μM. Nitrites ($N\text{-}NO_2$) were measured with sulfanilamide and N-1-naphthylethylendiamine dihydrochloride (Hansen and Koroleff, 1999). Nitrate ($N\text{-}NO_3$) was converted to nitrite using Cu-Cd columns. Absorbance was measured at 543 nm in a 50-mm cell; the precision of the technique was 0.02 μM. Ammonium ($N\text{-}NH_4$) was determined by the phenol-hypochlorite reaction (Solorzano, 1969). Absorbance was measured at 630 nm with a 10-mm cuvette; the precision of the technique was 0.06 μM.

The coordinates of the stations are presented in Table 1.

Statistical processing of samples was carried out using the methods of analysis of variance (MANOVA) in the STATISTICA 12 environment. The advantage of this method is the ability to use qualitative variables that form individual samples. The main idea of the method is to search for statistically significant differences between the average values of the parameter of interest, namely: the average values are statistically different if these differences exceed the variances within each sample.

A total of 2124 specimens of *C. gallina*, aged one, two, and three and more years were processed. Unfortunately, the uneven coverage of data by years, sections, and depths does not allow us to use them fully, since the lack of data strongly affects the reliability of the analysis as a whole. As a result, the samples were formed according to the following criteria (categories):

- year: 2016, 2017, 2018;
- age: 1, 2, 3+ years;
- section: 7, 18, 24, 29;
- depth: 6, 10 m.

The shell length is a dependent variable.

3. Results

3.1. Seawater chemical analysis

The salinity of seawater and concentration of the main biogenic elements are shown in Table 1. The concentration of N, P, and Si insignificantly varied within the selected sections. The average values of total nitrogen were as follows: 1.88 (section 18), 2.23 (section 24), 2.26 (section 7), 2.35 μM/l (section 29); the values of phosphorus were: 0.16 (29), 0.17 (7), 0.24 (24), 0.27 μM/l (18); while that of silica were: 3.12 (18), 3.19 (29), 3.25 (24), 3.27 (7) μM/l. The following trend prevailed over sections 18, 24, and 29: the amount of nutrients in the surface waters increased with

Table 2 Number and biomass of *Chamelea gallina* on Anapa bay bar in 2016—2018.

Sampling period at section	Number at depth [spm/m^2]			Biomass at depth [g/m^2]		
	6 m	10 m	Average for section	6 m	10 m	Average for section
June 2016						
Section 7	365.0	1130.0	505.0	488.0	1616.0	701.7
Section 18	510.0	2725.0	1081.7	363.3	357.0	240.3
Section 24	340.0	220.0	186.7	302.3	29.3	110.5
Section 29	270.0	490.0	383.3	185.5	57.5	209.0
Average for depth	371.3	1141.3	**756.3**[a]	334.8	515.0	**424.9**[a]
June 2017						
Section 7	253.0	450.0	351.3	245.0	448.0	346.5
Section 18	310.0	1925.0	1117.5	70.5	261.5	166.0
Section 24	3670.0	295.0	1982.5	325.0	62.5	193.8
Section 29	250.0	780.0	515.0	78.0	145.0	111.5
Average for depth	1120.6	862.5	**991.6**[a]	179.6	229.3	**204.5**[a]
May 2018						
Section 7	320.0	60.0	190.0	210.5	30.5	120.5
Section 18	390.0	710.0	550.0	221.5	337.5	279.5
Section 24	150.5	430.0	290.3	103.5	137.0	120.3
Section 29	555.0	1000.0	777.5	649.0	322.5	490.8
Average for depth	353.9	550.0	**452.0**[a]	296.1	206.9	**252.8**[a]

[a] Average for all sections and depths.

depth, while in the bottom layer, it was below average. There was no obvious tendency over section 7.

3.2. *Chamelea gallina* number and biomass

Average number and biomass of the clams in 2016—2018 are presented in Table 2. The maximum number (3670 spm/m^2) was observed at section 24 at a depth of 6 m in 2017, the highest biomass (1616 g/m^2) was at section 7 at a depth of 10 m in 2016. The average number was the largest in 2017 (991.6 spm/m^2) mainly due to the small-sized fingerlings; the average biomass in 2016 was 315.4 g/m^2. Comparative literature data on the number and biomass of *C. gallina* from the other parts of the Black Sea in the last 50 years are presented in Table 3.

3.3. *Chamelea gallina* general size and age structure

Shell length frequency distribution is presented in Fig. 2. The lengths of the majority of specimens were 5—7 mm in 2016, 5—9 mm in 2017, and 11—15 mm in 2018. The main problem of the study of *C. gallina* size and age population structure is the uneven distribution of samples within individual categories. Fig. 3 shows the dependence of *C. gallina* average size on their age on different sections. Average shell length of one-year-old clams was approximately the same on all sections: about 5.5—8.6 mm. The largest average shell lengths at the age of 2 and 3 years were of the clams collected at section 7 (probably, due to the proximity of the section to the Anapka River); the shell lengths of clams at sections 18, 24, and 29 were almost similar at the age of 2 years but differed at the age of 3 years so that the clams at section 29 had the largest average shell length, and the smallest was found at section 24. Thus, the differences in the average sizes became more and more tangible with age.

The age of clams varied within 1—8 years. The largest number corresponded to one-year-old mollusks, the lesser number to two-year-old ones; the one year and two-year-old mollusks comprised 60% of the total biomass. The much lesser number of mollusks aged 3 and more, was observed.

The average sizes are clearly divided in terms "year" — "section" — "age". At the same time, interannual variations of the average size are very strong in all age groups (Figs. 4 and 5). One more important detail can be noted: the average size of clams significantly increased in 2018 compared to 2016 and especially compared to 2017 (Fig. 6). It is true for all age categories with the exception of two-year-old mollusks at 6 m and three-year-old at 10 m at section 7, and one-year-old ones at 10 m at section 24 (Figs. 4 and 5).

Analysis of the significance levels of intra- and intergroup differences suggests that there are significant statistical differences in the average size of mollusks between the categories of samples: age, geographical location (section), year of observation, and depth.

3.4. The role of geographic location and year of observation

We found strong differences in the average size of *C. gallina* from different sections by means of statistical analysis (Figs. 4 and 5). The annual increment of shell length of clams from different sections at different depths is shown in Table 4. The largest annual increment was observed at a depth of 6 m on sections 24 and 29 in the period 2017—2018. Section 24 is interesting in one more aspect: it is the only section, where a

Table 3 Comparative data on number and biomass of *Chamelea gallina* in the northern part of the Black Sea.

Map position	Location	Depth [m]	Number, [spm/m^2]	Biomass, [g/m^2]	Date	Source
1	Karkinitsky Bay (northern Crimea)	6–26	–	383	1985–2000	Sinegub (2006)
2	Bakal Spit (Karkinitsky Bay, northern Crimea)	4–6	40–2650	34–637	06/2018	Kosyan (2018)
3	Western Crimea, 33.53135°E, 44.6634°N	11	894 ± 85	50–541	2010–2013	Revkov et al. (2014)
4	Crimea		–	138	1960–1970	Kiseleva (1981)
4	Crimea	1–32	–	375	1980–2004	Revkov (2011)
5	Kerch Pre-Strait	5–30	40–70	0–24	2007–2008	Nabozhenko (2011)
6–8	Anapa Bay bar – Gelendzhik	8–25	16–1008	10–389	1962	Kiseleva and Slavina (1965)
6	Anapa Bay bar	6–10	730	520	10.2010	Kosyan et al. (2012)
6	Anapa Bay bar	6–10	756	425	06.2016	Herein
6	Anapa Bay bar	6–10	992	205	06.2017	Herein
6	Anapa Bay bar	6–10	452	253	06.2018	Herein
7	Sukko (south to Anapa city)	5–30	1360	737	2007–2008	Nabozhenko (2011)
9	North-Caucasian coast, Inal Bay	10	9500	800	2001	Koluchkina et al. (2017a)
9	North-Caucasian coast, Inal Bay	10	4400	550	2002	Koluchkina et al. (2017a)
9	North-Caucasian coast, Inal Bay	10	3000	300	2004	Koluchkina et al. (2017a)
9	North-Caucasian coast, Inal Bay	10	<2000	<300	2007–2016	Koluchkina et al. (2017a)
10	Tuapse	20–30	<1500	<200	1968	Kiseleva and Slavina (1972)
10	Tuapse	13	833	54	10/2010	Zagorskaya (2014)
11	Kudepsta	16	3312	244	10/2010	Zagorskaya (2014)

decrease in the average shell length was observed (6 m depth, 2016–2017). The period 2016–2017 may be considered as a critical one for all other age groups as well, since its annual increment has been less than the increment in 2017–2018, with the exception of section 18 at 6 m depth.

3.5. Depth influence

The collected material allows us to estimate the dependence of the linear dimensions of the mollusk shells on the depth. Fig. 6 shows the average sizes of shells found at different depths in different years, regardless of their age and sex (i.e., for the entire population). We note the main features: (1) the average length of the shells decreases with increasing depth (away from the shore); (2) this trend is increasing from year to year. In 2016, the size reduction was observed at the level of statistical (including instrumental) errors, then in 2018, mollusk populations at depths of 6 and 10 m form separate samples with almost non-overlapping confidence intervals for medium sizes. The average length of shells at a depth of 10 m is by 3.5% less than at a depth of 6 m.

If we take into account the age categories (Fig. 7), these statistical properties are found mainly in adults (three years old and older). We also note that the overall decrease in the

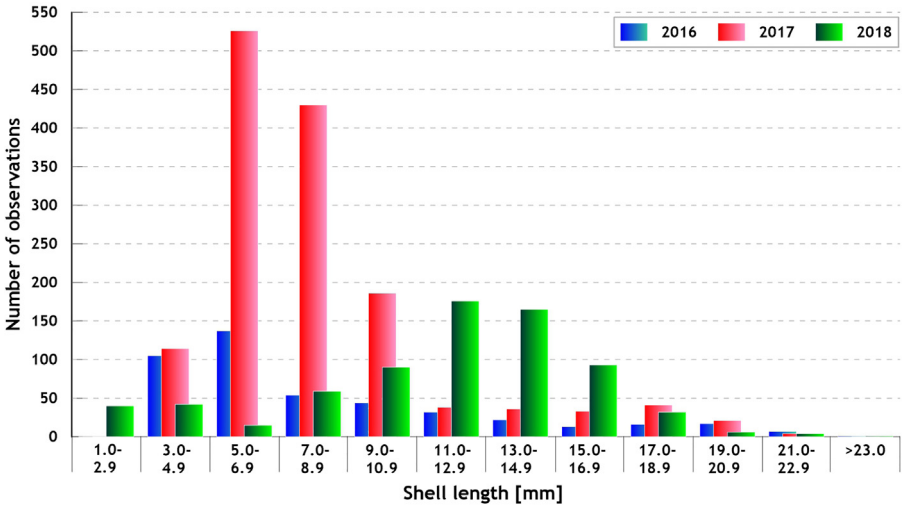

Figure 2 Shell length frequency distribution of *Chamelea gallina* at Anapa bay bar in 2016—2018.

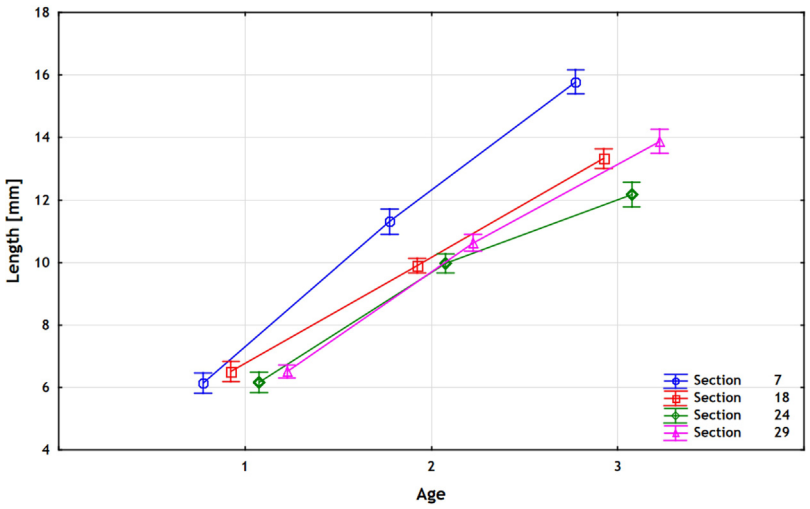

Figure 3 Geographic differences in average sizes of *Chamelea gallina*, sampled in 2016—2018. Hereinafter, vertical bars denote 0.95 confidence intervals.

average size of the mollusk shells over the entire study site, regardless of the depth, observed in 2017 (Fig. 6), is caused by a decrease in the average size of two-year-old individuals in the same year (Fig. 7).

The lack of differences at depths of 6 m and 10 m in 2016—2017 compared to 2018 might be caused by the peculiarities of wind waves responsible for transport, crushing, and redistribution of benthic animals in the sand layer resulting in mixing of mollusks from different depths. To check this assumption, we used a regularly updated database of wind wave parameters over the entire Black Sea based on the simulations using the DHI MIKE SW spectral wave model covering the period from 1979 to the present (Divinsky and Kosyan, 2017). The time step of the calculated parameters (wave heights, periods, directions of propagation, etc.) was 1 h.

We estimated the characteristics of the waves at a point located on section 18 (Fig. 1) at a depth of 15 m. Considering the wave parameters only at one point is quite justified in our research, since the shelf slope is characterized, in general, by the lack of large bathymetric features, the coastline is slightly curved (in our study site), and the isobaths are almost parallel to the coast (Fig. 1). We formed three sample periods from the database: June 2015—May 2016, June 2016—May 2017, and June 2017—May 2018, covering the periods between the mollusk collection expeditions. The sample periods are characterized by three parameters: significant wave heights (the use of these heights is most common in marine engineering practice), the direction of propagation, wave power. The power of the waves, proportional to the square of the height of the waves and the characteristic period of the waves, can be considered as some kind of integral characteristic of the waves. For further analysis, we restricted ourselves to the sector of strongest waves in the range from 135° to 270°, since the waves of these directions determined the main

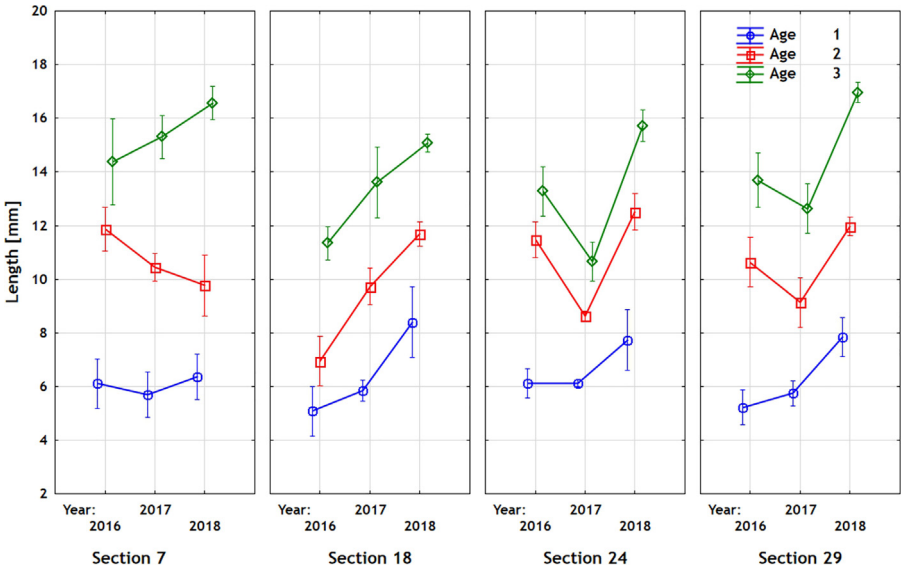

Figure 4 *Chamelea gallina* shell length dynamics at the depth of 6 m in 2016—2018.

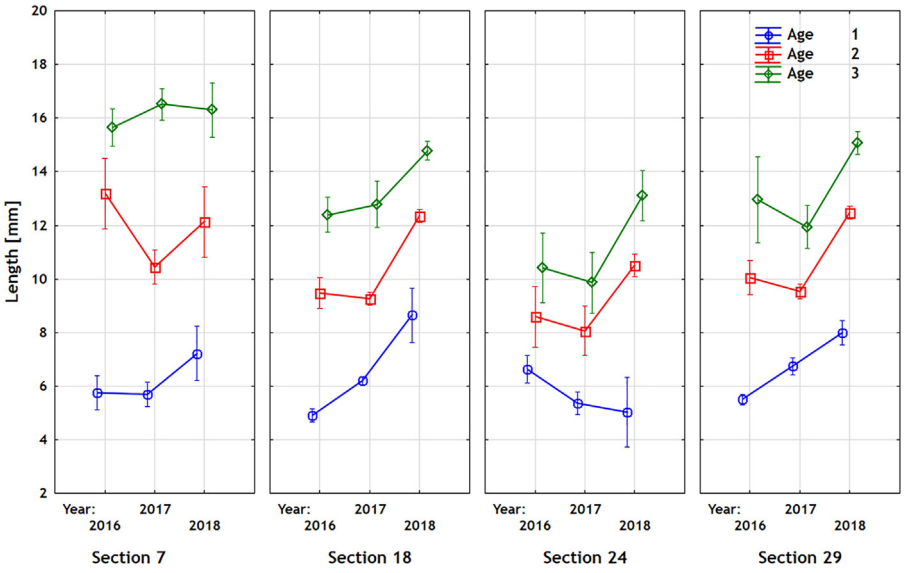

Figure 5 *Chamelea gallina* shell length dynamics at the depth of 10 m in 2016—2018.

lithodynamic load on the shelf zone of the Anapa bay bar (alongshore and transverse motions of the bottom sediments). Fig. 8 shows the average values of significant wave heights and wave powers for periods 06.2015—05.2016, 06.2016—05.2017, 06.2017—05.2018. As follows from Fig. 8, the seasons in 2015—2016 and in 2016—2017 were characterized by the surface waves with the average heights, which were by 15% higher than the average wave heights in the 2017—2018 season (Fig. 8a). As for the power of wind waves (Fig. 8b), the season in 2015—2016 exceeded the season 2017—2018 by almost 20%, and the season 2016—2017 by 40%. Based on the above mentioned facts, we can conclude that the wave forcing on the shelf slope of the Anapa bay bar in 2015—2016 and in 2016—2017 was much stronger than in the season of 2017—2018.

Thus, the average sizes of clams on the Anapa bay bar are different at different sections and depths. These differences, minimal for one-year-old clams, become more pronounced with age.

3.6. *Rapana venosa* biomass

Our preliminary results show that the average shell length of rapa whelks on the Anapa bay bar (Fig. 9c) increased by 10% in 2017 (the condition index remained unchanged), then it decreased by 4% in 2018 (condition index also decreased by 10%, Fig. 9d). The average biomass was the largest at all sections in 2016, decreasing from 20% to 50% in 2017 and from 30% to 85% (compared to 2016) in 2018 (Fig. 9b). The weakening of the rapa whelk's pressure on the *Chamelea*

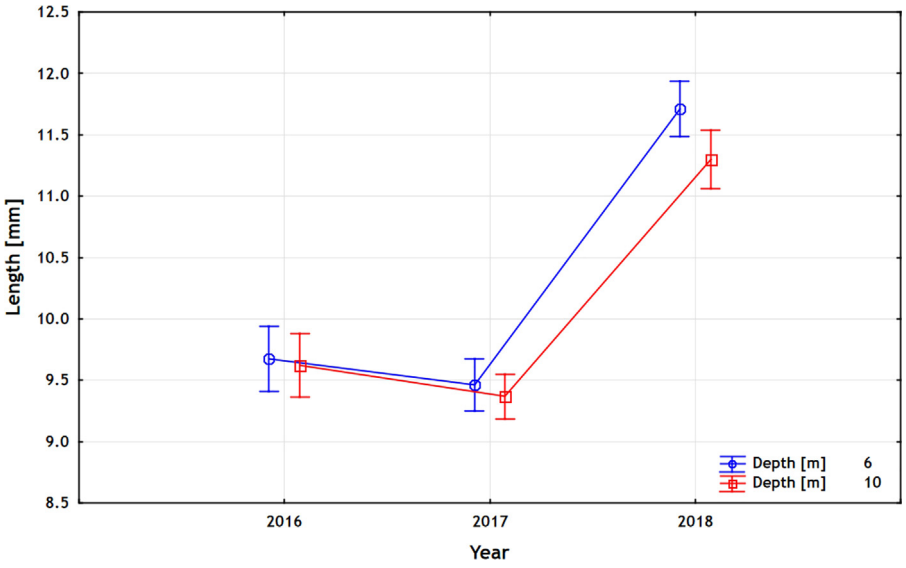

Figure 6 Shell length dynamics of *Chamelea gallina* at 6 and 10 m depths.

Table 4 Annual increment of *Chamelea gallina* shell length [mm] on Anapa bay bar in 2016—2018.

Depth [m]	6 m		10 m	
Time period	2016—2017	2017—2018	2016—2017	2017—2018
Section				
One-year-olds				
7	4	4.5	4.5	6
18	4	6	4	6
24	2.5	6	2	4.5
29	4	6	4	6
Two-year-olds				
7	3	5	3.5	6
18	7	5	3	5.5
24	1↓	8	2	5
29	2	8	2	5

community by 2018 might have led to an increase in clam biomass and average shell sizes.

4. Discussion

4.1. Biogenic nutrients concentration

We assumed that one of the factors contributing to the difference in growth rate on Anapa bay bar coast is related to the food supply. Hence, in 2018, we performed a chemical analysis to determine a rough assessment of the content of nutrients. However, these estimates should be treated with caution, as one measurement over three years is not representative, and the concentration of nutrients in the surface seawater can change rapidly.

Venerida mollusks are planktotrophic and sestonophagous, feeding on planktonic algae and suspended organic matter (Froglia, 1975b). The planktonic algae need nutrients for growth, first of all, nitrogen and phosphorus. It is known that an increase in the concentration of nitrogen sharply stimulates the growth of microalgae, which are the main sources of organic matter in the marine ecosystems; at the same time, an excess of phosphorus inhibits their growth (Eberly, 1967). The highest biomass of mollusks in 2018 was observed at section 29 (Table 2) (which is consistent with these data) where the maximum amount of nitrogen was recorded but a minimum of phosphorus was observed. This is also seen over section 18, where the maximum amount of phosphorus was found but a minimum of nitrogen. Intermediate, almost identical values of nitrogen (2.23 and 2.26) and more variable values of phosphorus (0.24 and 0.17) were recorded at sections 24 and 7, respectively, where intermediate values of biomass were also found. It can be assumed that under the conditions of the Anapa bay bar, phosphorus has a lesser effect than nitrogen on the development of the algae biomass and consequently on the development of mollusks. The analysis of nutrient concentrations on the Bakal Spit (Kosyan, 2018) provided nearly the same results for P and N, but the silica concentration several times

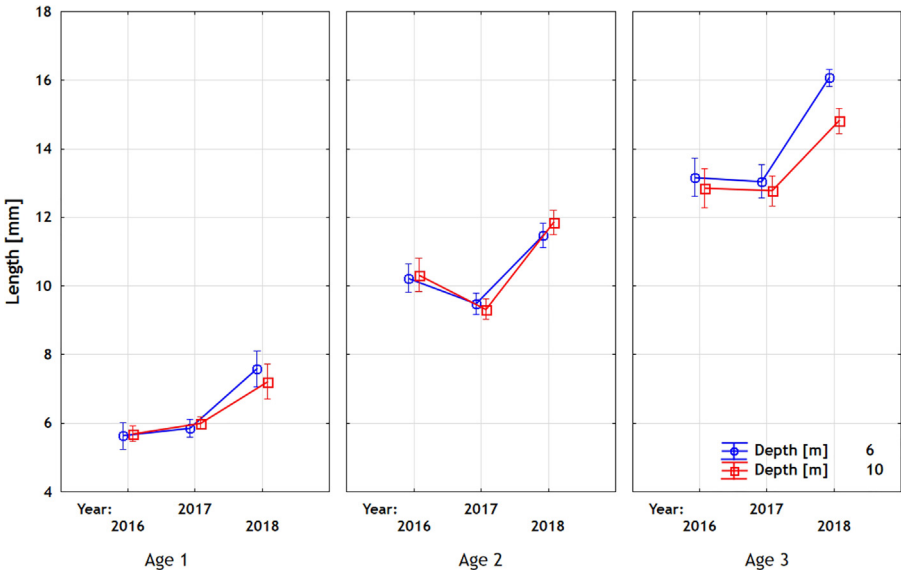

Figure 7 Shell length dynamics of *Chamelea gallina* of different age groups at 6 and 10 m depths.

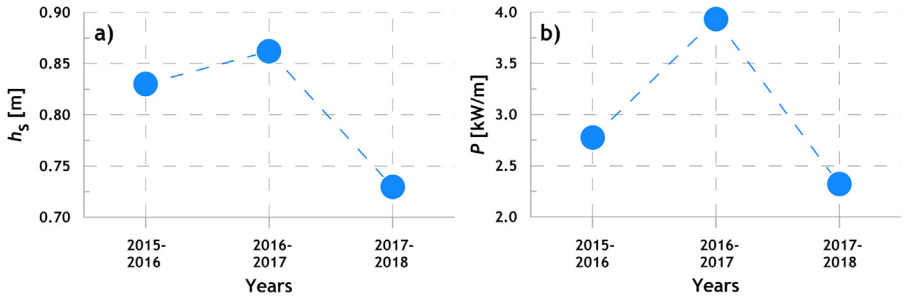

Figure 8 Mean values of significant wave heights (a) and wave powers (b) for the periods between sampling of mollusks.

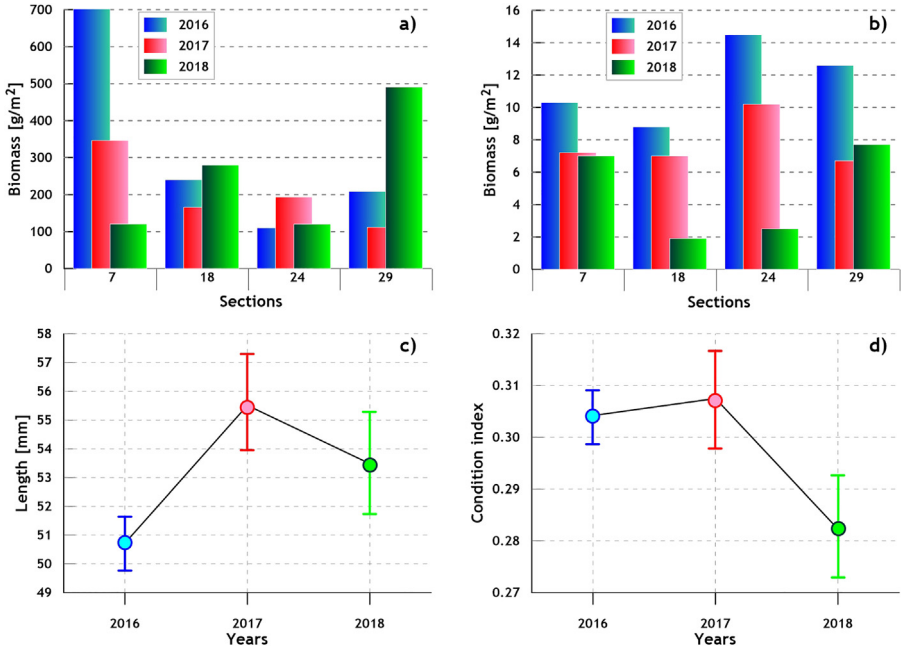

Figure 9 Biomass [g/m^2] dynamics of *Chamelea gallina* (a) and *Rapana venosa* (b) at different sections at the Anapa bay bar; dynamics of shell length (c) and condition index (d) of *Rapana venosa*, collected at 6–10 m on 7, 18, 24 and 29 sections.

exceeded that in the Anapa bay bar waters. Though the concentrations of nutrients do not indicate clear downward trends between sections 7 and 24 (Table 1), we presume that the following situation might take place. One of the important sources of nutrients is the Anapka River (Fig. 1), which is located close to section 7; here, the highest biomass and average population shell length of *C. gallina* was detected in 2016—2017 (Table 2). As the distance from the river increases, the amount of nutrients and organic matter decreases, and by section 24, it appears to be minimal. The improvement of the situation on section 29 is probably related to the fish passage channel located in the mullet farm 4 km to the north, dug in the Bugaz Spit, which connects the Kiziltash estuary with the sea. Although in spring and summer this channel is closed to the passage of fish, partial water exchange and the influx of nutrients from the estuary can have a positive effect on the marine biocenoses located nearby. Similarly to the Anapa bay bar, the biomass of clams on different sections of the Bakal Spit was also different (Kosyan, 2018). The highest biomass of *Chamelea* was observed near the Bird Island separated from the end of the spit and populated by large colonies of sea birds. The island is probably a source of biogenic nutrients, causing high mollusk productivity.

It was shown previously, that the concentration of stable isotope ^{13}C in live *C. gallina* shells, collected on the Anapa bay bar at various depths, was different: the concentration of ^{13}C at 5 m was 19.55‰, while at 10 m it was 20.29‰ (Antipushina, 2012). This means that the diets of clams on different depths could also differ and could be one of the causes of growth differences. Strong wind waves mix shells from different depths, and this trend is manifested only in relatively quiet years, as it was shown in Section 3.

4.2. Dynamics of abundance and biomass of mollusks

At the end of the 20th and beginning of the 21st century, significant changes occurred in the composition and abundance of Bivalvia, a key group of macrozoobenthos at depths of 10—30 m in the northern part of the Black Sea. As a result of anthropogenic eutrophication and introduction of alien species in 1999—2005, there was a significant decrease in species diversity, and fluctuations in the abundance and biomass of bivalve mollusks started to occur (Chikina, 2009; Kucheruk et al., 2002). *C. gallina* prefers sandy grounds, and sand silting is a major factor determining the differences in the modern structure of the northern Black Sea macrozoobenthos (Koluchkina et al., 2017c). The highest densities and biomasses were observed at sandy coasts of Crimea and northern part of the Caucasian coast (Table 3). *Chamelea* biomass in 2010 was approximately the same as the highest values observed in 1962 (Table 3), and then they gradually decreased up to 2017, when it decreased more than twice despite high density The number of specimens (density) was high while the biomass was low due to the decrease in the mean size of the individual clams. The 1.3 times biomass increase in 2018 was determined, mainly owing to the unusually high biomass of clams at sections 29 and 18 (Fig. 8a). In the southern part of the North-Caucasian coast (Inal Bay) (Table 3), a decrease in *Chamelea* biomass from 800 to 300 g/m^2 was observed in 2001—2004, but in 2007—2016, it varied only within 100—300 g/m^2 (Koluchkina et al., 2017b). The authors assumed that the system was unbalanced at the end of the twentieth century and then the system entered a new stationary state (Chikina, 2009) close to the one that was observed in the second half of the twentieth century before the eutrophication period. The same tendency seems to be true on the Anapa bay bar and vicinities, but longer monitoring is necessary to fully reveal it.

4.3. Biological factors influencing *Chamelea gallina* shell size and growth rate

According to Deval (2001), the largest observed specimen in the Marmara Sea was 34.3 mm long, and only 2.2% of the sampled specimens were larger than 30 mm indicating a rather high level of anthropogenic effect in the area. On the Anapa bay bar, we observed a further decrease in size: the largest *C. gallina* was 23.8 mm long and 2.3% of specimens were larger than 19 mm. Since the situation with water pollution and precipitation in the Anapa bay bar region is the most favorable (less polluted and silted) compared to the other areas of the northeastern coast of the Black Sea (Koluchkina et al., 2017a), it can be assumed that the decrease in size is due to another cause. The clams are not an object of fishery in Russia, but the effect of *R. venosa* (similar to anthropogenic load) influences the clams by selective elimination of the largest specimens (Kosyan, 2016). According to Nakaoka (2000), even the presence of chemical signals of a predator in water reduces the growth rate of *Mercenaria mercenaria* (Linnaeus, 1758), a member of the same family as *Chamelea*. Thus, *Rapana* can probably inhibit the growth of clams only by its presence. This is indirectly confirmed by the observation (Kosyan, 2018) that the average shell lengths of the clams from the Bakal Spit are larger than those from the Anapa bay bar, despite the same age (2 years). Unlike Anapa bay bar, live specimens of rapa whelks were not found during our studies in the Bakal Spit, only dead shells were found, despite findings of *Rapana* in the other parts of Karkinitsky Bay (Boltacheva et al., 2016). Kiseleva and Slavina (1966) noted, that in the northern part of the Caucasian coast (from Zhelezny Rog Cape to Gelendzhik city), the average shell lengths of *C. gallina* were 12—18 mm, while on the coast between Gelendzhik and Batumi they were 5—12 mm long. The authors also connect this observation with the effect of existence of predators *R. venosa*.

Another probable cause of different sizes of *C. gallina* of the same-age is population density. In a number of studies, both in the experiment (Olafsson, 1986; Peterson, 1982; Peterson and Beal, 1989) and in the natural conditions (Mills et al., 1993), the negative effect of the sestonophagous bivalves population density on their growth rate was noted. The average *C. gallina* shell lengths from different sections differ both within the regions of the Bakal Spit (Kosyan, 2018) and the Anapa bay bar (Figs. 4 and 5). At the same age group, the samples with the highest population density and the lowest average population weight had smaller average sizes of the shells (Figs. 4 and 5, Table 2). The longer lifespan was of *C. gallina* from the Anapa bay bar (8 years, single specimens reached 4—5 years on the Bakal Spit) and can also be associated with the slower growth (Ridgway et al., 2011).

4.4. Geographic factor influencing *Chamelea gallina* shell size and longevity

Longevity and maximum shell size of *C. gallina* are subject to significant variability. The maximum *Chamelea* life span in the Anapa bay bar coast was 8 years and its shell length was 23.8 mm, whereas in the northwestern Crimea (Bakal Spit) it was 5 years with a size of 23.5 mm (Kosyan, 2018).

Maximum longevity and shell length in the Black Sea was estimated at an age of 9 years, while the maximum length was 30 mm (in the southwestern Crimea; Boltacheva and Mazlumyan, 2003) versus formerly reported 43 mm (Scarlato and Starobogatov, 1972). Geographically distant populations along the Mediterranean and the Atlantic reveal even stronger differences. Due to the local environmental conditions, eastern populations of *C. gallina*, from the Marmara Sea and Adriatic, have greater longevities than the western populations in the Mediterranean (Spanish coast) and in the Atlantic (Algarve coast) (Gaspar et al., 2004). Thus, similarly to the Anapa clams, the longevity of *C. gallina* from Ancona (Italy) was reported as 8 years with a shell length of 49 mm (Polenta, 1993), from the northern Marmara Sea: 7 years and 34.3 mm shell length (Deval, 2001). The longevity of *C. gallina* from the South Adriatic, Spain, and Portugal usually did not exceed 5 years and 40 mm shell length (Cano and Hernández, 1987; Gaspar et al., 2004; Massé, 1971; Poggiani et al., 1973; Ramon and Richardson, 1992; Royo, 1984). The marked difference between the longevity maxima of *C. gallina* of approximately the same length from the distant populations may be explained by its significant negative correlation with the growth rate (Ridgway et al., 2011). Growth rate decreases, and lifespan increases, with latitude, both across the group as a whole and within well-sampled species (Moss et al., 2016). The greater longevity of the northern populations may, therefore, be related to reduced energy expenditure for growth and greater energy utilization for shell and tissue regeneration to sustain homeostasis (Ziuganov et al., 2000).

5. Conclusions

Comparative studies of quantitative parameters of *C. gallina* population show that its biomass in 2010 was approximately the same as the highest values observed 50 years earlier in 1962. Then it eventually decreased more than twice, up to 2017, despite high density: the mean size of the individual clams also decreased. The 1.3 times biomass increase in 2018 was determined, mainly by unusually high biomass of clams at particular sections. Our results show that the average sizes of clams on the Anapa bay bar differ at different sections and depths. These differences, minimal for one-year-old specimens, become more pronounced with age. One of the factors influencing shell length and age is the presence of carnivore gastropods *R. venosa* eliminating the largest specimens and probably inhibiting the growth of the other clams of the *C. gallina* population. The concentration of the main nutrients does not reveal a direct correlation with either the shell size or the density, but it must be taken into account that these data should be interpreted with great caution and more sampling is needed during a longer time period. Slightly longer shells at a depth of 6 m compared to 10 m may be explained by different diets at different depths. Wind waves, responsible for the transport and redistribution of benthic animals in the sand layer, result in mixing of mollusks from different depths and leveling of these differences. Comparison with the long-term monitoring results of the macrozoobenthos in Inal Bay (southern part of the North-Caucasian coast) reveals that similar processes might take place at the Anapa bay bar: after fluctuations in the abundance and biomass of bivalve mollusks, the ecosystem entered a new stationary state, close to that observed in the second half of the twentieth century.

Acknowledgements

The authors are grateful to Zhanna Antipushina (Timiryazev Biological Museum, Moscow), Igor Darovskikh, Alexander Kochergin and Valery Chasovnikov (SBSIO, Gelendzhik) for sampling and processing assistance, and to an anonymous reviewer for valuable comments on the manuscript. Research has been supported by the Russian Foundation for Basic Research (grants No. 18-55-34002, 18-05-80035). The statistical analysis was carried out within the framework of the state program No. 0149-2018-0014. The data analysis was supported by the Russian Foundation for Basic Research (grants No. 19-05-00041, 19-45-230001).

References

Antipushina, Zh., 2012. Results of the stable isotope analysis of bivalve shell organic matrix from different depth. In: III Independent Meeting of ICAZ Archaeomalacology Group, Cairns, Australia, June 18—23, 2012. Archaeomalacology Working Group Conference Booklet, Cairns, Australia, p. 9.

Backeljau, T., Bouchet, P., Gofas, S., de Bruyn, L., 1994. Genetic variation, systematics and distribution of the venerid clam *Chamelea gallina*. J. Mar. Biol. Assoc. U.K. 74 (1), 211—223, http://dx.doi.org/10.1017/S0025315400035773.

Boltacheva, N.A., Mazlumyan, S.A., 2003. The growth and longevity of *Chamelea gallina* (Mollusca, Veneridae) in the Black Sea. Vestnik Zoologii 37 (3), 71—74.

Boltacheva, N.A., Revkov, N.K., Bondarenko, L.V., Kolesnikova, E.A., Timofeev, V.A., Kopiy, V.G., 2016. Taxonomic composition of macrozoobenthos of Karkinitsky Bay (the Black Sea) in early XXI century. In: Gayevskaya, A.V. (Ed.), Proc. All-Russian Scientific-Practical Conference with International Participation, 145th Anniversary of Sevastopol Biological Station, vol. 2. Sevastopol, 19—24 September, 2016. EKOSI-Gidrofizika, Sevastopol, 36—39, (in Russian).

Cano, F.V., Hernández, J.M., 1987. Biometría y reproducción de *Chamelea gallina* L. en la Bahia de Mazarrón (SE de la Península Ibérica) y algunas consideraciones sobre su pesca. FAO Fish. 395, 107—111.

Chikina, M.V., 2009. Macrozoobenthos of soft bottoms of North-Caucasian coast of the Black Sea: spatial structure and the long-term dynamics. Abstract PhD Dissertation, Moscow. 25 pp., (in Russian).

Delgado, M., Silva, L., Júares, A., 2013. Aspects of reproduction of striped venus *Chamelea gallina* in the Gulf of Cadiz (SW Spain): implications for fishery management. Fish. Res. 146, 86—95, http://dx.doi.org/10.1016/j.fishres.2013.04.005.

Deval, M.C., 2001. Shell growth and biometry of the striped venus *Chamelea gallina* (L) in the Marmara Sea, Turkey. J. Shellfish Res. 20 (1), 155—159.

Divinsky, B., Kosyan, R., 2017. Spatiotemporal variability of the Black Sea wave climate in the last 37 years. Cont. Shelf Res. 136 (1), 1—19, http://dx.doi.org/10.1016/j.csr.2017.01.008.

Eberly, W.R., 1967. Problems in the laboratory culture of planktonic blue-green algae. In: Environmental Requirements of Blue-Green Algae. Proc. Joint Symposium of University of Washington and Federal Water Pollution Control Administration, U.S. Department of the Interior, September 1966, 7—34.

Fedorova, E.A., Krylenko, V.V., Kosyan, A.R., 2018. Granulometric analysis of the Anapa bay-bar sediments (the Black Sea, Russia). In: Proc. SPIE — The International Society for Optical Engineering 10773, 107731D, http://dx.doi.org/10.1117/12.2324438.

Froglia, C., 1975a. Aspetti biologici, tecnologici e statistici della pesca delle vongole (*Venus gallina*). Incontri Tecn. Lab. Tecnol. Pesca Ancona 9, 7—22.

Froglia, C., 1975b. Osservazioni sull'accrescimento di *Chamelea gallina* (L.) e *Ensis minor* (Chenu) nel Medio Adriatico. Quad. Lab. Tecnol. Pesca Ancona 2 (1), 37—48.

Gaspar, M.B., Pereira, A.M., Vasconcelos, P., Monteiro, C.C., 2004. Age and growth of *Chamelea gallina* from the Algarve coast (Southern Portugal): influence of seawater temperature and gametogenic cycle on growth rate. J. Moll. Stud. 70 (4), 371—377, http://dx.doi.org/10.1093/mollus/70.4.371.

Grashoff, K., Kremling, K., Ehrhard, M., 1999. Methods of Seawater Analysis, 3rd edn. Wiley-VCH, Weinheim, New York, Chichester, Brisbane, Singapore, Toronto, http://dx.doi.org/10.1002/9783527613984, 632 pp.

Hansen, H.P., Koroleff, F., 1999. Determination of nutrients. In: Grasshoff, K., Kremling, K., Ehrhardt, M. (Eds.), Methods of Seawater Analysis. 3rd edn. Wiley-VCH, Weinheim, New York, Chichester, Brisbane, Singapore, Toronto, 159—228, http://dx.doi.org/10.1002/9783527613984.ch10.

Kiseleva, M.I., 1981. Benthos of Soft Grounds of the Black Sea. Naukova Dumka, Kiev, 168 pp., (in Russian).

Kiseleva, M.I., Slavina, O.Ya., 1965. Qualitative composition and quantitative distribution of macro- and meiobenthos off the northern coast of the Caucasus. In: Benthos. Naukova Dumka, Kiev, 62—80, (in Russian).

Kiseleva, M.I., Slavina, O.Ya., 1966. Quantitative distribution of macrozoobenthos near Caucasian Coast. In: Benthos Distribution and Biology of Benthic Animals in the Southern Seas. Naukova Dumka, Kiev, 55—74, (in Russian).

Kiseleva, M.I., Slavina, O.Ya., 1972. Distribution of benthos near Caucasian coast in the region between Tuapse-Shepsi. Biologia Morya, Naukova Dumka, Kiev 26, 125—133, (in Russian).

Koluchkina, G.A., Budko, D.F., Chasovnikov, V.K., Chzhu, V.P., 2017a. Influence of the bottom sediment characteristics on the bivalve mollusk *Anadara kagoshimensis* histopathology's variability in the northeastern coast of the Black Sea. Oceanology 57 (6), 828—840, http://dx.doi.org/10.1134/S0001437017060066.

Koluchkina, G.A., Chikina, M.V., Basin, A.B., Prokhorova, T.D., Liubimov, I.V., 2017b. Taxocene of Bivalvia of the Black Sea northeastern coast: 16-years monitoring results. In: Proc. Conference on Marine Research Education MARESEDU-17. 30 October—2 November 2017, Moscow, Russia. OOO "Polipress", Tver, 410—413, (in Russian).

Koluchkina, G.A., Semin, V.L., Grigorenko, K.S., Basin, A.B., Liubimov, I.V., 2017c. The role of abiotic factors in the vertical distribution of macrozoobenthos northeast coast of the Black Sea. In: Proceedings of the Conference on Marine Research Education MARESEDU-17, 30 October—2 November 2017, Moscow, Russia. OOO "Polipress", Tver, 414—418, (in Russian).

Kont, A., Jaagus, J., Aunap, R., 2003. Climate change scenarios and the effect of sea-level rise for Estonia. Global Planet. Change 36 (1—2), 1—15, http://dx.doi.org/10.1016/S0921-8181(02)00149-2.

Koroleff, F., 1983. Determination of silicon. In: Grasshoff, K., Ehrhardt, M., Kremling, K. (Eds.), Methods of Seawater Analysis. 2nd edn. Verlag Chemie, Weinheim, Deerfield Beach, 174—187.

Kosyan, A.R., 2016. Predation mechanisms of *Rapana venosa* (Gastropoda: Muricidae) in different biotopes along the Black Sea coast. Mar. Pollut. Bull. 102 (2), 265—270, http://dx.doi.org/10.1016/j.marpolbul.2015.07.069.

Kosyan, A.R., 2017. Dynamics of *Rapana venosa* Anapa bay-bar population structure. In: Ozhan, E. (Ed.), Proceedings of Thirteenth International MEDCOAST Congress on Coastal and Marine Sciences, Engineering, Management and Conservation, MEDCOAST'17, vol. 1, 31 October—04 November 2017, Mellieha, Malta. MEDCOAST, Dalyan, Mugla, Turkey, 437—448.

Kosyan, A.R., 2018. Carbonate sediments of the Bakal spit and their producers — coastal shells. Ecol. Safety of Coast. Sea Shelf Areas 4, 81—91, http://dx.doi.org/10.22449/2413-5577-2018-4-81-91, (in Russian).

Kosyan, R.D., Divinsky, B.V., Fedorova, E.A., 2018. Sandy sediment transport along Anapa Bay Bar (the Black Sea, Russia). In: Proc. SPIE — The International Society for Optical Engineering 10773, 107731A, http://dx.doi.org/10.1117/12.2322835.

Kosyan, R.D., Kosyan, A.R., Krylenko, V.V., Krylenko, M.V., Kuklev, S.B., 2011. The forecast of Anapa bay-bar coast evolution and sand body thickness change. In: Magoon, O.T., Noble, R.M., Treadwell, D.D., Kim, Y.C. (Eds.), Coastal Engineering Practice 2011. Conference on Coastal Engineering Practice, San-Diego, California, USA, August 21—24, 2011, 42—55, http://dx.doi.org/10.1061/9780784411902.

Kosyan, R.D., Krylenko, V.V., 2014. The current state of the Black Sea and the Sea of Azov accumulative coasts and recommendations about their rational using M. Sci. World, Moscow 256 pp., (in Russian).

Kosyan, A.R., Kucheruk, N.V., Flint, M.V., 2012. Role of bivalve mollusks in the sediment balance of the Anapa bay bar. Oceanology 52 (1), 72—78, http://dx.doi.org/10.1134/S0001437012010122.

Krylenko, V.V., Kosyan, R.D., Kochergin, A.D., 2011. Regularities of the formation of the granulometric composition of the bottom and beach deposits of the Anapa bay bar. Oceanology 51 (6), 1061—1071, http://dx.doi.org/10.1134/S0001437011060099.

Kucheruk, N.V., Basin, N.V., Kotov, A.V., Chikina, M.V., 2002. Macrozoobenthos of soft grounds of the North Caucasus coast of the Black Sea: long-term dynamics of the communities. In: Zatsepin, A.G., Flint, M.V. (Eds.), Complex Studies of the Northeastern Part of the Black Sea, Nauka, Moscow, 289—298, (in Russian).

Massé, H., 1971. Contribution à l'étude de la macrofaune de peuplements des sables fins infralittoraux des côtes de Provence. III. L'anse de Verdon. IV. L'anse de Saint-Gervais (Golfe de Fos). Tethys 3, 283—319.

Mills, E.L., Dermott, R.M., Roseman, E.F., Dustin, D., Mellina, E., Conn, D.B., Spidle, A.P., 1993. Colonization, ecology and population structure of the "Quagga" mussel (Bivalvia: Dreissenidae) in the lower Great Lakes. Can. J. Fish. Aquat. Sci. 50 (11), 2305—2314, http://dx.doi.org/10.1139/f93-255.

Mimura, N., 1999. Vulnerability of island countries in the South Pacific to sea level rise and climate change. Clim. Res. 12 (2—3), 137—143, http://dx.doi.org/10.3354/cr012137.

Moss, D.K., Ivany, L.C., Judd, E.J., Cummings, P.W., Bearden, C.E., Kim, W.-J., Artruc, E.G., Driscoll, J.R., 2016. Lifespan, growth rate, and body size across latitude in marine Bivalvia, with implications for Phanerozoic evolution. Proc. R. Soc. B: Biol. Sci. 283 (1836), 1—7, http://dx.doi.org/10.1098/rspb.2016.1364.

Nabozhenko, M.V., 2011. Recent distribution of bivalve mollusks (Mollusca: Bivalvia) in the northeastern Black Sea. Herald of SSC RAS 7 (3), 79—86, (in Russian).

Nakaoka, M., 2000. Nonlethal effects of predators on prey populations: predator-mediated change in bivalve growth. Ecology 81 (4), 1031—1045, http://dx.doi.org/10.1890/0012-9658(2000)081[1031:NEOPOP]2.0.CO;2.

Nicholls, R.J., Cazenave, A., 2010. Sea-level rise and its impact on coastal zones. Science 328 (5985), http://dx.doi.org/10.1126/science.1185782.

Nicholls, R.J., Mimura, N., 1998. Regional issues raised by sea level rise and their policy implications. Clim. Res. 11 (1), 5—18, http://dx.doi.org/10.3354/cr011005.

Olafsson, E.B., 1986. Density dependence in suspension-feeding and deposit-feeding populations of the bivalve *Macoma balthica*: a field experiment. J. Anim. Ecol. 55 (2), 517—526, http://dx.doi.org/10.2307/4735.

Özden, Ö., Erkan, N., Deval, M.C., 2009. Trace mineral profile of the bivalve species *Chamelea gallina* and *Donax trunculus*. Food Chem. 113 (1), 222—226, http://dx.doi.org/10.1016/j.foodchem.2008.06.069.

Peltier, W.R., 1999. Global sea level rise and glacial isostatic adjustment. Global Planet. Change 20 (2—3), 93—123, http://dx.doi.org/10.1016/S0921-8181(98)00066-6.

Peterson, C.H., 1982. The importance of predation and intra- and interspecific competition in the population biology of two infaunal suspension-feeding bivalves, *Protothaca staminea* and *Chione undatella*. Ecol. Monogr. 52 (4), 437—475, http://dx.doi.org/10.2307/2937354.

Peterson, C.H., Beal, B.F., 1989. Bivalve growth and higher order interactions: importance of density, site, and time. Ecology 70 (5), 1390—1404, http://dx.doi.org/10.2307/1938198.

Poggiani, L., Piccinetti, C., Manfrin-Piccineti, G., 1973. Osservazioni sulla biologia dei molluschi bivalvi *Venus gallina* L. e *Tapes aureus* Gmelin nell'Alto Adriatico. Note del Laboratorio di Biologia Marina e Pesca. Fano 4, 189—212.

Polenta, R., 1993. Osservazioni sull'accrescimento della vongola *Chamelea gallina* L. nel Medio adriatico, Tezi di Laurea in Scienze Biologiche. Università degli studi di Bologna.

Ramon, M., Richardson, C.A., 1992. Age determination and shell growth of *Chamelea gallina* (Bivalvia: Veneridae) in the western Mediterranean. Mar. Ecol. Prog. Ser. 89 (1), 15—23, http://dx.doi.org/10.3354/meps089015.

Revkov, N.K., 2011. Macrozoobenthos of the Ukrainian zone of the Black Sea shelf. In: Eremeev, V.N., Gaevskaya, A.V., Shulman, G.E., Zagorodnyaya, Ju.A. (Eds.), Biological Resources of the Black Sea and Sea of Azov, Institute of Biology of the southern Seas NAS of Ukraine, EKOSI-Gidrofizika, Sevastopol, 140—162.

Revkov, N.K., Timofeev, V.A., Lisitskaya, E.V., 2014. Composition and seasonal dynamics of macrozoobenthos in local biotic complex *Chamelea gallina* (western Crimea, Black Sea). Optim. Prot. Ecosys. 11 (30), 247—259, (in Russian).

Ridgway, I.D., Richardson, C.A., Austad, S.N., 2011. Maximum shell size, growth rate, and maturation age correlate with longevity in bivalve molluscs. J. Gerontol. A: Biol. 66A (2), 183—190, http://dx.doi.org/10.1093/gerona/glq172.

Romanelli, M., Cordisco, C.A., Giovanardi, O., 2009. The long-term decline of the *Chamelea gallina* L (Bivalvia: Veneridae) clam fishery in the Adriatic Sea: is a synthesis possible? Acta Adriatica 50 (2), 171—205.

Royo, A., 1984. La chirla, *Venus gallina* L., en el litoral Onubense. In: Actas del IV Simposio Ibérico de Estudios del Benthos Marino, Lisboa, 21—25 de Maio 1984, vol. 2, 49—66.

Scarlato, O.A., Starobogatov, Y.E., 1972. Class — Bivalvia. Keys to the Fauna of the Black and Azov Seas, vol. 3. Naukova Dumka, Kiev, 178—249, (in Russian).

Sinegub, I.A., 2006. Macrozoobenthos. Bottom Communities. 1984—2002. North-western Part of the Black Sea: Biology and Ecology. Naukova Dumka, Kiev, 276—286, (in Russian).

Solorzano, L., 1969. Determination of ammonia in natural waters by the phenol hypochlorite method. Limnol. Oceanogr. 14 (5), 799—801, http://dx.doi.org/10.4319/lo.1969.14.5.0799.

Zagorskaya, A.S., 2014. Macrozoobenthos of soft grounds of the north-eastern part of the Black Sea (Dzhubga — Kudepsta). Izvestia vuzov, North-Caucasian region. Earth Sci. 3, 64—71, (in Russian).

Zerbini, S., Plag, H.-P., Baker, T., Becker, M., Billiris, H., Bürki, B., Kahle, H.-G., Marson, I., Pezzoli, L., Richter, B., Romagnoli, C., Sztobryn, M., Tomasi, P., Tsimplis, M., Veis, G., Veronne, G., 1996. Sea level in the Mediterranean: a first step towards separating crustal movements and absolute sea-level variations. Global Planet. Change 14 (1—2), 1—48, http://dx.doi.org/10.1016/0921-8181(96)00003-3.

Ziuganov, V., Miguel, E.S., Neves, R.J., Longa, A., Fernándes, C., Amaro, R., Beletsky, V., Popkovitch, E., Kaliuzhin, S., Johnson, T., 2000. Life span variation of the freshwater pearl shell: a model species for testing longevity mechanisms in animals. Ambio 29 (2), 102—105, http://dx.doi.org/10.1579/0044-7447-29.2.102.

Oceanologia (2019) 61, 484—504

Available online at www.sciencedirect.com

ScienceDirect

journal homepage: www.journals.elsevier.com/oceanologia/

ORIGINAL RESEARCH ARTICLE

Recent sea surface temperature trends and future scenarios for the Red Sea

Mohamed Shaltout *

Faculty of Science, Department of Oceanography, University of Alexandria, Alexandria, Egypt

Received 10 September 2018; accepted 7 May 2019
Available online 24 May 2019

KEYWORDS
Red Sea;
Sea surface temperature;
Chlorophyll-*a*;
Heat exchange;
Climate models;
Ensemble forecast

Summary The current paper analyses the recent trends of Red Sea surface temperature (SST) using 0.25° daily gridded Optimum Interpolation Sea Surface Temperature (OISST) data from 1982 to 2016. The results of 3 different GFDL (Geophysical Fluid Dynamics Laboratory) model simulations are used to project the sea surface temperature (hereafter called Tos) under the four representative concentration pathway scenarios through 2100.

The current research indicates that the spatially annual mean (from 1982 to 2016) Red Sea surface temperature is 27.88 ± 2.14°C, with a significant warming trend of 0.029°C yr^{-1}. The annual SST variability during the spring/autumn seasons is two times higher than during the winter/summer seasons. The Red Sea surface temperature is correlated with 13 different studied parameters, the most dominant of which are mean sea level pressure, air temperature at 2 m above sea level, cross-coast wind stress, sensible heat flux, and Indian Summer Monsoon Index.

For the Red Sea, the GFDL-CM3 simulation was found to produce the most accurate current SST among the studied simulations and was then used to project future scenarios. Analysis of GFDL-CM3 results showed that Tos in the Red Sea will experience significant warming trends with an uncertainty ranging from 0.6°C $century^{-1}$ to 3.2°C $century^{-1}$ according to the scenario used and the seasonal variation.

* Corresponding author at: Laboratory Faculty of Science, Department of Oceanography, University of Alexandria, Alexandria 21151, Egypt. Tel.: +20 1005255393; fax: +203 3911794.
E-mail address: mohamed.shaltot@alexu.edu.eg.

Peer review under the responsibility of Institute of Oceanology of the Polish Academy of Sciences.

ELSEVIER | Production and hosting by Elsevier

https://doi.org/10.1016/j.oceano.2019.05.002

1. Introduction

The Red Sea and its surrounding sea region (Gulf of Aden) extending from 32°E to 51°E and from 10°N to 30°N (hereafter "Red+"; Fig. 1) can be divided into several subbasins, for example, the Gulf of Aden subbasin (hereafter "GOA subbasin") south of Bab el-Mandeb Strait, Southern Red Sea (SRed), Central Red Sea (CRed) and Northern Red Sea (NRed). Red+, which is considered an arid climate region with negligible precipitation and runoff (Al-Horani et al., 2006), provides a significant resource for tourism, fishing, coral reefs, and oil and gas extraction. Moreover, the Red Sea supports a high volume of shipping activity, which links European harbors to China and eastern Asia. The vulnerability of Red+ to SST warming trends during the current century is highly expected (Hoegh-Guldberg et al., 2014), which may lead to a potentially harmful impact on marine entities and ecosystems (e.g., the decline in the average coral colony size). The IPCC (2014) shows that the global SST will experience warming trends during the current century. The warming trends are expected to continue even if greenhouse gas emissions remain constant or decrease (Collins et al., 2013).

During the 1950–2007 period, the Red Sea SST reached its highest value during August and reached its lowest value during February (Hoegh-Guldberg et al., 2014). The Red Sea's seasonal summer to winter SST difference is approximately 6°C (Berman et al., 2003). In a study of the Red Sea SST during the period 1985–2007, Raitsos et al. (2011) found that the coldest year was 1992 and that the annual mean SST was 27.4°C from 1985 to 1993 and 28.1°C from 1994 to 2007.

Raitsos et al. (2011) also confirmed that there was intense warming of the Red Sea surface temperature in the mid-90s. Hoegh-Guldberg et al. (2014) found no significant trend in the Red Sea surface temperature from 1950 to 2007. However, there was a significant warming from 1982 to 2006, indicating

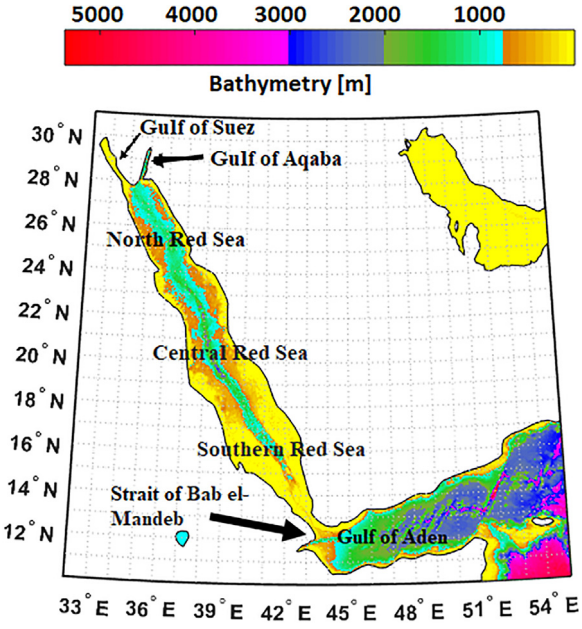

Figure 1 Bathymetric chart of the Red Sea (data acquired from a global 30 arc-second interval grid (GEBCO: https://www.gebco.net/data_and_products/gridded_bathymetry_data/)).

that the absence of a significant trend in the Red Sea surface temperature over the long period of 1950 to 2007 may be caused by the large-scale variability prior to 1982, which may be due to the influence of the Atlantic Multidecadal Oscillation (AMO) and North Atlantic Oscillation (NAO). In addition, the authors noted that the Red Sea SST exhibits a significant trend of 0.5 and 0.3°C decade^{-1} for the warmest and coolest months, respectively. The Red Sea surface temperature warming trends are spatially distributed, most clearly in the central Red Sea for the period 1950–1997 [0.31°C decade^{-1}] (Cantin et al., 2010). Recently, Chaidez et al. (2017) showed that the maximum Red Sea temperature experienced a warming trend of 0.017°C yr^{-1} for the 1982–2015 period. They found that the Gulfs of Suez and Aqaba exhibit lower temperatures than the open Red Sea. Moreover, the maximum Red Sea temperature occurred during July in the northern Red Sea and from late July to mid-August in the southern Red Sea. Karnauskas and Jones (2018) showed that the interannual variability of the Red Sea SST occurs in both summer and winter, most markedly in NRed during winter.

Heat waves were observed more frequently in the northern half of the Red Sea over the period 1982–2015 (Chaidez et al., 2017). Thomas et al. (2012) and Sawall et al. (2014) showed that the warming process in the Red Sea may lead to thermal collapse (thermal collapse occurs when the temperature exceeds the thermal capacity of organisms).

The Red Sea SST is significantly affected by the Indian monsoon (Raitsos et al., 2011). The Atlantic Multidecadal Oscillation Index (AMOI) and North Atlantic Oscillation Index (NAOI) have an effect on the Red Sea SST long-term variability (Hoegh-Guldberg et al., 2014). The SST is mainly affected by the air temperature at 2 m above sea level (T_{2m}), mean sea level pressure (SLP), total cloud cover (TCC), wind stress components at 10 m above sea level (i.e., cross-coast surface wind stress (τ_{ac}) and along-coast surface wind stress (τ_{al})) and air-sea heat fluxes (Shaltout and Omstedt, 2014; Skliris et al., 2012).

In general, the exchange through Bab el-Mandeb Strait has a significant effect on SST distribution, especially in SRed. The water exchange through Bab el-Mandeb Strait is described as a two-layer flow during cold months; dense intermediate Red Sea water flows out into the Gulf of Aden and the warmer, fresher surface water from the Gulf of Aden flows into the Red Sea. In the summer season, this exchange represents a three-layer structure; surface and intermediate Red Sea water flow out to the Gulf of Aden; however, a third layer, with a density between that of the surface layer and that of the intermediate Red Sea water, flows into the Red Sea (Smeed, 1997). The summer exchange in the strait is remotely induced by the monsoonal wind over the Indian Ocean (Aiki et al., 2006). During the winter monsoon, the predominant winds over the strait blow towards the Red Sea enhancing the surface layer inflow and bottom layer outflow, whereas, during the summer monsoon, the wind blows toward the Indian Ocean suppressing the surface layer inflow (Aiki et al., 2006).

Clearly, significant warming can potentially lead to ecological collapse (Richardson and Schoeman, 2004). According to Cantin et al. (2010) and Roik et al. (2016), the decrease of coral growth in CRed is a result of warming conditions. In addition, the NRed SST has a significant negative correlation with chlorophyll-*a* (chl-a) concentration (Eladawy et al., 2017). Recently, Osman et al. (2018) showed that the maximum annual water temperatures are close to coral thermal

limits in CRed, however, over NRed corals live well as their thermal limits are not close to maximum annual water temperature. Corals in the northern Red Sea have a much higher heat tolerance than their prevailing temperature regime would suggest. In contrast, corals from the central Red Sea are close to their thermal limits.

Hoegh-Guldberg et al. (2014) have discussed the projected changes of the Red Sea SST up to the end of the current century using AOGCM model simulations from the Coupled Model Intercomparison Project Phase 5 (CMIP5, http://cmip-pcmdi.llnl.gov/cmip5/) under four representative concentration pathway scenarios (i.e., RCP2.6, RCP4.5, RCP6.0, and RCP8.5). They have predicted that the Red Sea SST may experience significant warming ranging from 0.35°C (RCP2.6) to 0.77°C (RCP8.5) over the period from 2010–2039, whereas from 2010–2099 the warming ranges from 0.88°C (RCP2.6) to 3.45°C (RCP8.5).

Although many other works have been published recently about the Red+ SST, studying its maximum values and heat waves characteristics (Chaidez et al., 2017) or studying its interannual variability (Karnauskas and Jones, 2018), the comparison between the 4 Red+ subbasins together with projection of the future Red+ SST scenarios have not received enough attention. Moreover, studying the effect of heat waves on the chl-a concentration for each Red+ SST cluster is quite new. This information is needed to extend our knowledge about the seasonal/spatial variability of the Red+ SST from 1982 through 2100. This information supports the decision makers in reducing the impacts of expected warming trends in Red+, especially on chl-a concentrations.

The present research uses a 35-year (1982–2016) high-resolution SST database: (1) to examine temporal and spatial SST variability in Red+; (2) to analyze the relationship between Red+ SST and various atmospheric parameters, such as T_{2m}, SLP, TCC, τ_{ac}, τ_{al}, air-sea heat fluxes, AMOI, NAOI and Indian Summer Monsoon Index (ISMI); (3) to examine SST characteristics in the different Red+ subbasins (Red+ is treated as 4 sub-basins); (4) to study the effect of heat wave events on chl-a concentrations; and (5) to examine the projected Red+ SST through the year 2100 using available GFDL future simulations. Data and methods used are presented in Section 2, the results and the discussion are in Section 3, and the conclusions are in Section 4.

2. Data and methods

2.1. Data used

This paper analyses the present Red+ SST characteristics and future warming uncertainties based on various available data sources, as follows.

i. Gridded daily 0.25° NOAA Optimum Interpolation Sea Surface Temperature data (OISST; version 2), from 1982 to 2016, were used to study recent SST characteristics. OISST (version 2) merges satellite ocean skin temperatures and in situ platforms (ships and buoys) on a regular global grid (Reynolds et al., 2007; Reynolds, 2009). The in situ platform measurements were acquired from ICOADS (International Comprehensive Ocean-Atmosphere Data Set) (Worley et al., 2005). The methodology includes applying the Optimum Interpolation (OI) statistical method to fill the gaps. Moreover, a bias adjustment step of satellite data to in situ data is performed prior to interpolation. The daily OISST is a combination of data collected over the entire day, so this method does not capture diurnal variability and does not represent a particular time of day (Banzon et al., 2018). These data are freely available as gridded netCDF Data via FTP (ftp://eclipse.ncdc.noaa.gov/pub/OI-daily-v2/NetCDF/). The OISST is relevant to study local oceanic features (Nykjaer, 2009). The OISST database is described as a scientific tool to study SST variability in the Red Sea, especially due to the high density of in situ measurements in the ICOADS data bank of the Red Sea (Karnauskas and Jones, 2018).

ii. In situ SST data were downloaded from various databases:
- WOD2013 – World Ocean Database 2013 (Boyer et al., 2013, http://www.nodc.noaa.gov/). The WOD2013 data are mostly collected from multiple datasets: Ocean Station Data (**OSD**), Conductivity-Temperature-Depth (**CTD**) data, **MBT** (Mechanical Bathythermograph) data, expendable bathythermograph (**XBT**), and drifting buoy (**DRB**) data.
- GOSUD – Global Ocean Surface Underway data (GOSUD, 2016, https://www.seanoe.org/data/00363/47403/). The GOSUD data are mostly collected using thermosalinographs (TSG) installed on research vessels, on commercial ships and, in some cases, on sailing exploration ships. GOSUD manages delayed-mode together with near-real-time data. The methods contain a quality control process.

iii. Simulated surface circulation data were extracted from the HYbrid Coordinate Ocean Model (HYCOM) daily output with 1/12° horizontal grid resolution and 32 vertical layers. These data can be freely accessed from ftp://ftp.hycom.org/datasets/GLBa0.08/ for the 2007–2016 period. The HYCOM is a primitive equation ocean general circulation model that evolved from the MICOM (Miami Isopycnic-Coordinate Ocean Model) as described in Halliwell (2004). HYCOM is relevant to study the Red Sea surface circulation (Eladawy et al., 2017).

iv. Atlantic Multidecadal Oscillation Index (AMOI), North Atlantic Oscillation Index (NAOI) and Indian Summer Monsoon Index (ISMI) data were used to study the link between climate indices and Red+ SST.
- Monthly AMOI captured by the NOAA Earth System Research Laboratory (https://www.esrl.noaa.gov/psd/data/correlation/amon.us.data) over the period from 1982 to 2016 were used. The AMOI is characterized by the annual mean area-average of detrended SST anomalies over the North Atlantic from 0°N to 60°N. Detrended SST anomalies are derived by removing the global mean SST time series from each grid point (Trenberth and Shea, 2006).
- Daily NAOI data from 1982 to 2016 were extracted from the KNMI Climate Explorer (https://climexp.knmi.nl). The NAOI is the sea level pressure (SLP) difference between the high latitudes of the North Atlantic and the central latitudes of the North Atlantic, which are from 30°N to 40°N. The negative phase of the NAOI reflects below-normal SLP over the central North Atlantic and above-normal SLP across the

high latitudes of the North Atlantic. The positive phase describes the opposite pattern (Hurrell, 1995).

- Daily ISMI data were extracted from the Asia-Pacific Data-Research Center (http://apdrc.soest.hawaii.edu/projects/monsoon/daily-data.html#mon) from 1982 to 2015. The ISMI lasts only from June until September and contributes to temperature distribution and wind circulation (Sarthia et al., 2012). The ISMI is an 850-hPa zonal wind difference between a southern region (40°–80°E, 5°–15°N) and a northern region (70°–90°E, 20°–30°N) as described in Wang et al. (2001). The strength of an Indian summer monsoon system increases with the increase of ISMI positive values.

v. Gridded daily data, from 1982 to 2016, on several surface meteorological parameters (T_{2m}, SLP, and TCC) and air-sea heat fluxes were extracted from the ERA-Interim full-resolution (0.125° × 0.125°) database (http://apps.ecmwf.int/datasets/data/interim-full-daily/levtype=sfc/). Era-Interim data were originally of a 0.75° × 0.75° grid size and recently were bilinearly interpolated to a 0.125° grid to provide a finer resolution (Owens and Hewson, 2018). This interpolation employs a land-sea mask to decrease undesired smoothing of gradients along coastlines; thus, Era-Interim fine-resolution (0.125°) data were used in the current study to study their relationship to the SST dynamic. Surface metrological parameters are produced with the observation fields; however, air-sea heat fluxes are produced with a forecasting model. The forecasting model uses the Monin–Obukhov formulation (Dee et al., 2011; Zhou and Wang, 2016).

vi. Daily surface wind speed components were extracted from the ERA-Interim full-resolution (0.125° × 0.125°) database from 1982 to 2000. From 2000 to 2016, remotely sensed daily ocean with 0.25° grid resolution wind data were used; the Quick Scatterometer (QUICK SCAT; Ricciardulli et al., 2011) from 2000 to 2007 and Advanced Scatterometer (ASCAT) wind maps (Bentamy and Croize-Fillon, 2012) from 2007 to 2016 were used. QUICK SCAT and ASCAT data were freely accessed via (ftp://ftp.ifremer.fr/ifremer/cersat/products/gridded/MWF/L3/).

vii. Gridded daily data on chlorophyll-*a* (chl-a) concentrations were extracted from the MODIS (Moderate Resolution Imaging Spectroradiometer) sensor database. MODIS, which is a sensor operating on the NASA Aqua satellite, was launched on May 2002 to support scientists to study global change with many standard data products. The current paper uses the Level 3 standard mapped image (SMI, MODIS_L3_Chl-a) to study the variability of chl-a concentration over Red+. MODIS_L3_Chl-a dataset validations and documentations are fully described in Anonymous (2014). These data are freely available with a 4.6 km (at the equator) spatial resolution from 2003 to 2016 via https://oceandata.sci.gsfc.nasa.gov/MODIS-Aqua/Mapped/Daily/4km/chlor_a/. Many authors have used MODIS_L3_Chl-a to study marginal seas including Red+ (Bai et al., 2018; Eladawy et al., 2017). Moreover, MODIS_L3_Chl-a has shown very good agreement with in situ data in the Red Sea (Brewin et al., 2013).

viii. Future SST (hereafter, Tos): Model output from three different GFDL simulations for current century CMIP5 scenarios (i.e., RCP2.6, RCP4.5, RCP6.0, and RCP8.5) were used. RCP stands for "Representative Concentration Pathways," and the following numbers indicate the assumed radiative forcing in 2100. These data were used to project SST uncertainty up to 2100. GFDL simulation is based on coupled atmospheric/oceanic circulation models with respect to land and iceberg dynamics (Delworth et al., 2006; Dunne et al., 2013) to understand future climate behavior.

2.2. Estimated quality of the OISST database used for the study area

A direct comparison of the spatiotemporal Red+ SST variability between the OISST data and in situ SST data were used to test the quality of OISST database over Red+ during the overlapping period (1982–2012). Thus, the correlation coefficients (R) and the number of observations (n) were calculated between the daily OISST and in situ data to compare the two datasets. Moreover, the bias between OISST and in situ data was also calculated to determine the error in OISST. Generally, each in situ SST data is compared with simultaneous OISST grid that contains in situ positions (hereafter called matched OISST data).

To extract the OISST data at the in situ positions, the OISST grid that contains in situ positions was chosen. If the OISST data was missing at the in situ location, then the nearest OISST was chosen.

Finally, a direct comparison was performed between two samples; the first sample includes in situ SST data, however, the second sample includes simultaneous matched OISST data.

2.3. Statistical methods for studying recent Red Sea SST characteristics

The present study employs five statistical methods steps for studying recent Red Sea SST characteristics as follows:

I. The OISST daily dataset was used to describe the spatial and temporal SST variability in Red+ over a 35-year period focusing on seasonal and annual variability.
   - The annual mean (from 1982 to 2016) SST refers to the average of daily OISST data for the 1982–2016 period. However, the annual mean SST refers to the average of daily OISST for a specific year. Moreover, the minimum (maximum) annual mean SST refers to the annual mean SST during the coldest (warmest) year.
   - The annual linear trend (from 1982 to 2016) were calculated using the ordinary least squares estimation of daily OISST data.
   - All the previous calculations were done for each grid, then averaged spatially for each subbasin and the entire study area. Thus:
     - The spatially annual mean (from 1982 to 2016) SST over Red+ refers to spatially averaging of the annual mean (from 1982 to 2016) SST for each grid over Red+.
     - The spatially annual warming trend (from 1982 to 2016) over Red+ refers to spatially averaging of the annual warming (from 1982 to 2016) for each grid over Red+.

- The spatially annual standard deviation (from 1982 to 2016) SST over Red+ refers to spatially averaging of the standard deviation (from 1982 to 2016) SST for each grid over Red+.

II. HYCOM's daily surface currents were used to calculate seasonal and annual averaged surface current over Red+ for the 2007–2016 period. This calculated seasonal and annual averaged surface current was used to elaborate on the SST spatial and temporal dynamics.

III. Seasonality and time lag over the most significant Red+ SST cycle were studied using Fourier analysis based on the daily OISST dataset by calculating the amplitude and phase angle of a one-year cycle to each grid (i, j) as follows:

$$f_{i,j}(t) = ao_{i,j} + \sum_{n=1}^{N} an_{i,j} \cos\left(\frac{2\pi nt}{T}\right) + \sum_{n=1}^{N} bn_{i,j} \sin\left(\frac{2\pi nt}{T}\right), \quad (1)$$

where T is the one-year period, and t is the time; when the seasonal cycle is predominant, only the terms up to $n = 1$ can be retained and the Fourier analysis becomes

$$f_{i,j}(t) = ao_{i,j} + a1_{i,j} \cos\left(\frac{2\pi t}{T}\right) + b1_{i,j} \sin\left(\frac{2\pi t}{T}\right) = ao_{i,j} + A_{i,j} \cos\left(\frac{2\pi t}{T} - \vartheta_{i,j}\right), \quad (2)$$

where ao, $a1$ and $b1$ are the Fourier coefficients

$$ao = \frac{1}{T}\int_{-T/2}^{T/2} f(t)\,dt,$$

$$a1 = \frac{2}{T}\int_{-T/2}^{T/2} f(t)\cos\left(\frac{2\pi t}{T}\right)dt,$$

$$b1 = \frac{2}{T}\int_{-T/2}^{T/2} f(t)\sin\left(\frac{2\pi t}{T}\right)dt$$

and

$$A\ (\text{Amplitude}) = \sqrt{a1^2 + b1^2} \text{ and } \vartheta\ (\text{phase lag}) = \tan^{-1}\frac{b1}{a1}.$$

IV. The monthly and interannual effects of various atmospheric parameters, i.e., T_{2m}, SLP, TCC, τ_{ac} (cross-coast surface wind stress), τ_{al} (cross-coast surface wind stress), air-sea heat fluxes, AMOI, NAOI and ISMI, on SST variability were studied using the correlation coefficient (R) and the number of observations (n).

ERA-Interim surface wind data are available only in the form of zonal and meridional wind speed at a 10-m height; thus, the τ_{ac} and τ_{al} were calculated as follows:

- Eastward wind stress (τ_{ax}) and northward wind stress (τ_{ay}) were calculated from the wind components at 10 m above sea level (zonal and meridional wind components) using a standard bulk formula with a calculation of the air drag coefficient from its nonlinear form (Large and Pond, 1981) and with a modification for low wind speeds (Trenberth et al., 1990).
- τ_{ac} and τ_{al} were calculated from τ_{ax} and τ_{ay} using the coastal orientation (θ) as follows:

$$\tau_{al} = \tau_{ax}\cos(\theta) - \tau_{ay}\sin(\theta), \quad (3)$$

$$\tau_{ac} = \tau_{ax}\sin(\theta) + \tau_{ay}\cos(\theta). \quad (4)$$

In general, the air-sea heat fluxes were defined by the net heat loss from the sea (F_n) and solar radiation to the open water surface (Fsw), where

$$F_n = \text{sensible heat flux } (F_h) + \text{latent heat flux } (F_e) + \text{net longwave radiation } (F_l). \quad (5)$$

V. Principal component analysis (PCA) was applied to 13 daily variables (SST, T_{2m}, SLP, TCC, τ_{ac}, τ_{al}, F_e, F_l, F_h, F_n, Fsw, NAOI and ISMI) from 1982 to 2016 to interpret the linear combination between them. PCA is an unsupervised mathematical method to replace original variables by a much smaller number of uncorrelated variables called principal components (PC). The first PC is dominated by the variable with the largest variance, the second PC is dominated by the variable with the second largest variance, and so on. The computation of principal components is fully described by Jolliffe (2002).

In this study, Red+ is divided into four subbasins: GOA, SRed, CRed, and NRed. All correlation coefficients and linear trends have been tested for significance at the 95% level.

2.4. Heat waves and chlorophyll-*a*

Heat waves are typically defined as three consecutive hot days (a hot day is determined by the temperature exceeding the summer mean plus twice the summer standard deviation). Heat waves are calculated to evaluate the effect of recent warming trends on marine biota, especially when their thermal limits may be approached or exceeded (Chaidez et al., 2017). The Red Sea was divided into a number of clusters to study heat wave characteristics in each cluster.

Clustering of daily SST was performed to classify Red+ into several clusters. A cluster contains a number of grids that are more similar between themselves than to any grids not in the cluster. The k-means clustering algorithm depends on calculating the distance between each object in the dataset to the center of each cluster (k) as described in MacQueen (1967). Clearly, the distance calculation together with a specific number of clusters play a vital role in the algorithm. In the current paper, the correlation, mean and geographical position were used for distance calculations in the k-means algorithm.

The current calculation was designed to: (1) run k-means clustering algorithm (mean is the distance measured) for several iterations with increasing k; (2) choose the best iteration based on each cluster that contains grids with a range of 0.4°C; (3) calculate the correlation coefficient between each grid and the other grids in the same cluster and remove the grids that describe a low correlation ($R < 0.95$) with the other grids from the cluster; (4) remove from the cluster the grids that lie on abnormal geospatial

distance from other grids in the same cluster; and (5) repeat the steps 1 to 4 only for the removed grids (according to correlation or geospatial distance) to classify new clusters.

To understand the effect of heat waves on the Red Sea, the effect of heat waves on chl-a concentrations was analyzed for each cluster.

2.5. Projected Red+ Tos for the 21st century using the GFDL model result

GFDL model simulation databases were used to simulate projected sea surface temperature (Tos) under three different simulations. The GFDL-ESM2M simulation is the result of a system of coupling different models: AM2 (Anderson et al., 2004) for the atmospheric component, LM3 for the land component (Anderson et al., 2004; Milly et al., 2014), and the Modular Ocean Model, version 4p1 (MOM4p1) for sea ice and ocean content (Griffies, 2009). The GFDL-ESM2G simulation, unlike the GFDL-ESM2M simulation, employs the Generalized Ocean Layer Dynamics (GOLD; Adcroft and Hallberg, 2006) model for ocean components instead of MOM4p1. The GFDL-CM3 simulation is intended to improve on GFDL-ESM2M by using AM3 (Donner et al., 2011) for the atmospheric component, LM3 (Milly et al., 2014) for the land component, the sea ice simulator (SIS) for the ice component (Griffies et al., 2011) and MOM 5 for the ocean components (Griffies et al., 2011).

The Tos results from the three different GFDL model simulations (i.e., CM3, ESM2G and ESM2M) under the four RCP scenarios for the 2006–2010 period was tested using OISST SST data. The GFDL model ensemble mean for these three simulations was also calculated. Direct annual biases (Tos minus SST) were calculated for the four simulations to evaluate their performance in describing the current Red+ SST. Only the simulations that realistically describe the current SST were used to project Tos through 2100.

Future Tos trends and uncertainties under the four RCP scenarios were calculated using the 30-year running average. In the current research, there are four sources of uncertainty, which are associated with the scenario design, the model simulation, and seasonal and regional variations.

3. Results and discussion

3.1. In situ SST and OISST data sets

In this section, the feasibility of using OISST datasets in describing the Red+ sea surface temperature is investigated by determining the direct correlation and bias between OISST and in situ SST.

In situ data cover the period from 1982 to 2012, as shown in Fig. 2a, most markedly collecting data during 2007; however, in situ data cover Red+ most markedly in NRed (Fig. 2b). In situ data cover both coastal and open water areas.

The daily OISST data adequately follow the in situ data at a 99% significance level ($R = 0.98$, $n = 53{,}682$). The average bias (OISST, in situ) is -0.2°C. OISST data shows a bias range from -0.3°C to 0.3°C in 65% of the in situ data, as shown in Fig. 3. Thus, OISST data can be used to study the local features of Red+.

3.2. Spatial/temporal distribution of Red Sea surface temperature

It is clear from Figs. 4 and 5 that the annual mean (from 1982 to 2016) SST in Red+ reaches its maximum value over grids concentrated in SRed and is associated with the surface current system. From autumn to spring, the maximum SST occurred along the southeastern Red Sea coast from 15°N to 18°N. This finding can be explained by the fact that the SRed surface water is significantly influenced by the surface flow from the Gulf of Aden (which has a lower SST than SRed). Most of the GOA surface water inflow passes through the western part of SRed, leading to a significant moderating process along the southwestern coast of SRed in comparison to the southeastern coast of SRed as seen in Fig. 5. During the summer season, the maximum SST occurred along the southwestern coast from 14°N to 16°N. The water in SRed is influenced by the water flows from CRed (which has lower SST than SRed) that pass along the southeastern coast and moderate its SST. However, the southwestern coast is not influenced by the water flows from CRed (Fig. 5d).

The annual mean (from 1982 to 2016) SST in Red+ reaches its minimum values (22.5°C) over grids concentrated in the Gulf of Suez as shown in Fig. 5a. The SST in the Gulf of Suez is colder than that in the Gulf of Aqaba, which is at the same latitude, most markedly in summer. This finding is due to the shallow water characteristics of the Gulf of Suez. Moreover, a cyclonic gyre in NRed inducing more flow of relatively warmer Red Sea surface water to the Gulf of Aqaba results in an increase of the Gulf of Aqaba SST compared to the Gulf of Suez.

The Red Sea SST temporal variation from 1982 to 2016 is described in terms of the means of the seasonal and annual cycle, while its spatial variation treats Red+ as four subbasins (the Gulf of Aden, SRed, CRed, and NRed). The spatially annual mean (from 1982 to 2016) SST over Red+ is $27.88 \pm 2.14^{\circ}$C (Fig. 4a and Table 1). In addition, the Red Sea SST increased meridionally from south to north, partly due to the amount of absorbed solar energy. However, GOA is colder than SRed, due to the moderation process in GOA resulting from the upwelling process in GOA during the Indian summer monsoon (Bower and Furey, 2012; Wilson and Rebecca, 2000) together with the exchange with relatively cold water from the Arabian Sea (northern Indian Ocean). Moreover, the maximum value of annual mean (from 1982 to 2016) SST across Red+ shows a significant variation with latitude (data are not shown), where this value ranges from 34.92°C at 16° latitude to 29.06°C at 30° latitude. This result agrees with Chaidez et al. (2017) and Karnauskas and Jones (2018).

Moreover, grid to grid correlation between the annual mean (from 1982 to 2016) from one side and the four different seasons from the other side is used to quantify the similarities between their SST patterns. Autumn, winter and spring mean (from 1982 to 2016) SST patterns are quantitatively close to the annual (from 1982 to 2016) pattern with correlation coefficients of 0.9, 0.87 and 0.86 respectively ($n = 1119$). However, the summer mean (from 1982 to 2016) SST pattern is the quantitatively least close to the annual pattern ($R = 0.71$, $n = 1119$). This result indicates that the mean summer SST pattern significantly differs from the other three seasonal patterns, supporting the previous finding of Karnauskas and Jones (2018), while

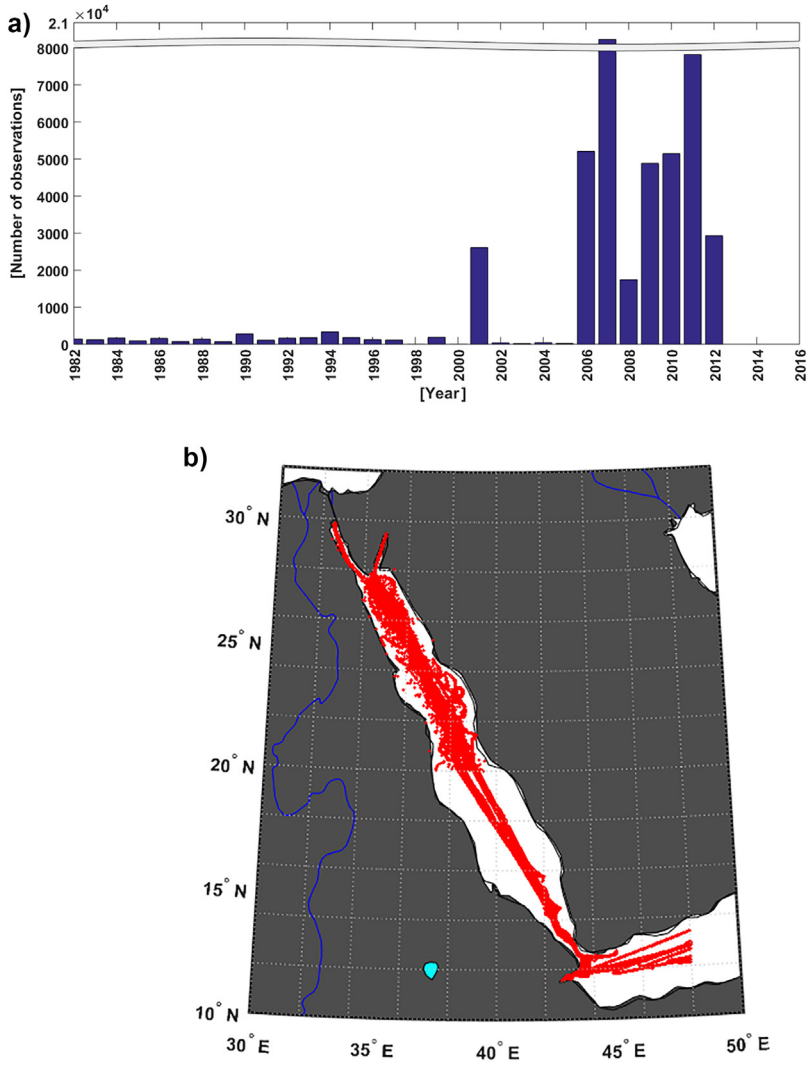

Figure 2 Temporal (a) and spatial (b) distribution of the in situ data. *y*-axis break is used to improve visualization of the plot (a).

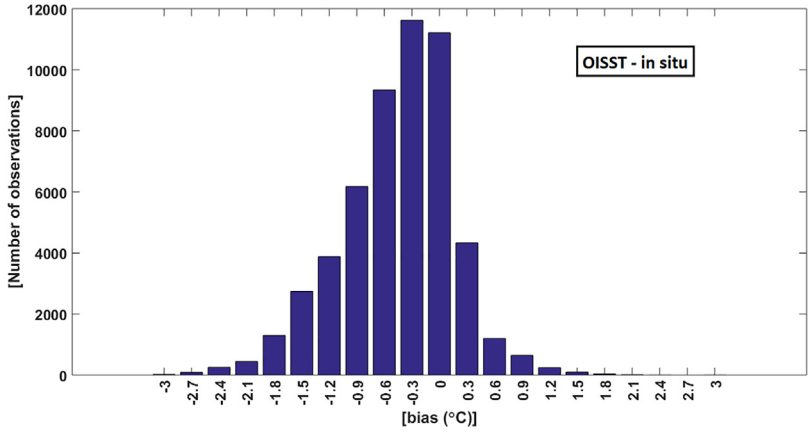

Figure 3 Histogram of the difference between satellite data and in situ data. Positive values represent a warm bias in the OISST data with respect to in situ data.

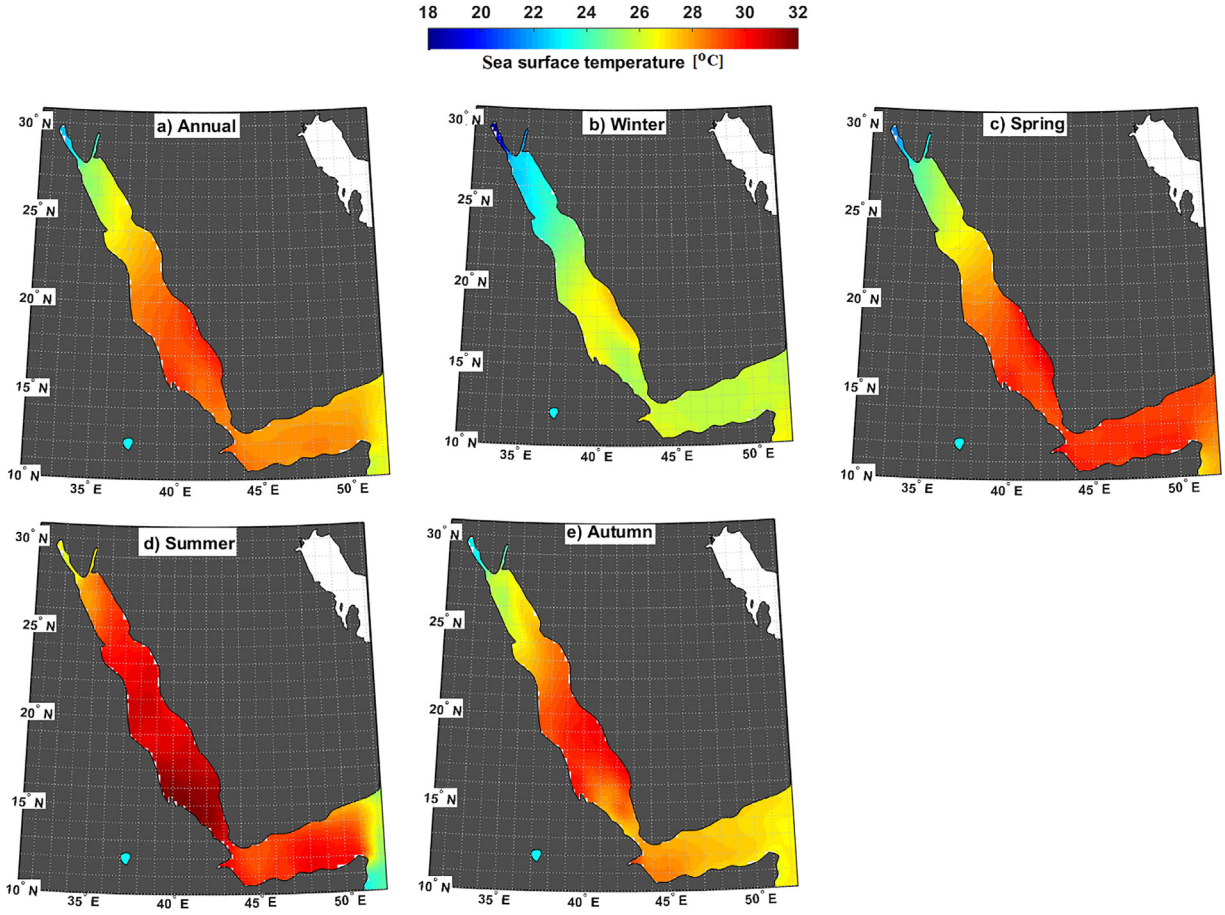

Figure 4 Spatial distribution of the mean annual/seasonal Red+ SST over the period from 1982 to 2016.

improving the analysis from qualitative to quantitative and including autumn/spring seasons.

The spatially annual standard deviation (from 1982 to 2016) based on daily SST ranges from 1.55°C in GOA to 2.42°C in NRed. This gradient of the variability is relatively higher during summer than winter in GOA, SRed, and NRed, whereas in CRed, the variability is relatively higher during winter than summer (Table 1). Although the previous finding of Karnauskas and Jones (2018) showed that the standard deviation is relatively higher in winter than summer, the current research shows that the standard deviation in the Red Sea shows similar values (=0.62°C) during winter and summer. This disagreement with Karnauskas and Jones (2018) is probably because the current research uses daily SST data in the calculation, while Karnauskas and Jones (2018) used monthly SST. In addition, the current research provides more details about the variations between the four Red+ subbasins.

Generally, OISST data show a significant seasonal range of 4.2°C and 5.1°C in the Red+ and the Red Sea, respectively (Table 1). This seasonal range in the Red Sea is less than the value previously calculated by Berman et al. (2003), due to the longer study period in the current research.

Fig. 6 shows that the SST in NRed is colder than in the other three zones. The highest percentages of SST occurrences are 26°C, 30°C, 30°C and 24°C in the Gulf of Aden, SRed, CRed, and NRed, respectively. For the highest SST (>30°C), the percentages of occurrences are 16.3%, 42%, 30% and 7.5% in the Gulf of Aden, SRed, CRed, and NRed, respectively. Although GOA receives much amount of insolation in comparison to SRed and CRed, GOA showed a lower occurrence of the highest SST. This finding indicates a more intensive cooling process resulting from the upwelling process during the Indian summer monsoon that dominates in GOA. On the other hand, for the lowest SST (<24°C), the percentage of occurrences are 0.95%, 0.09%, 2% and 25.8% in the Gulf of Aden, SRed, CRed, and NRed, respectively.

The annual SST warming trends (from 1982 to 2016) in Red+ (Fig. 7 and Table 1) range from 0.034°C yr^{-1} over grids concentrated in NRed to 0.017°C yr^{-1} over grids concentrated in the Gulf of Aden, with average values of 0.025 $\pm$ 0.006°C yr^{-1}. The semi-enclosed nature of NRed is responsible for its intensive warming trend (Belkin and Rapid, 2009); however, the upwelling process and exchange with the Indian Ocean explain the slowed warming in GOA.

The Red Sea warming trend (from 1982 to 2016) is approximately 2.6-times higher than the global ocean warming trend from 1980 to 2005 (=0.011°C yr^{-1}, IPCC (2014)). Cantin et al. (2010) noted that the highest warming trend occurred in CRed, which counters the current finding due to the calculations based on different time scales and the more accurate SST database used in the current research. Moreover, the warming rate of the Red Sea is higher than that previously estimated (=0.017°C yr^{-1}) by Chaidez et al. (2017), because the current study uses the average daily temperature in trend

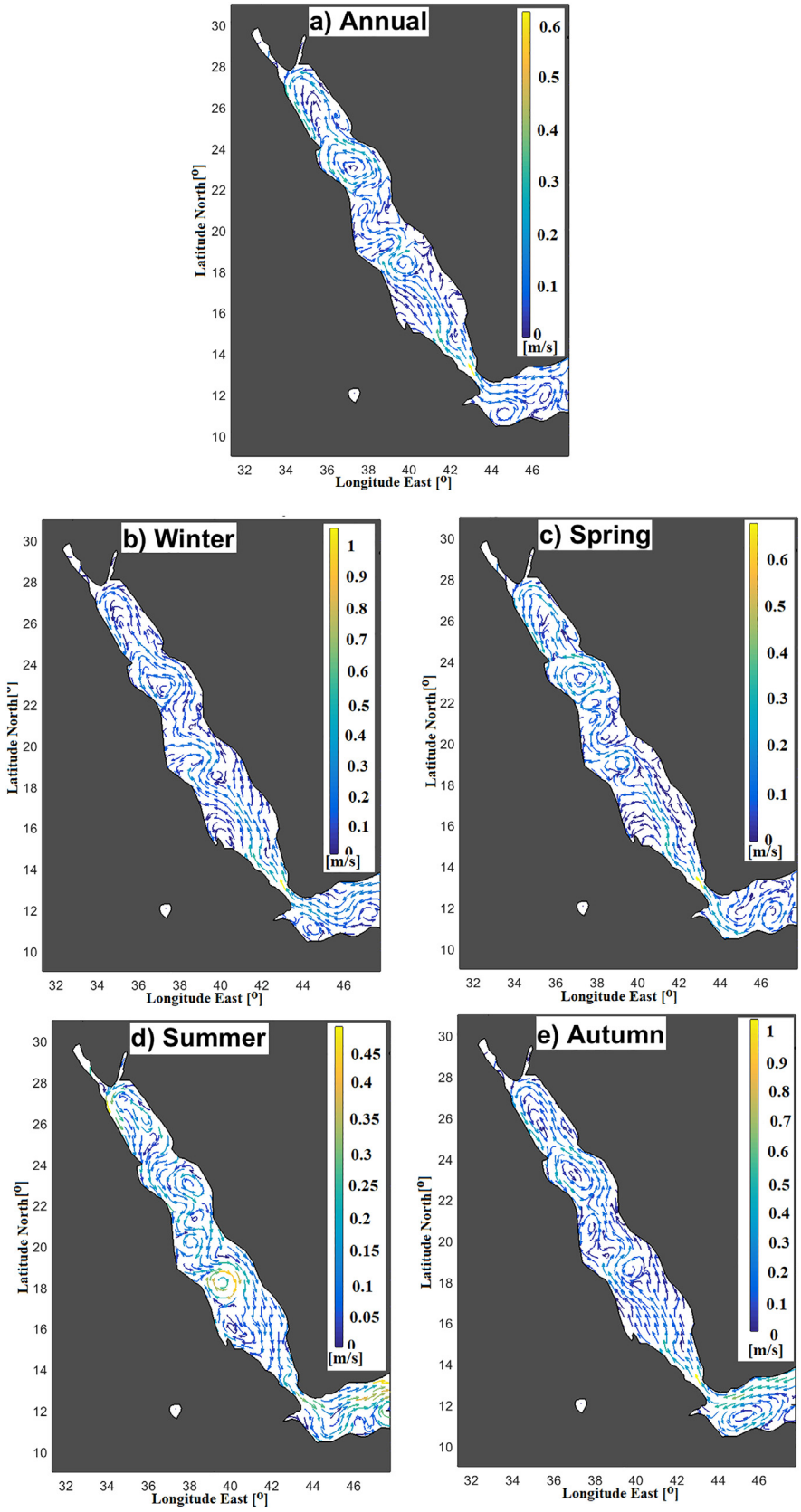

Figure 5 Annual/seasonal surface Red+ current over the 1993–2016 period, calculated from the HYCOM database output for the 2007–2016 period.

Table 1 Daily sea surface temperature characteristics (mean, minimum, maximum and trend) in the studied subbasins from 1982 to 2016 (the linear trends were tested using a t-test at a 99% significance level for significance). Light gray rows indicate summer, while dark gray rows denote the winter season. All the calculations used daily OISST daily data.

	Red+	GOA	Red Sea	SRed	CRed	NRed
Spatially mean (from 1982 to 2016) ± standard deviation [°C]						
Annual	27.84 ± 1.78	27.78 ± 1.55	27.88 ± 2.14	29.03 ± 2.13	28.43 ± 2.02	26.06 ± 2.42
Winter	25.44 ± 0.52	25.93 ± 0.69	25.11 ± 0.62	26.26 ± 0.61	25.80 ± 0.78	23.15 ± 0.79
Spring	28.35 ± 1.12	29.21 ± 1.04	27.78 ± 1.27	29.44 ± 1.25	28.22 ± 1.21	25.52 ± 1.51
Summer	29.62 ± 0.49	28.63 ± 0.74	30.28 ± 0.62	31.26 ± 0.65	30.53 ± 0.69	28.95 ± 0.85
Autumn	27.91 ± 1.31	27.35 ± 1.09	28.29 ± 1.51	29.13 ± 1.73	29.12 ± 1.41	26.55 ± 1.54
Minimum of spatially mean [°C] (year)						
Annual	27.27 (1984)	27.05 (1984)	27.25 (1992)	28.42 (1984)	27.68 (1992)	25.16 (1983)
Winter	24.72 (1992)	25.03 (1984)	24.00 (1992)	25.39 (1992)	24.39 (1992)	22.08 (1992)
Spring	27.64 (1982)	28.63 (1984)	26.93 (1982)	28.65 (1982)	27.21 (1982)	24.67 (1983)
Summer	28.87 (1984)	27.47 (1984)	29.44 (1991)	30.38 (1984)	29.63 (1991)	27.87 (1983)
Autumn	27.29 (1984)	26.53 (1984)	27.65 (1985)	28.23 (1991)	28.43 (1985)	25.83 (1993)
Maximum of spatially mean [°C] (year)						
Annual	28.47 (2010)	28.29 (2015)	28.59 (2010)	29.64 (2016)	29.06 (2016)	27.20 (2010)
Winter	26.16 (2016)	26.78 (2016)	25.96 (2010)	27.20 (2016)	26.74 (1999)	24.66 (2010)
Spring	29.20 (2016)	30.07 (2010)	28.86 (2016)	30.18 (2016)	29.40 (2016)	26.86 (2016)
Summer	30.17 (2001)	29.55 (2015)	31.01 (2001)	32.04 (2001)	31.39 (2001)	29.72 (2012)
Autumn	28.66 (2010)	28.32 (2015)	29.25 (2010)	30.05 (2015)	30.05 (2010)	28.12 (2010)
Spatially trend (from 1982 to 2016) [°C yr^{-1}]						
Annual	0.025	0.017	0.029	0.026	0.028	0.034
Winter	0.021	0.012	0.027	0.022	0.032	0.027
Spring	0.022	0.014	0.027	0.022	0.027	0.034
Summer	0.020	0.014	0.024	0.021	0.018	0.034
Autumn	0.025	0.026	0.024	0.025	0.020	0.026

calculations, while Chaidez et al. (2017) used the maximum daily temperature in trend calculations. The Red Sea spatially annual warming trend is not uniform throughout the study period, ranging from 0.056°C yr^{-1} in the 2005–2016 period, to 0.051°C yr^{-1} in the 1994–2005 period and to 0.040°C yr^{-1} in the 1982–1993 period, indicating that the warming trends have become more intense over time in the Red Sea.

There is a significant seasonal average warming trend (from 1982 to 2016) in Red+, ranging from 0.025°C yr^{-1} during autumn to 0.020°C yr^{-1} during summer. The annual warming trend (from 1982 to 2016) in NRed is concentrated during spring and summer. However, the annual warming trend dominated during winter in CRed and during autumn in GOA/SRed. The Gulf of Aden's warming trend is less significant than SRed's warming trend over the entire year, except during autumn; the Gulf of Aden's warming trend is more intensive than that in SRed. Moreover, the warming trend in the Gulf of Aqaba is more intensive than that in the Gulf of Suez, indicating that the SST difference between the two Gulfs may increase in the future.

3.3. Variability of Red Sea surface temperature

The Fourier analysis of 35 years of daily Red+ SST indicates that the annual SST cycle is the most significant. There is an obvious SST seasonality variation (Fig. 8) ranging from its maximum amplitude (5°C) in the Gulf of Suez to its minimum amplitude (less than 2°C) in the Gulf of Aden together with the zone that extends from 17° latitude to 21° latitude. The SST seasonality is much higher in northern Bab el-Mandeb Strait in comparison to the southern part, partly due to the moderate SST effect in the Gulf of Aden. Moreover, SST seasonality is much higher in the Gulf of Suez in comparison to the same latitude in the Gulf of Aqaba, where the Gulf of Aqaba has a similar SST seasonality (approximately 3°C) as the northern part of NRed.

The seasonality of the Red+ SST phase lag displays a mix of zonal/meridional variation ranging from its minimum value (nearly −110 days) in the GOA to its maximum (nearly −150 days) value off Al Lith (lies along the Saudi Arabian Red Sea coast at approximately 20° latitude). This finding indicates that the seasons begin earlier in GOA where the maximum SST occurred around July 20th, while the seasons come later off Al Lith where the maximum SST occurred around August 29th (i.e., there is an obvious seasonal shift in Red+ by approximately 40 days). The current analysis supports the previous finding of Chaidez et al. (2017), who stated that the maximum time delay for the maximum SST in the Red Sea occurred off the Al Lith coast from mid-August to early September using normal analysis of daily maximum SST.

The phase lag distribution of the annual SST signal exhibits a zonal pattern in GOA, followed by a meridional pattern in SRed until 18° latitude. This finding can be explained by the surface current system (Fig. 5). From 18° to 28° latitude, the phase lag of the annual SST signal distribution decreases zonally from east (−150 days) to west (−140 days) following the cyclonic gyre system in the study area.

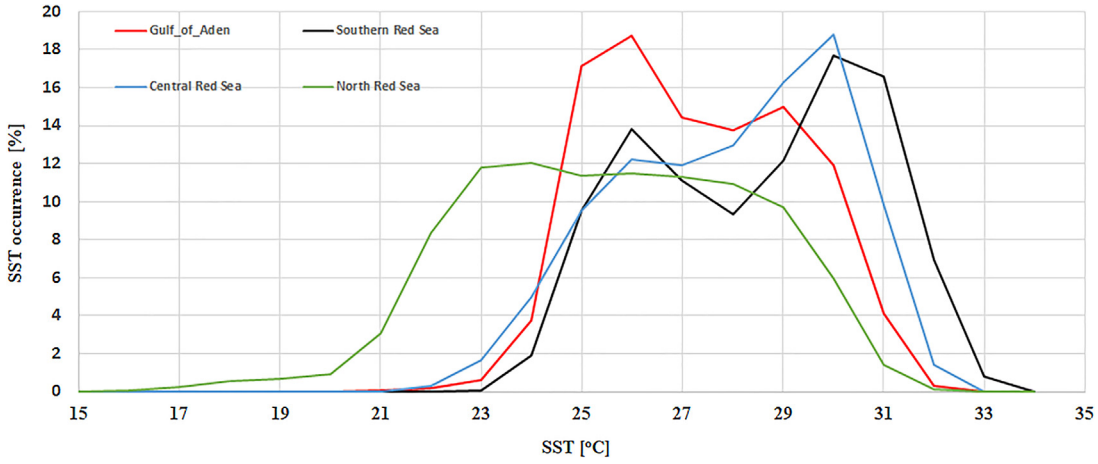

Figure 6 Occurrence percentage of the sea surface temperature in the four studied subbasins over the period from 1982 to 2016.

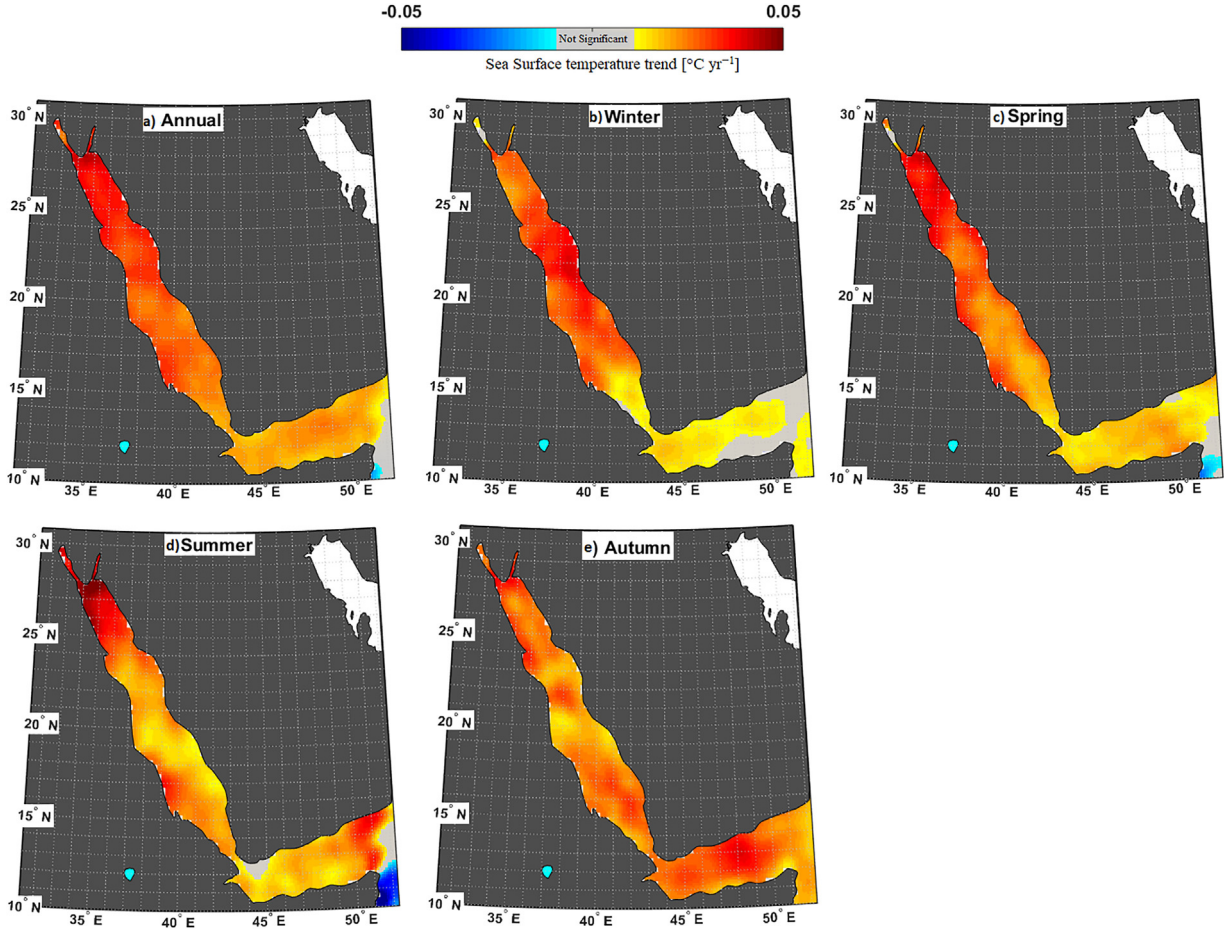

Figure 7 Spatial distribution of the annual/seasonal Red+ SST trends over the period from 1982 to 2016.

3.4. Correlation between the ten studied atmospheric parameters and the Red Sea surface temperature

Previous studies suggest that the ten studied atmospheric parameters have relationships with SST. The features of these relationships in Red+ were evaluated using correlation coefficients to provide insightful information about different atmospheric phenomena that are associated with changing SST. For example, these relationships should be considered for designing a simple model of Red+.

In general, the Red+ SST is negatively correlated with SLP, F_n, and NAOI. The Red+ SST, however, is positively correlated with T_{2m}, Fsw, AMOI, and ISMI. In addition, TCC, τ_{ac}, and τ_{al}

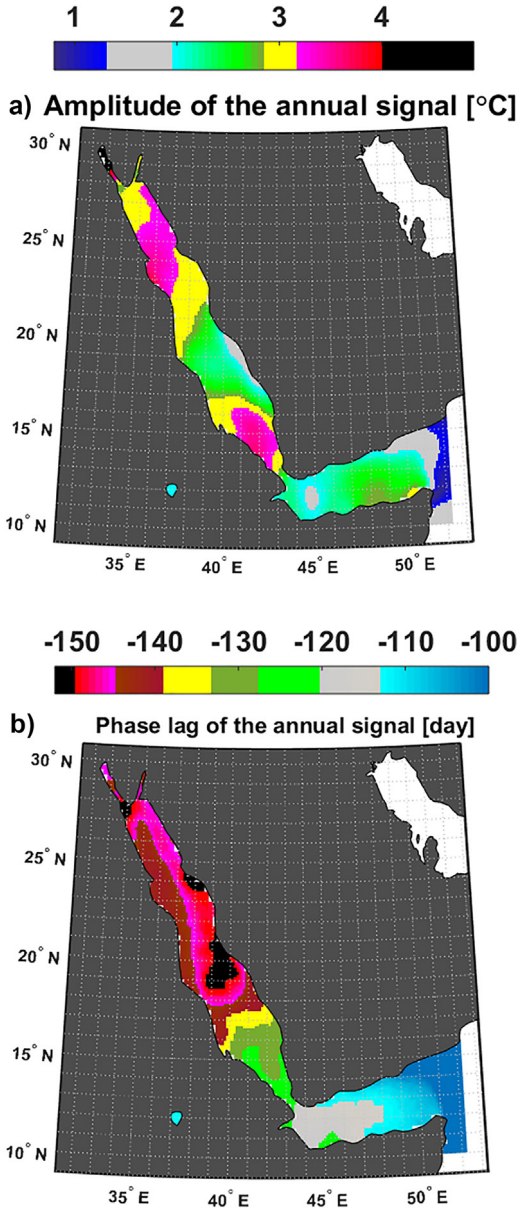

Figure 8 Spatial distribution of the amplitude (a) and phase lag (b) of the annual Red+ SST signal over the period from 1982 to 2016.

have spatially varying correlations, either positive or negative (Fig. 9).

The monthly correlation coefficient (R) between SLP and SST in Red+ has an average value of −0.75 (n = 420), with a markedly low value in CRed. There is a significant seasonal variation in the correlation between SST and SLP, ranging from the maximum values (R = −0.89, n = 105) during autumn to the minimum values (R = 0.14, n = 105) during summer. Only during summer does the monthly correlation between SLP and SST exhibit a significant positive correlation in 30% of Red+, most markedly off Al Lith and to the north and south of Bab el-Mandeb Strait (data are not shown). This significant positive correlation indicates that the processes controlling the relationship between SST and SLP (e.g., atmospheric stability and circulation and thermal conditions) are quite different in summer than in the other seasons. You et al. (2017) stated that SST could exhibit a positive correlation with SLP in a season under considerable conditions (e.g., during the winter season in the Tibetan Plateau).

Monthly correlation analysis between SST and TCC shows three patterns in Red+; the first pattern is at 22° latitude and has a strong negative correlation; the second pattern is from 12° to 16° latitude and has a strong positive correlation, and the third pattern is concentrated in CRed and GOA where the correlation is not significant. The negative correlation suggests that the cloud cover affects SST with negative radiative forcing; however, the positive correlation suggests that SST has a significant effect on day-to-day cloud formation and no significant impact on the radiation balance. The correlation between SST and TCC reaches its maximum value during the autumn season.

The monthly correlation coefficient between SST and τ_{ac} generally shows a strong positive correlation in NRed, CRed and GOA, while the correlation shows a strong negative relationship in the southern part of the Red Sea (northern and southern Bab el-Mandeb Strait). There is no significant correlation between SST and τ_{ac} in the borders between areas of negative and positive correlation.

The monthly correlation coefficient between SST and τ_{al} generally shows a strong positive correlation in SRed and in GOA related to the monsoonal forcing of a long-basin wind in SRed, while the correlation shows a moderate negative correlation in NRed. There is no significant correlation between SST and τ_{al} in CRed. These positive and negative correlations occurred when the surface current moves parallel to the coastline toward the north or the Indian Ocean, respectively, as seen in Fig. 5. It can be concluded that the wind direction drives the correlation between SST and τ_{ac}/τ_{al} to be positive or negative.

Direct correlation analysis between SST and wind speed was then carried out to show the relationship between SST and wind speed (Fig. 10). In general, SST and wind speed are negatively correlated (R = −0.47, n = 420), which supports the previous finding of Qu et al. (2012). This result is explained by the fact that increasing wind speed affects seawater stratification and raises subsurface water. Moreover, Wang et al. (1999) showed that increases in surface wind speed are associated with more evaporation and a surface cooling process, which leads to an additional increase in surface wind speed and vice versa (i.e., there is a feedback system between surface wind, evaporation, and SST). The correlation between SST and wind speed shows a strong seasonal variation ranging from R = −0.6 (n = 105) during autumn, to R = −0.5 (n = 105) during winter and finally to a very low value with no significant correlation during summer and spring, indicating that the difference between SST and T_{2m} plays a significant role in this seasonal variation between SST and wind speed. The significant negative correlation between SST and wind speed during cold seasons supports the previous findings of Samelson et al. (2006). Moreover, Samelson et al. (2006) indicate that during warm seasons, the correlation between SST and wind speed shows a strong positive correlation. This result runs counter to the current finding such that correlation between SST and wind speed is not significant during warm seasons, due to the low wind speed characteristics in the study area during warm seasons.

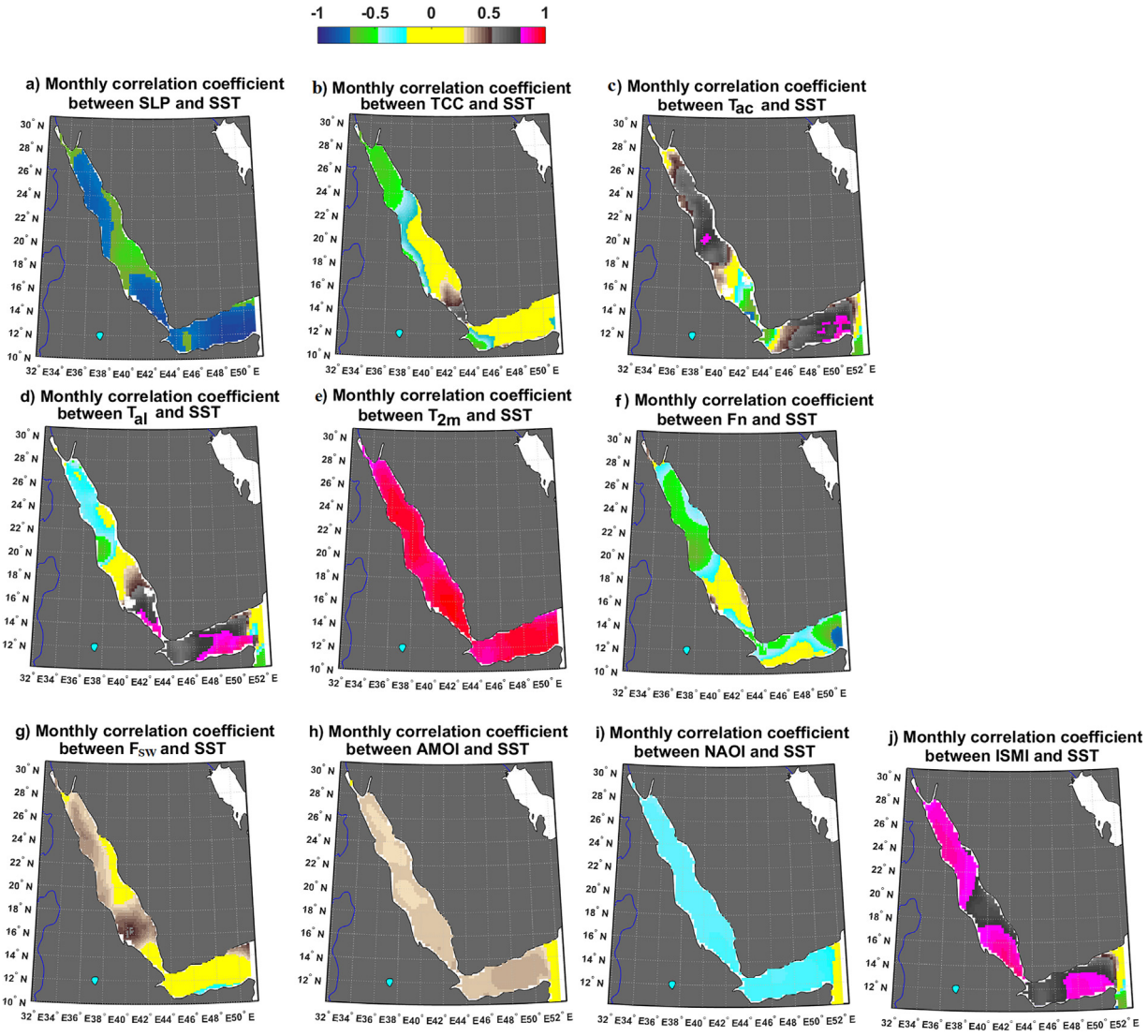

Figure 9 Monthly correlation coefficients between the ten studied atmospheric parameters and the Red Sea surface temperature. Yellow indicates no significant correlation. (For interpretation of the references to color in this figure legend, the reader is referred to the web version of this article.)

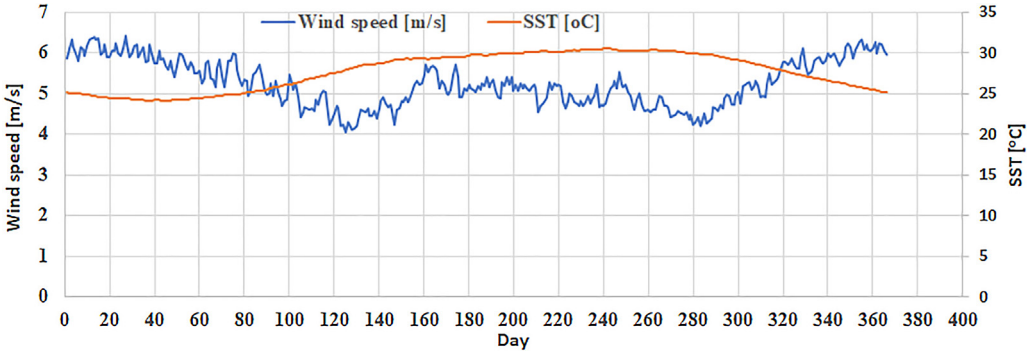

Figure 10 Average daily means of sea surface temperature (SST) and surface wind speed in Red+ over the period from 1982 to 2016.

Table 2a Principal component analysis for the entire study region (Red+) based on the correlation matrix before removing the seasonal cycle. Bold numbers refer to highly significant correlations over 0.30.

Variables	Principal component				
	1	2	3	4	5
Sea surface temperature (SST)	**−0.334**	0.120	0.107	0.160	**0.337**
Mean sea level pressure (SLP)	**0.379**	−0.065	−0.054	0.066	0.059
Air temperature at 2 m above sea level (T_{2m})	**−0.382**	0.079	0.061	0.069	0.193
Total cloud cover (TCC)	−0.014	**0.327**	**−0.511**	−0.233	**−0.569**
Along-coast wind stress (τ_{al})	0.168	**−0.312**	**−0.418**	0.221	0.409
Cross-coast wind stress (τ_{ac})	**0.347**	−0.117	0.057	0.031	−0.031
Latent heat flux (F_e)	0.188	**0.569**	0.187	0.074	0.093
Net longwave radiation (F_l)	0.147	−0.261	**0.567**	0.050	−0.210
Sensible heat flux (F_h)	**0.364**	0.043	0.074	0.029	−0.013
Net heat loss from the sea ($F_n = F_h + F_e + F_l$)	0.266	**0.439**	0.288	0.079	0.034
Solar radiation to the open water surface (Fsw)	0.260	0.313	−0.290	0.179	**0.366**
North Atlantic Oscillation Index (NAOI)	0.106	−0.008	0.069	**−0.902**	**0.396**
Indian Summer Monsoon Index (ISMI)	**−0.332**	0.269	0.095	0.002	0.091

Table 2b Principal component analysis for the entire study region (Red+) based on the correlation matrix after removing the seasonal cycle. Bold numbers refer to highly significant correlations over 0.30.

Variables	Principal component							
	1	2	3	4	5	6	7	8
Sea surface temperature (SST)	0.16	**−0.35**	0.07	**0.50**	−0.03	**−0.43**	−0.11	**0.33**
Mean sea level pressure (SLP)	−0.14	−0.27	**0.45**	0.04	−0.11	0.10	**0.74**	0.02
Air temperature at 2 m above sea level (T_{2m})	**0.41**	−0.04	−0.23	**0.33**	0.03	**−0.36**	0.08	−0.27
Total cloud cover (TCC)	−0.10	**0.43**	0.26	0.22	−0.05	−0.19	−0.18	−0.02
Along-coast wind stress (τ_{al})	**0.39**	0.08	0.09	0.10	−0.05	−0.07	**0.36**	0.08
Cross-coast wind stress (τ_{ac})	−0.12	**−0.37**	**0.38**	0.07	−0.03	−0.06	−0.22	**−0.73**
Latent heat flux (F_e)	**−0.46**	0.10	−0.29	0.23	0.01	−0.16	0.16	−0.19
Net longwave radiation (F_l)	−0.04	**−0.43**	**−0.46**	−0.07	0.03	0.10	0.14	0.12
Sensible heat flux (F_h)	**−0.34**	−0.28	0.29	0.09	−0.04	−0.05	**−0.31**	**0.47**
Net heat loss from the sea ($F_n = F_h + F_e + F_l$)	**−0.48**	−0.05	**−0.33**	0.21	0.01	−0.13	0.14	−0.08
Solar radiation to the open water surface (Fsw)	−0.19	**0.44**	0.13	0.23	−0.07	−0.11	0.22	0.08
North Atlantic Oscillation Index (NAOI)	−0.09	−0.01	0.09	**−0.57**	**0.39**	**−0.70**	0.12	0.04
Indian Summer Monsoon Index (ISMI)	0.01	0.01	0.11	**0.30**	**0.90**	**0.28**	0.03	0.01

There is a strong monthly correlation between SST and T_{2m} in Red+ ($R = 0.92$, $n = 420$), and this correlation ranges from $R = 0.94$ ($n = 105$) during autumn, to $R = 0.91$ ($n = 105$) during spring, to $R = 0.67$ ($n = 105$) during winter and to $R = 0.44$ ($n = 105$) during summer. T_{2m} shows a higher value than SST over the entire year by approximately 0.51°C. This difference shows a significant seasonal variation, where T_{2m} is warmer than SST during summer (1.40°C) and spring (0.94°C) and colder than SST during autumn (0.88°C) and winter (0.87°C). This result can explain the previous finding such that the correlation between wind speed and SST has a significant seasonal variation (during the cold seasons when SST is warmer than T_{2m}, wind speed is inversely proportional to SST, while in the warm seasons when SST is cooler than T_{2m}, wind speed is not significantly proportional to SST).

The monthly net heat loss from the sea (F_n) correlates negatively with the monthly SST ($R = -0.32$, $n = 420$) most markedly in NRed and during winter. However, the monthly solar radiation to the open water surface (Fsw) correlates positively with SST especially between 16°N and 18°N during autumn. Although ERA-Interim used the Monin–Obukhov formulation, which includes SST as an input variable to forecast air-sea heat fluxes, the current analysis used these data set to assess the relative role of air-sea heat fluxes to SST changes in Red+. This procedure followed the previous analysis of He et al. (2017) who studied the correlation between Re-Analysis (ERA-40) and SST in tropical oceans.

The influence of monthly climate indices (AMOI, NAOI, and ISMI) on monthly SST was analyzed spatially (Fig. 9) and temporally. ISMI shows the strongest effect on SST ($R = 0.71$, $n = 420$) compared with the effects of NAOI ($R = -0.33$, $n = 420$) and AMOI ($R = 0.31$, $n = 408$). There is a significant seasonal correlation between SST and NAOI/ISMI peaks in autumn; however, there is no significant seasonal correlation between SST and AMOI.

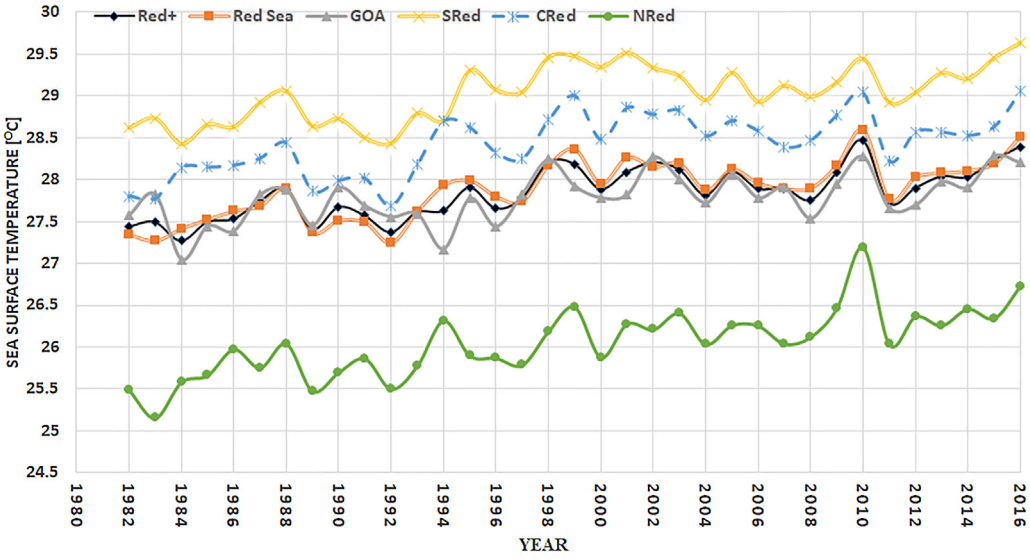

Figure 11 Annual sea surface time series for the studied subbasins. GOA, Gulf of Aden; SRed, Southern Red Sea; CRed, Central Red Sea; NRed, Northern Red Sea; Red+, Red Sea + Gulf of Aden.

With 13 daily variables (SST, T_{2m}, SLP, TCC, τ_{ac}, τ_{al}, F_e, F_l, F_h, F_n, Fsw, NAOI and ISMI) from 1982 to 2016, principal component analysis (PCA) is a meaningful tool to interpret the linear combination between them. PCA reduces the number of variables to a few principal components (Table 2).

PCA shows that only five principal components (PCs) account for 90% of the studied parameter variance in Red+ before removing the seasonal cycle. Their percentages of variance are 48%, 16%, 12%, 8% and 6%. The first PC shows a strong correlation with six of the studied variables. This first PC decreases with SST, T_{2m}, and ISMI but increases with SLP, τ_{ac}, and F_h, indicating that these six variables are highly correlated. The second PC shows a strong correlation with four of the studied variables (increasing with TCC, F_e, and F_n while decreasing with τ_{al}), which similarly indicates that TCC, F_e, F_n, and τ_{al} vary together. The third principal component can be considered a measure of TCC, τ_{al}, and F_l. The fourth principal component, which is responsible for 8% of the overall change in variance in Red+, can be considered a measure of NAOI; additionally, the fifth principal component can be considered a measure of SST, TCC, τ_{al}, Fsw and NAOI, as described in Table 2a.

After removing the seasonal cycle, PCA shows that eight PCs account for 90% of the variance in Red+, and this result is shown in Table 2b. The Fourier analysis technique was used to remove the seasonal cycle.

3.5. Sea surface temperature characteristics in different Red+ subbasins

The spatially annual mean SST (from 1982 to 2016) in Red+ ranges from its maximum value of 29.03 ± 2.13°C in SRed, followed by 28.43 ± 2.02°C in CRed, 27.78 ± 1.55°C in GOA, and 26.06 ± 2.42°C in NRed (Fig. 11 and Table 1). The maximum of spatially annual mean SST in the Red Sea (=28.59°C) occurred during 2010. This finding can be explained by NAOI. In 2010, NAOI showed a dramatic decrease in its positive phase within the studied period. NRed, which is highly correlated to NAOI in comparison to the other studied subbasins, exhibited a 0.72°C increase (1.9 times the Red+ increase) from 2009 to 2010; it was followed by a 1.16°C decrease (1.6 times the Red+ decrease) from 2010 to 2011. On the other hand, the minimum of spatially annual mean SST in the Red Sea (=27.25°C) occurred during 1992 (most notably in CRed). This result agrees with the previous finding of Raitsos et al. (2011), who showed that 1992 was the coldest year for the Red Sea. A comparison between the hottest and coldest years in the Red Sea indicates that the range of the spatially annual mean temperature during the study period is only 1.34°C.

The SST time series analysis of the studied subbasins displays a spatially annual positive trend with varying significance from north to south, in detail, ranging from 0.034°C yr^{-1} in NRed to 0.017°C yr^{-1} in GOA. There is a significant seasonal variation in the spatially seasonal warming trend ranging from 0.027°C yr^{-1} during winter to 0.024°C yr^{-1} during summer and autumn.

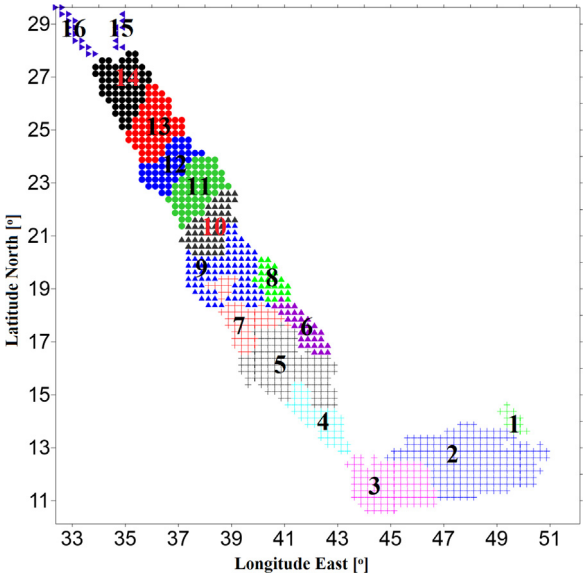

Figure 12 Spatial clustering of SST data (1982–2016) for Red+.

Table 3 Heat wave characteristics. The relationship between heat waves and chl-a concentrations is also shown (NA indicates low-quality calculations of chl-a concentrations in the area).

Cluster number	1982–2016			2003–2016	
	heat wave days [%]	Most pronounced heat wave events	Minimum heat wave temperature [°C]	Average chl-a concentration [mg/m^3] during	
				the entire year	heat wave events
1	0.23	7 days (12/06/1988 to 18/06/1988)	31.46	0.57	0.16
2	0.23	5 days (12/06/1988 to 16/06/1988)	31.98	0.92	0.37
3	0.17	5 days (27/05/2005 to 31/05/2005)	31.94	0.84	0.17
4	0.25	5 days (24/09/1995 to 28/09/1995) (16/09/1998 to 20/09/1998)	33.11		NA
5	0.13	7 days (13/08/2001 to 19/08/2001)	33.20	No heat wave events occurred from 2003–2016	
6	0.31	9 days (7/10/2001 to 15/10/2001)	32.79		NA
7	0.19	6 days (6/10/2002 to 11/10/2002)	32.65	No heat wave events occurred from 2003–2016	
8	0.31	7 days (27/10/2002 to 02/11/2002)	32.51	0.64	0.18
9	0.22	4 days (14/10/2002 to 17/10/2002)	32.36	No heat wave events occurred from 2003–2016	
10	0.34	11 days (03/08/1998 to 13/08/1998)	32.46		NA
11	0.39	14 days (14/07/2001 to 27/07/2001)	32.14	0.21	0.11
12	0.38	13 days (15/07/2001 to 27/07/2001)	31.82	0.16	0.13
13	0.31	11 days (25/08/2003 to 04/09/2003)	31.31	0.16	0.09
14	0.40	10 days (24/07/2007 to 02/08/2007) (18/09/2015 to 27/09/2015)	30.43	0.17	0.12
15	0.50	18 days (29/07/2012 to 15/08/2012)	29.02	0.30	0.14
16	0.42	9 days (22/08/1995 to 30/08/1995) (26/07/2007 to 03/08/2007)	28.07	0.35	0.20

Moreover, a cross-correlation among the 4 subbasins annual time series was used to quantify the similarities between different subbasins. The spatially annual SST variation in GOA is relatively different than those in SRed ($R = 0.56$, $n = 35$) and CRed ($R = 0.55$, $n = 35$). Moreover, the spatially annual SST variation in CRed is much closer to the SRed pattern ($R = 0.86$, $n = 35$) than to NRed ($R = 0.73$, $n = 35$). In general, the spatially annual SST variation in the Red Sea is much closer to the CRed spatially annual SST pattern ($R = 0.98$, $n = 35$).

3.6. Heat waves and chlorophyll-*a*

To understand the Red+ heat waves, cluster analysis was conducted to divide Red+ into 16 clusters (Fig. 12). Each cluster contains a number of grids that have a correlation over 0.95 between themselves and a range of 0.4°C together with minimum distance (clustering was performed using daily SST for the entire data series). The cluster regime runs generally from east to west across the Gulf of Aden and runs from south to north in the Red Sea.

Heat waves were considered at least three days with hot SST. A day was considered a hot day with an SST equal to or higher than two standard deviations plus the mean SST of the hottest month within each cluster. This method indicates that the heat wave minimum temperature varies from one cluster to another (Table 3) and ranges from 33.2°C in cluster 5 to 28.07°C in cluster 16 (the Gulf of Suez). Red+ experiences heat waves for approximately 0.30% of the year, most pronounced in cluster 15 (the Gulf of Aqaba) and least pronounced in cluster 5. The most pronounced Red+ heat waves events occurred for

Table 4 Performance of various GFDL simulations (CM3, ESM2M and ESM2G) in the Red Sea during the control period (2006–2016). GFDL model ensemble mean = ensemble mean of all 3 GFDL simulations. The shaded column shows the best performing simulation.

Simulation	Scenario	Subbasin	Annual (Tos-SST)	Simulation	Scenario	Subbasin	Annual (Tos-SST)
GFDL-CM3		Red+	0.30			Red+	−0.72
	RCP2.6	Red	0.55		RCP2.6	Red	−0.67
		GOA	−0.23			GOA	−0.82
		Red+	0.25			Red+	−0.81
	RCP4.5	Red	0.53		RCP4.5	Red	−0.77
		GOA	−0.34			GOA	−0.90
		Red+	0.05	GFDL-ESM2M		Red+	−0.86
	RCP6.0	Red	0.31		RCP6.0	Red	−0.80
		GOA	−0.49			GOA	−0.98
		Red+	0.16			Red+	−0.93
	RCP8.5	Red	0.43		RCP8.5	Red	−0.90
		GOA	−0.40			GOA	−0.99
GFDL-ESM2G		Red+	−1.22			Red+	−0.53
	RCP2.6	Red	−1.34		RCP2.6	Red	−0.49
		GOA	−0.90			GOA	−0.61
		Red+	−1.25			Red+	−0.59
	RCP4.5	Red	−1.36		RCP4.5	Red	−0.54
		GOA	−0.94			GOA	−0.68
		Red+	−1.21	GFDL model-ensemble mean		Red+	−0.66
	RCP6.0	Red	−1.30		RCP6.0	Red	−0.61
		GOA	−0.94			GOA	−0.75
		Red+	−1.32			Red+	−0.68
	RCP8.5	Red	−1.43		RCP8.5	Red	−0.64
		GOA	−1.00			GOA	−0.75

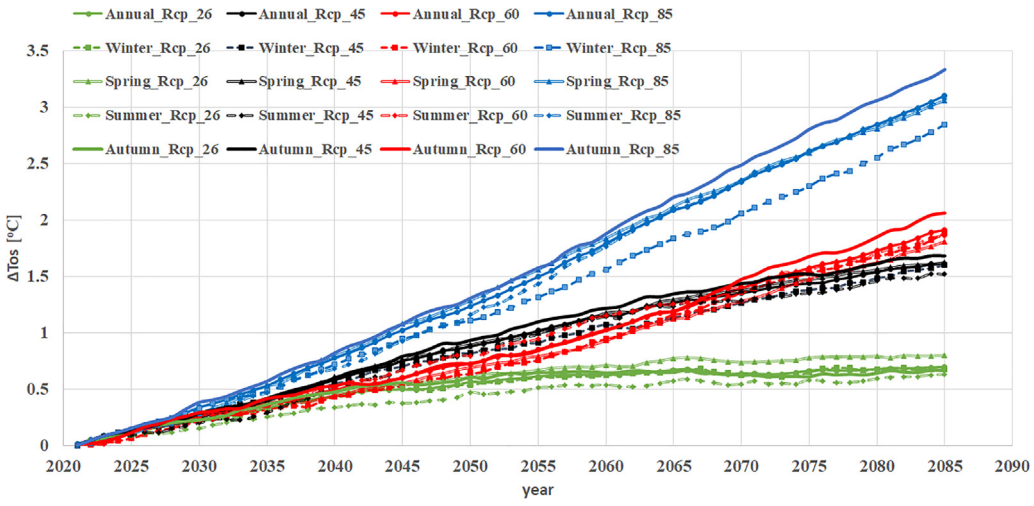

Figure 13 Thirty-year running annual means of projected sea surface temperatures (Tos) under the four representative concentration pathway scenarios studied (RCP2.6, RCP4.5, RCP6.0, and RCP8.5) relative to the 2006–2035 period for the GFDL-CM3 model simulation in Red+.

18 days (29/07/2012 to 15/08/2012) in the Gulf of Aqaba and for 14 days (14/07/2001 to 27/07/2001) in cluster 11.

Heatwave events have a negative effect on chlorophyll-*a* concentrations (as an indicator of bleaching) as described by Caputi et al. (2014). It is clear from Table 3 that the chl-a concentrations reached a minimum during heat wave events, indicating that the heat wave events have a negative effect on marine biota and may lead to thermal collapse, especially because the Red Sea is a semi-enclosed basin (marine biota cannot migrate north). This result is in accordance with the previous findings of Maor-Landaw et al. (2014) and Chaidez et al. (2017).

3.7. Projected sea surface temperature (Tos) scenario calculations

3.7.1. Model performance under the control period, 2006–2016

GFDL exhibits relatively good skills in modeling Tos in some regions including the eastern Bering Sea, Gulf of Alaska and Insular Pacific Islands–Hawaii (Hervieux et al., 2017; Stock et al., 2011). However, this model has shown relatively lower abilities in other regions (e.g., California Current System; Jacox et al., 2017). Thus, the current analysis assessed three GFDL simulations (GFDL-ESM2M, GFDL-ESM2G, and GFDL-CM3) against OISST prior to use in the analysis of the projected warming scenario in Red+.

Table 4 shows the performance of three GFDL simulations under the RCP2.6, RCP4.5, RCP6.0 and RCP8.5 scenarios for three studied subbasins (the Red Sea, Red+ and GOA). The GFDL model ensemble mean of simulation was calculated for each scenario. To determine whether the simulation results overestimate or underestimate SST, the result was subjected to a *t*-test with 95% significance.

GFDL-CM3 simulations overestimate SST by approximately 0.30, 0.25, 0.05 and 0.16°C in Red+ under the RCP2.6, RCP4.5, RCP6.0 and RCP8.5 scenarios, respectively (Table 4). The GFDL-ESM2M, GFDL-ESM2G and GFDL model ensemble mean simulations show underestimations of SST in Red+ by approximately 1.22, 0.72 and 0.53°C, respectively, under the RCP2.6 scenario.

In general, the GFDL-CM3 simulation results best describe SST during the control period in comparison to the other studied simulations. This finding indicates that the upgrade from the old GFDL simulations to the most recent simulation (GFDL-CM3) improves the result significantly.

3.7.2. Future sea surface temperature, 2006–2100

The GFDL-CM3 simulation of projected SST scenarios in the current century indicates significant warming during the 2006–2100 period in the study area, especially for the RCP8.5 scenario (Fig. 13). The expected warming up to 2100 (hereafter $\Delta Tos = Tos_{2100} - Tos_{2006}$) ranges from 2.8–3.2°C under the RCP8.5 scenario, 1.75–2.1°C under the RCP6.0 scenario, 1.5–1.7°C under the RCP4.5 scenario and 0.6–0.85°C under the RCP2.6 scenario.

There is no significant regional variation in projected warming trends under the GFDL-CM3 simulation (data are not shown). However, there is a significant seasonal variation in projected warming trends, reaching the minimum values during the winter seasons under the RCP2.6, RCP6.0 and RCP8.5 scenarios and during summer during RCP4.5. The maximum values of the seasonal warming trend occurred during the spring season for RCP2.6 and during the autumn season for the RCP4.5, RCP6.0 and RCP8.5 scenarios.

The current research related the uncertainty in projected Tos to only two sources: the seasonal variations and the scenario used. The uncertainty associated with the region was not significant, while the uncertainty related to the simulation used was negligible as the research used only the best simulation that described the current SST. Uncertainties in projected ΔTos were estimated to be 2.6°C, where the scenario used and the seasonal variations account for 2.45°C and 0.25°C, respectively. Hoegh-Guldberg et al. (2014) showed that the uncertainties in projected ΔTos according to the scenario used is 2.57°C. Both of current and previous findings confirm that the emission assumptions dominating the uncertainties of different sources.

4. Conclusions

Based on the daily OISST time series, the current research studied the current SST changes in Red+ from 1982 to 2016. Moreover, GFDL model simulations were used to analyze the uncertainty of Red+ warming trends.

The results showed that the gridded OISST data is a relevant tool to study the SST in Red+ due to excellent OISST agreement with in situ data. Moreover, the finer OISST resolution (0.25°) seemed fine enough to analyze local-scale features of Red+. Thus, the current findings constitute a basis for future research seeking to study coastal phenomena such as coastal upwelling occurrence and its influence on SST variability, which is explicitly an updated topic.

The annual mean (from 1982 to 2016) of gridded OISST in Red+ confirms the presence of a 7°C spatial variation ranging from 22.5°C over grids concentrated in the northern part of the Gulf of Suez to 29.5°C over grids concentrated in the eastern part of SRed. The gridded OISST data confirms that the daily Red+ SST seldom falls outside the range of 20°C to 33°C. Moreover, the coldest years were 1984 and 1992 in Red+ and the Red Sea, respectively; however, the hottest year was 2010 in both Red+ and the Red Sea, and that was due to the dramatic drop of NAOI during 2010. In addition, the Red Sea and Red+ confirm a significant spatially warming trend (from 1982 to 2016) of 0.029°C yr^{-1} and 0.025°C yr^{-1}, respectively, peaking over NRed. However, NRed exhibits a more intensive warming trend than GOA and SRed; the SST in NRed remains cooler than in GOA and SRed. Generally, the intensive Red+ warming trend compared to the average global warming trend (0.011°C yr^{-1}) leads to an accelerated increase in the Red+ temperature together with associated increases in seawater acidification and decreases in oxygen level. This combination will duplicate risks to marine ecosystems, biodiversity and fisheries.

The Red+ SST describes a complex SST pattern with significant regional dependence and seasonal fluctuation of Red+ SST and warming trends, which should be considered in the future analysis of Red+. For example, simple modeling of Red+ based on dividing the study area into several subbasins should consider the uniform SST distribution in Red+.

The current research shows that the studied atmospheric parameters (T_{2m}, SLP, TCC, τ_{ac}, τ_{al}, F_n, Fsw, AMOI, NAOI, and ISMI) and SST, in general, are significantly correlated in most of the studied area. There is seasonal variation in the correlation coefficient between nine of the ten studied parameters and SST; however, ISMI shows no significant seasonal variation in the correlation coefficient with SST. Moreover, the influences of the thirteen studied atmospheric parameters on SST suggests that 98% of the daily Red+ SST variation can be explained by only T_{2m}, ISMI, SLP, τ_{ac}, and F_h before removing the annual cycle, while 77% can be explained after removal. In addition, the PCA results showed that the first five principal components can explain 90% of the overall variance before removing the annual cycle, while the first eight principal components can explain 90% of the

overall variance after removing the annual cycle, highlighting the importance of the annual cycle in the correlation between the studied parameters.

As expected, the chl-a concentration during the heat wave events decreased by approximately 33% from its annual average values. In the warm environment of the Red Sea, the temperature is expected to increase in the future (according to the GFDL-CM3 projection results), which would lead to more frequently occurring future heat events. Thus, Red Sea marine organisms are clearly extremely vulnerable to heat wave events, especially because the Red Sea is a semi-enclosed basin, and marine organisms cannot migrate north. This finding highlights the need to develop reasonable mitigation/adaptation tools to cope with the future warming issues during the current century, including the issue of chl-a growth vulnerability.

To support future management in Red+, Tos up to 2100 were described by GFDL-CM3 that best describe the recent Red+ SST. The GFDL-CM3 simulations showed that ΔTos ranges from 3.2°C during autumn under the RCP8.5 scenario to 0.6°C during summer under the RCP2.6 scenario, where the emissions used and seasonal variations account for 90% and 10%, respectively, of the studied uncertainty. This finding indicates that more global management efforts are needed to reduce green gas emissions.

The current results provide a context for descriptive and statistical analyses describing recent and future SST over Red+ in terms of annual and seasonal cycles. In comparison to the previous scientific studies in the region, the current study improves our understanding of SST and the associated phenomena for the period 1982–2100. The current paper gives the first scientific comparison between different studied subbasins to understand spatial SST variations. Moreover, the current paper classifies the Red+ into 16 clusters to match heat wave occurrence with chl-a concentration for each cluster to qualify the thermal effect on marine biota. Moreover, the current research analyses the SST projection over Red+ up to 2100 to understand future warming uncertainty. This result provides a powerful scientific tool to coop with climate change.

Acknowledgements

The author would like to thank Mr. Mohamed Gad at the National Institute of Oceanography and Fisheries, Egypt, for his valuable comments. This research work is part of a research project sponsored by: IDRC-Canada for establishing Alexandria Research Centre for Adaptation to Climate Change (ARCA), Alexandria University, Egypt.

Appendix A. Supplementary data

Supplementary data associated with this article can be found, in the online version, at https://doi.org/10.1016/j.oceano.2019.05.002.

References

Adcroft, A., Hallberg, R., 2006. On methods for solving the oceanic equations of motion in generalized vertical coordinates. Ocean Model. 11, 224–233.

Aiki, H.A., Takahashi, K., Yamagata, T., 2006. The Red Sea outflow regulated by the Indian Monsoon. Cont. Shelf Res. 26, 1448–1468.

Al-Horani, F.A., Al-Rousan, S.A., Al-Zibdeh, M., Khalaf, M.A., 2006. The status of coral reefs on the Jordanian coast of the Gulf of Aqaba, Red Sea. Zool. Middle East 38, 99–110, http://dx.doi.org/10.1080/09397140.2006.10638171.

Anderson, J.L., Balaji, V., Broccoli, A.J., Cooke, W.F., Delworth, T.L., Dixon, K.W., Donner, L.J., Dunne, K.A., Freidenreich, S.M., 2004. The new GFDL global atmosphere and land model AM2-LM2: evaluation with prescribed SST simulations. J. Climatol. 17, 4641–4673, http://dx.doi.org/10.1175/JCLI-3223.1.

Anonymous, 2014. NASA Goddard Space Flight Center, Ocean Ecology Laboratory, Ocean Biology Processing Group: Sea-viewing Wide Field-of-view Sensor (SeaWiFS) Ocean Color Data, NASA OB.DAAC, accessed on 2016/02/29, 10.5067/ORBVIEW-2/SEAWIFS_OC.2014.0.

Bai, Y., He, X., Yu, S., Chen, C., 2018. Changes in the ecological environment of the marginal seas along the Eurasian continent from 2003 to 2014. Sustainability 10, article no. 635, 15 pp., http://dx.doi.org/10.3390/su10030635.

Banzon, V., Reynolds, R., Coauthors, 2018. The Climate Data Guide: SST data: NOAA Optimal Interpolation (OI) SST Analysis, version 2 (OISSTv2) 1x1, accessed 17 December 2018, https://climatedataguide.ucar.edu/climate-data/sst-data-noaa-optimal-interpolation-oi-sst-analysis-version-2-oisstv2-1x1.

Belkin, I., Rapid, M., 2009. Warming of large marine ecosystems. Prog. Oceanogr. 81, 207–213.

Bentamy, A., Croize-Fillon, D., 2012. Gridded surface wind fields from Metop/ASCAT measurements. Int. J. Remote Sens. 33 (6), 1729–1754, http://dx.doi.org/10.1080/01431161.2011.600348.

Berman, T., Paldor, N., Brenner, S., 2003. Annual SST cycle in the Eastern Mediterranean, Red Sea and Gulf of Elat. Geophys. Res. Lett. 30, 1261, http://dx.doi.org/10.1029/2002GL015860.

Bower, A.S., Furey, H.H., 2012. Mesoscale eddies in the Gulf of Aden and their impact on the spreading of Red Sea Outflow Water. Prog. Oceanogr. 96, 14–39.

Boyer, T.P., Antonov, J.I., Baranova, O.K., Coleman, C., Garcia, H.E., Grodsky, A., Johnson, D.R., Locarnini, R.A., Mishonov, A.V., O'Brien, T.D., Paver, C.R., Reagan, J.R., Seidov, D., Smolyar, I. V., Zweng, M.M., 2013. World Ocean Database 2013. NOAA Atlas NESDIS, 72. NOAA Printing Office, Silver Spring, MD, 208 pp., http://hdl.handle.net/11329/357.

Brewin, R.J.W., Raitsos, D.E., Pradhan, Y., Hoteit, I., 2013. Comparison of chlorophyll in the Red Sea derived from MODIS-Aqua and in vivo fluorescence. Remote Sens. Environ. 136, 218–224, http://dx.doi.org/10.1016/j.rse.2013.04.018.

Cantin, N.E., Cohen, A.L., Karnauskas, K.B., Tarrant, A.M., McCorkle, D.C., 2010. Ocean warming slows coral growth in the central Red Sea. Science 329 (5989), 322–325.

Caputi, N., Jackson, G., Pearce, A.F., 2014. The marine heat wave off Western Australia during the summer of 2010/11 – 2 years on. Fisheries Res. Rep. No. 250. Dpt. Fisheries, Western Australia, 40 pp.

Chaidez, V., Dreano, D., Agusti, S., Duarte, C.M., Hoteit, I., 2017. Decadal trends in Red Sea maximum surface temperature. Sci. Rep. 7, article no. 8144, http://dx.doi.org/10.1038/s41598-017-08146-z.

Collins, M., Knutti, R., Arblaster, J., Dufresne, J.L., Fichefet, T., Friedlingstein, P., Gao, X., Gutowski, W.J., Johns, T., Krinner, G., Shongwe, M., Tebaldi, C., Weaver, A.J., Wehner, M., 2013. Long-term climate change: projections, commitments and irreversibility. In: Stocker, T.F., Qin, D., Plattner, G.-K., Tignor, M., Allen, S. K., Boschung, J., Nauels, A., Xia, Y., Bex, V., Midgley, P.M. (Eds.), Climate Change 2013: The Physical Science Basis. Contribution of Working Group I to the Fifth Assessment Report of the Intergovernmental Panel on Climate Change. Cambridge University Press, Cambridge, 1535 pp.

Dee, D.P., Uppala, S.M., Simmons, A.J., Berrisford, P., Poli, P., Kobayashi, S., Andrae, U., Balmaseda, M.A., Balsamo, G., Bauer, D.P., 2011. The ERA-Interim reanalysis: configuration and performance of the data assimilation system. Q. J. R. Meteorolog. Soc. 137, 553–597, http://dx.doi.org/10.1002/qj.828.

Delworth, T.L., Broccoli, A.J., Rosati, A., Stouffer, R.J., Balaji, V., Beesley, J.A., Cooke, W.F., Dixon, K.W., Dunne, J., Dunne, K.A., Durachta, J.W., Findell, K.L., Ginoux, P., Gnanadesikan, A., Gordon, C.T., Griffies, S.M., Gudgel, R., Harrison, M.J., Held, I.M., Hemler, R.S., Horowitz, L.W., Klein, S.A., Knutson, T.R., Kushner, P.J., Langenhorst, A.R., Lee, H., Lin, S., Lu, J., Malyshev, S.L., Milly, P.C., Ramaswamy, V., Russell, J., Schwarzkopf, M.D., Shevliakova, E., Sirutis, J.J., Spelman, M.J., Stern, W.F., Winton, M., Wittenberg, A.T., Wyman, B., Zeng, F., Zhang, R., 2006. GFDL's CM2 Global Coupled Climate Models. Part I: Formulation and simulation characteristics. J. Climatol. 19, 643–674, http://dx.doi.org/10.1175/JCLI3629.1.

Donner, L.J., Wyman, B.L., Hemler, R.S., Horowitz, L.W., Ming, Y., Zhao, M., Golaz, J., Ginoux, P., Lin, S., Schwarzkopf, M.D., Austin, J., Alaka, G., Cooke, W.F., Delworth, T.L., Freidenreich, S.M., Gordon, C.T., Griffies, S.M., Held, I.M., Hurlin, W.J., Klein, S.A., Knutson, T.R., Langenhorst, A.R., Lee, H., Lin, Y., Magi, B.I., Malyshev, S.L., Milly, P.C., Naik, V., Nath, M.J., Pincus, R., Ploshay, J.J., Ramaswamy, V., Seman, C.J., Shevliakova, E., Sirutis, J.J., Stern, W.F., Stouffer, R.J., Wilson, R.J., Winton, M., Wittenberg, A.T., Zeng, F., 2011. The dynamical core, physical parameterizations, and basic simulation characteristics of the atmospheric component AM3 of the GFDL Global Coupled Model CM3. J. Climatol. 24, 3484–3519, http://dx.doi.org/10.1175/2011JCLI3955.1.

Dunne, P.J., John, G.J., Shevliakova, E., Stouffer, J.R., Krasting, P.J., Malyshev, L.S., Milly, D.C.P., Sentman, T.L., Adcroft, J.A., Cooke, W., Dunne, A.K., Stephen, M., Griffies, M.S., Hallberg, W.R., Harrison, J.M., Levy, H., Wittenberg, T.A., Peter, J., Phillips, J. P., Zadeh, N., 2013. GFDL's ESM2 global coupled climate–carbon earth system models. Part II: Carbon system formulation and baseline simulation characteristics. J. Climatol. 26, 2247–2267, http://dx.doi.org/10.1175/JCLI-D-12-00150.1.

Eladawy, A., Nadaoka, K., Negm, A., Abdel-Fattah, S., Hanafy, A., Shaltout, M., 2017. Characterization of the northern Red Sea's oceanic features with remote sensing data and outputs from a global circulation model. Oceanologia 59 (3), 213–237, http://dx.doi.org/10.1016/j.oceano.2017.01.002.

GOSUD, 2016. GOSUD Project-Global Ocean Surface Underway data. SEANOE (SEA scieNtific Open data Edition), http://dx.doi.org/10.17882/47403.

Griffies, S.M., 2009. Elements of MOM4p1. GFDL Ocean Group Tech. Rep. No. 6, 444 pp., https://www.gfdl.noaa.gov/wp-content/uploads/files/model_development/ocean/guide4p1.pdf.

Griffies, S.M., Winton, M., Donner, L.J., Horowitz, L.W., Downes, S. M., Farneti, R., Gnanadesikan, A., Hurlin, W.J., Lee, H., Liang, Z., Palter, J.B., Samuels, B.L., Wittenberg, A.T., Wyman, B.L., Yin, J., Zadeh, N., 2011. The GFDL CM3 Coupled Climate Model: Characteristics of the ocean and sea ice simulations. J. Climatol. 24, 3520–3544, http://dx.doi.org/10.1175/2011JCLI3964.1.

Halliwell, G.R., 2004. Evaluation of vertical coordinate and vertical mixing algorithms in the HYbrid-Coordinate Ocean Model (HYCOM). Ocean Model. 7 (3), 285–322, http://dx.doi.org/10.1016/j.ocemod.2003.10.002.

He, Z., Wu, R., Wang, W., Wen, Z., Wang, D., 2017. Contributions of surface heat fluxes and oceanic processes to tropical SST changes: seasonal and regional dependence. J. Climatol. 30, 4185–4205, http://dx.doi.org/10.1175/JCLI-D-16-0500.1.

Hervieux, G., Alexander, M.A., Stock, C.A., Jacox, M.G., Pegion, K., Becker, E., Castruccio, F., Tommasi, D., 2017. More reliable coastal SST forecasts from the North American multimodel ensemble. Clim. Dyn., http://dx.doi.org/10.1007/s00382-017-3652-7.

Hoegh-Guldberg, O., Cai, R., Poloczanska, E.S., Brewer, P.G., Sundby, S., Hilmi, K., Fabry, V.J., Jung, S., 2014. The ocean – supplementary material. In: Barros, V.R., Field, C.B., Dokken, D. J., Mastrandrea, M.D., Mach, K.J., Bilir, T.E., Chatterjee, M., Ebi, K.L., Estrada, Y.O., Genova, R.C., Girma, B., Kissel, E.S., Levy, A. N., MacCracken, S., Mastrandrea, P.R., White, L.L. (Eds.), Climate Change 2014: Impacts, Adaptation, and Vulnerability. Part B: Regional Aspects. Contribution of Working Group II to the Fifth Assessment Report of the Intergovernmental Panel on Climate Change. Cambridge University Press, Cambridge, 1655–1731, accessed on 29 April 2019, https://www.ipcc.ch/site/assets/uploads/2018/02/WGIIAR5-Chap30_FINAL.pdf.

Hurrell, J.W., 1995. Decadal trends in the North Atlantic Oscillation regional temperatures and precipitation. Science 269, 676–679.

IPCC, 2014. Climate Change 2013 – The Physical Science Basis: Working Group I Contribution to the Fifth Assessment Report of the Intergovernmental Panel on Climate Change. Cambridge University Press, Cambridge, 1535 pp., http://dx.doi.org/10.1017/CBO9781107415324.

Jacox, M.G., Alexander, M.A., Stock, C.A., Hervieux, G., 2017. On the skill of seasonal sea surface temperature forecasts in the California Current System and its connection to ENSO variability. Clim. Dyn., http://dx.doi.org/10.1007/s00382-017-3608-y.

Jolliffe, I.T., 2002. Principal Component Analysis, 2nd edn. Springer, New York, 518 pp.

Karnauskas, K.B., Jones, B.H., 2018. The interannual variability of sea surface temperature in the Red Sea from 35 years of satellite and in situ observations. J. Geophys. Res. 123, 5824–5841, http://dx.doi.org/10.1029/2017JC013320.

Large, W.G., Pond, S., 1981. Open ocean momentum flux measurements in moderate to strong winds. J. Phys. Oceanogr. 11, 324–336, http://dx.doi.org/10.1175/1520-0485(1981)011<0324:OOMFMI>2.0.CO;2.

MacQueen, J.B., 1967. Some methods for classification and analysis of multivariate observations. In: Proc. 5th Berkeley Symposium on Mathematical Statistics and Probability. University of California Press, Berkeley, 281–297.

Maor-Landaw, K., Karako-Lampert, S., Waldman Ben-Asher, H., Goffredo, S., Falini, G., Dubinsky, Z., Levy, O., 2014. Gene expression profiles during short-term heat stress in the red sea coral *Stylophora pistillata*. Global Change Biol. 20 (10), 3026–3035.

Milly, P.C., Malyshev, S.L., Shevliakova, E., Dunne, K.A., Findell, K.L., Gleeson, T., Liang, Z., Phillipps, P., Stouffer, R.J., Swenson, S., 2014. An enhanced model of land water and energy for global hydrologic and earth-system studies. J. Hydrometeorol. 15, 1739–1761, http://dx.doi.org/10.1175/JHM-D-13-0162.1.

Nykjaer, L., 2009. Mediterranean Sea surface warming 1985–2006. Clim. Res. 39, 11–17, http://dx.doi.org/10.3354/cr00794.

Osman, E.O., Smith, D.J., Ziegler, M., Kürten, B., Conrad, C., El-Haddad, K.M., Voolstra, C.R., Suggett, D.J., 2018. Thermal refugia against coral bleaching throughout the northern Red Sea. Global Change Biol. 24, e474–e484.

Owens, R.G., Hewson, T.D., 2018. European Centre for Medium-Range Weather Forecasts Forecast User Guide. ECMWF, Reading, http://dx.doi.org/10.21957/m1cs7h.

Qu, B., Gabric, A., Zhu, J., Lin, D., Qian, F., Zhao, M., 2012. Correlation between sea surface temperature and wind speed in Greenland Sea and their relationships with NAO variability. Water Sci. Eng. 5 (3), 304–315, http://dx.doi.org/10.3882/j.issn.1674-2370.2012.03.006.

Raitsos, D.E., Hoteit, I., Prihartato, P.K., Chronis, T., Triantafyllou, G., Abualnaja, Y., 2011. Abrupt warming of the Red Sea. Geophys. Res. Lett. 38, article no. L14601, http://dx.doi.org/10.1029/2011GL047984.

Reynolds, R.W., 2009. What's New in Version 2 of daily optimum interpolation (OI) sea surface temperature (SST) analysis, 10 pp., https://www.ncdc.noaa.gov/sites/default/files/attachments/Reynolds2009_oisst_daily_v02r00_version2-features.pdf.

Reynolds, R.W., Smith, T.M., Liu, C., Chelton, D.B., Casey, K.S., Schlax, M.G., 2007. Daily high-resolution blended analyses for sea surface temperature. J. Climatol. 20, 5473–5496, http://dx.doi.org/10.1175/2007JCLI1824.1.

Ricciardulli, L., Wentz, F.J., Smith, D.K., 2011. Remote Sensing Systems QuikSCAT Ku-2011 Daily Orbital Swath Ocean Vector Winds L2B, Version 4. Remote Sensing Systems, Santa Rosa. CA. Available online at www.remss.com/missions/qscat. [Accessed 01/04/2019].

Richardson, A.J., Schoeman, D.S., 2004. Climate impact on plankton ecosystems in the northeast Atlantic. Science 305, 1609–1612, http://dx.doi.org/10.1126/science.1100958.

Roik, A., Roder, C., Rothig, T., Voolstra, C.R., 2016. Spatial and seasonal reef calcification in corals and calcareous crusts in the central Red Sea. Coral Reefs 35, 681–693.

Samelson, R.M., Skyllingstad, E.D., Chelton, D.B., Esbensen, S.K., O'Neill, L.W., Thum, N., 2006. On the coupling of wind stress and sea surface temperature. J. Climatol. 19 (8), 1557–1566, http://dx.doi.org/10.1175/JCLI3682.1.

Sarthia, P.P., Dash, S.K., Mamgain, A., 2012. Possible changes in the characteristics of Indian Summer Monsoon under warmer climate. Global Planet. Change 92, 17–29, http://dx.doi.org/10.1016/j.gloplacha.2012.03.006.

Sawall, Y., Al-Sofyani, A., Banguera-Hinestroza, E., Voolstra, C.R., 2014. Spatio-temporal analyses of *Symbiodinium* physiology of the coral *Pocillopora verrucosa* along large-scale nutrient and temperature gradients in the Red Sea. PLoS ONE 9 (8), article no. e103179, http://dx.doi.org/10.1371/journal.pone.0103179.

Shaltout, M., Omstedt, A., 2014. Recent sea surface temperature trends and future scenarios for the Mediterranean Sea. Oceanologia 56 (3), 411–443, http://dx.doi.org/10.5697/oc.56-3.411.

Skliris, N., Sofianos, S., Gkanasos, A., Mantziafou, A., Vervatis, V., Axaopoulos, P., Lascaratos, A., 2012. Decadal scale variability of sea surface temperature in the Mediterranean Sea in relation to atmospheric variability. Ocean Dyn. 62, 13–30, http://dx.doi.org/10.1007/s10236-011-0493-5.

Smeed, D., 1997. Seasonal variation of the flow in the strait of Bab al Mandab. Oceanol. Acta 20 (6), 773–781.

Stock, C.A., Alexander, M.A., Bond, N.A., Brander, K.M., Cheung, W.W., Curchitser, E.N., Delworth, T.L., Dunne, J.P., Griffies, S.M., Haltuch, M.A., 2011. On the use of IPCC-class models to assess the impact of climate on living marine resources. Prog. Oceanogr. 88, 1–27.

Thomas, M.K., Kremer, C.T., Klausmeier, C.A., Litchman, E., 2012. A global pattern of thermal adaptation in marine phytoplankton. Science 338, 1085–1088.

Trenberth, K.E., Large, W.G., Olson, J.G., 1990. The mean annual cycle in global ocean wind stress. J. Phys. Oceanogr. 20 (11), 1742–1760, http://dx.doi.org/10.1175/1520-0485(1990)020<1742:TMACIG>2.0.CO;2.

Trenberth, K.E., Shea, D.J., 2006. Atlantic hurricanes and natural variability in 2005. Geophys. Res. Lett. 33, article no. L12704, http://dx.doi.org/10.1029/2006GL026894.

Wang, B., Wu, R., Lau, K., 2001. Interannual variability of Asian summer monsoon: contrast between the Indian and western North Pacific-East Asian monsoons. J. Climatol. 14, 4073–4090.

Wang, C., Weisberg, R.H., Yang, H., 1999. Effects of the wind speed-evaporation-SST feedback on the El Niño-Southern Oscillation. J. Atmos. Sci. 56 (10), 1391–1403, http://dx.doi.org/10.1175/1520-0469(1999)0562.0.CO;2.

Wilson, S., Rebecca, K., 2000. The Gulf of Aden. In: Sheppard, C. (Ed.), Seas at the Millennium: An Environmental Evaluation. Elsevier Science, Oxford, 47–61.

Worley, S.J., Woodruff, S.D., Reynolds, R.W., Lubker, S.J., Lott, N., 2005. ICOADS release 2.1 data and products. Int. J. Climatol. 25, 823–842.

You, Q., Jiang, Z., Moore, G.W.K., Bao, Y., Kong, L., Kang, S., 2017. Revisiting the relationship between observed warming and surface pressure in the Tibetan Plateau. J. Climatol. 30, 1721–1737, http://dx.doi.org/10.1175/JCLI-D-15-0834.1.

Zhou, C., Wang, K., 2016. Evaluation of surface fluxes in ERA-Interim using flux tower data. J. Climatol. 29, 1573–1582, http://dx.doi.org/10.1175/JCLI-D-15-0523.1.

Oceanologia (2019) 61, 505—521

Available online at www.sciencedirect.com

ScienceDirect

journal homepage: www.journals.elsevier.com/oceanologia/

ORIGINAL RESEARCH ARTICLE

Seasonal changes in particulate organic matter (POM) concentrations and properties measured from deep areas of the Baltic Sea

Aleksandra Winogradow*, **Anna Mackiewicz**, **Janusz Pempkowiak**

Institute of Oceanology, Polish Academy of Sciences, Sopot, Poland

Received 3 April 2019; accepted 27 May 2019
Available online 13 June 2019

KEYWORDS
Suspended particulate matter;
Particulate organic carbon;
Particulate nitrogen;
Chl *a*;
Pheo *a*;
$\delta^{13}C_{POC}$;
Gdańsk Deep;
Gotland Deep

Summary In seawater particulate organic matter (POM) serves as a food source for heterotrophic bacteria and zooplankton and is a source of dissolved organic compounds and nutrients. POM plays a critical role in transporting carbon to marine sediments where a fraction of it is buried in subsurface sediments and thus avoids conversion to carbon dioxide on shorter time scales.

Distribution and properties of POM were investigated in the Baltic Proper from 2013 to 2015. Particulate organic carbon (POC) was used to investigate POM sources and dynamics. Stable carbon isotopes ($\delta^{13}C$), elemental composition (C, N), chlorophyll *a* and POM contribution to suspended particulate matter (SPM) were also measured and interpreted. The water column exhibited concentrations ranging from 0.2 mg POC/l (deep water layer — DWL, cold season — CS) to 1.7 mg POC/l (surface water layer — SWL, warm season — WS). POM represented 0.15 to 0.45 of SPM during respective cold and warm seasons. Stable carbon isotopes ($\delta^{13}C_{POC}$) ranged from −22.5‰ (WS) to −28.0‰ (CS), while the POC/Chl *a* ratio ranged from 180 g/g (SWL-WS) to 300 g/g (DWL-CS). Seasonal changes were attributed to high primary production in the SWL during the WS, which represented a major POM source. Continuous mineralization/sedimentation throughout the water column constituted a major POM sink.

* Corresponding author at: Institute of Oceanology, Polish Academy of Sciences, Powstańców Warszawy 55, 81-712 Sopot, Poland. Tel.: +48587311735.
E-mail address: aleksandra@iopan.gda.pl (A. Winogradow).

Peer review under the responsibility of Institute of Oceanology of the Polish Academy of Sciences.

Production and hosting by Elsevier

https://doi.org/10.1016/j.oceano.2019.05.004

1. Introduction

Particulate organic matter (POM) nominally consists of detritus, fecal pellets, phyto- and zooplankton cells and bacteria (Chen and Wagnersky, 1993; Dzierzbicka-Głowacka et al., 2010; Hygum et al., 1997). POM is a minor but important constituent of seawater, because it causes most of the light scattering and some of the light absorption observed in natural waters (Ferrari et al., 2003; Meler et al., 2017b; Woźniak et al., 2016). It thereby significantly influences euphotic zone thickness. POM also serves as a food source for heterotrophic bacteria and zooplankton (Andersson et al., 2017; Dzierzbicka-Głowacka et al., 2010; Hygum et al., 1997; Lowe et al., 2014) and is a source of dissolved organic compounds and nutrients (Dzierzbicka-Głowacka et al., 2011; Hygum et al., 1997). POM plays a critical role in transporting carbon to marine sediments where a fraction of it is buried in subsurface sediments and thus avoids conversion to carbon dioxide on shorter time scales (Koziorowska et al., 2018; Omstedt et al., 2014). Since POM transports carbon to sediment, it represents a critical mechanism in the biological pump (De La Rocha, 2006). High phytoplankton productivity and associated carbon burial thus modulate atmospheric CO_2 concentration (Hagström et al., 2001; Thomas et al., 2003).

Properties of land and marine-derived POM (e.g. C/N ratio, particles size spectrum, light scattering and absorption, susceptibility to biochemical oxidation) can vary significantly to form a relatively heterogeneous trophic reservoir (Lowe et al., 2014, 2016) and may cause variable oxygen consumption (Omstedt et al., 2014; Pempkowiak, 1983). Studies have thus sought to differentiate POM according to its origin. C/N molar ratios, chlorophyll *a* (Chl *a*) concentration and both carbon and nitrogen stable isotopic compositions have been analyzed and interpreted to this end (Liu et al., 2018). Previous studies have differentiated a low nitrogen (C/N molar ratio $>$ 20) terrestrial vegetation contribution to organic matter based on carbon and nitrogen isotopic signatures ($\delta^{15}N$: $-2.0‰$ to $0‰$ and $\delta^{13}C$: $-30.0‰$ to $-23.0‰$) from marine plankton exhibiting both nitrogen (C/N $<$ 10) and heavy carbon and nitrogen isotopes enrichments ($\delta^{15}N$ in the range of 4–6‰ and $\delta^{13}C$ equal to $-22.0‰$) (Thornton and McManus, 1994; Voss et al., 2005). An end-member approach has been used to evaluate proportions of marine-derived versus terrestrial POM fractions (Thornton and McManus, 1994). Quantifying contributions of marine and terrestrial POM using this model requires detailed knowledge on the natural elementals and isotopic ranges of end-members for a given study region (e.g. Goñi et al., 2003; Liu et al., 2018; Thornton and McManus, 1994). However, most reports simply cite "typical" end-member values such as $-22.0‰$ and $-27.0‰$ for $\delta^{13}C_{POC}$ values representing respective marine phytoplankton and terrestrial POC sources (Coban-Yıldız et al., 2006; Koziorowska et al., 2016; Kravchishina et al., 2018; Liu et al., 2018; Maksymowska et al., 2000; Szczepańska et al., 2012; Voss et al., 2005; Winogradow and Pempkowiak, 2014).

As the major component of POM, particulate organic carbon (POC) is interpreted as a proxy for POM (Chester, 2003). Recent optical methods, including remote sensing, have been used to directly assess both POM concentrations in seawater as well as inorganic and organic proportions in suspended particulate matter (SPM) (Meler et al., 2017b; Woźniak et al., 2016). Results obtained by these new approaches are a subject to substantial uncertainties. Reducing this uncertainty requires local empirical data. Remote sensing methods provide efficient, high coverage data on water bodies but can only survey surface layers for the parameters interpreted here.

Several sources contribute POM to seawater. The contribution of POM derived from a particular source to total POM depends on factors such as phytoplankton and zooplankton productivity, abrasion in coastal environments and proximity to estuaries. Atmospheric transport is considered to be of only minor importance (Dzierzbicka-Głowacka et al., 2010; Kuliński and Pempkowiak, 2011). Concentrations of POM in coastal areas are typically much higher than in open ocean environments as most POM sources derive, directly or indirectly, from river run-off. The sources include also seepage (Szymczycha et al., 2014) and direct discharges (Pempkowiak and Obarska-Pempkowiak, 2002). This is the case with coastal environments and land-locked seas like the Baltic Sea. The Baltic experiences enhanced primary production that reaches 250 g/m^2 per annum (Andersson et al., 2017; Kuliński and Pempkowiak, 2011; Leppakowski and Mihnea, 1996). POC concentrations in the Baltic Sea depend on Chl *a*, river run-off and on both water salinity and depth variation resulting from stratification of the Baltic water column (Kuliński and Pempkowiak, 2008; Maciejewska and Pempkowiak, 2014). Statistical studies have found that phytoplankton activity followed by water depth are the most important factors influencing POC concentrations in the water column of the southern Baltic (Maciejewska and Pempkowiak, 2015; Szymczycha et al., 2017). High phytoplankton productivity thus enhances POM abundance in the Baltic (Maciejewska and Pempkowiak, 2015). Concentrations of POC in the Baltic range from 0.05–1.80 mg/dm^3, while POC mass contribution to total SPM ranges from 0.13–0.42 (Andersson and Rudehall, 1993; Burska et al., 2005; Maciejewska and Pempkowiak, 2014; Meler et al., 2017b; Woźniak et al., 2018). POC concentrations exhibit seasonal and vertical gradients (Burska et al., 2005; Dzierzbicka-Głowacka et al., 2010; Maciejewska and Pempkowiak, 2014) and significant spatial variation in open water areas. These might arise due to shifts in the start of the growing season and its duration at different locations (Maciejewska and Pempkowiak, 2014). POM is exchanged horizontally through the Danish Straits with the North Sea (Hakanson and Eckhell, 2005; Kuliński et al., 2011; Thomas et al., 2003). The POM concentration depends on the distance from land with coastal and estuarine areas hosting more organic matter than open waters (Maciejewska and Pempkowiak, 2014). Planktonic activity may contribute to large seasonal fluctuations in POM (Dzierzbicka-Głowacka et al., 2011).

Many studies have examined POM properties and distribution in the Baltic Sea. The sampling campaigns from which these studies drew, however, often lasted only a matter of days and occurred mostly during the summer (Bianchi et al., 1997; Burska et al., 2005; Engel et al., 2002; Lundsgaard et al., 1999; Schumann et al., 2001; Tamelander and Heiskanen, 2004; Voss et al., 2005). Few studies have addressed seasonal variation in POM dynamics for open water environments (Schneider et al., 2015; Struck et al., 2004; Szymczycha et al., 2017) but considerable uncertainties about this topic remain. Studies on Baltic Sea POM revealed that in summer C/N ratios range from 7–10, $\delta^{13}C$ values – from $-22.5‰$ to $-28.0‰$ and $\delta^{15}N$ values – from 1.0‰ to 6.0‰

(Maksymowska et al., 2000; Szymczycha et al., 2017; Voss and Struck, 1997; Voss et al., 2005). A recent three-year study quantified organic carbon concentrations in Baltic waters to elucidate factors influencing this reservoir. Temperature, pH (photosynthesis intensity), Chl *a* (abundance of phytoplankton), Pheo *a* (sloppy feeding by zooplankton) and salinity (provenance of water masses) were used as proxies for environmental factors conditioning POC distribution (Maciejewska and Pempkowiak, 2014, 2015; Szymczycha et al., 2017). Using temperature to track seasonality, Chl *a* was interpreted as an index of live phytoplankton biomass (Wasmund and Uhlig, 2003) and Pheo *a* concentrations served as an index of phytoplankton mortality, including sloppy zooplankton grazing (Collos et al., 2005; Meyer-Harms et al., 1999). The influence of fluvial and oceanic water masses was interpreted from salinity measurements (Abril et al., 2002; Kuliński and Pempkowiak, 2011). The intensity of photosynthesis was interpreted from pH values.

Results of numerical modeling indicate that POC concentrations depend on the light intensity, water temperature and nutrient availability (Almroth-Rosell et al., 2011; Dzierzbicka-Głowacka et al., 2010; Gustafsson et al., 2015; Segar, 2012).

The parameters listed above (C/N, $\delta^{13}C$, $\delta^{15}N$, Chl *a*, Pheo *a*, POC) depend on primary productivity. As such, they should vary systematically with season and water depth due to the interplay between marine and fluvial contributions in establishing the halocline and contributing POM from their respective marine and terrestrial sources. The nature of this systematic variation has never been documented for the Baltic Sea.

While studies have documented the concentration dynamics of organic matter in the Baltic, properties of POM have not been monitored in tandem with factors affecting its spatial and temporal variation. For example, little is known about POM and Chl *a* seasonal variations. Several studies have predicted shifts in both particulate and dissolved organic matter in the near future (Dzierzbicka-Głowacka et al., 2011; Gustafsson et al., 2015; Straat et al., 2018). Acquiring a robust baseline or present-day understanding of these parameters and of basin dynamics can help contextualize future changes. This study monitored POM characteristics and relationships between POM and environmental parameters in open water areas of the Baltic Sea from 2013–2015. The aim was to document and interpret seasonal changes in both POM concentrations and POM properties.

2. Study area

The Baltic Sea extends from 10–30°E and 54–64°N (Fig. 1) and represents the second largest brackish water body in the world. The connection with the North Sea via Danish straits and the Kattegat results in saline water inflows and stable stratification of the basinal water columns. Within the halocline, fully saline waters occur at 60–80 m depth. The sea water volume reaches some 22,000 km^3 with annual runoff equal to 440 km^3. Average annual precipitation is 270 km^3 and net inflow from the North Sea is 470 km^3 (Björck, 1995; HELCOM, 2007; Łomniewski et al., 1975). The Baltic Sea receives considerable volumes of freshwater (440 km^3; Voipio, 1981) and organic carbon (2.93 Tg C yr^1, Tg = 10^{12} g; Kuliński and Pempkowiak, 2011; Szymczycha et al., 2014).

The Baltic is a bathymetrically complex, brackish and enclosed shelfal sea (Leppakowski and Mihnea, 1996). The basin has an average depth of about 53 m but also consists of deeper bathymetric features called 'deeps'. These exhibit well-developed water column stratification. The main deeps of the Southern Baltic are the Gdańsk Deep, the Gotland Deep and the Bornholm Deep.

The Gdańsk Deep (maximum depth: 118 m) hosts a permanent halocline located at 60–80 m depth. Surface water layers have relatively low salinity ranges of between 7.1 and 7.8.

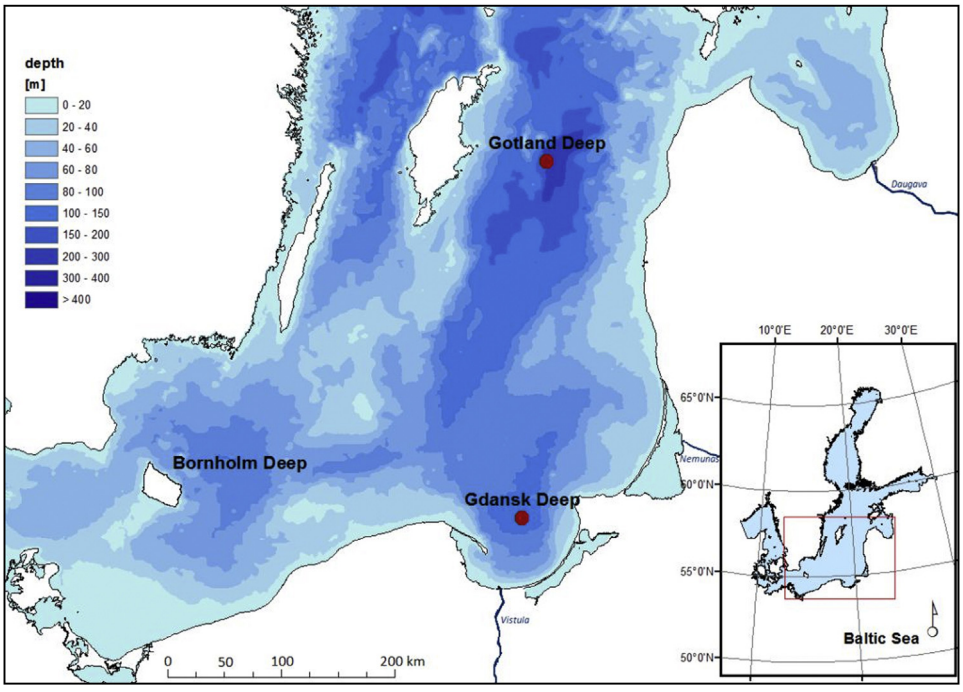

Figure 1 Location of the study sites, the Gdańsk Deep and Gotland Deep.

Seasonal temperature variation ranges from 1°C (January) and 20°C (July). Subsurface layers have higher salinity ranging from 10–13 and temperature of around 4°C (Szczepańska and Uścinowicz, 1994; Voipio, 1981). The Gotland Deep reaches a maximum depth about 250 m and is a stratified basin with a halocline developed at 60–70 m depth. The stratification of the water column limits oxygen concentration at depth and promotes bottom water oxygen depletion (Leipe et al., 2011; Szczepańska and Uścinowicz, 1994; Voipio, 1981).

Plankton in the Baltic Sea mostly appear during two seasonal blooms. The spring bloom (March–May) is typically dominated by dinophytes and/or diatoms (80–95% of total biomass) with a minority of chlorophytes, cryptophytes and cyanobacteria. This bloom contributes about half of the annual primary production. The autumn bloom (August–September) is dominated by cyanobacteria along with dinophytes and chlorophytes as the other main contributors (Andersson et al., 2017; Stoń et al., 2002; Wasmund and Uhlig, 2003). Previous field studies have suggested that Baltic primary production is mostly nitrogen limited, but the activity of nitrogen-fixing cyanobacteria during some periods of the year may result in phosphorus limitation (Kivi et al., 1993).

Primary productivity in the Baltic proper is nitrogen limited in the summer, and constrained by light and temperature in the winter (Dzierzbicka-Głowacka et al., 2010). Annual primary productivity showed distinct spatial and temporal variations of 100–200 g C m^{-2} yr^{-1} with the highest rates during late spring. Primary productivity increased between 1950 and 1990 by some 50% but has more or less stabilized since then (HELCOM, 2007; Szymczycha et al., 2019).

3. Material and methods

3.1. Sampling sites, temperature and salinity measurements

Sampling and analysis focused on two sites, the Gdańsk Deep (ϕ = 54°50′N, λ = 18°17′E) and Gotland Deep (ϕ = 57°18′N, λ = 19°53′E). Both sites are at a spatial remove from the influence of river run-off (Voss et al., 2005). The sites were sampled and monitored over 23 visits from March 2013 to July 2016. Site visits included in situ temperature and salinity measurements using a Sea-Bird Scientific SBE 911 Plus CTD profiler. The samples are attributed to two seasons: warm (WS) and cold (CS). The former includes samples collected in the period from April to September, while the latter samples collected from November to March.

3.2. Water sampling, pH measurements and SPM: separation and storage

Seawater samples were collected from several depths at study sites using Niskin bottles deployed during r/v *Oceania*, r/v *Alkor* and r/v *Aranda* research cruises. Immediately after sampling, pH was measured using a WTW Multi 3400i pH meter (0.01 unit accuracy), while 1–2 liters of seawater were passed through pre-combusted and pre-weighted MN GF 5 (0.4 μm nominal pore size) glass-fiber filters to collect SPM. Filters with SPM were stored at −80°C until further laboratory analysis. To characterize SPM, we measured POC (particulate organic carbon), PN (particulate nitrogen), Chl *a* (chlorophyll *a*), Pheo *a* (pheopigment *a*), $\delta^{13}C$ of POM ($\delta^{13}C_{POC}$) and $\delta^{15}N$ of PN.

3.3. Chlorophyll *a* (Chl *a*) and pheopigment *a* (Pheo *a*) analyses

Chl *a* was measured spectrophotometrically (Hitachi U-2800 spectrophotometer) from solvent extracted SPM. Filters bearing SPM samples were rinsed in 90% acetone following procedures described in Parsons (1966). Chl *a* concentrations were calculated using the Lorenzen (1967) formulas. Spectrophotometry was also used to measure Pheo *a* from acetone extracts after acidification (60 μl of 1 M HCl were added to 5 ml of the extract). Quality control included measurements of blanks. Limit of detection, defined as average blank plus five times standard deviations of blank measurements, was far below the results of actual samples measurements (it was smaller than 3% of the smallest measured Chl *a* concentration).

3.4. Particulate organic carbon (POC), particulate nitrogen (PN) and stable isotopic analyses ($\delta^{13}C_{POC}$ and $\delta^{15}N$)

For carbon and nitrogen analyses, the MN GF 5 (0.4 μm pore size) glass fiber filters with SPM samples were dried at 60°C for 24 h and then weighed (0.01 mg accuracy) and homogenized. POC, PN, $\delta^{13}C_{POC}$ and $\delta^{15}N$ analyses were carried out using an Elemental Analyzer Flash EA 1112 Series combined with the Isotopic Ratio Mass Spectrometer IRMS Delta V Advantage (Thermo Electron Corp., Germany). Analytical procedures followed those described in Winogradow and Pempkowiak (2018). Dry, homogenized filter with POM (30–40 mg) was weighed, transferred into a silver crucible and acidified with 2 M HCl to remove carbonates. After additional drying, samples were transferred to the instrument for high-temperature combustion (oxidation at 1020°C, followed by reduction over copper at 680°C). Analytical blanks were used to verify measurement stability. The LKSD-1 reference material was analyzed after every 10 unknowns to confirm accuracy. The average recovery (n = 5) was 97.1 ± 1.0%. Isotopic ratios $\delta^{13}C_{POC}$ and $\delta^{15}N$ were calculated using pure, laboratory grade CO_2 and N_2 reference gases calibrated against IAEA standards CO-8 and USGS40 for $\delta^{13}C$ and N-1 and USGS40 for $\delta^{15}N$. Sample $\delta^{13}C_{POC}$ and $\delta^{15}N$ values are given in the conventional delta notation relative to PDB for $\delta^{13}C_{POC}$ and relative to atmospheric nitrogen for $\delta^{15}N$.

Quality control included measurements of blanks and reference materials. Limit of POC and PON detections was respectively 0.001 mg/l and 0.002 mg/l, and was smaller than 3% of the smallest measured POC, and 8% of the smallest measured PN concentrations.

4. Results and interpretation

4.1. Temperature and salinity

Fig. 2 shows profiles of water column salinity for the Gdańsk Deep and the Gotland Deep. Surface water layers (SWL) for both deeps are characterized by a salinity range of 7.2 to 7.6 psu. Salinity increases up to 12.5 psu within the halocline

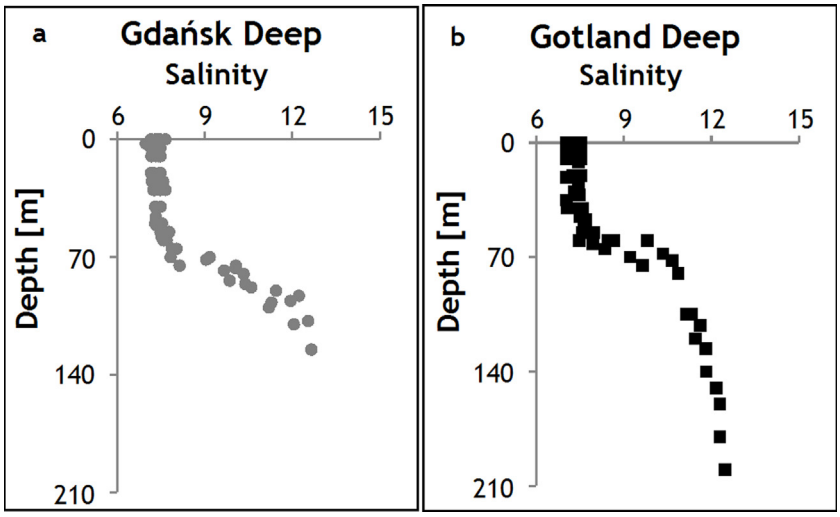

Figure 2 Vertical salinity profiles for the (a) Gdańsk Deep and (b) Gotland Deep as measured during the 2013—2015 study period.

and remains within a 12.5—12.8 psu range below the halocline, hereafter referred to as the deep water layer, or DWL (in the figures the 'deep water layer' is addressed as the 'subsurface water layer'). In both deeps, the halocline resides between 60 and 85 m depth requiring careful sampling of the Gdańsk Deep DWL so as not to re-suspend sediment. Both deeps exhibited halocline salinity gradients of 0.2 psu/m. Salinity showed no signs of systematic shifts over the course of a year. The salinity distribution in the study area indicates stratification caused by the salinity/density gradient and clearly distinguishes both the DWL and SWL. These two water layers persist throughout the year above and below the halocline. Stratification of the Baltic Proper water column arises due to the relatively high density of saline seawater entering the Baltic from the North Sea and fresher surface water contributed by river runoff (Burska et al., 2005; Rak, 2016; Voipio, 1981).

Fig. 3a shows typical water column temperature profiles for the two deeps. Temperatures for the SWL were lower during the cold season (4°C) than during the warm season (17°C) and displayed a range typical of the Baltic Proper (Szymczycha et al., 2019; Voipio, 1981). Temperature profiles for the WS did not appear to show well-developed thermoclines, possibly due to surface water mixing at the time of measurement (Szymczycha et al., 2017). The DWL exhibited a relatively consistent 4—6°C temperature range. Fig. 3b shows average monthly temperatures for the Gdańsk Deep (Figure S1 — Gotland Deep). The SWL exhibited temperature increases in April—July and decreases in September—January. The surface water layer thus appears to experience a cold season (CS: November to March) and a warm season (WS: April to October). This type of seasonal temperature oscillations is typical of seas in temperate climate regions (Sheppard (2019)) and is consistent with numerous previous observations of the Baltic (Rak, 2016; Szymczycha et al., 2019; Voipio, 1981).

4.2. Chlorophyll *a* (Chl *a*) and pheopigment *a* (Pheo *a*)

Fig. 4a shows typical profiles of Chl *a* concentrations in the water column for both deeps. Concentrations reached up to

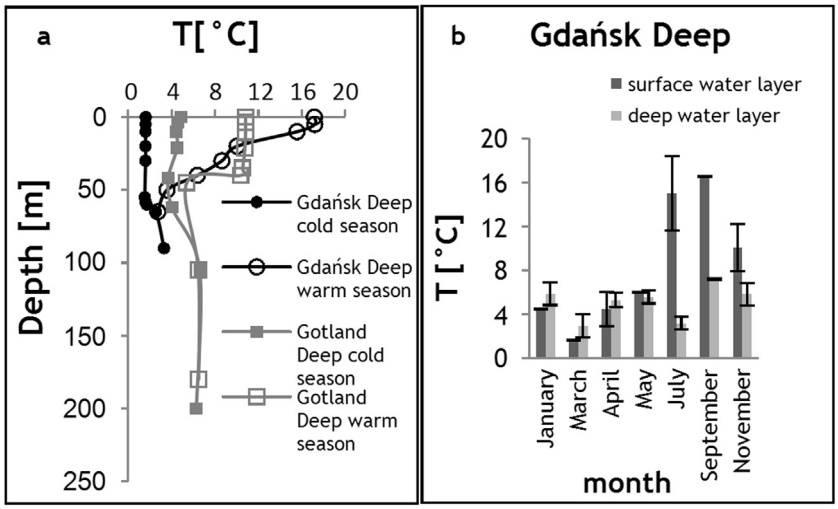

Figure 3 (a) Typical vertical profiles of water temperature in Gdańsk Deep and Gotland Deep during the cold season and warm season; (b) average monthly temperatures measured from surface and deep water layers of the Gdańsk Deep.

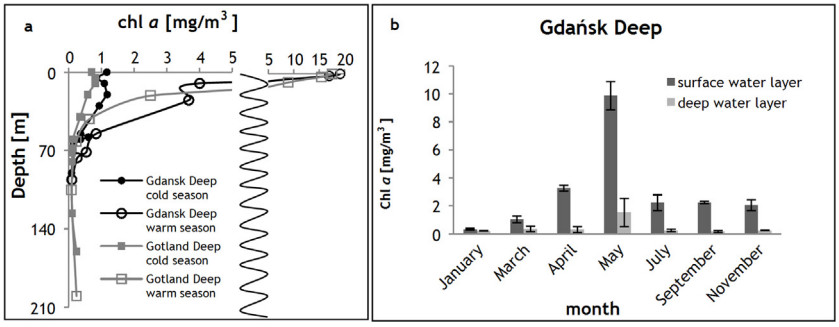

Figure 4 (a) Typical vertical profiles of chlorophyll *a* concentrations in water of Gdańsk Deep and Gotland Deep in cold season and warm season; (b) average monthly chlorophyll *a* concentrations in the surface and deep water layers of the Gdańsk Deep.

20 mg/m^3 in the SWL during the WS due to the spring bloom (Maciejewska and Pempkowiak, 2014). Concentrations in the DWL did not exceed 0.3 mg/m^3 indicating that sinking POM originating from the spring bloom had not reached the DWL at the time of measurement. Previous studies have reported similar Chl *a* values and water column distribution (Heiskanen et al., 1998; Maciejewska and Pempkowiak, 2014). Vertical Chl *a* profiles sometimes showed a shoulder or even a clear maximum at around 20 m depth (Fig. 4a shows Gdańsk Deep). This 'deep Chl *a* maximum' has been interpreted as evidence of increased phytoplankton abundance (Liu et al., 2018).

Fig. 4b shows the average monthly Chl *a* concentrations in the Gdańsk Deep (Figure S2 — Gotland Deep). The SWL exhibited greater Chl *a* concentrations (>1 mg/m^3, except January) than the DWL (<0.3 mg/m^3, except May). The SWL also showed an increase of Chl *a* beginning in March with a peak in May, followed by a decrease between November and January. During the CS, SWL Chl *a* concentrations did not exceed 1.3 mg/m^3 but were never lower than 2 mg/m^3 during the WS. Concentrations of Chl *a* in the DWL were constant at 0.3 mg/m^3 (except May) throughout the year.

Shifts in both temperature and Chl *a* concentrations (Fig. 3a and Fig. 4a) indicate that the SWL can assume two states. In one, the WS experiences increased Chl *a* concentrations indicative of phytoplankton abundance and high growth rates. In the other, the CS exhibits low Chl *a* concentrations indicating limited phytoplankton activity and lack of growth. The temperature and Chl *a* concentrations in the DWL remain constant throughout the year, except for Chl *a* in May. Elevated Chl *a* concentrations in the Gdańsk Deep in May most likely arise from the sinking of biomass products of a spring bloom that must have begun early enough for products to reach the DWL within several weeks. Previous studies have described similar concentration ranges and timing of Chl *a* changes in the Gdańsk Deep (Burska et al., 2005; Szymczycha et al., 2017) and the Gotland Deep (Maciejewska and Pempkowiak, 2014).

Fig. 5a shows concentrations of Pheo *a* measured from the Gdańsk Deep and Gotland Deep. Fig. 5b shows monthly averages of Pheo *a* in Gdańsk Deep (Figure S3 — Gotland Deep). Concentrations from the SWL (0.1—0.5 mg/m^3 during the CS and 0.7—1.5 mg/m^3 during the WS) exceeded those measured from the DWL (0.1—0.3 during the CS and 0.1—0.5 mg/m^3 during the WS). The observed concentrations fell within the range of previously reported values for the Gdańsk Deep by Burska et al. (2005). Pheo *a* concentrations and dynamics were interpreted as reflecting cycling of phytoplankton biomass (Burska et al., 2005; Struck et al., 2004) and sloppy zooplankton feeding (Collos et al., 2005; Meyer-Harms et al., 1999; Spence and Steven, 1974).

4.3. Suspended particulate matter (SPM)

Fig. 6a shows typical SPM profiles from water columns of the study area. Concentrations in the SWL (0.6—1.1 mg/l during the CS and 2—4 mg/l during the WS) exceeded those observed

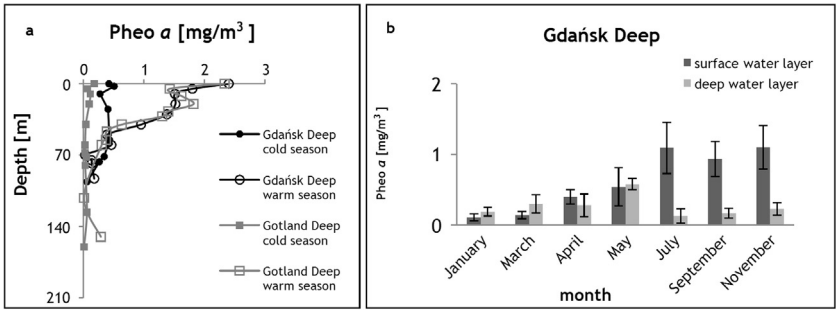

Figure 5 (a) Typical vertical profiles of pheopigment *a* concentrations measured from the Gdańsk Deep and Gotland Deep during the cold and warm seasons; (b) average monthly pheopigment *a* concentrations measured from surface and deep water layers of the Gdańsk Deep.

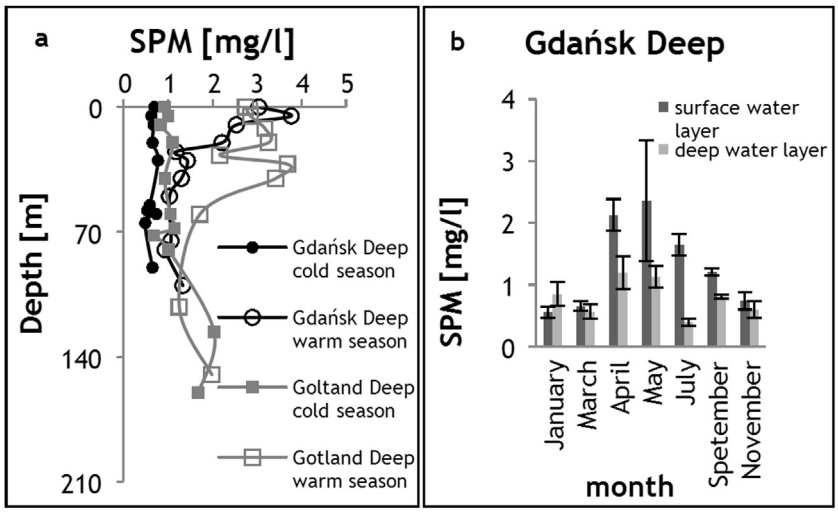

Figure 6 (a) Typical vertical profiles of suspended particulate matter (SPM) concentrations measured from the Gdańsk Deep and Gotland Deep during the cold and warm seasons; (b) average monthly SPM concentrations measured from surface and deep water layers of the Gdańsk Deep.

from the DWL (0.6 mg/l during the CS and 1.6 mg/l during the WS). The concentrations fell within ranges reported in previously published studies of the Gdańsk Deep (Burska et al., 2005; Maciejewska and Pempkowiak, 2014) and the Gotland Deep (Maciejewska and Pempkowiak, 2014; Meler et al., 2017b; Struck et al., 2004; Woźniak et al., 2018). Concentration profiles shown in Fig. 6a indicate similar SPM values for the SWL and DWL during the CS (concentrations were constant at some 0.4 mg/l) but higher SPM concentrations in the SWL (1.5 mg/l) relative to the DWL (0.4 mg/l) during the WS.

Fig. 6b shows monthly average SPM concentrations in the Gdańsk Deep (Figure S4 shows monthly average SPM for the Gotland Deep). From November to March, the DWL and SWL exhibited similar SPM concentrations of about 0.6–0.8 mg/l. Average SPM concentrations exceeding 2 mg/l (SWL) and 1 mg/l (DWL) were measured in April and May. Previously published studies have described seasonal variation in vertical SPM gradients (Burska et al., 2005; Struck et al., 2004; Szymczycha et al., 2017; Tamelander and Heiskanen, 2004). Burska et al. (2005) and Woźniak et al. (2018) reported that the POM contribution to SPM varies over the course of a year from 30% (CS) to 80% (WS). This highlights the significance of the planktonic biomass contribution to SPM.

4.4. Particulate organic carbon (POC) and particulate nitrogen (PN)

Fig. 7a and b show vertical POC and PN profiles. The SWL POC concentrations during the WS (up to 1.4 mg/l) exceeded those observed during the CS (0.1 mg/l). Respective CS and WS PN concentrations were 0.03 mg/l and up to 0.15 mg/l. The respective CS and WS DWL POC concentrations were 0.02 mg/l and 0.4 mg/l while PN concentrations were 0.04 mg/l and 0.015 mg/l (respectively for CS and WS). Fig. 7c and d show average monthly POC and PN concentrations for the Gdańsk Deep (Figure S5 – Gotland Deep). These show an increase in SWL POC between March (0.1 mg/l) and April (0.3 mg/l) with maximum concentrations observed in May (0.8 mg/l). These were followed by a steady decline to 0.3 mg/l in September, 0.15 mg/l in November and 0.08 mg/l in January. The DWL POC concentrations ranged from 0.07 mg/l (March) to 0.23 mg/l (May). These variations reflect phytoplankton and cyanobacterial abundance (source) vs grazing activity of zooplankton, POM mineralization and POM particle sedimentation (sinks) (Grossart and Ploug, 2001; Maciejewska and Pempkowiak, 2015; Struck et al., 2004).

The period from November to March experienced low PN concentrations (below 0.05 mg/l in the SWL and 0.02 mg/l in the DWL). The period from April to September experienced elevated PN concentrations (0.08 mg/l in the SWL and 0.02 mg/l in the DWL). May observations include exceedingly high PON concentrations (on average 0.08 mg/l in the SWL and 0.02 mg/l in the DWL). The concentrations observed fell within ranges reported for the Baltic Proper water column and typical seasonal SWL and DWL values therein (Andersson and Rudehall, 1993; Burska et al., 2005; Engel et al., 2002; Maciejewska and Pempkowiak, 2014; Struck et al., 2004; Szymczycha et al., 2017).

4.5. POM stable isotopic data: $\delta^{13}C_{POC}$ and $\delta^{15}N$

Fig. 8a shows water column $\delta^{13}C_{POC}$ profiles for selected areas. These exhibit a steep vertical $\delta^{13}C_{POC}$ gradient during both the CS and WS. In Gotland Deep the WS SWL values exceeded those measured from the DWL (−24.0‰ vs. −27.5‰) but CS data showed the opposite trend (−27.5‰ vs. −25.5‰). Average monthly $\delta^{13}C_{POC}$ values in the Gdańsk Deep (Fig. 8b) increased from January to May and decreased from July to January in the SWL. The DWL data exhibits a similar but more subtle trend. SWL $\delta^{13}C_{POC}$ ranged from −27.0‰ to −28.0‰ during the CS, while WS $\delta^{13}C_{POC}$ ranged from −23.0‰ to −26.0‰ (except July: −25.0‰). DWL $\delta^{13}C_{POC}$ values ranged from −26.0‰ to −28.0‰ throughout the year. Both deeps exhibit similar $\delta^{13}C_{POC}$ values and patterns (Fig. 8a, Figure S6) indicating comparable $\delta^{13}C$ distribution and dynamics (Table 1). The $\delta^{13}C_{POC}$ also resembled that reported from earlier studies of the Gdańsk

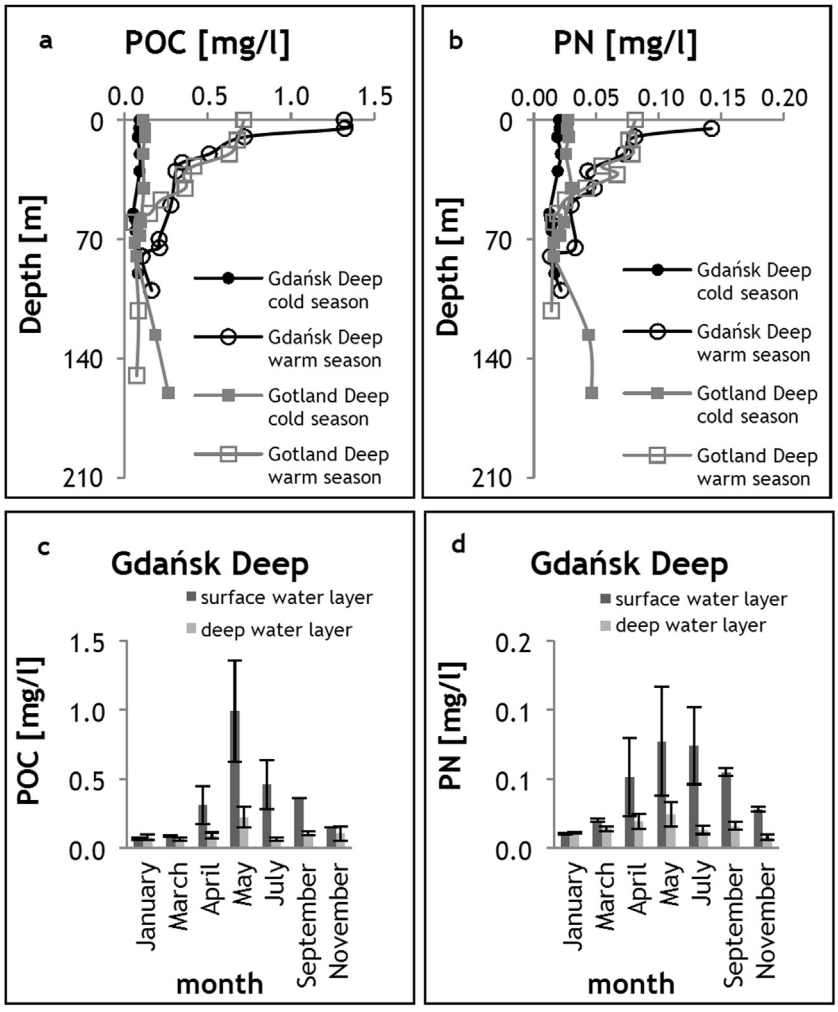

Figure 7 (a) Typical vertical profiles of POC concentrations in Gdańsk Deep and Gotland Deep; (b) typical vertical profiles of PN concentrations measured from the Gdańsk Deep and Gotland Deep; (c) average monthly POC concentrations measured from the Gdańsk Deep; (d) average monthly PN concentrations measured from the Gdańsk Deep.

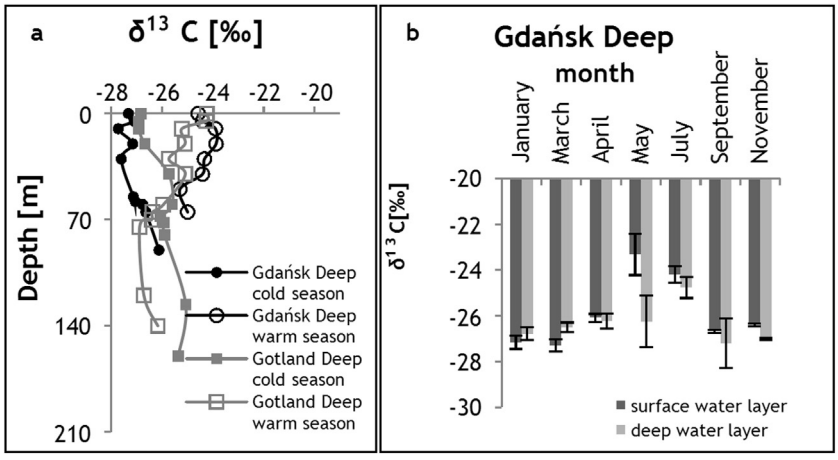

Figure 8 (a) Typical vertical profiles of $\delta^{13}C_{POC}$ values measured from the Gdańsk Deep and Gotland Deep during the cold and warm seasons; (b) average monthly $\delta^{13}C_{POC}$ values measured from surface and deep water layers of the Gdańsk Deep.

Table 1 Average concentrations and properties of particulate organic matter analyzed from the Gdańsk Deep and the Gotland Deep in surface water layer (SWL) and deep water layer (DWL) during warm season (WS) and cold season (CS).

Property	Unit	Average ± σ(*)							
		Gdańsk Deep				Gotland Deep			
		SWL		DWL		SWL		DWL	
		WS	CS	WS	CS	WS	CS	WS	CS
Salinity	–	7.19 ± 0.16	7.27 ± 0.13	11.78 ± 0.63	11.18 ± 0.64	7.34 ± 0.12	7.29 ± 0.17	11.50 ± 0.87	11.53 ± 0.42
Temperature	°C	10.75 ± 4.51	4.94 ± 1.94	4.29 ± 1.08	4.27 ± 1.37	11.09 ± 4.52	308 ± 1.22	4.15 ± 1.57	4.68 ± 0.47
pH	–	8.62 ± 0.61	8.00 ± 0.32	7.79 ± 0.30	7.58 ± 0.58	8.34 ± 0.11	7.97 ± 0.16	7.73 ± 0.40	7.34 ± 0.14
Chl *a*	mg/m^3	6.11 ± 4.09	1.18 ± 0.99	1.66 ± 0.78	0.33 ± 0.20	6.77 ± 3.59	0.70 ± 0.10	0.50 ± 0.31	0.18 ± 0.11
Pheo *a*	mg/m^3	0.82 ± 0.61	0.71 ± 0.31	0.31 ± 0.11	0.21 ± 0.13	0.88 ± 0.64	0.11 ± 0.06	0.24 ± 0.19	0.08 ± 0.04
SPM	mg/l	1.92 ± 0.38	0.83 ± 0.21	0.62 ± 0.19	0.64 ± 0.16	1.68 ± 0.87	0.69 ± 0.30	0.84 ± 0.41	1.21 ± 0.42
POC	mg/l	0.96 ± 0.41	0.19 ± 0.13	0.22 ± 0.11	0.10 ± 0.03	0.58 ± 0.32	0.13 ± 0.02	0.19 ± 0.05	0.10 ± 0.04
POC	mg/g	332.5 ± 41.1	194.7 ± 77.9	181.3 ± 71.7	160.7 ± 57.0	263.6 ± 62.00	176.1 ± 23.29	145.1 ± 64.73	130.1 ± 16.7
PN	mg/l	0.16 ± 0.34	0.03 ± 0.02	0.02 ± 0.01	0.01 ± 0.001	0.10 ± 0.11	0.02 ± 0.01	0.03 ± 0.06	0.01 ± 0.005
PN	mg/g	37.82 ± 13.30	28.69 ± 11.43	16.88 ± 7.95	23.21 ± 5.46	37.90 ± 11.63	28.12 ± 4.51	22.03 ± 9.52	18.58 ± 2.78
$\delta^{13}C$	‰	−24.20 ± 0.63	−26.90 ± 0.51	−26.48 ± 0.72	−26.88 ± 0.70	−25.45 ± 0.39	−25.81 ± 0.49	−25.86 ± 0.74	−25.94 ± 0.34
$\delta^{15}N$	‰	4.2 ± 0.4	nd	4.9 ± 0.6	nd	4.3 ± 0.3	4.8 ± 0.5	nd	nd

σ, standard deviation; nd, no data available.

Deep during the WS (Maksymowska et al., 2000; Szymczycha et al., 2017; Voss et al., 2005), of the Gotland Deep's DWL (Struck et al., 2004) and northern areas of the Baltic Sea (Heiskanen et al., 1998). The surface most sediment layers in both the Gdańsk Deep and the Gotland Deep exhibited $\delta^{13}C_{POC}$ values ranging from −26.0‰ to −27.0‰ (Szczepańska et al., 2012; Winogradow and Pempkowiak, 2014, 2018). This indicates transport and burial of PSM from the water column to surface sediments without considerable fractionation. Geochemical modeling by Gustafsson et al. (2015), surprisingly, indicates that $\delta^{13}C_{POC}$ in the Gotland Deep will shift from −24.0‰ to −23.0‰ by 2050 with seasonal variation limited to 2 ppm.

The low amounts of PTN captured by water sample filtration methods used here limited $\delta^{15}N$ measurements. Table 1 lists the few results obtained.

5. Discussion

5.1. Hydrological and seasonal constraints

Data presented in Figs. 2–5 and Figures S1–S5 clearly indicate two water masses (SWL and DWL) of different salinity separated by a well-established halocline. The SWL experiences annual temperature variation associated with seasonal irradiance effects (Dera and Woźniak, 2010; Voipio, 1981). This variation was parsed as warm and cold seasons (WS and CS) in data interpretation. Favorable conditions during the WS lead to increased abundance and activity of phytoplankton (Schneider et al., 2006, 2015; Wasmund and Uhlig, 2003) evident as elevated Chl *a* concentrations during the WS relative to the CS (Fig. 4a and b). An increased supply of planktonic POM however also causes a rapid increase in SPM concentrations (Fig. 6a and b) as well as concentrations of both measured components of POM (POC and PN; Fig. 7a and b). The WS also experiences increased contribution of POC to SPM (Fig. 9) and exhibits higher $\delta^{13}C_{POC}$ values (Fig. 10a and b). Interpretation of SWL dynamics must, therefore, assume seasonal variation in POM. A stable halocline separates the DWL from the SWL and the DWL exhibits constant salinity and temperature throughout the year. These stable stratification parameters suggest that surface and bottom water masses do not mix at any time. Many other studies have detected this feature of the Baltic Proper water column (Łomniewski et al., 1975; Rak, 2016; Voipio, 1981). Schneider et al. (2003) suggested that diffusion due to a concentration gradient causes widening of the halocline. This mechanism could influence salinity and possibly other dissolved species without affecting POM.

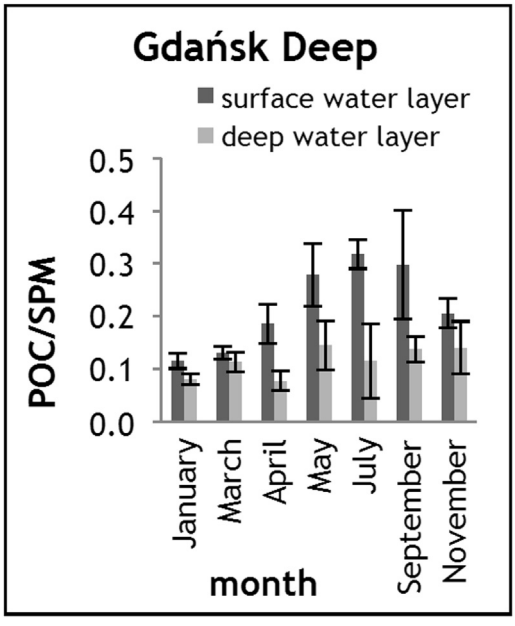

Figure 9 Average monthly POC/SPM ratios measured from surface and deep water layers of the Gdańsk Deep.

Mass transfer of SPM across the halocline occurs due to sedimentation (Burska et al., 2005; Lundsgaard et al., 1999; Struck et al., 2004). This causes deep water POM and Pheo *a* concentrations to increase in May during peak primary productivity in the SWL (see Fig. 5a and b, Figure S4). However, the DWL experiences only limited POM and Pheo *a* variation relative to the SWL. Data indicate a time lag between maximum Pheo *a* concentrations in the SWL and DWL (Fig. 5b and Figure S4). Conversion of Chl *a* to Pheo *a* evident from visible shifts and timing of peak concentrations takes several weeks as previously documented (Burska et al., 2005; Collos et al., 2005).

The consistency of salinity values in the SWL throughout the year signifies that river run-off does not significantly influence the water column of open sea regions. Similarly, Voss et al. (2005), found that run-off from the Vistula River does not influence the Baltic water column beyond a distance of 50 km from the river mouth (also see Maksymowska et al., 2000; Szymczycha et al., 2017).

As a proxy for phytoplankton abundance, SWL POM concentrations and other properties consistently varied according to seasonal forcing. POM concentrations and properties in the DWL remained more or less stable throughout a year (excluding the period of phytoplankton bloom in the SWL during May). Major saline water inflows from the North Sea to the Baltic Sea may influence POM in the DWL. The last major inflow occurred in 2015 however (Mohrholz et al., 2015; Rak, 2016), after DWL sampling for this study had already been completed. The general frequency of major saline inflows has decreased to one or two per decade within the last fifty years (Mohrholz et al., 2015; Szymczycha et al., 2019).

5.2. POM properties

5.2.1. POM contribution to SPM

Recent research on Baltic Proper seawater found that POC constitutes 49% of the POM mass. Regression analysis of POM and POC gave correlation coefficients $R^2 = 0.99$ (Woźniak et al., 2018). These relationships are typical of marine POM (Ríos et al., 1998), which represents a much larger (2×) contribution to SPM than POC.

The POC contribution to SPM (or POC/SPM ratio) for the study area varied by season as well as between surface and deep water layers (DWL: 0.12 for the CS and 0.14 for the WS; SWL: 0.15 for the CS and 0.32 for the WS) (Table 2; Fig. 9, Figure S7 – Gotland Deep). The POC/SPM ratio has been studied previously for both the Gdańsk Deep (Burska et al., 2005; Woźniak et al., 2018) and the Baltic Proper (Hakanson and Eckhell, 2005; Meler et al., 2017a, 2017b; Schumann et al., 2001; Woźniak et al., 2016, 2018). Contributions to the

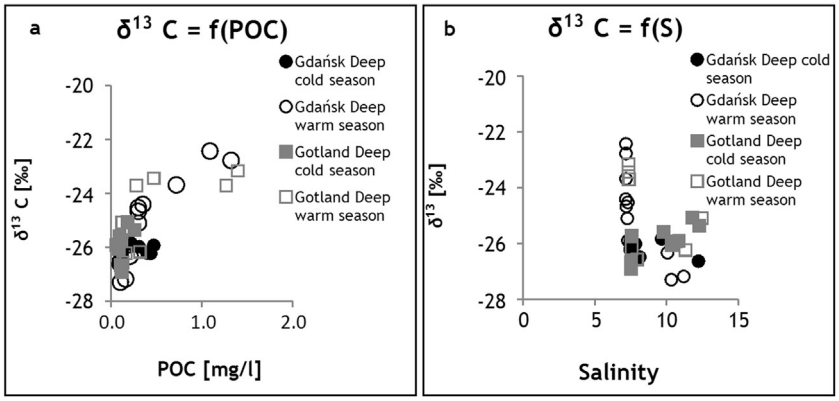

Figure 10 (a) Relationship between $\delta^{13}C_{POC}$ and POC; (b) the relationship between $\delta^{13}C_{POC}$ and salinity observed from the study area.

Table 2 Average ratios of selected POM constituents in surface water layer (SWL) and deep water layer (DWL) during warm season (WS) and cold season (CS).

Ratio	Unit	Average ± σ							
		Gdańsk Deep				Gotland Deep			
		SWL		DWL		SWL		DWL	
		WS	CS	WS	CS	WS	CS	WS	CS
POC/PN	mg/mg	5.8 ± 0.5	6.3 ± 0.6	10.8 ± 0.7	10.1 ± 1.2	5.9 ± 0.7	6.5 ± 0.4	7.7 ± 1.0	9.6 ± 0.6
POC/chl *a*	g/mg	0.14 ± 0.05	0.17 ± 0.08	0.13 ± 0.07	0.31 ± 0.22	0.085 ± 0.06	0.18 ± 0.07	0.38 ± 0.08	0.55 ± 0.18
PN/chl *a*	g/mg	0.04 ± 0.02	0.03 ± 0.01	0.02 ± 0.01	0.03 ± 0.01	0.02 ± 0.01	0.03 ± 0.01	0.04 ± 0.02	0.06 ± 0.04
POC/SPM	mg/mg	0.32 ± 0.07	0.15 ± 0.07	0.14 ± 0.07	0.12 ± 0.02	0.33 ± 0.06	0.18 ± 0.02	0.23 ± 0.06	0.08 ± 0.03
PN/SPM	mg/mg	0.08 ± 0.01	0.04 ± 0.01	0.03 ± 0.01	0.015 ± 0.01	0.06 ± 0.04	0.03 ± 0.02	0.03 ± 0.02	0.01 ± 0.00

σ, standard deviation.

SWL were 0.29 during the WS and 0.16 during the CS. Respective DWL contributions were about 2 times smaller. The POC/SPM ratio reported in the literature resembles that reported here. Seasonal dynamics reflect the increased inflow of planktonic organic matter to the POM reservoir during the WS (Andersson and Rudehall, 1993; Woźniak et al., 2018). Lower DWL ratios indicate POM mineralization during particle sinking (Andersson and Rudehall, 1993; Burska et al., 2005; Gustafsson et al., 2013). Increases of $\delta^{13}C_{POC}$ (Fig. 8) and POC concentration (Fig. 7a) during the WS support this interpretation as do the respective lower and higher C/N molar ratios in the DWL and SWL (Table 2; Fig. 11a).

5.2.2. Dynamics of $\delta^{13}C_{POC}$

Fig. 10a shows the relationship between POM $\delta^{13}C_{POC}$ and salinity. Salinity ranges of 9–13 psu indicate that SPM was filtered out of water samples collected from the DWL. These POM samples also gave depleted $\delta^{13}C_{POC}$ values. The SWL POM (salinity ranging from 7.3–7.6 psu) exhibited $\delta^{13}C_{POC}$ values of −22.5‰ to −27.0‰ (WS) and −25.5‰ to −27.3‰ (CS). This means that larger $\delta^{13}C_{POC}$ values measured in marine POM (−22.5‰ to −26.0‰) occur during increased primary production. The surface water layer of the Baltic Proper during this period also displays $(CO_2)_{aq}$ partial pressures well below 300 μatm (Schneider et al., 2006, 2015). Relative enrichment in $^{13}C_{POC}$ may arise from limited isotopic fractionation under low CO_2 availability or other disequilibrium conditions (Kopczyńska et al., 1995; Laws et al., 1995; Liu et al., 2018). During the CS, the equilibrium between $(CO_2)_{aq}$ and seawater is restored (Omstedt et al., 2014; Schneider et al., 2015) leading to lower $\delta^{13}C_{POC}$ values in POM.

Fig. 10b shows dependent relations between POC concentration and $\delta^{13}C_{POC}$. Plots generally show increasing $\delta^{13}C_{POC}$ with increasing POC concentrations, which accord with increased primary production during the WS. Measured $\delta^{13}C_{POC}$ values could be incorrectly interpreted as indicating a terrestrial POM contribution to the open Baltic POM, since its range overlaps with that of mixed land/marine-derived POM (Goñi et al., 2003; Hayes, 1993; Sauer et al., 2016; Szczepańska et al., 2012; Thornton and McManus, 1994; Voss and Struck, 1997). Recent studies have reported $\delta^{13}C_{POC}$ values ranging from −23.0‰ to −26.0‰ for marine planktonic biomass (Liu et al., 2018; Lowe et al., 2016; Miller et al., 2013). Neither hydrologic (salinity) nor biochemical (C/N ratios, POM/Chl *a* ratios) data ranges would support the interpretation that terrestrial organic matter makes a direct contribution to open water Baltic POM. The POM measured here thus appears to derive from planktonic biomass. Earlier studies of marine POM reported $\delta^{13}C_{POC}$ values ranging from −24.0‰ to −26.0‰ for coastal areas (Liu et al., 2018; Lowe et al., 2016; Miller et al., 2013) including the Baltic Sea coastal areas (Maksymowska et al., 2000; Struck et al., 2004). As indicated above these values may reflect limited fractionation of carbon isotopes due to low $(CO_2)_{aq}$ partial pressure

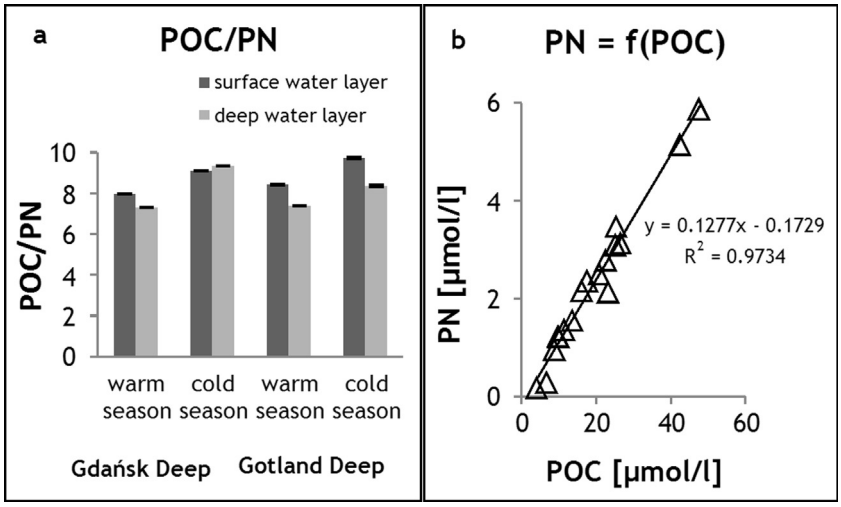

Figure 11 (a) Seasonal POC/PN ratios observed for the Gdańsk Deep and Gotland Deep; (b) relationship between PN and POC for the study area.

caused by intensive $(CO_2)_{aq}$ uptake during photosynthesis (Kopczyńska et al., 1995; Laws et al., 1995; Liu et al., 2018). Reports on Baltic Sea $\delta^{13}C_{POC}$ values indicate major seasonal variation in $\delta^{13}C_{POC}$ (Struck et al., 2004; Szymczycha et al., 2017). The relatively wide range of $\delta^{13}C_{POC}$ values observed throughout the year and throughout the water column reflects general $\delta^{13}C_{POC}$ increase with increasing phytoplankton abundance and variations due to temperature and compositional shifts in phytoplankton assemblages (Liu et al., 2018).

The observed $\delta^{13}C_{POC}$ values for water column POM shift from −22.5‰ to −27.0‰ but still, most likely, represent marine phytoplankton derived biomass generated during primary production or subjected to aging.

5.2.3. Molar ratios of organic carbon to nitrogen (C/N)

Molar ratios of carbon to nitrogen (C/N) are frequently used to assess POM provenance and/or age (Burska et al., 2005; Chester, 2003; Liu et al., 2018). Carbon to nitrogen (C/N) ratios of less than 9 (Koziorowska et al., 2016) or 12 (Liu et al., 2018) have been attributed to POM originating from marine primary production. Ratios measured by this study ranged from 5.8–10.8 (Table 2, Fig. 11). These values are typical of marine POM measured from the southern Baltic (Burska et al., 2005; Struck et al., 2004) but they differ from the Redfield ratio of 6.6. The departure from the Redfield ratio reported here (Fig. 11a) may arise from a contribution of zooplankton and relatively rapid PON ammonification in the SWL during the WS (Burska et al., 2005). Certain phytoplankton assemblages developed in the open Baltic during the WS could also give rise to the departure (Andersson et al., 2017; Wasmund et al., 1998). Hagström et al. (2001) attributed plankton biomass POC/PON ratios measured from the Baltic to this latter cause. During the CS, the DWL exhibited greater C/N ratios than during the WS (Fig. 11a) probably due to preferential mineralization of organic nitrogen relative to organic carbon during the sinking and/or aging of POM particles (Burska et al., 2005; Struck et al., 2004). The relatively narrow range of POC/PN ratios observed throughout most of the water column indicates, again, that terrestrial POM depleted of organic nitrogen contributes but little to SPM of the deeps studied (Liu et al., 2018). Lower POC/PN values from near-bottom water layer may reflect microbial communities in SPM floc settled out as surface sediment (Burska et al., 2005; Emeis et al., 2002; Rheinheimer et al., 1989).

A linear relationship observed between POC and PN (PN = 0.13, POC = 0.173, R^2 = 0.97) indicates that PN covaries with POM (Fig. 11b). A regression coefficient of 0.13 indicates the average total nitrogen to organic carbon ratio. This dependence can also be used to document inorganic nitrogen contribution to the PON pool (Liu et al., 2018). Studies interpreting C/N ratios have sometimes considered nitrogen speciation into organic and inorganic fractions (Grossart and Ploug, 2001; Koziorowska et al., 2016; Liu et al., 2018; Schubert and Calvert, 2001). The occurrence of ammonium ions in PSM could influence C/N ratios if SPM contains sufficient amounts of ammonium. Contrary to the expected effect of inorganic nitrogen, a plot of POC versus PN (Fig. 11b) predicts negative PN values for POC = 0. This indicates the presence of carbon that, under the analytical procedure used, is assumed to be sedimentary organic carbon. This fraction of carbon is deprived of organic nitrogen. The evidence thus indicates inorganic nitrogen (IN) is not incorporated into SPM in amounts influencing POC/TN ratio.

5.2.4. POC/Chl *a* ratio

The POC/Chl *a* ratio indicates the amount of biomass related to a Chl *a* unit and serves as a proxy for live phytoplanktonic contribution to the POM pool. Fig. 12a shows POC dependence on Chl *a*. Observed POC/Chl *a* values range from 85 (WS) to 180 (CS) in the SWL and from 170 (WS) to 550 (CS) in the DWL (Table 2, Fig. 12a). While seasonal oscillation in the SWL POC/Chl *a* ratio intuitively results from phytoplankton growth during the WS (Stoń et al., 2002; Tamm et al., 2019), variation in the DWL is more difficult to interpret. Live phytoplankton cells host abundant Chl *a*. Phytoplankton expiry and zooplankton grazing lyses cells to release labile components into the environment (Conover et al., 1988). This process and the exposure to environmental factors can transform Chl *a* into Pheo *a*. The POC/Chl *a* ratios for live marine phytoplankton varies from 50 mg/mg to 200 mg/mg. Values below 200 indicate POM derived from living

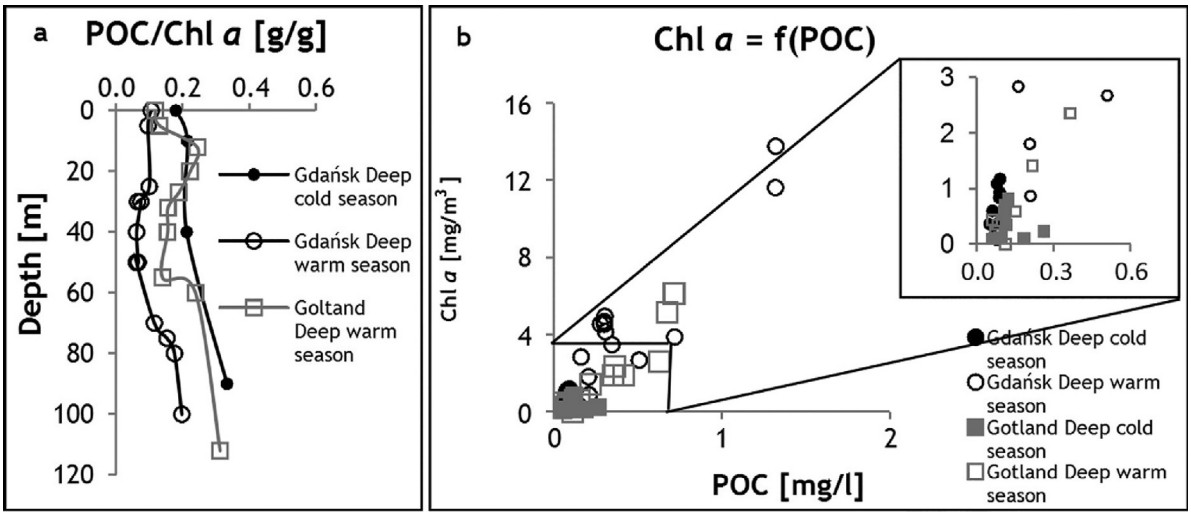

Figure 12 (a) Typical vertical profiles of the POC/Chl *a* ratio measured from the Gdańsk Deep and Gotland Deep; (b) relationship between Chl *a* and POC.

phytoplankton cells (Liu et al., 2018). The intercept of the Chl *a* versus POC curve at Chl *a* = 0 ranges from 40–50 μg POC/l, while the Chl *a* increase is equal to 0.008 mg Chl *a*/mg POC.

Woźniak et al. (2018) reported that the Baltic Sea samples exhibit an average POC/Chl *a* ratio of 125 for the SWL during the WS. The coefficient of variation assigned to the ratio was 68% indicating that the ratio varies over a relatively large range (Woźniak et al., 2018). The POC/Chl *a* ratios reported here range from 80–300. Differences in literature and measured ranges may result from different analytical methods used. For example, Liu et al. (2018) and Woźniak et al. (2018) used remote sensing while this study used extraction and spectroscopic absorption measurements, as did Andersson and Rudehall (1993), Burska et al. (2005) and Maciejewska and Pempkowiak (2014). The considerable POC/Chl *a* gradient at the halocline (Fig. 12b) indicates aged POM in the DWL consistent with other POM characteristics observed (smaller $\delta^{13}C_{POC}$, smaller contribution of POC to SPM, larger POC/PN ratio). Properties thus indicate POM produced by phytoplankton in the SWL during the WS and then aged in the DWL throughout the year.

An extended study devoted to optical properties of SPM in Baltic surface waters (Meler et al., 2017b; Woźniak et al., 2016; Woźniak et al., 2018) reported Chl *a*/POM ratios ranging from 2.5×10^{-3} g/g to 5.0×10^{-3} g/g. These data were derived from samples mostly collected from coastal localities, however, which showed considerable seasonal variation. The Chl *a*/POM values reported correspond to respective POC/Chl *a* ratios of 400 g/g and 200 g/g (using standard biogeochemical conventions; Liu et al., 2018). As such, they fell within the range of values reported in this study. The POC/Chl *a* ratios reported by Burska et al. (2005) study of the Gdańsk Deep ranged from 200–300 (g/g) in surface waters and from 2000–4000 in deeper layers. The latter range indicates that sediment was re-suspended and collected with analyzed samples.

The depth and seasonal dependence of Pheo *a* concentrations (Fig. 5a and b) relate to production rates of Pheo *a* and associated microzooplankton grazing rates. Pheopigment production in the absence of grazing may indicate irradiance and photo-degradation of these compounds. Year to year variation in the timing of the spring bloom between regions supports the interpretation that the Chl *a*/Pheo *a* ratio primarily reflects the rate of phytoplankton growth and is most strongly influenced by chlorophyll *a* levels. Zooplankton digestion of phytoplankton cells can account for observed correlations (Collos et al., 2005; Conover et al., 1988; Spence and Steven, 1974). The occurrence of Chl *a* in the DWL indicates that Chl *a* associated with POM persists long enough to be present after POM transport below the halocline. The Chl *a* concentration in the DWL is higher during the more productive WS than during the CS.

5.2.5. Implications of $\delta^{13}C_{POC}$ values and dynamics: POM origin

The $\delta^{13}C_{POC}$ data can help constrain the origin of POM and sedimentary organic matter in coastal waters (Goñi et al., 2003; Koziorowska et al., 2017; Sauer et al., 2016; Schubert and Calvert, 2001; Szczepańska et al., 2012; Thornton and McManus, 1994; Voss and Struck, 1997; Winogradow and Pempkowiak, 2018). Large differences between $\delta^{13}C_{POC}$ values for phytoplankton biomass and fluvial POM delivered to the marine environment form an end member model (Thornton and McManus, 1994). End members vary within a relatively narrow range of −21.0‰ to −22.5‰ for marine phytoplankton biomass (Sauer et al., 2016; Winogradow and Pempkowiak, 2018) and −27.0‰ to −28.5‰ for terrestrial POM (Sauer et al., 2016). Studies addressing the origin of POM in the Baltic Sea defined respective marine and terrestrial $\delta^{13}C_{POC}$ values of −22.0‰ (marine) and −27.0‰ (terrestrial) (Pempkowiak and Pocklington, 1983; Szczepańska et al., 2012; Winogradow and Pempkowiak, 2018), −21.5‰ and −27.0‰ (Voss et al., 2005) and −21.0‰ and −29.0‰ (Maksymowska et al., 2000) as end members.

As shown above (Fig. 10a, Table 1), $\delta^{13}C_{POC}$ values for POM from open Baltic Sea water ranged from −22.5‰ to −27.5‰. The POM $\delta^{13}C_{POC}$ contributed by river run-off also differs from that reported as characteristic of terrestrial POM. Two recent studies of POM contributions from river runoff into the Bay of Gdańsk (Gębka et al., 2018) and the Curonian Lagoon

(Lesutienė et al., 2018) reported average $\delta^{13}C_{POC}$ values of −30.1‰ and −31.8‰. The $\delta^{13}C_{POC}$ measurements reported in this study suggest that while WS $\delta^{13}C_{POC}$ POM values (−23.0‰) resemble those reported in the literature, $\delta^{13}C_{POC}$ values vary considerably throughout the year (Fig. 8a and b) but generally exhibit lower $\delta^{13}C$ values (−27.5‰) in the DWL during the CS. Struck et al. (2004) reported similar annual trends in both POM concentrations and $\delta^{13}C$ values for the Gotland Deep at 140 m water depth.

This study measured an annual average $\delta^{13}C_{POC}$ value for POM from the Gdańsk Deep and the Gotland Deep POM of −24.2‰. Concentrations of POM vary throughout the year from 3.1 mg/l during the WS to 0.4 mg/l during the CS. A weighted average of surface water POM $\delta^{13}C_{POC}$ is −23.2‰. This indicates that Baltic Sea average (end member) $\delta^{13}C_{POC}$ values are: −31.7‰ for fluvial POM and −23.2‰ for planktonic POM. Comparing marine and terrestrial $\delta^{13}C_{POC}$ values to those measured from sedimentary organic matter (e.g. −26.0‰; Szczepańska et al., 2012) indicates a terrestrial organic matter fraction of 0.70 or 0.67 assuming older estimates. Comparison with values from literature sources indicates that the proportion of terrestrial/planktonic organic matter in Baltic sedimentary organic matter does not significantly change (Maksymowska et al., 2000; Szczepańska et al., 2012; Voss et al., 2005; Winogradow and Pempkowiak, 2018).

While interpretations of sedimentary organic matter sources in the Baltic Sea remain somewhat tentative, the evidence suggests a major terrestrial contribution (43–67%; Winogradow and Pempkowiak, 2018). This is contradictory to the conclusion of preferentially autochthonous provenience of POC in the open Baltic. However, most sedimentary POC is transported and deposited, in the above bottom water layer, as floc (Emeis et al., 2002; Winogradow and Pempkowiak, 2018) and thus there is no contradiction between the reported here and the literature results.

6. Conclusions

This research investigated seasonal changes in the concentrations and character of POM from open water areas of the Baltic Sea, the landlocked sea characterized by a permanent stratification.

POM concentrations exhibited considerable seasonal variation indicating primary production as a major POM source. Mineralization and sedimentation serve as POM sinks for fresh and aged planktonic biomass. The POM properties measured included Chl *a*, contribution of POM to SPM, POM/Chl *a* ratio, C/N molar ratio and $\delta^{13}C_{POC}$ values. These revealed the interplay between live planktonic biomass and aged POM.

Measured POM $\delta^{13}C$ values were more depleted than those reported for other coastal areas. These lower values may arise from relatively short productive periods with low $(CO_2)_{aq}$ concentrations when assimilation of ^{13}C-enriched CO_2 takes place, at variance with longer periods of CO_2 assimilation in seawater at equilibrium with the atmosphere. Average $\delta^{13}C_{POC}$ of POM values adjusted for POM concentrations oscillations were −23.2‰. Literature-reported $\delta^{13}C_{POC}$ values for terrestrial POM range from −31.0‰ to −33.0‰. Given these values, terrestrial/marine end-member models indicate no significant shifts in sedimentary organic matter provenance.

Acknowledgements

The results reported herein were obtained within the framework of the statutory activities of the Institute of Oceanology Polish Academy of Sciences (theme II.7) and the EU 7FP 'Baltic C'. The authors are grateful to K. Koziorowska, B. Szymczycha and K. Kuliński for collecting some of the POM samples analyzed here.

Appendix A. Supplementary data

Supplementary data associated with this article can be found, in the online version, at https://doi.org/10.1016/j.oceano.2019.05.004.

References

Abril, G., Nogueira, M., Etcheber, H., Cabeçadas, G., Lemaire, E., Brogueira, M.J., 2002. Behaviour of organic carbon in nine contrasting European estuaries. Estuar. Coast. Shelf Sci. 54, 241–262, http://dx.doi.org/10.1006/ecss.2001.0844.

Almroth-Rosell, E., Kari, E., Hordoir, R., Meier, M., Hall, P., 2011. Transport of fresh and resuspended particulate organic material in the Baltic Sea – a model study. J. Mar. Syst. 87, 1–12, http://dx.doi.org/10.1016/j.jmarsys.2011.02.005.

Andersson, A., Rudehall, A., 1993. Proportion of plankton biomass in particulate organic carbon in the northern Baltic Sea. Mar. Ecol. Prog. Ser. 95, 133–139.

Andersson, A., Tomminen, T., Lehtinen, S., Jurgensk, K., Labrenz, M., Vitasalo, M., 2017. The pelagic food web. In: Snoeijs-Leijonmalm, P., Schubert, H., Radziejewska, T. (Eds.), Biological Oceanography of the Baltic Sea. Springer, Dordrecht, 281–332.

Bianchi, T.S., Rolff, C., Lambert, C.D., 1997. Sources and composition of particulate organic carbon in the Baltic Sea: the use of plant pigments and lignin-phenols as biomarkers. Mar. Ecol. Prog. Ser. 156, 25–31, http://dx.doi.org/10.3354/meps156025.

Björck, S., 1995. A review of the history of the Baltic Sea. Quatern. Int. 27, 19–40, http://dx.doi.org/10.1016/1040-6182(94)00057-C.

Burska, D., Pryputniewicz, D., Falkowska, L., 2005. Stratification of particulate organic carbon and nitrogen in the Gdańsk Deep (southern Baltic Sea). Oceanologia 47 (2), 201–217.

Chen, W., Wagnersky, P.J., 1993. High-temperature combustion analysis of dissolved organic carbon produced in phytoplankton cultures. Mar. Chem. 41, 167–171, http://dx.doi.org/10.1016/0304-4203(93)90115-5.

Chester, R., 2003. Marine Geochemistry, 2nd edn., Blackwell Sci., London, 506 pp.

Coban-Yıldız, Y., Altabet, M.A., Yılmaz, A., Tugrul, S., 2006. Carbon and nitrogen isotopic ratios of suspended particulate organic matter (SPOM) in the Black Sea water column. Deep-Sea Res. Pt. II 53, 1875–1892, http://dx.doi.org/10.1016/j.dsr2.2006.03.021.

Collos, Y., Husseini-Ratrema, J., Bec, B., Vaquer, A., Hoai, T.L., Rougier, C., Pons, V., Souchu, P., 2005. Pheopigment dynamics, zooplankton grazing rates and the autumnal ammonium peak in a Mediterranean lagoon. Hydrobiologia 550 (1), 83–93, http://dx.doi.org/10.1007/s10750-005-4365-1.

Conover, R.J., Durvasula, R., Roy, S., Wang, R., 1988. Probable loss of chlorophyll-derived pigments during passage through the gut of zooplankton, and some of the consequences. Limnol. Oceanogr. 31, 878–887, http://dx.doi.org/10.4319/lo.1986.31.4.0878.

De La Rocha, C.L., 2006. The biological pump. Treatise on Geochemistry, vol. 6. Pergamon Press, 83–111.

Dera, J., Woźniak, B., 2010. Solar radiation in the Baltic. Oceanologia 50 (4), 533–582, http://dx.doi.org/10.5697/oc.52-4.533.

Dzierzbicka-Głowacka, L., Kulinski, K., Maciejewska, A., Jakacki, J., Pempkowiak, J., 2011. Numerical modelling of POC dynamics in the southern Baltic under possible future conditions determined by nutrients, light and temperature. Oceanologia 53 (4), 1–22, http://dx.doi.org/10.5697/oc.53-4.971.

Dzierzbicka-Głowacka, L., Kulinski, K., Maciejewska, A., Pempkowiak, J., 2010. Particulate organic carbon in the southern Baltic Sea. Numerical simulation and experimental data. Oceanologia 52 (4), 621–648, http://dx.doi.org/10.5697/oc.52-4.621.

Emeis, K., Christiansen, C., Edelvang, K., Jähmlich, S., Kozuch, J., Laima, M., Leipe, T., Löffler, A., Lund-Hansen, L.C., Miltner, A., Pazdro, K., Pempkowiak, J., Pollehne, F., Shimmield, T., Voss, M., Witt, G., 2002. Material transport from the nearshore to the basinal environment in the southern Baltic Sea II. Synthesis of data on origin and properties of material. J. Mar. Syst. 35, 151–168, http://dx.doi.org/10.1016/S0924-7963(02)00127-6.

Engel, A., Meyerhofer, M., von Broker, K., 2002. Chemical and biological composition of suspended particles and aggregates in the Baltic Sea in summer (1999). Estuar. Coast. Shelf Sci. 55, 729–741, http://dx.doi.org/10.1006/ecss.2001.0927.

Ferrari, G., Bo, F., Babin, M., 2003. Geo-chemical and optical characterization of suspended matter in European coastal waters. Estuar. Coast. Shelf Sci. 57, 17–24, http://dx.doi.org/10.1016/S0272-7714(02)00314-1.

Gębka, K., Bełdowska, M., Saniawska, D., Kuliński, K., Bełdowski, J., 2018. Watershed characteristics and climate factors effect on the temporal variability of mercury in the southern Baltic Sea rivers. J. Environ. Sci. 68, 55–64, http://dx.doi.org/10.1016/j.jes.2017.11.030.

Goñi, M.A., Teixera, M.J., Perkey, D.W., 2003. Sources and distribution of organic matter in a river dominated estuary (Winyah Bay, SC, USA). Estuar. Coast. Shelf Sci. 57, 1023–1048, http://dx.doi.org/10.1016/S0272-7714(03)00008-8.

Grossart, H.-P., Ploug, P., 2001. Microbial degradation of organic carbon and nitrogen on diatom aggregates. Limnol. Oceanogr. 46, 267–277, http://dx.doi.org/10.4319/lo.2001.46.2.0267.

Gustafsson, O., Gelting, J., Andersson, P., Larsson, U., Roos, P., 2013. An assessment of upper ocean carbon and nitrogen export fluxes on the boreal continental shelf: A 3-year study in the open Baltic Sea comparing sediment traps, ^{234}Th proxy, nutrient, and oxygen budgets. Limnol. Oceanogr.-Meth. 11 (9), 495–510, http://dx.doi.org/10.4319/lom.2013.11.495.

Gustafsson, E., Morth, C.-M., Humborg, Ch., Gustafsson, B.G., 2015. Modelling the ^{13}C and ^{12}C isotopes of inorganic and organic carbon in the Baltic Sea. J. Mar. Syst. 148, 122–130, http://dx.doi.org/10.1016/j.jmarsys.2015.02.008.

Hagström, Å., Azam, F., Kuparinen, J., Zweifel, U.-L., 2001. Pelagic plankton growth and resource limitations in the Baltic Sea. In: Wulff, F.V., Rahm, L.A., Larsson, P. (Eds.), A systems analysis of the Baltic Sea. Springer-Verlag, Berlin, 177–210.

Hakanson, L., Eckhell, J., 2005. Suspended particulate matter (SPM) in the Baltic Sea — new empirical data and models. Ecol. Model. 189, 130–150, http://dx.doi.org/10.1016/j.ecolmodel.2005.03.015.

Hayes, J.M., 1993. Factors controlling the δ^{13}C contents of sedimentary organic compounds: principles and evidence. Mar. Geol. 113, 111–125, http://dx.doi.org/10.1016/0025-3227(93)90153-M.

Heiskanen, A.-S., Haapala, J., Gundersen, K., 1998. Sedimentation and sources of settling C, N and P in the coastal Northern Baltic Sea. Estuar. Coast. Shelf Sci. 46, 703–712, http://dx.doi.org/10.1006/ecss.1997.0320.

HELCOM, 2007. Climate change in the Baltic Sea area. In: Baltic Sea Environ. Proc. 111, 54 pp.

Hygum, B.H., Petersen, J.W., Søndergaard, M., 1997. Dissolved organic carbon released by zooplankton grazing activity – a high quality substrate pool for bacteria. J. Plankton Res. 19, 97–111, http://dx.doi.org/10.1093/plankt/19.1.97.

Kivi, K., Kaitala, S., Kuosa, H., Kuparinen, J., Leskinen, E., Lignell, R., Marcussen, B., Tamminen, T., 1993. Nutrient limitation and grazing control of the Baltic plankton during annual succession. Limnol. Oceanogr. 38, 893–905, http://dx.doi.org/10.4319/lo.1993.38.5.0893.

Kopczyńska, E., Goeyenes, L., Semeneh, M., Dehairs, F., 1995. Phytoplankton composition and cell carbon distribution in Prydz Bay, Antarctica: relation to organic particulate matter and its δ^{13}C values. J. Plankton Res. 17, 685–707, http://dx.doi.org/10.1093/plankt/17.4.685.

Koziorowska, K., Kuliński, K., Pempkowiak, J., 2016. Sedimentary organic matter in two Spitsbergen fjords: terrestrial and marine contribution based on carbon and nitrogen contents and stable isotopes composition. Cont. Shelf Res. 113, 38–46, http://dx.doi.org/10.1016/j.csr.2015.11.010.

Koziorowska, K., Kuliński, K., Pempkowiak, J., 2017. Distribution and origin of inorganic and organic carbon in the sediments of Kongsfjorden, Northwest Spitsbergen, European Arctic. Cont. Shelf Res. 150, 27–35, http://dx.doi.org/10.1016/j.csr.2017.08.023.

Koziorowska, K., Kuliński, K., Pempkowiak, J., 2018. Comparison of the burial rate estimation methods of organic and inorganic carbon and quantification of carbon burial in two high Arctic fjords. Oceanologia 60 (3), 405–418, http://dx.doi.org/10.1016/j.oceano.2018.02.005.

Kravchishina, M.D., Klyuvitkin, A.A., Pautova, L.A., Politova, N.V., Lein, A.Yu, 2018. Stable isotopic composition of particulate organic carbon in the Caspian Sea. Oceanology 58 (1), 45–56, http://dx.doi.org/10.1134/S0001437018010083.

Kuliński, K., Pempkowiak, J., 2008. Dissolved organic carbon in the southern Baltic Sea: quantification of factors affecting its distribution. Estuar. Coast. Shelf Sci. 78, 38–44, http://dx.doi.org/10.1016/j.ecss.2007.11.017.

Kuliński, K., Pempkowiak, J., 2011. The carbon budget of the Baltic Sea. Biogeosciences 8, 3219–3230, http://dx.doi.org/10.5194/bg-8-3219-2011.

Kuliński, K., She, J., Pempkowiak, J., 2011. Short and medium term dynamics of the carbon exchange between the Baltic Sea and the North Sea. Cont. Shelf Res. 31, 1611–1619, http://dx.doi.org/10.1016/j.csr.2011.07.001.

Laws, E.A., Popp, B.N., Bidigare, R.P., Kennicutt, M.C., Macko, S.A., 1995. Dependence of phytoplankton carbon isotopic composition on growth rate and [CO_2]aq: theoretical considerations and experimental results. Geochim. Cosmochim. Acta 59, 1131–1138, http://dx.doi.org/10.1016/0016-7037(95)00030-4.

Leipe, T., Tauber, F., Vallius, H., Virtasalo, J., Uścinowicz, Sz., Kowalski, N., Hille, S., Lindgren, S., Myllyvirta, T., 2011. Particulate organic carbon (POC) in surface sediments of the Baltic Sea. Geo-Mar. Lett. 31 (3), 175–188, http://dx.doi.org/10.1007/s00367-010-0223-x.

Leppakowski, E., Mihnea, P.E., 1996. Enclosed seas under man induced change: a comparison between the Baltic and Black Seas. Ambio 25, 380–389.

Lesutienė, J., Bukaveckas, P.A., Gasiūnaitė, Z.R., Pilkaitytė, R., Razinkovas-Baziukas, A., 2018. Assessing nature and dynamics of POM in transitional environment (the Curonian Lagoon, SE Baltic Sea) using a stable isotope approach. Ecol. Indic. 82, 217–226, http://dx.doi.org/10.1016/j.ecolind.2017.06.035.

Liu, Q., Solvaray, K., Lin, B., Wang, H., Chen, Ch-T.A., 2018. Biogeochemical characteristics of suspended particulate matter in deep chlorophyll maximum layers in the south East China Sea. Biogeosciences 15, 2091–2109, http://dx.doi.org/10.5194/bg-15-2091-2018.

Łomniewski, K., Mańkowski, W., Zaleski, J., 1975. Morze Bałtyckie. PWN, Warsaw, 508 pp.

Lorenzen, C.J., 1967. Determination of chlorophyll *and* pheopigments: spectrophotometric equations. Limnol. Oceanogr. 12 (2), 343–346, http://dx.doi.org/10.4319/lo.1967.12.2.0343.

Lowe, A.T., Galloway, A., Yeung, J., Dethier, M.N., Duggins, D.O., 2014. Broad sampling and diverse biomarkers allow characterization of nearshore particulate organic matter. Oikos 123 (11), 1341–1348, http://dx.doi.org/10.1111/oik.01392.

Lowe, A.T., Roberts, E.A., Galloway, A., 2016. Improved marine-derived POM availability and increased pH related to freshwater influence in an inland sea. Limnol. Oceanogr. 61 (6), 2122–2138, http://dx.doi.org/10.1002/lno.10357.

Lundsgaard, C., Olsen, M., Reigstad, M., Olli, K., 1999. Sources of settling material: aggregation and zooplankton mediated fluxes in the Gulf of Riga. J. Mar. Syst. 23, 197–210, http://dx.doi.org/10.1016/S0924-7963(99)00058-5.

Maciejewska, A., Pempkowiak, J., 2014. DOC and POC in the water column of the southern Baltic. Part I. Evaluation of factors influencing sources, distribution and concentration dynamics of organic matter. Oceanologia 56 (3), 523–548, http://dx.doi.org/10.5697/oc.55-3.523.

Maciejewska, A., Pempkowiak, J., 2015. DOC and POC in the water column of the southern Baltic. Part II. Evaluation of factors influencing organic matter concentration using multivariate methods. Oceanologia 57 (2), 168–176, http://dx.doi.org/10.1016/j.oceano.2014.11.003.

Maksymowska, D., Richard, P., Piekarek-Jankowska, H., Riera, P., 2000. Chemical and isotopic composition of the organic matter sources in the Gulf of Gdańsk (Southern Baltic Sea). Estuar. Coast. Shelf Sci. 51, 585–598, http://dx.doi.org/10.1006/ecss.2000.0701.

Meler, J., Ostrowska, M., Ficek, D., 2017a. Light absorption by phytoplankton in the southern Baltic and Pomeranian lakes: mathematical expressions for remote sensing application. Oceanologia 59 (3), 195–212, http://dx.doi.org/10.1016/j.oceano.2017.03.010.

Meler, J., Ostrowska, M., Ston-Egiert, J., Zdun, A., 2017b. Seasonal and spatial variability of light absorption by suspended particles in the southern Baltic. J. Mar. Syst. 170, 68–87, http://dx.doi.org/10.1016/j.jmarsys.2016.10.011.

Meyer-Harms, B., Reckermann, M., Voss, M., Sigmund, H.v., Bodungen, B., 1999. Food selection by calanoids in the euphotic layer of the Gotland Sea (Baltic Proper) during mass occurrence of N_2-fixing cyanobacteria. Mar. Ecol. Prog. Ser. 191, 243–250.

Miller, R., Page, H., Brzezinski, M.A., 2013. $\delta^{13}C$ and $\delta^{15}N$ of particulate organic matter in the Santa Barbara Channel: drivers and implications for trophic inference. Mar. Ecol. Prog. Ser. 474, 53–66, http://dx.doi.org/10.3354/meps10098.

Mohrholz, V., Naumann, M., Nausch, G., Krüger, S., Gräwe, U., 2015. Fresh oxygen for the Baltic Sea – an exceptional saline inflow after a decade of stagnation. J. Mar. Syst. 148, 152–166, http://dx.doi.org/10.1016/j.jmarsys.2015.03.005.

Omstedt, A., Humborg, Ch, Pempkowiak, J., Perttila, M., Rutgersson, A., Schneider, B., Smith, B., 2014. Biogeochemical control of the coupled CO_2–O_2 system of the Baltic Sea: a review of the results of Baltic-C. Ambio 43 (1), 49–59, http://dx.doi.org/10.1007/s13280-013-0485-4.

Parsons, T.R., 1966. Determination of Photosynthetic Pigments in Seawater. A Survey of Methods. UNESCO, Paris, 69 pp.

Pempkowiak, J., 1983. C_{18} reversed-phase trace enrichment of short- and long-chain (C_2-C_8-C_{20}) fatty acids from dilute aqueous solutions and sea water. J. Chromatogr. A 258, 93–102, http://dx.doi.org/10.1016/S0021-9673(00)96401-X.

Pempkowiak, J., Obarska-Pempkowiak, H., 2002. Long-term changes in sewage sludge stored in a reed bed. Sci. Total Environ. 297, 59–65, http://dx.doi.org/10.1016/S0048-9697(02)00023-2.

Pempkowiak, J., Pocklington, R., 1983. Phenolic aldehydes and stable carbon isotopes as indicators of the origin of humic substances in the marine environment. In: Christman, J., Gjessing, E. (Eds.), Aquatic and Terrestrial Humic Materials. Ann Arbor Sci. Publ., Ann Arbor, 371–386.

Rak, D., 2016. The inflow in the Baltic Proper as recorded in January–February 2015. Oceanologia 58 (3), 241–247, http://dx.doi.org/10.1016/j.oceano.2016.04.001.

Rheinheimer, G., Gocke, K., Hoppe, H., 1989. Vertical distribution of microbiological and hydro-chemical parameters in different areas of the Baltic Sea. Mar. Ecol. Prog. Ser. 52 (1), 55–70, http://dx.doi.org/10.3354/meps052055.

Ríos, A.F., Fraga, F., Pérez, F., Figueiras, F.G., 1998. Chemical composition of phytoplankton and particulate organic matter in the Ría de Vigo (NW Spain). Sci. Marina 62 (3), 257–271, http://dx.doi.org/10.3989/scimar.1998.62n3257.

Sauer, S., Hong, W.-Li, Knies, J., Lepland, A., Forwick, M., Klug, M., Eichinger, F., Baranwal, S., Cremiere, A., Chand, S., Schubert, C. J., 2016. Sources and turnover of organic carbon and methane in fjord and shelf sediments off northern Norway. Geochem. Geophys. Geosyst. 17 (10), 4011–4031, http://dx.doi.org/10.1002/2016GC006296.

Schneider, B., Buecker, S., Kaitala, S., Maunula, P., Wasmund, N., 2015. Characteristics of the spring/summer production in the Mecklenburg Bight (Baltic Sea) as revealed by long-term pCO_2 data. Oceanologia 57 (4), 375–385, http://dx.doi.org/10.1016/j.oceano.2015.07.001.

Schneider, B., Kaitala, S., Maunula, P., 2006. Identification and quantification of plankton bloom events in the Baltic Sea by continuous pCO_2 and chlorophyll *a* measurements on a cargo ship. J. Mar. Syst. 59, 238–248, http://dx.doi.org/10.1016/j.jmarsys.2005.11.003.

Schneider, B., Nauscg, G., Nagel, K., Wasmund, N., 2003. The surface water CO_2 budget for the Baltic Proper: a new way to determine nitrogen fixation. J. Mar. Syst. 42, 53–64, http://dx.doi.org/10.1016/S0924-7963(03)00064-2.

Schubert, C.J., Calvert, S.E., 2001. Nitrogen and carbon isotopic composition of marine and terrestrial organic matter in Arctic ocean sediments: implications for nutrient utilization and organic matter composition. Deep Sea Res. 48, 789–810, http://dx.doi.org/10.1016/S0967-0637(00)00069-8.

Schumann, R., Rentsch, D., Görs, S., Schiewer, U., 2001. Seston particles along a eutrophication gradient in coastal waters of the Southern Baltic Sea: significance of detritus and transparent mucoid material. Mar. Ecol. Prog. Ser. 218, 17–31, http://dx.doi.org/10.3354/meps218017.

Segar, D.A., 2012. Introduction to Ocean Science, 3rd edn., 1st digit. edn., ver. 3.0, 525 pp.

Sheppard, Ch. (Ed.), 2019. World Seas: An Environmental Evaluation, vol. I. Elsevier, Acad. Press, London, 912 pp.

Spence, C., Steven, D.M., 1974. Seasonal variation of the chlorophyll *a*: pheopigment ratio in the Gulf of St. Lawrence. J. Fish. Res. Board Can. 31 (7), 1263–1268, http://dx.doi.org/10.1139/f74-155.

Stoń, J., Kosakowska, A., Lotocka, M., Łysiak-Pastuszak, E., 2002. Pigment composition in relation to phytoplankton community structure and nutrient content in the Baltic Sea. Oceanologia 44 (4), 419–437.

Straat, K., Morth, C.-M., Undeman, E., 2018. Future export of particulate and dissolved organic carbon to coastal zones of the Baltic Sea. J. Mar. Syst. 177, 8–20, http://dx.doi.org/10.1016/j.jmarsys.2017.09.002.

Struck, U., Pollehne, F., Bauerfeind, E., Bodungen, B., 2004. Sources of nitrogen for the vertical particle flux in the Gotland Sea (Baltic Proper). The results from sediment trap studies. J. Mar. Syst. 45, 91–101, http://dx.doi.org/10.1016/j.jmarsys.2003.11.012.

Szczepańska, A., Zaborska, A., Maciejewska, A., Kuliński, K., Pempkowiak, J., 2012. Distribution and origin of organic matter in the Baltic sediments dated with ^{210}Pb and ^{137}Cs. Geochronometria 39 (1), 1–9, http://dx.doi.org/10.2478/s13386-011-0058-x.

Szczepańska, T., Uścinowicz, Sz., 1994. Geochemical Atlas of the Southern Baltic; 1:500 000. Polish Geological Institute, Warsaw.

Szymczycha, B., Maciejewska, A., Winogradow, A., Pempkowiak, J., 2014. Could submarine groundwater discharge be a significant carbon source to the southern Baltic Sea? Oceanologia 56 (2), 327–347, http://dx.doi.org/10.5697/oc.56-2.327.

Szymczycha, B., Winogradow, A., Kuliński, K., Koziorowska, K., Pempkowiak, J., 2017. Diurnal and seasonal DOC and POC variability in the land locked sea. Oceanologia 59 (3), 379—387, http://dx.doi.org/10.1016/j.oceano.2017.03.008.

Szymczycha, B., Zaborska, A., Bełdowski, J., Kuliński, K., Beszczyńska-Möller, A., Kędra, M., Pempkowiak, J., 2019. The Baltic Sea. World Seas: An Environmental Evaluation, vol. I. Elsevier, Acad. Press, London, 912 pp.

Tamelander, T., Heiskanen, A.-S., 2004. Effects of spring bloom phytoplankton dynamics and hydrography on the composition of settling material in the coastal northern Baltic Sea. J. Mar. Syst. 52, 217—234, http://dx.doi.org/10.1016/j.jmarsys.2004.02.001.

Tamm, M., Ligi, M., Panksep, K., Teeveer, K., Freiberg, R., Laas, P., Paavel, B., Kutser, T., Reinart, A., Tõnno, I., Nõges, T., 2019. Boosting the monitoring of phytoplankton in optically complex coastal waters by combining pigment-based chemotaxonomy and *in situ* radiometry. Ecol. Indic. 97, 329—340, http://dx.doi.org/10.1016/j.ecolind.2018.10.024.

Thomas, H., Pempkowiak, J., Wulff, F., Nagel, K., 2003. Autotrophy, nitrogen accumulation, and nitrogen limitation in the Baltic Sea: a paradox or a buffer for eutrophication. Geophys. Res. Lett. 30 (21), 8-1—8-4, http://dx.doi.org/10.1029/2003GL017937.

Thornton, S.F., McManus, J., 1994. Application of organic carbon and nitrogen stable isotope and C/N ratios as source indicators of organic matter provenance in estuarine systems: evidence from the Tay Estuary, Scotland. Estuar. Coast. Shelf Sci. 38, 219—233, http://dx.doi.org/10.1006/ecss.1994.1015.

Wasmund, N., Naush, G., Matthäus, W., 1998. Phytoplankton spring blooms in the southern Baltic Sea — spatio-temporal development and long-term trends. J. Plankton Res. 20 (6), 1099—1117, http://dx.doi.org/10.1093/plankt/20.6.1099.

Wasmund, N., Uhlig, S., 2003. Phytoplankton trends in the Baltic Sea. J. Mar. Sci. 60 (2), 177—186, http://dx.doi.org/10.1093/plankt/20.6.1099.

Winogradow, A., Pempkowiak, J., 2014. Organic carbon burial rates in the Baltic Sea sediments. Estuar. Coast. Shelf Sci. 138, 27—36, http://dx.doi.org/10.1016/j.ecss.2013.12.001.

Winogradow, A., Pempkowiak, J., 2018. Characteristics of sedimentary organic matter in coastal and depositional areas in the Baltic Sea. Estuar. Coast. Shelf Sci. 204, 66—75, http://dx.doi.org/10.1016/j.ecss.2018.02.011.

Woźniak, S., Darecki, M., Zabłocka, M., Burska, D., Dera, J., 2016. New simple statistical formulas for estimating surface concentrations of suspended particulate matter (SPM) and particulate organic carbon (POC) from remote sensing reflectance in the southern Baltic Sea. Oceanologia 58 (3), 161—175, http://dx.doi.org/10.1016/j.oceano.2016.03.002.

Woźniak, S., Sagan, S., Zabłocka, M., Stoń-Egiert, J., Borzycka, K., 2018. Light scattering and backscattering by particles suspended in the Baltic Sea in relation to the mass concentration of particles and the proportions of their organic and inorganic fractions. J. Mar. Syst. 182, 79—96, http://dx.doi.org/10.1016/j.jmarsys.2017.12.005.

Voipio, A., 1981. The Baltic Sea. Elsevier Sci. Publ., Amsterdam, 148 pp.

Voss, M., Liskow, I., Pastuszak, M., Rüβ, D., Schulte, U., Dippner, J. W., 2005. Riverine discharge into a coastal bay: a stable isotope study in the Gulf of Gdansk, Baltic Sea. J. Mar. Syst. 57 (1—2), 127—145, http://dx.doi.org/10.1016/j.jmarsys.2005.04.002.

Voss, M., Struck, U., 1997. Stable nitrogen and carbon isotopes as indicator of eutrophication of the Oder river (Baltic Sea). Mar. Chem. 59, 35—49, http://dx.doi.org/10.1016/S0304-4203(97)00073-X.

Oceanologia (2019) 61, 522—526

Available online at www.sciencedirect.com

ScienceDirect

journal homepage: www.journals.elsevier.com/oceanologia/

SHORT COMMUNICATION

Addendum to "Stokes transport in layers in the water column based on long-term wind statistics: assessment using long-term wave statistics"

Dag Myrhaug *, **Hong Wang, Lars Erik Holmedal**

Department of Marine Technology, Norwegian University of Science and Technology (NTNU), Trondheim, Norway

Received 21 January 2019; accepted 16 March 2019
Available online 27 April 2019

KEYWORDS
Marine litter;
Random surface gravity waves;
Stokes transport velocity;
Wave statistics;
Wind statistics

Summary This article addresses the Stokes drift in layers in the water column for deep water random waves based on wave statistics in terms of the sea state wave parameters significant wave height and mean zero-crossing wave period. This is exemplified by using long-term wave statistics from the North Atlantic, and is supplementary to Myrhaug et al. (2018) presenting similar results based on long-term wind statistics from the same ocean area. Overall, it appears that the results based on long-term wave statistics and long-term wind statistics are consistent. The simple analytical tool provided here is useful for estimating the wave-induced drift in layers in the water column relevant for the assessment of the transport of, for example, marine litter in the ocean based on, for example, global wave statistics.

* Corresponding author at: Department of Marine Technology, Norwegian University of Science and Technology (NTNU), Otto Nielsens vei 10, NO-7491 Trondheim, Norway. Tel.: +4773595697; fax.: +4773595697.
E-mail address: dag.myrhaug@ntnu.no (D. Myrhaug).
DOI of original article: 10.1016/j.oceano.2017.12.004.
Peer review under the responsibility of Institute of Oceanology of the Polish Academy of Sciences.

Production and hosting by Elsevier

Myrhaug et al. (2018) (hereafter referred to as MWH18) provided estimates of the Stokes transport in layers in the water column based on long-term wind statistics. The results were exemplified by using the Phillips and the Pierson-Moskowitz model wave spectra together with open ocean long-term mean wind speed statistics from one location in the northern North Sea and from four locations in the North Atlantic. This article is supplementary to MWH18 with the purpose to demonstrate how similar results of the Stokes transport in layers in the water column can be obtained by using long-term wave statistics in terms of the sea state parameters significant wave height and mean zero-crossing wave period. Results are exemplified by

https://doi.org/10.1016/j.oceano.2019.03.003

using open ocean deep water wave data from five locations in the North Atlantic, including comparison with the MWH18 results based on long-term wind statistics from four locations in the same ocean area. Overall, it appears that the results are consistent.

The recent attention on environmental issues associated with plastic and microplastic litter in the oceans is the main motivation for this supplement. It is well documented that plastic litter occurs and is transported in different layers in the water column beneath the ocean surface; see, for example, the references in the Introduction of MWH18 as well as in Van Canwenberghe et al. (2015), Acampora et al. (2016), and Ruiz-Orejon et al. (2016). One important component, which is responsible for the transport of plastic and microplastic located in different layers in the water column, is the Stokes drift. The Stokes drift is the wave-average of the water particle trajectory in the wave propagation direction, i.e. corresponding to the Lagrangian velocity. Furthermore, the volume Stokes transport corresponds to the integral over the water depth of the Stokes drift (Rascle et al., 2008). The background and more details of the Stokes drift are found in, for example, Dean and Dalrymple (1984). Myrhaug et al. (2016) gives a brief review of the literature up to that date (see the references therein) and of the more recent works referred to in MWH18. Furthermore, Paprota et al. (2016) presented results from an experimental study of wave-induced mass transport, while Paprota and Sulisz (2018) developed a theoretical model of the kinematics of water particles and mass transport under nonlinear waves generated in a closed flume and verified their results against the data from Paprota et al. (2016). Grue and Kolaas (2017) presented experimental results from wave tank measurements on particle paths and drift velocity in steep waves at finite water depth. Song et al. (2018) derived a theoretical statistical distribution of wave-induced drift for long-crested random waves in finite water depth. A recent comprehensive review of wave-induced drift was given by van den Bremer and Breivik (2018).

The article is organized as follows. This introduction is followed by the theoretical background of the Stokes transport velocity in layers in terms of the sea state wave parameters significant wave height and mean zero-crossing wave period. Then examples of results for long-term wave statistics from the North Atlantic are presented, including comparison with the results in MWH18 based on long-term wind statistics from the same area. Finally, the main conclusions are given.

The theoretical background follows that given in Section 2 of MWH18, where more details are provided. Since the main issue here is the transport of material in the water column, the drift velocity associated with the Stokes transport in different layers of the water column is a quantity of interest, which within a sea state of random waves is given by Eq. (9) in MWH18 as (where ω_1 replaces ω_p = spectral peak frequency).

$$V = \frac{1}{\Delta h}\left(e^{-2(\omega_1^2/g)h_1} - e^{-2(\omega_1^2/g)h_2}\right)\frac{\pi H_s^2}{8T_1}. \quad (1)$$

Here g is the acceleration of gravity, $H_s = 4\sqrt{m_0}$ is the spectral significant wave height, $T_1 = 2\pi/\omega_1 = 2\pi m_0/m_1$ is the spectral mean period, ω_1 is the spectral mean frequency, $\Delta h = h_2 - h_1$, h_1 and h_2 are two elevations in the water column, and the nth spectral moments are defined in terms of the wave spectrum $S(\omega)$ as

$$m_n = \int_0^\infty \omega^n S(\omega)\, d\omega; \quad n = 0, 1, 2, \ldots \quad (2)$$

where ω is the cyclic wave frequency. Thus, V is defined in terms of the sea state parameters H_s and T_1 in deep water.

Long-term wave statistics are commonly given in terms of joint frequency tables of H_s and T_p (= spectral peak period) or H_s and T_z (= mean zero-crossing wave period). In the following, an example of results will be presented for long-term wave statistics, where the wave statistics is given in terms of joint distributions of H_s and $T_z = 2\pi\sqrt{m_0/m_2}$. Thus, in this article T_1 is replaced with T_z, justified by that both these wave periods obtained from the wave spectrum are estimates of the mean zero-crossing wave period calculated from zero-crossing analysis of the time series of the wave elevation. For the Pierson-Moskowitz (PM) spectrum used in MWH18, $T_z = 0.92T_1$ (Tucker and Pitt, 2001).

The results are exemplified by the two locations $h_1 = 0$ and $h_2 = \lambda_z/s$ where $s \geq 2$, i.e. the Stokes transport velocity corresponds to the mean drift velocity over the thickness of the subsurface layer equal to a fraction of the wave length. The wave length is $\lambda_z = 2\pi/k_z$, where k_z is the wave number obtained from the deep water dispersion relationship $\omega_z^2 = gk_z$; here $\omega_z = 2\pi/T_z$ and

$$\lambda_z = \frac{g}{2\pi}T_z^2. \quad (3)$$

For $s = 2$ the result represents the mean drift velocity over the whole water column since the wave motion in deep water penetrates down to about half the wavelength. Thus, by taking $h_1 = 0$, $h_2 = \lambda_z/s$ and substituting Eq. (3) in Eq. (1), Eq. (1) is given as

$$V = \frac{\pi^2 s}{4g}\left(1 - e^{-4\pi/s}\right)\frac{H_s^2}{T_z^3}; \quad s \geq 2. \quad (4)$$

Then, by defining $\hat{V}(H_s, T_z)$, Eq. (4) is rearranged to

$$\hat{V}(H_s, T_z) \equiv \frac{V}{\frac{\pi^2 s}{4g}\left(1 - e^{-4\pi/s}\right)} = \frac{H_s^2}{T_z^3}. \quad (5)$$

Now $\hat{V}$ (and V) is defined in terms of the sea state parameters H_s and T_z in deep water (i.e. representing a sea state where each pair of H_s, T_z represents one storm condition with a duration of e.g. 3 h). Different parametric models for the joint probability density function (*pdf*) of H_s and T_z are given in the literature; a recent review is given by Bitner-Gregersen (2015). In this study, the statistical properties of $\hat{V}$ are exemplified by using the joint *pdf* of H_s and T_z fitted by Bitner-Gregersen and Guedes Soares (2007) (hereafter referred to as BGGS07) to five data sets from the North Atlantic, given in the Appendix.

Statistical quantities of interest are, for example, the expected (mean) value of $\hat{V}(H_s, T_z)$, $E[\hat{V}(H_s, T_z)]$, and the variance of $\hat{V}(H_s, T_z)$, $Var[\hat{V}(H_s, T_z)]$. This requires calculation of $E[\hat{V}^n(H_s, T_z)]$, obtained as (Bury, 1975)

$$E[\hat{V}^n(H_s, T_z)] = \int_0^\infty \int_0^\infty \hat{V}^n(H_s, T_z) p(H_s, T_z)\, dH_s\, dT_z. \quad (6)$$

Furthermore (Bury, 1975),

$$Var[\hat{V}(H_s, T_z)] = E[\hat{V}^2(H_s, T_z)] - (E[\hat{V}(H_s, T_z)])^2. \quad (7)$$

The BGGS07 distribution results are obtained from Eqs. (5), (6), (7), (A1), (A2), (A3) and (A4) and are given in Table 1, where Datasets 1 to 5 hereafter are referred to as Wa1 to Wa5. It appears that $E[V]$ is in the range of 0.00803 to 0.0216 m s^{-1}, and that the standard deviation to mean value ratios of $E[V]$ are large, that is, in the range 0.65 to 1.

Similarly, a characteristic value of λ_z, that is, $E[\lambda_z]$, can be obtained from Eq. (3) as

$$E[\lambda_z] = \frac{g}{2\pi} E[T_z^2] = \frac{g}{2\pi} \int_0^\infty \int_0^\infty T_z^2 p(H_s, T_z)\, dH_s\, dT_z. \quad (8)$$

From Table 1 it appears that $E[\lambda_z]$ is in the range of 82 m to 150 m.

A quantity of interest, for example, for the assessment of marine litter, is the volume Stokes transport per crest length. Table 1 gives the values of $M = E[V]E[\lambda_z]/2$, that is, the volume Stokes transport per crest length over the whole water column where there is wave activity, since the wave motion goes down to about half the wavelength. It appears that M is in the range of 0.6 m^2 s^{-1} (Wa5) to 0.9 m^2 s^{-1} (Wa1). For Wa1 this means, for example, that the mean volume Stokes transport ± one standard deviation is 0.13 m^2 s^{-1} and 1.7 m^2 s^{-1}, respectively, in the water column from the surface down to about 41 m. The corresponding intervals (i.e. the mean value ± one standard deviation) of the volume Stokes transport for the water columns from the surface ($z = 0$ m) to about $z = -21$ m, -10 m, -5 m, -2.5 m are (0.065, 0.85) m^2 s^{-1}, (0.033, 0.43) m^2 s^{-1}, (0.016, 0.21) m^2 s^{-1}, (0.008, 0.11) m^2 s^{-1}, respectively. This is of direct relevance, for example, to the volume transport of near neutrally buoyant litter as discussed in Fig. 3 of MWH18.

Now these results will be compared with those based on the PM spectrum given in Table 3 of MWH18. However, in order to be consistent with the present results, the MWH18 results should be based on T_z (instead of T_p). For a PM spectrum $T_p/T_z = 1.41$ (Tucker and Pitt, 2001), and thus $E[\lambda_z]/E[\lambda_p] = (T_z/T_p)^2 = 0.503$. Then, the $E[V]$ results for the PM spectrum given in Table 1 (referred to as Wi1 to Wi4) are obtained by multiplying the PM results in Table 2 of MWH18 by the factor $E[V_z]/E[V_p] = (T_p/T_z)^3 = 2.80$.

It appears that $E[V]$ is in the range 0.0143 m s^{-1} (Wi2) to 0.0223 m s^{-1} (Wi3), which overall agrees with the wave statistics results, except for Wa5, which is significantly smaller. It is noted that the standard deviation to the mean value ratios of $E[V]$ are in the range 0.43 to 0.46, i.e. smaller than those based on wave statistics. The three values in the columns for $E[V]$ represent $E[V] - 1$SD (=st.dev.), $E[V]$, $E[V] + 1$SD, respectively. It appears that the wave statistics and the wind statistics values for $E[V]$ are partly in the same range. This is also the case for the values of M, except for datasets Wa2 and Wi2 (see Table 1; the three values given in the column for M are based on using $E[V] - 1$SD, $E[V]$, $E[V] + 1$SD, respectively). Overall, the values of M are larger based on wave statistics than based on wind statistics. This is mainly due to that the standard deviation of V and $E[\lambda_z]$ are larger based on wave statistics, which might be attributed to the different inherent features of the data.

The main conclusions are as follows:

1. Overall, it appears that the present assessment of Stokes transport in layers in the water column based on long-term wave statistics from five deep water locations in the North Atlantic are consistent with similar results in Myrhaug et al. (2018) based on long-term wind statistics from four locations in the same ocean area.
2. More specifically, the mean values of the surface Stokes drift based on wave statistics agree with those based on wind statistics except for one of the wave statistics datasets, which is significantly smaller. However, by comparing the results including the mean values plus and minus one standard deviation there is overlap between the wave and wind statistics results. This is also the case for the Stokes transport in the water

Table 1 Example of results using wind and wave statistics from the North Atlantic. The three values in the columns for $E[V]$ represent $E[V] - 1$SD (=st.dev.), $E[V]$, $E[V] + 1$SD, respectively, and the three values of M are based on the three values in the column for $E[V]$, respectively.

Distribution	$E[V]$ [m s^{-1}]	st.dev./m.v.	$E[\lambda_z]$ [m]	$M = \frac{E[V]E[\lambda_z]}{2}$ [m^2 s^{-1}]
WAVES				
BGGS07				
Dataset 1, Wa1	0.0030, 0.0216, 0.0401	0.86	82	0.124, 0.886, 1.65
Dataset 2, Wa2	0.0054, 0.0154, 0.0254	0.65	96	0.259, 0.739, 1.22
Dataset 3, Wa3	0.0033, 0.0204, 0.0375	0.84	85	0.139, 0.867, 1.60
Dataset 4, Wa4	0, 0.0112, 0.0224	1	118	0, 0.661, 1.32
Dataset 5, Wa5	0.00016, 0.00803, 0.0159	0.98	150	0.012, 0.602, 1.19
WIND				
Location				
20°W 60°N, Wi1	0.0127, 0.0222, 0.0317	0.43	55	0.348, 0.610, 0.873
10°W 40°N, Wi2	0.0077, 0.0143, 0.0209	0.46	23	0.089, 0.165, 0.241
40°W 50°N, Wi3	0.0127, 0.0223, 0.0319	0.43	55	0.349, 0.613, 0.877
20°W 45°N, Wi4	0.0107, 0.0188, 0.0269	0.43	39	0.209, 0.366, 0.523

column when the mean values plus and minus one standard deviation are taken into account. However, overall the values of the Stokes transport in the water column are larger than those based on wind statistics, which is attributed to that the standard deviation and the characteristic wave length are larger based on wave statistics.

The strength of this work together with that of Myrhaug et al. (2018) is that it demonstrates how the presented methods can be used to assess the Stokes transport velocity and the volume Stokes transport for deep water random waves within sea states using available wind and wave statistics, which is important for assessing further the drift of, for example, marine litter in the ocean.

Acknowledgements

This work was carried out as part of the project "Air-Sea Interaction and Transport Mechanisms in the Ocean" funded by the Norwegian Research Council, Norway Grant Id (221988). This support is gratefully acknowledged.

Appendix. Joint distributions of H_s, T_z

The joint *pdf* by BGGS07 is given as

$$p(H_s, T_z) = p(T_z|H_s)p(H_s), \tag{A1}$$

where $p(H_s)$ is the marginal *pdf* of H_s, given by the following three-parameter Weibull distribution

$$p(H_s) = \frac{r}{s}\left(\frac{H_s - t}{s}\right)^{r-1} \exp\left[-\left(\frac{H_s - t}{s}\right)^{r}\right], \quad H_s \geq t, \tag{A2}$$

where r, s and t are the Weibull parameters given in BGGS07; see Table A1.

$p(T_z|H_s)$ is the conditional *pdf* of T_z given H_s, given by the lognormal distribution

$$p(T_z|H_s) = \frac{1}{\sqrt{2\pi}\sigma T_z} \exp\left[-\frac{(\ln T_z - \mu)^2}{2\sigma^2}\right], \tag{A3}$$

where μ and σ^2 are the mean value and the variance, respectively, of $\ln T_z$ given as

$$\mu = a_1 + a_2 H_s^{a_3}, \qquad \sigma = b_1 + b_2 H_s^{b_3}, \tag{A4}$$

where the parameters in μ,σ are given in BGGS07; see Tables A2 and A3. All the BGGS07 data represent wave conditions in the North Atlantic. Datasets 1, 2 and 3 are numerically generated wave data taken from global databases representing 44 years (1958–2004) at 59°00′N, 19°00′W. Dataset 4 refers to Global Wave Statistics (GWS) zone 9 (the zone located south of Iceland and west of UK) representing visual observations collected from ship in normal service all over the world in the period 1949–1986. Dataset 5 refers to Juliet Shipborne Wave Recorder (SBWR) representing data registered at the Ocean Weather Station Juliet during 13 years since 1952 at 52°00′N, 20°00′W. More details are given in BGGS07.

Table A1 Weibull parameters for H_s, see Eq. (A2).

BGGS07, North Atlantic	s	r	t
Dataset 1	3.104	1.357	0.906
Dataset 2	2.848	1.419	1.021
Dataset 3	2.939	1.240	0.896
Dataset 4	2.857	1.449	0.838
Dataset 5	2.420	1.169	1.258

Table A2 BGGS07: The parameters in the mean value of $\ln T_z$, see Eq. (4).

BGGS07, North Atlantic	a_1	a_2	a_3
Dataset 1	1.350	0.366	0.392
Dataset 2	1.365	0.375	0.453
Dataset 3	0.790	0.805	0.292
Dataset 4	0.835	1.139	0.119
Dataset 5	1.952	0.168	0.499

Table A3 BGGS07: The parameters in the standard deviation of $\ln T_z$, see Eq. (A4).

BGGS07, North Atlantic	b_1	b_2	b_3
Dataset 1	0.020	0.165	−0.166
Dataset 2	0.033	0.285	−0.752
Dataset 3	0.055	0.195	−0.269
Dataset 4	0.140	0.030	−0.958
Dataset 5	0.070	0.066	−0.081

References

Acampora, H., Lyashevska, O., van Franeker, J.A., O'Connor, F., 2016. The use of beached bird surveys for marine plastic litter monitoring in Ireland. Mar. Environ. Res. 120, 122–129, http://dx.doi.org/10.1016/j.marenvres.2016.08.002.

Bitner-Gregersen, E.M., 2015. Joint met-ocean description for design and operations of marine structures. Appl. Ocean Res. 51, 279–292, http://dx.doi.org/10.1016/j.apor.2015.01.005.

Bitner-Gregersen, E., Guedes Soares, C., 2007. Uncertainty of average steepness prediction from global wave databases. In: Guedes Soares, C., Das, P.K. (Eds.), Advancements in Marine Structures. Taylor and Francis Group, London, UK, 3–10.

Bury, K.V., 1975. Statistical Models in Applied Science. John Wiley & Sons, New York, 646 pp.

Dean, R.G., Dalrymple, R.A., 1984. Water Wave Mechanics for Engineers and Scientists. Prentice-Hall, Inc., New Jersey, USA, 353 pp.

Grue, J., Kolaas, J., 2017. Experimental particle paths and drift velocity in steep waves at finite water depth. J. Fluid Mech. 810, R1, http://dx.doi.org/10.1017/jfm.2016.726.

Myrhaug, D., Wang, H., Holmedal, L.E., 2018. Stokes transport in layers in the water column based on long-term wind statistics. Oceanologia 60 (3), 305–311, http://dx.doi.org/10.1016/j.oceano2017.12.004.

Myrhaug, D., Wang, H., Holmedal, L.E., Leira, B.J., 2016. Effects of water depth and spectral bandwidth on Stokes drift estimation based on short-term variation of wave conditions. Coastal Eng. 114, 169–176, http://dx.doi.org/10.1016/j.coastaleng.2016.04.001.

Paprota, M., Sulisz, W., 2018. Particle trajectories and mass transport under mechanically generated nonlinear water waves. Phys. Fluids 30, 102101, http://dx.doi.org/10.1063/1.5042715.

Paprota, M., Sulisz, W., Reda, A., 2016. Experimental study of wave-induced mass transport. J. Hydraul. Res. 54 (4), 423—434, http://dx.doi.org/10.1080/00221686.2016.1168490.

Rascle, N., Ardhuin, F., Queffeulou, P., Croizè-Fillon, D., 2008. A global wave parameter database for geophysical applications. Part 1: Wave-current-turbulence interaction parameters for the open ocean based on traditional parameterizations. Ocean Model. 25 (3—4), 154—171, http://dx.doi.org/10.1016/j.ocemod.2008.07.006.

Ruiz-Orejon, L.F., Sarda, R., Ramis-Pujol, J., 2016. Floating plastic debris in the Central and Western Mediterranean Sea. Mar. Environ. Res. 120, 136—144, http://dx.doi.org/10.1016/j.marenvres.2016.08.001.

Song, J., He, H., Cao, A., 2018. Statistical distribution of wave-induced drift for random ocean waves in finite water depth. Coastal Eng. 135, 31—38, http://dx.doi.org/10.1016/j.coastaleng.2018.01.002.

Tucker, M.J., Pitt, E.G., 2001. Waves in Ocean Engineering. Elsevier, Amsterdam, 548 pp.

Van Canwenberghe, L., Devriese, L., Galgani, F., Robbens, J., Janssen, C.R., 2015. Microplastics in sediments: a review of techniques, occurrence and effects. Mar. Environ. Res. 111, 5—17, http://dx.doi.org/10.1016/j.marenvres.2015.06.007.

van den Bremer, T.S., Breivik, Ø., 2018. Stokes drift. Phil. Trans. R. Soc. A 376 (2111), http://dx.doi.org/10.1098/rsta.2017.0104.

Oceanologia (2019) 61, 527—533

Available online at www.sciencedirect.com

ScienceDirect

journal homepage: www.journals.elsevier.com/oceanologia/

SHORT COMMUNICATION

Thin chlorophyll layer concomitant of the thermohaline intrusion in the confluence of the Gulf Stream and Labrador Current (a case study)

Genrik S. Karabashev *

Laboratory of Ocean Optics, Shirshov Institute of Oceanology, Russian Academy of Sciences, Moscow, Russia

Received 5 January 2019; accepted 7 May 2019
Available online 22 May 2019

KEYWORDS
Chlorophyll distribution;
CDOM fluorescence;
Seawater temperature;
Depth-cycling fluorometer;
Labrador water intrusion;
Northwestern Atlantic Ocean

Summary Based on the depth-cycling data of a fluorometer probe in the northwestern Atlantic ocean, this paper considers features of the chlorophyll fluorescence layer against a background of concurrent variability of seawater temperature and fluorescence of CDOM (Colored Dissolved Organic Matter). The vertical distributions of chlorophyll fluorescence complied with the criteria of a thin chlorophyll layer at the site where changes of temperature and CDOM fluorescence were indicative of the intrusion of Labrador waters into adjacent warmer waters below the upper mixed layer. As may be supposed, the thin chlorophyll layer was due to the gyrotactic trapping of phytoplankton cells induced by water shear between the upper mixed layer and the intrusion.

This presentation is based on observations accomplished in September 1991 in the northwestern Atlantic ocean (the 23rd cruise of the r/v *Vityaz*, Shirshov Institute of Oceanology (SIO), USSR Academy of Sciences). In brief, the use of a fluorometer probe resulted in evidence of a thin chlorophyll layer away from coastal zone and shallows. Nothing of this kind was observable during two previous decades of fluorimetric measurements carried out by the author in the oceans. For a number of circumstances, the thin layer results of the *Vityaz* cruise remained unpublished. Recent researches on thin chlorophyll layers in the marine environment (Durham and Stocker, 2012) suggest examining the abandoned data in the context of present-day achievements and difficulties.

The airborne laser lidars show a capacity for detecting subsurface thin layers of particles in aquatic areas spanning hundreds of miles (Churnside and Donaghay, 2009; Vasilkov

* Corresponding author at: Laboratory of Ocean Optics, Shirshov Institute of Oceanology RAS, 36 Nahimovskiy Prospekt, 117997 Moscow, Russia. Tel.: +7 4954224333; fax. (499)124-59-83.
E-mail address: genkar@mail.ru.
Peer review under the responsibility of Institute of Oceanology of the Polish Academy of Sciences.

Production and hosting by Elsevier

https://doi.org/10.1016/j.oceano.2019.05.001

et al., 2001). However, such sensors are unable to discriminate mineral and living (chlorophyll-bearing) particles in the backscattered light or to take advantage of red chlorophyll fluorescence from subsurface clouds of phytoplankton because pure water severely attenuates the red light (Jerlov, 1976). The advent of submersible fluorimeters and other optical instruments in the seventies–eighties of the 20th century facilitated obtaining high-resolution vertical profiles of chlorophyll concentration and resulted in the discovery of thin layers of phytoplankton mainly in coastal and shelf waters (Dekshenieks et al., 2001; Durham et al., 2009; Sullivan et al., 2010).

Impressive results regarding thin layers of chlorophyll in a coastal environment were obtained with the help of moored autonomous profilers (Sullivan et al., 2010) but this approach is difficult to implement in offshore regions. The Bio-Argo-buoys may be useful for obtaining a general idea of thin layer occurrence. However, being uncontrollable after start up, these buoys are unsuitable for monitoring the evolution of a thin layer of moderate extent. The underwater gliders (Rudnick et al., 2004) are much more flexible owing to their suitability to be operated as a fleet of gliders (Bhatta et al., 2005). A glider travel speed makes up 40–45 cm/s (Rudnick et al., 2004) and is comparable to or lower than a flow speed typical of chlorophyll-bearing subsurface waters. Therefore, a single glider does not allow us to distinguish spatial changes of a mesoscale structure from its variations in time. Among others, such structures involve the thermohaline intrusions of roughly 10–15 km in extent and about 10 h in residence time (Schmitt, 1994). The present communication aims to demonstrate the suitability of a ship-borne submersible fluorometer probe for studying thin chlorophyll layers associated with the intrusions common in large-scale thermohaline fronts.

The submersible fluorometer MZF (transliterated Russian capital letters for Marine Fluorometer Probe) is a ship-borne probe for recording the vertical profiles of four quantities from zero to the 250 m depth and transmitting respective signals via armored cable into the laboratory data processing unit (Karabashev and Khanaev, 1988). These quantities are the hydrostatic pressure as a measure of submersion depth z, seawater temperature T°C, the intensity of fluorescence of CDOM (Colored Dissolved Organic Matter) F_{CDOM}, and the intensity of chlorophyll fluorescence F_{chl}. Both fluorescences are excited with light pulses of a xenon flash lamp in separate seawater volumes outside the housing of a submersible module. Light traps protect these volumes from ambient light. Their design allows filling them with standard samples for on-deck calibration of F_{chl} channel in units of chlorophyll concentration. The CDOM fluorescence is excited in the near UV spectral range and recorded in the blue-green window. The chlorophyll fluorescence is excited in the blue and recorded in the red where the peak of F_{chl} belongs.

The rate of data acquisition is 8 Hz. The signals of T°C, F_{CDOM}, F_{chl}, and z are digitized and transmitted to the laboratory module. Successful operation of the MZF probe in the SIO RAS field missions in 1984–1987 demonstrated its reliability. Depending on the signal level, the accuracy of optical signal estimates is 5–10%. The resolution of the temperature channel is 0.03°C in the range from zero to 33°C. The resolution of the depth channel is 0.25 m from zero to 250 m depth.

Fig. 1 displays the localization of cruise stations 3579, 3581, 3587, and 3588 in reference to main currents and

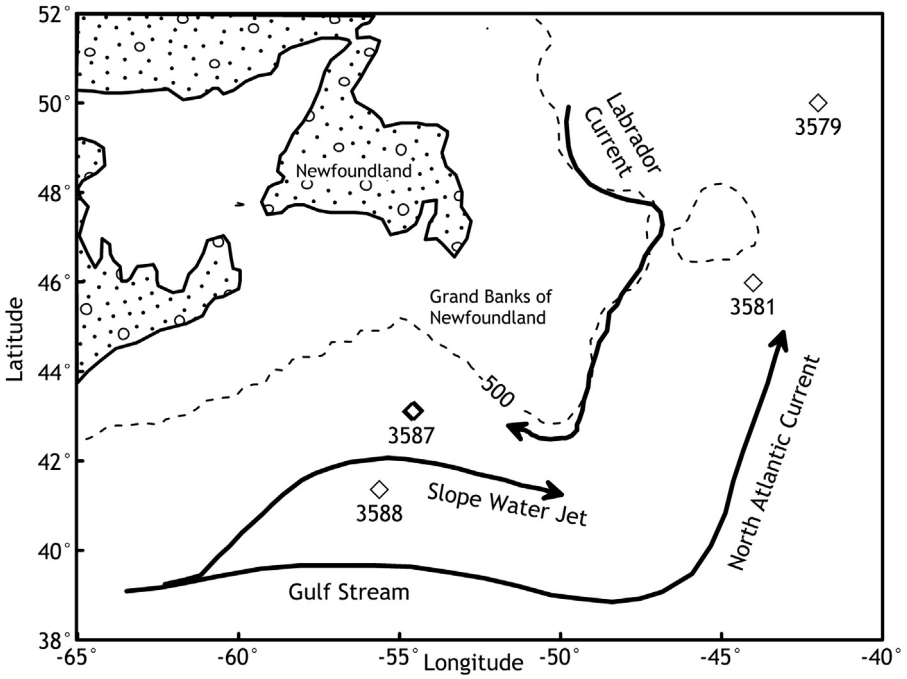

Figure 1 Coordinates, date, and initial local time of stations 3579 (42.00°W, 49.98°N, 09/08/1991, 15:22), 3581 (43.98°W, 45.96°N, 09/09/1991, 11:14), 3587 (54.53°W, 43.05°N, 09/18/1991, 00:25), and 3588 (55.61°W, 41.34°N), 09/18/1991, 15:22) occupied with the MZF fluorometer during the 23rd cruise of r/v *Vityaz* in the NW Atlantic Ocean. The pathways of the Gulf Stream, North Atlantic Current, Slope Water Jet, and Labrador Current are adapted from Pickart et al. (1999). Depth contours 0 m (solid) and 500 m (dashed) are plotted from the bathymetry gridded with the help of GEBCO Grid Demonstrator (https://www.bodc.ac.uk/).

continental slope (500 m isobath as dashed contour). When *Vityaz* arrived at scheduled station 3587 on the evening of September 17, 1991, the wind enhanced up to 18 m/s, and the MZF probe proved to be the only instrument suitable for on-deck activity without breaking the safety rules. This opened the way to a depth cycling in the upper 250 m thick layer by means of the MZF probe during nighttime. The following considerations justified this activity.

(i) Station 3587 located in the Gulf Stream and Labrador Current confluence between the shelf-break and the Slope Water Jet (Fig. 1). This is an appropriate place for monitoring the impact of water dynamics on the distribution of natural seawater admixtures.

(ii) The MZF channel of chlorophyll fluorescence has been calibrated in units of chlorophyll concentration C_{chl} [mg/m^3] based on water samples taken concurrently with the MZF casts at the earlier station of the same cruise. The linear dependence of F_{chl} upon C_{chl} has been found at $R^2 > 0.9$.

(iii) Night time is optimal for determinations of chlorophyll with a submersible fluorometer because specific fluorescence of chlorophyll in living phytoplankton cells is unaffected by sunlight at night (Karabashev, 1987). Elimination of probable sunlight impact on the chlorophyll fluorescence is desirable when using depth-dependence of chlorophyll fluorescence F_{chl} as a proxy for the vertical distribution of chlorophyll in the water.

(iv) Fast vessel's drift of wind as strong as 18 m/s promised high spatial resolution of observations by means of the MZF depth-cycling for several hours.

Operations at station 3587 took place on September 18 and involved four series of seven MZF casts each. Their timing and results are given in Fig. 2. The following findings merit attention.

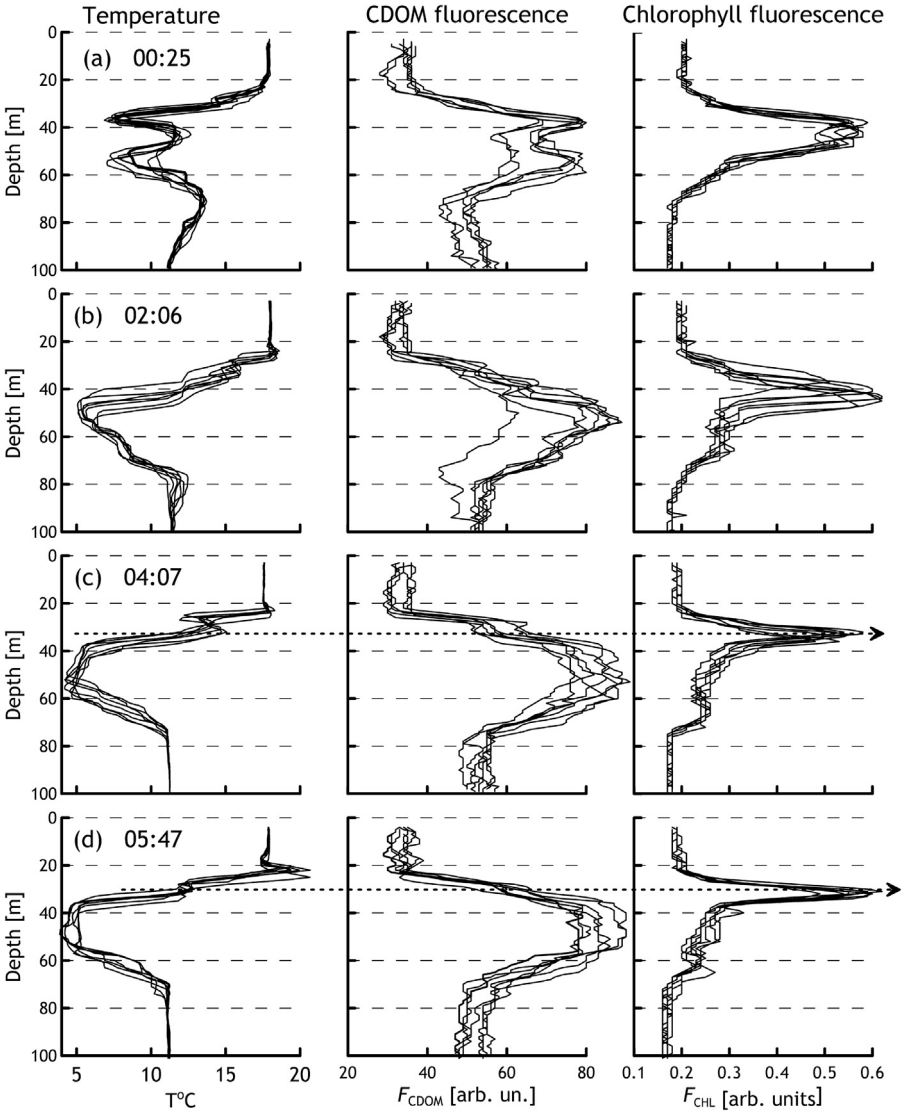

Figure 2 The results of using the MZF fluorometer at station 3587 on September 18, 1991, in the depth-cycling mode for concurrently recording seawater temperature T°C, the CDOM fluorescence intensity F_{CDOM}, and chlorophyll fluorescence intensity F_{chl}. The cycling series (a)–(d) took roughly 20–25 min each and started at 00:25, 02:06, 04:07, and 05:47 local time.

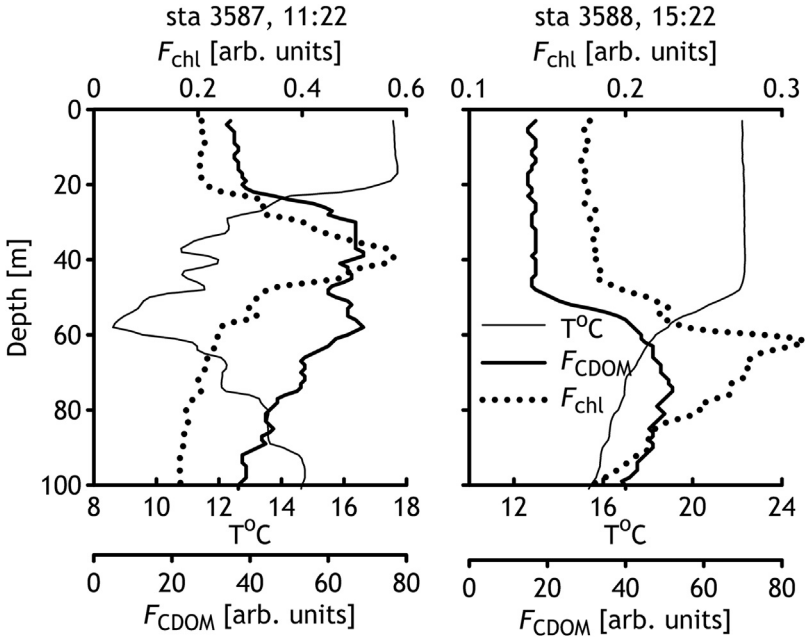

Figure 3 Profiles of T°C, F_{CDOM}, and F_{chl} recorded with the MZF fluorometer on September 18, 1991, at stations 3587 (11:22) and 3588 (15:22).

(a) The profiles of every quantity exhibited specific shapes. They changed from one series to another and remained hardly distinguishable within individual series.
(b) A strong inverse correlation was inherent to the vertical distributions of T°C and F_{CDOM}.
(c) The temperature minima and CDOM fluorescence maxima enhanced from series to series. The F_{chl} maxima decreased in the half-width and increased in amplitude. They occurred at the same depth that remained shallower in reference to the extrema of T°C and F_{CDOM}.

These changes took place against a background of unsteady wind. It was permanent in the direction from west to east, but changed in strength. The wind speed dropped from 18 m/s during the first series to 5–6 m/s during the fourth one. As a result, the lengths of depth-cycling tracks made up 3.1, 1.5, 1.1, and 0.8 km from the first series to the last one and the whole drift of the vessel was 12–15 km long.

Wind easing in the morning of September 18 allowed resuming the works in the scheduled section at 55°W, and *Vityaz* returned to the site of the first profiling series at station 3587 (stations 3587 and 3588 in Fig. 1 indicate the northern part of this section). Fig. 3 displays the profiles of F_{chl}, F_{CDOM}, and T°C recorded at station 3587 where the first MZF series has been started 11 h earlier. It is evident that the general view of vertical distributions of F_{chl}, F_{CDOM}, and T°C remained the same, but later profiles exhibited larger half-widths as compared to the earlier ones. Fifty miles south of station 3587, the distributions of the same quantities have radically changed in thickness of the upper mixed layer and shape of vertical distributions of F_{chl}, F_{CDOM}, and T°C (Fig. 3, station 3588).

It is remarkable that the shapes of F_{chl}, F_{CDOM}, and T°C profiles at earlier stations (Fig. 4 and Fig. 5 at 11:32) were similar to those at station 3587 in Fig. 3.

By now, there is solid evidence that (1) high-latitude waters are more abundant in refractory CDOM as compared to waters of moderate latitudes and (2) the CDOM is a tracer of ocean interior mixing (Nelson et al., 2010). The map of the climatology of surface water CDOM shows a fast decrease of this tracer from north to south exactly where above stations of the *Vityaz* cruise belong (Fig. 1 in Nelson et al. (2010)). These and earlier findings (Kalle, 1963; Karabashev and

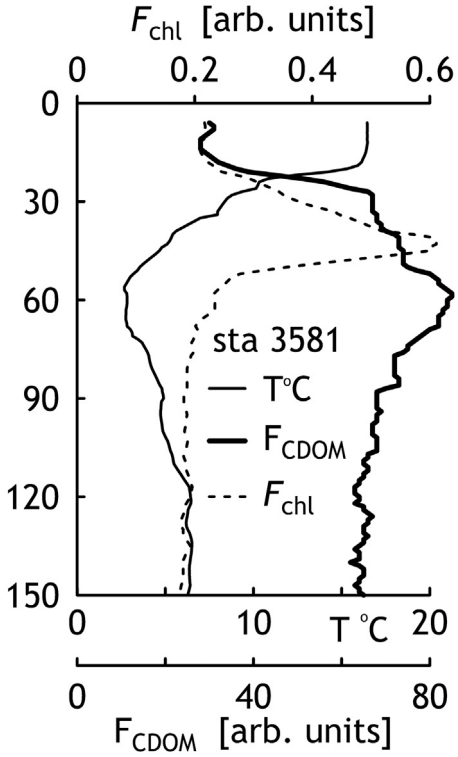

Figure 4 Profiles of T°C, F_{CDOM}, and F_{chl} recorded on September 9, 1991, at station 3581 (11:22).

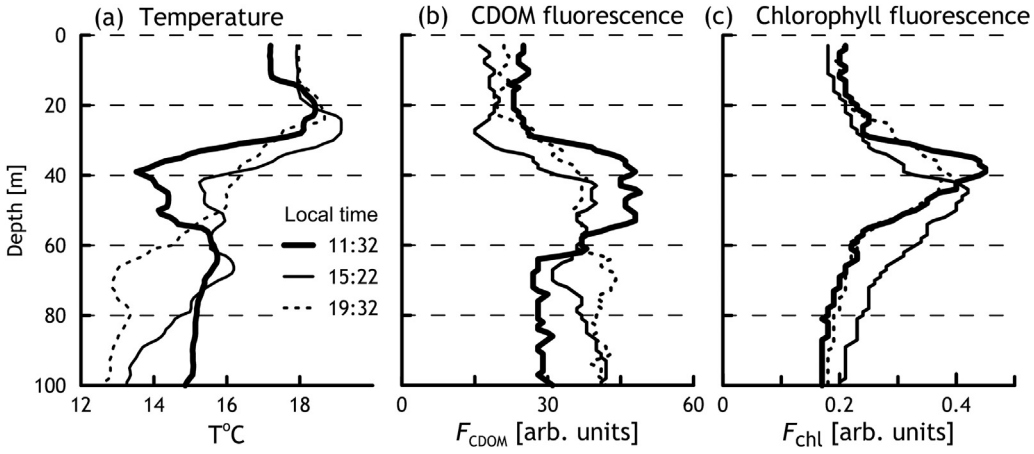

Figure 5 Profiles of T°C (a), F_{CDOM} (b), and F_{chl} (c) recorded on September 8, 1991, at station 3579 (11:32, 15:22, and 19:32 local time).

Solov'yov, 1973) justify the use of CDOM fluorescence as a universal conservative tracer of water exchange in the ocean thickness.

The seasonal variations of subsurface chlorophyll maximums in the northwestern Atlantic Ocean were investigated in Cox et al. (1982). They relied on determinations of this pigment performed from 1961 to 1977 to the west of 60°W in slope waters (484 samples at 67 stations) and in the northern Sargasso Sea (379 samples at 43 stations). The above profiles of chlorophyll fluorescence are consistent with the generalized vertical distributions of chlorophyll in depth and amplitude of early-autumn chlorophyll maximums (Fig. 1 and Fig. 2 in Cox et al. (1982)).

The area in Fig. 1 refers to a region known for the particular complexity of its water dynamics (Fratantoni, 2001). The flow arrows in this figure represent a pattern of local currents based on a generalization of observational data (Pickart et al., 1999) relevant to the period of the 23rd cruise of the r/v *Vityaz*. The hydro-physics team led by S.N. Shustenko observed a thermohaline front between stations 3587 and 3588 and revealed the intrusion-favorable thermohaline structure of waters in the vicinity of station 3581 and found that the North Atlantic Current bifurcated and turned eastwards in the vicinity of station 3579.

At station 3587, the vessel drifted in the direction 78°–90° toward the cold waters of the Labrador Current rich in CDOM. The latter agrees well with the shape of the profiles in Fig. 2: the temperature decreased and CDOM fluorescence increased from earlier depth-cycling series to the later ones in the layer between 20 m and 70 m depth levels. The vertical distributions of T°C and F_{CDOM} exhibited more intricate shapes and lower amplitudes during the first series as compared to the later one. This is expectable of a liquid medium inhomogeneity at the final stage of its disintegration. The shape and features of T°C and F_{CDOM} profiles behaved as if they were shaped by an intrusion of the Labrador Current waters into the local warmer waters. The depth of the chlorophyll maximum remained unchanged throughout the drift, but the half-width of chlorophyll profile decreased noticeably with the approach to the source of the intrusion (depth-cycling series (c) and (d) in Fig. 2).

At a minimum distance from the presumed source of the intrusion, the F_{chl} maximum occurred at the depth of the thermocline ledge noticeable in the profiles of T°C and F_{CDOM} (dashed arrows in panels (c) and (d) in Fig. 2 designate the depth of ledge). Apparently, the ledge marks the junction of local profiles of temperature and CDOM fluorescence with profiles of the same characteristics in the intrusion of Labrador waters.

It is conventional to distinguish the deep chlorophyll maxima up to tens of meters thick and the thin layers (Durham and Stocker, 2012). Specific features of the thin layers: (i) they are reproducible when depth-cycling, (ii) their vertical extent is smaller than 5 m, (iii) maximal content of chlorophyll is at least thrice as large as its background concentration in water. Profiles of F_{chl} in panel (d) of Fig. 2 adequately satisfy criteria (i)–(iii). The average peak of these profiles measures 6.2 $\pm$ 0.5 m in half-width and is the largest in amplitude relative to those in panels (a)–(c). At that, the amplitudes of T°C minimum and F_{CDOM} maximum in panel (d) exceed their estimates in panels (a)–(c). These relations suggest that the distributions in panel (d) were obtained at the point, which was nearest to the source of the intrusion. Respectively, the profiles in panel (a) were obtained at the maximum distance from the same point where chlorophyll peak exhibited much larger half-width.

Durham and Stocker (2012) consider six mechanisms responsible for the origination of thin chlorophyll layers in areas where coastal and riverine waters interact with the ocean waters. The authors give emphasis to the fact that chlorophyll bearers are living particles able to aggregate contrary to the instability of water flows. One of the mechanisms is the intrusion proper when intruding waters are richer in phytoplankton in reference to local waters. Such is not the case for patterns in Fig. 2 because chlorophyll fluorescence maximum is shallower than the core of intrusion. The constancy of the depth and amplitude of chlorophyll maximum in Fig. 2 is contradictory to straining of a phytoplankton patch by differential advection over depth (mechanism (a) in Durham and Stocker (2012)).

In panels (c) and (d) in Fig. 2, the arrows mark the depth of the thin chlorophyll layer interfacing the subsurface mixed

water thickness and the intrusion. There is a good probability of the largest water shear at a depth of contact of oppositely sensed flows. According to Durham and Stocker (2012), high fluid shear suppresses the vertical migration of motile phytoplankton to the extent that living particles turn out to be trapped in a thin layer (gyrotactic trapping). This scenario appears the most appropriate for explaining the patterns in Fig. 2.

Intrusion slowing is destructive for shear-driven layering of non-conservative chlorophyll-bearing cells. In contrast, the conservative water properties, the temperature and CDOM fluorescence alike, are much less sensitive to short-lived forcings of local significance. That is why intrusive shapes of T°C and F_{CDOM} profiles at station 3587 survive while an intrusion-induced thin layer of F_{chl} transforms into a broad unimodal distribution (Fig. 3). By analogy with the daytime patterns at station 3587, it may be assumed that co-existence of extrema of T°C and F_{CDOM} with a broad vertical profile of F_{chl} below the upper mixed layer (Fig. 4 and Fig. 5) is indicative of the final stages of thermohaline intrusions of Labrador waters in the study area. According to modeling results (Durham and Stocker, 2012), the residence time of a thin chlorophyll layer due to gyrotactic trapping may be more than 12 h long. This is consistent with time scales of the above changes of distributions of T°C, F_{CDOM}, and F_{chl}. In total, the foregoing estimates and patterns are consistent with the inference that fine-scale horizontal intrusions occur in water mass fronts at all latitudes and measure 5—100 m in vertical extent at a horizontal scale of order 10 km (Schmitt, 1994).

The thermohaline intrusions in the offshore ocean waters may be accompanied by chlorophyll layers only a few meters thick much like the thin phytoplankton layers associated with the coastal zone phenomena. Further studies are needed to obtain an adequate notion of thin chlorophyll layers induced by intrusions in the offshore thermohaline fronts. This information is difficult to be obtained from determinations of light scattering because inorganic particles are usually the main contributors into the seawater turbidity and exhibit much longer residence time in the subsurface waters of the offshore areas as compared to the chlorophyll in living phytoplankton cells.

It is obvious that the scarcity of information on chlorophyll behavior in the offshore thermohaline intrusions is due to their covertness and unpredictable occurrence. Therefore, the accumulation of such information is likely to occur due to improvised research during ship expeditions in the frontal zones of the ocean. Modest dimensions of the intrusions in offshore fronts and high precision of present-day marine guidance are favorable for mapping an intrusion by means of a ship-based CTD probe, completed with a fluorometer module and operated at the low-speed depth-cycling mode. It is highly desirable to accompany this activity with observations of the sub-mesoscale water dynamics combined with the determination of species composition and the state of local phytoplankton. This again counts in favor of the ship-based approach.

Acknowledgments

This study was carried out under the state assignment topic no. 0149-2019-0003.FASO 0149-2019-0003).

The author is grateful to Sergey Khanaev for ensuring the uninterrupted operation of the MZF probe in the ocean under any weather conditions in the course of a long expedition.

This research did not receive any specific grant from funding agencies in the public, commercial, or not-for-profit sectors.

References

Bhatta, P., Fiorelli, E., Lekien, F., Leonard, N.E., Paley, D.A., Zhang, F., Bachmayer, R., Davis, E., Fratantoni, D.M., Sepulchre, R., 2005. Coordination of underwater glider fleet for adaptive sampling. In: Proc. Internat. Workshop on Underwater Robotics, Genoa, Italy, 61—69.

Churnside, J.H., Donaghay, P.L., 2009. Thin scattering layers observed by airborne lidar. ICES J. Mar. Sci. 66 (4), 778—789, http://dx.doi.org/10.1093/icesims/fspQ29.

Cox, J.L., Wiebe, P.H., Ortner, P., Boyd, S., 1982. Seasonal development of subsurface chlorophyll maxima in slope water and the Northern Sargasso Sea of the Northwestern Atlantic Ocean. Biol. Oceanogr. 1 (3), 271—285, http://dx.doi.org/10.1080/01965581.1982.10749444.

Dekshenieks, M.M., Donaghay, P.L., Sullivan, J.M., Rines, J.E.B., Osborn, T.R., Twardowski, M.S., 2001. Temporal and spatial occurrence of thin phytoplankton layers in relation to physical processes. Mar. Ecol. Prog. Ser. 223, 61—71.

Durham, W.M., Kessler, J.O., Stocker, R., 2009. Disruption of vertical motility by shear triggers formation of thin phytoplankton layers. Science 323, 1067—1070, http://dx.doi.org/10.1126/science.1167334.

Durham, W.M., Stocker, R., 2012. Thin phytoplankton layers: characteristics, mechanisms, and consequences. Annu. Rev. Mar. Sci. 4, 177—207, http://dx.doi.org/10.1146/annurev-marine-120710-100957.

Fratantoni, D.M., 2001. North Atlantic surface circulation during the 1990s observed with satellite-tracked drifters. J. Geophys. Res. Oceans 106 (C10), 22067—22093, http://dx.doi.org/10.1029/2000JC000730.

Jerlov, N.G., 1976. Marine Optics. Elsevier, Amsterdam, 233 pp.

Kalle, K., 1963. Über das Verhalten und die Herkunft der in den Gewässern und in der Atmosphäre vorhandenen himmelblauen Fluoreszenz. Deutsche Hydrogr. Zt. 16, 153—166.

Karabashev, G.S., 1987. Fluorescence in the ocean. Gidrometeoizdat, Leningrad, 200 pp. (in Russian), http://dx.doi.org/10.13140/2.1.3439.7128.

Karabashev, G.S., Khanaev, S.A., 1988. Underwater multichannel fluorimeter for marine ecological research. J. Appl. Spectrosc. 49 (3), 979—981, http://dx.doi.org/10.1007/BF00662796.

Karabashev, G.S., Solov'yov, A.N., 1973. Photoluminescence of seawater, an indicator of dynamic processes in the ocean. Oceanology (USSR) 13, 490—493, (in Russian).

Nelson, N.B., Siegel, D.A., Carlson, C.A., Swan, C.M., 2010. Tracing global biogeochemical cycles and meridional overturning circulation using chromophoric dissolved organic matter. Geophys. Res. Lett. 37 (3), L03610, 1—5, http://dx.doi.org/10.1029/2009GL042325.

Pickart, R.S., McKee, T.K., Torres, D.J., Harrington, S.A., 1999. Mean structure and interannual variability of the Slope water system south of Newfoundland. J. Phys. Oceanogr. 29, 2541—2558, http://dx.doi.org/10.1175/1520-0485(1999)029<2541:MSAIVO>2.0.CO;2.

Rudnick, D.L., Davis, R.E., Eriksen, C.C., Fratantoni, D.M., Perry, M.J., 2004. Underwater gliders for ocean research. Mar. Technol. Soc. J. 38 (1), 48—59, http://dx.doi.org/10.4031/002533204787522703.

Schmitt, R.W., 1994. Double-diffusion in oceanography. Annu. Rev. Fluid Mech. 26, 255—285, http://dx.doi.org/10.1146/annurev.fl.26.010194.001351.

Sullivan, J.M., Donaghay, P.L., Rines, J.E.B., 2010. Coastal thin layer dynamics: consequences to biology and optics. Cont. Shelf Res. 30 (1), 50—65, http://dx.doi.org/10.1016/j.csr.2009.07.009.

Vasilkov, A.P., Goldin, Y.A., Gureev, B.A., Hoge, F.E., Swift, R.N., Wright, C.W., 2001. Airborne polarized lidar detection of scattering layers in the ocean. Appl. Optics 40 (24), 4353—4364, http://dx.doi.org/10.1364/AO.40.004353.

Oceanologia (2019) 61, 534—539

Available online at www.sciencedirect.com

ScienceDirect

journal homepage: www.journals.elsevier.com/oceanologia/

SHORT COMMUNICATION

Oocyte hydration in round goby *Neogobius melanostomus* from the Gulf of Gdańsk: another invasive strategy?

Hanna Kalamarz-Kubiak *, **Tatiana Guellard**

Department of Genetics and Marine Biotechnology, Institute of Oceanology, Polish Academy of Sciences, Sopot, Poland

Received 18 February 2019; accepted 5 June 2019
Available online 18 June 2019

KEYWORDS
Oocyte hydration;
Estradiol;
Female round goby

Summary The round goby (*Neogobius melanostomus*) is one of the most abundant non-native species in the Gulf of Gdańsk that use various strategies to increase fecundity and achieve invasive success. Oocyte hydration appears to be a specific osmotic adaptation of round goby's gametes for successful fertilization and hatching. The aim of this study was to demonstrate details of oocyte final maturation and hydration during the spawning-capable phase in round goby and also compare various indices such as 17β-estradiol (E_2), hepatosomatic index (HSI) and gonadosomatic index (GSI) among oocyte final maturation stages. E_2 fluctuated according to the development of oocyte batches. HSI did not show significant differences throughout the oocyte maturation. GSI was an inaccurate estimator of oocyte maturation in round goby. This study, for the first time, shows that hydration does accompany oocyte final maturation in this species. These findings are important to the cognition of biology and the adaptive strategies of this invasive species to environmental factors and can be essential components of the protection and preservation of native living resources in the Gulf of Gdańsk.

* Corresponding author at: Department of Genetics and Marine Biotechnology, Institute of Oceanology, Polish Academy of Sciences, Powstańców Warszawy 55, 81-712 Sopot, Poland. Tel.: +48 58 7311766; fax: +48 58 5512130.
E-mail address: hkalamarz@iopan.gda.pl (H.i. Kalamarz-Kubiak).
Peer review under the responsibility of Institute of Oceanology of the Polish Academy of Sciences.

https://doi.org/10.1016/j.oceano.2019.06.001

The round goby (*Neogobius melanostomus*) is a well-known, non-native species in the Baltic Sea and the Laurentian Great Lakes, probably transported to both ecosystems in ballast waters of ships from the Ponto-Caspian region (Crossman et al., 1992; Skóra and Stolarski, 1993). The first individuals of round goby in the Baltic Sea were observed in the Gulf of Gdańsk in 1990 (Skóra and Stolarski, 1993). Since then, round goby has become one of the most abundant species in the western part of the Gulf of Gdańsk and has successfully colonized other regions of the Baltic Sea (Sapota, 2012). The rapid expansion of this euryhaline, benthic species has motivated widespread research on life history, morphology, reproduction, habitat preferences, environmental tolerances, parasites and environmental effects (Kornis et al., 2012). Extremely aggressive, territorial behaviour, a fast genetic divergence and high adaptation to variability in environmental factors, have made round goby one of the most invasive species in the Baltic Sea (Björklund and Almqvist, 2010; Ojaveer et al., 2015). The species' varied diet and reproductive strategy also contribute to the invasion success (Kornis et al., 2012; Ojaveer et al., 2015). In the Gulf of Gdańsk, high densities of *N. melanostomus* slightly shifted the area of occurrence and foraging of native flounder (*Platichthys flesus*), viviparous eelpout (*Zoarces viviparous*) and black gobies (*Gobius niger*), which live in the same or similar habitats as intruders (Jażdżewski and Konopacka, 2002). In this area of the Baltic Sea, round goby diet consists of 60% of mussels, which can severely impact native benthic invertebrate populations and may result in the competition for food with both juvenile and adult flounder (Puntila et al., 2018). On the other hand, *N. melanostomus* may also predate on small individuals of the flounder and eggs of commercially valuable fish such as Atlantic herring (*Clupea harengus*) (Puntila et al., 2018; Wiegleb et al., 2019). In consequence, round goby as a competitor for food and habitats of native demersal fish can reduce the number of their populations and disturb biodiversity of native ecosystems.

N. melanostomus, as with many species of the family Gobiidae, is a batch spawner, which means that females can spawn several times throughout the same spawning period, releasing ovulated eggs in batches (Dinh, 2018). In the Baltic Sea, females may lay eggs from two to four times in the same spawning period (Sapota, 2012). This spawning strategy can be seen as a successful invasive strategy to increase fecundity and the survival probability of offspring by spreading out hatch times to mitigate predation risk and increase the likelihood that some offspring hatch during favourable conditions (McEvoy and McEvoy, 1992). *N. melanostomus* is a fish species that exhibits male parental care. Prior to spawning, the male of round goby excavates a nest underneath a stone or other hard substratum. During spawning, the female and male repeatedly deposit eggs or spread sperm on the nest ceiling. After spawning, the territorial male guards the nest against predators and continuously ventilates the eggs containing developing embryos (Meunier et al., 2009).

Another strategy of round goby to increase fecundity and achieve invasive success appears to be oocyte hydration as a specific osmotic adaptation of gametes for successful fertilization and hatching. It should be mentioned that this adaptive mechanism is considered as one of the crucial steps in the evolutionary history of the vertebrates (Finn et al., 2008). Fish oocyte hydration is a unique biological process that has been described as a marked increase in oocyte volume caused by the rapid uptake of fluid by the oocyte and the coalescence of yolk spheres and/or oil droplets (Cerdà et al., 2007; Milla et al., 2006). This process is based on the interplay between protein hydrolysis and ion accumulation to create an osmotic gradient, and aquaporins to regulate water influx (Cerdà et al., 2007; Fabra et al., 2006). The pre-ovulatory oocyte hydration is an important osmotic adaptation for the development of viable gametes when hypo-osmotic eggs are released into the hyperosmotic environment. What is more, this fluid influx ensures the physiological hydration of the embryos prior to the development of osmoregulatory organs (gill, kidney and gut) and maintains homeostasis (Wright and Fyhn, 2001). In the Gulf of Gdańsk, salinity varies from 7 to 12 PSU as a result of Vistula River water inflow and irregular inflows of saline water from the North Sea (Sztobryn et al., 1997). Therefore, euryhaline species such as round goby and their eggs can be exposed to different osmoregulatory challenges, on account of salinity changes in their habitats (Behrens et al., 2017). The adaptive strategy of euryhaline teleosts to the environmental salinity enables a switch from plasma hyperosmoregulation (environmental salinity $<$9 PSU) to plasma hypo-osmoregulation (environmental salinity $>$9 PSU) (Kültz, 2015). In turn, eggs' hydration of these teleosts protects against water loss to the hyperosmotic environment and against environmental ions diffusion into eggs, and the relatively low water content and low vitelline membrane permeability protect eggs against water influx and a continuous ion loss in the hypo-osmotic environment (Wright and Fyhn, 2001).

Although knowledge about *N. melanostomus*' reproductive cycle seems to be extensive, the presence of hydrated oocytes in round goby was only mentioned by Tomczak and Sapota (2006). However, so far, to the authors' knowledge, the histological analysis of oocyte hydration has not been presented and described in this species. The objective of this study was to demonstrate details of oocyte final maturation and hydration during the spawning-capable phase in invasive *N. melanostomus* and also compare various indices such as 17β-estradiol (E_2), hepatosomatic index (HSI) and gonadosomatic index (GSI) among oocyte final maturation stages. In female fish, E_2 is responsible for the regulation of oocyte growth within the gonads and supports the hepatic synthesis and secretion of vitellogenin (Lubzens et al., 2010). Moreover, changes in the circulating E_2 reflect well the oocyte batch recruitment cycle in batch spawners (Mandich et al., 2004). HSI is a measure of the energy reserves of an animal, especially in fish. GSI is used to measure sexual maturity in relation to the ovaries' development.

Adult females of *N. melanostomus* (n = 50) were caught in the Gulf of Gdańsk (Gdynia, Poland) during the spawning-capable phase (April—August). Fish were held in tanks with aerated water of salinity 8 $\pm$ 0.5 PSU ($\pm$S.E.), at the Institute of Oceanology Polish Academy of Sciences (Sopot, Poland) for one week before the experiments. Fish were maintained under a lighting regime and temperature according to conditions mimicking the natural environment. Fish were fed frozen mussels *ad libitum*. All experiments on fish complied with the EC Directive 2010/63/EU for animal experiments and with the guidelines (Resolution No 19/2012) of the Local Ethics Committee on Animal Experimentation. At the time of

sampling, the fish were anaesthetized in bicarbonate-buffered MS-222 water solution (50 mg L^{-1}) (Sigma-Aldrich) and blood samples were collected by cardiac puncture. Blood samples were centrifuged at 3 000 *g* for 10 min and stored at −70°C prior to E_2 analysis. After transection of the spinal cord, their gonads and livers were collected, examined morphologically and then the ovaries underwent histological analysis. GSI was calculated as gonad weight/body weight × 100. HSI was calculated as liver weight/body weight × 100. The maturity stage of the ovary was determined according to the scale described by Tomczak and Sapota (2006). The diameter of fresh oocytes was measured for each ovary under a stereomicroscope (MSZ800/100T; mikroLAB) connected to a digital colour camera (HDCE-X3; mikroLAB) using ScopeImage 9.0 imaging software (Novel Optics). For histological analysis, ovaries were fixed in 4% buffered formalin, dehydrated, embedded in paraffin, cross-sectioned at 6 μm slices and stained using the standard haematoxylin and eosin protocol. Slides were examined with a light microscope (Leica DM500; Leica Microsystems GmbH) connected to a digital colour camera (Leica ICC50 HD; Leica Microsystems GmbH). The developmental stage of ovaries was determined according to the terminology proposed by Brown-Peterson et al. (2011). E_2 levels were determined using a Spectria Estradiol radioimmunoassay kit (Orion Diagnostica) according to the method described previously by Kalamarz-Kubiak et al. (2017). The radioactivity in each tube was measured for 1 min using a gamma counter (Wallac Wizard 1470; PerkinElmer Life Science). The detection limit of the assay was 38 pmol L^{-1}. The intra-assay coefficient of variation was 6.5%. The interassay variation was not determined because all samples were measured in the same assay. Statistical analysis was performed using STATISTICA 7.1 software (StatSoft). A one-way ANOVA followed by Spjotvoll and Stoline's *post hoc* test for unequal numbers of cases was used to compare the three indices (E_2, GSI and HSI) among different stages of oocyte maturation. $P < 0.05$ was considered significant. The results of the statistical analysis are presented in Fig. 1.

In this study, the following stages of oocyte final maturation and ovulation in *N. melanostomus* were identified using histological analysis: 1 – germinal vesicle migration (GVM); 2 – late germinal vesicle migration; early hydration (late GVM; early HO); 3 – germinal vesicle breakdown; middle hydration (GVBD; middle HO); 4 – final hydration (final HO); 5 – ovulation; post-ovulatory follicles (OV; POFs) (Fig. 2). It is apparent that as in other fish species, the oocyte maturation in *N. melanostomus* begins with GVM to the animal pole. During the GVM stage in this species, the nucleus (germinal vesicle; GV) is situated between the centre of the oocyte and half-way to the animal pole and oil droplets fuse into single oil globules while yolk globules begin to fuse to each other at the vegetal pole of the oocyte (ST-1) (Fig. 2). In *N. melanostomus* in the present study, oocyte hydration is observed precisely during late GVM, when oil vesicles are coalescing and yolk granules fuse into plates (ST-2) (Fig. 2). It has been shown that hydration in different fish species, including batch spawners, may occur during different stages of final oocyte maturation but is most pronounced between the start of final maturation and GVBD (Fabra et al., 2006; Skoblina, 2010). During the GVBD stage in *N. melanostomus*, the nucleus is disintegrated, hydration is continued and yolk is fused into a homogeneous mass but the cytoplasm and the cortical alveoli are restricted to a thin peripheral layer (ST-3) (Fig. 2). The final hydration in this species is characterized by fully clear ovoplasm and whole fusion and coalescence of the yolk mass that becomes homogeneous and fluid (ST-4) (Fig. 2), as has often been noted in the literature (for reviews: Fabra et al., 2006; Kjesbu et al., 1996; Lubzens et al., 2017). According to Brown-Peterson et al. (2011), the ovulation stage is characterized by the presence of POFs, not hydrated oocytes (ST-5) (Fig. 2).

It should be mentioned here that not only histology is suitable for determining the reproductive maturity of round goby and stage of gonadal development but also the macroscopic analysis of gonadal morphology is a common and sufficient method for the general differentiation of gonadal maturity stages (Ferreri et al., 2016; Tomczak and Sapota, 2006; Tomkiewicz et al., 2003).

It has been indicated that hydration of oocytes during maturation occurs in a less pronounced way in fish that produce demersal eggs or not floating ones, like *N. melanostomus* than

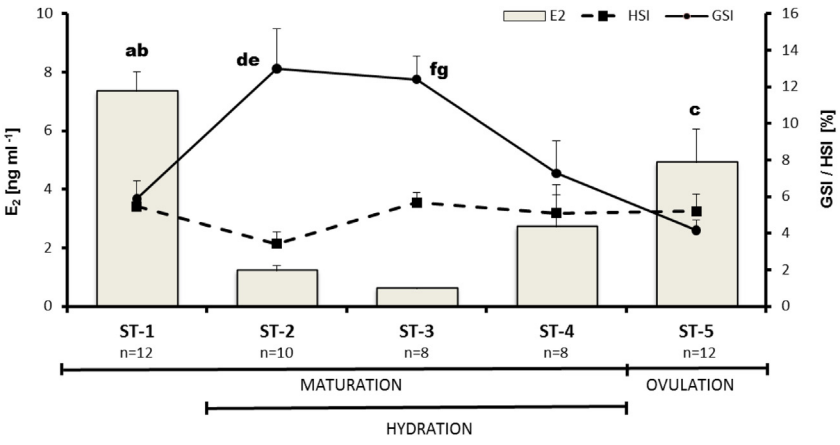

Figure 1 Plasma E_2 concentration and values of GSI and HSI during different stages of final maturation and ovulation in *Neogobius melanostomus*. n – number of individuals. Lowercase letters above bars and lines indicate significantly different values. E_2: **a**, $P < 0.001$ *vs* ST-2 and ST-3; **b**, $P < 0.05$ *vs* ST-4; **c**, $P < 0.05$ *vs* ST-2 and ST-3. I_G: **d**, **f**, $P < 0.001$ *vs* ST-1 and ST-5; **e**, **g**, $P < 0.01$ *vs* ST-4.

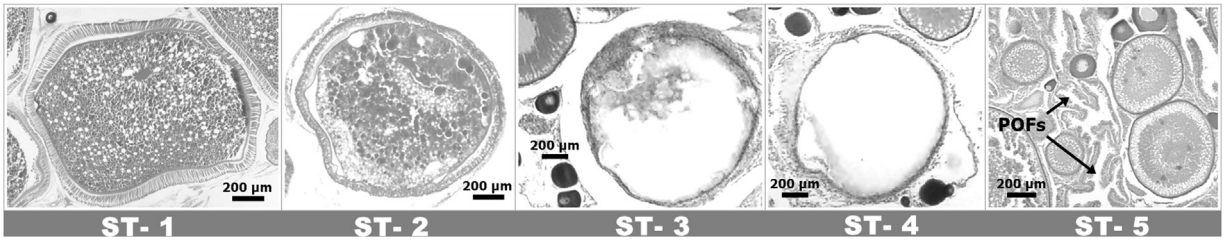

Figure 2 Transverse sections of *Neogobius melanostomus* ovaries illustrating stages of final oocyte maturation and ovulation: ST-1 — germinal vesicle migration (GVM); ST-2 — late germinal vesicle migration; early hydration (late GVM; early HO); ST-3 — germinal vesicle breakdown; middle hydration (GVBD; middle HO); ST-4 — final hydration (final HO); ST-5 — ovulation; post-ovulatory follicles (OV; POFs).

in species that have pelagic or floating eggs. The changes in the oocyte volume range from slight (1.0- to 3.0-fold) in most freshwater and euryhaline fish to several folds in marine species (3.1- to 8.4-fold) (Cerdà et al., 2007; Lubzens et al., 2017). In the present study, the diameter of not transparent oocytes, which presented GVM, was 2.324 $\pm$ 0.02 mm ($\pm$S.E.). The diameter of oocytes exhibiting hydration was 2.452 $\pm$ 0.02 mm ($\pm$S.E.) for semi-transparent oocytes and 2.987 $\pm$ 0.03 mm ($\pm$S.E.) for transparent oocytes. So, the 1.2-fold changes in the volume of oocytes undergoing hydration in *N. melanostomus* are in the ranges of euryhaline, benthophil fish.

In batch spawners, the circulating level of E_2 may fluctuate according to the oocyte batch recruitment cycle. However, if the time of spawning intervals is relatively short, E_2 may remain at a relatively high level throughout the whole spawning season (Mandich et al., 2004; Methven et al., 1992). In the present study, fluctuations in *N. melanostomus*' plasma E_2 levels were observed in the intervals between batches of oocyte development that may indicate that one batch of oocytes starts to develop further well before the previous one has been released from the ovary. What is more, in *N. melanostomus*, a considerable statistically significant decline in E_2 level was noticed in the late GVM stage(ST-2; $P < 0.001$) and GVBD stage (ST-3; $P < 0.001$) followed by a renewed statistically significant increase of this hormone until oocyte ovulation (ST-5; $P < 0.05$) (Fig. 1). Similar fluctuations in plasma E_2 levels during the maturation process have been found in other batch spawners such as Atlantic halibut (*Hippoglossus hippoglossus*), Atlantic cod (*Gadus morhua*), Striped trumpeter (*Latris lineata*) and Eurasian perch (*Perca fluviatilis*) (Hutchinson, 1995; Kjesbu et al., 1996; Methven et al., 1992; Migaud et al., 2003).

In batch spawners, the recruitment of vitellogenic follicles and intense hepatocyte activity seems to be a continuous process during the whole spawning season, as was found in northern anchovy (*Engraulis mordax*), sand soles (*Solea lascaris* and *Solea impar*), snubnose darter (*Etheostoma rafinesquei*) and Atlantic croaker (*Micropogonias undulatus*) (Barbieri et al., 1994; Deniel et al., 1989; Hunter and Macewicz, 1985; Weddle and Burr, 1991). Therefore, the HSI value remains relatively stable during the main spawning season (Nunes et al., 2011). So, it was not surprising that in *N. melanostomus* in the present study, HSI values did not show significant differences throughout the final maturation and ovulation stages (Fig. 1).

Until recently, a widely used method for determining the reproductive status in *N. melanostomus* was to calculate the GSI value and regard any females with GSI greater than 8% to be mature and those less than 8% to be immature (Young et al., 2010). Indeed, if GSI reaches the maximum value together with significant gonad growth during the spawning season, it may be a useful indicator for division into reproductive stages (Kagawa, 2013). On the other hand, it should be noticed that GSI may be an inaccurate indicator of gonadal development because it assumes isometry between gonad mass and somatic mass and also consistency between total gonad mass and gonad developmental stage (DeVlaming et al., 1982). In addition, it has been demonstrated that spawning-capable *N. melanostomus* females may possess GSI values below 8% (~4—5%), thus the commonly used 8% cut-off may result in an incorrect classification of the reproductive stage (Zeyl et al., 2014). In this study, GSI values were below 8% in stages 1 (early GVM), 4 (final HO) and 5 (OV) while histological analysis indicated that all females were spawning-capable (Fig. 1). In multiple-spawning fish, GSI seems to be a less reliable estimator of fish maturity, which does not provide an accurate estimation of ovarian maturity or differentiation between females in a spawning-capable stage and those in a post-spawning stage (Zeyl et al., 2014).

In conclusion, this is the first histological report demonstrating that hydration does accompany oocyte final maturation in *N. melanostomus*. Moreover, it was shown that E_2 fluctuated according to the development of oocyte batches in this species. HSI did not show significant differences throughout the examined stages. However, GSI appeared to be an inaccurate estimator of oocyte maturation in *N. melanostomus*. The cognition of biology of invasive fish species such as round goby, their reproductive strategies and adaptation processes to environmental factors are important components of the protection and preservation of native living resources in the Gulf of Gdańsk. Therefore, further studies will be required to elucidate the possible mechanism of hydration in *N. melanostomus*.

Acknowledgements

This study was supported by the National Science Centre (Narodowe Centrum Nauki) [2012/05/B/NZ9/01024 to H. Kalamarz-Kubiak]. Special thanks go to K. Demska-Zakęś (University of Warmia and Mazury in Olsztyn, Poland) for providing helpful advice in histological analysis.

References

Barbieri, L.R., Chittenden Jr., M.E., Lowerre-Barbieri, S.K., 1994. Maturity, spawning, and ovarian cycle of Atlantic croaker, *Micropogonias undulatus*, in the Chesapeake Bay and adjacent coastal waters. Fish. Bull. 92 (4), 671—685, https://spo.nmfs.noaa.gov/sites/default/files/pdf-content/1994/924/barbieri.pdf, (accessed: 15 April 2019).

Behrens, J.W., van Deurs, M., Christensen, E.A.F., 2017. Evaluating dispersal potential of an invasive fish by the use of aerobic scope and osmoregulation capacity. PLoS One 12 (4), e0176038, http://dx.doi.org/10.1371/journal.pone.0176038.

Björklund, M., Almqvist, G., 2010. Rapid spatial genetic differentiation in an invasive species, the round goby *Neogobius melanostomus* in the Baltic Sea. Biol. Invasions 12 (8), 2609—2618, http://dx.doi.org/10.1007/s10530-009-9669-z.

Brown-Peterson, N.J., Wyanski, D.M., Saborido-Rey, F., Macewicz, B. J., Lowerre-Barbieri, S.K., 2011. A standardized terminology for describing reproductive development in fishes. Mar. Coast. Fish. Dynam. Manag. Ecosys. Sci. 3, 52—70, http://dx.doi.org/10.1080/19425120.2011.555724.

Cerdà, J., Fabra, M., Raldúa, D., 2007. Physiological and molecular basis of fish oocyte hydration. In: Babin, P.J., Cerdà, J., Lubzens, E. (Eds.), The Fish Oocyte: From Basic Studies to Biotechnological Applications. Springer, Dordrecht, 349—396, http://dx.doi.org/10.1007/978-1-4020-6235-3_12.

Crossman, E.J., Holm, E., Cholmondeley, R., Tunninga, K., 1992. First record for Canada of the rudd, *Scardinius erythrophthalmus*, and notes on the introduced round goby, *Neogobius melanostomus*. Can. Field-Nat. 106 (2), 206—209, https://www.biodiversitylibrary.org/item/106990#page/5/mode/1up.

Deniel, C., Le Blanc, C., Rodriguez, A., 1989. Comparative study of sexual cycles, oogenesis and spawning of two Soleidae, *Solea lascaris* (Risso, 1810) and *Solea impar* (Bennet, 1831), on the western coast of Brittany. J. Fish Biol. 35 (1), 49—58, http://dx.doi.org/10.1111/j.1095-8649.1989.tb03392.x.

DeVlaming, V., Grossman, G., Chapman, F., 1982. On the use of the gonadosomatic index. Comp. Biochem. Physiol. A 73 (1), 31—39, http://dx.doi.org/10.1016/0300-9629(82)90088-3.

Dinh, Q.M., 2018. Aspects of reproductive biology of the red goby *Trypauchen vagina* (Gobiidae) from the Mekong Delta. J. Appl. Ichthyol. 34 (1), 103—110, http://dx.doi.org/10.1111/jai.13521.

Fabra, M., Raldúa, D., Bozzo, M.G., Deen, P.M., Lubzens, E., Cerdà, J., 2006. Yolk proteolysis and aquaporin-1o play essential roles to regulate fish oocyte hydration during meiosis resumption. Dev. Biol. 295 (1), 250—262, http://dx.doi.org/10.1016/j.ydbio.2006.03.034.

Ferreri, R., Ganias, K., Genovese, S., Fontana, I., Giacalone, G., Bonanno, A., Mazzola, S., Aronica, S., Mangano, S., Basilone, G., 2016. Oocyte batch development and enumeration in the European anchovy (*Engraulis encrasicolus*). Medit. Mar. Sci. 17 (3), 670—677, http://dx.doi.org/10.12681/mms.1693.

Finn, R.N., Kolarevic, J., Kristoffersen, B.A., 2008. Heterogeneous expression of vitellogenin genes in marine teleosts: how maturational proteolysis of derivative yolk proteins determines the size and nature of the egg. Comp. Biochem. Physiol. Part A 151 (1), S44—S47, http://dx.doi.org/10.1016/j.cbpa.2008.05.131.

Hunter, J.R., Macewicz, B., 1985. Rates of atresia in the ovary of captive and wild northern anchovy, *Engraulis mordax*. Fish. Bull. 83 (2), 119—136, https://spo.nmfs.noaa.gov/sites/default/files/pdf-content/1985/832/hunter.pdf.

Hutchinson, W.G., 1995. The reproductive biology and induced spawning of striped trumpeter, *Latris lineata*. Coursework Master Thesis, Univ. Tasmania https://eprints.utas.edu.au/20347/, (accessed: 17 October 2017).

Jażdżewski, K.A., Konopacka, A., 2002. Invasive Ponto-Caspian species in waters of the Vistula and Oder basins and of the southern Baltic Sea. In: Leppäkoski, E., Gollasch, S., Olenin, S. (Eds.), Invasive Aquatic Species of Europe. Kluwer Acad. Publ., Dordrecht, Boston, London, 384—398, http://dx.doi.org/10.1007/978-94-015-9956-6_39.

Kagawa, H., 2013. Oogenesis in teleost fish. Aqua-BioScience Monographs 6 (4), 99—127, http://dx.doi.org/10.5047/absm.2013.00604.0099.

Kalamarz-Kubiak, H., Gozdowska, M., Guellard, T., Kulczykowska, E., 2017. How does oestradiol influence the AVT/IT system in female round gobies during different reproductive phases? Biol. Open 6 (10), 1493—1501, http://dx.doi.org/10.1242/bio.024844.

Kjesbu, O.S., Kryvi, H., Norberg, B., 1996. Oocyte size and structure in relation to blood plasma steroid hormones in individually monitored, spawning Atlantic cod. J. Fish Biol. 49 (6), 1197—1215, http://dx.doi.org/10.1111/j.1095-8649.1996.tb01789.x.

Kornis, M.S., Mercado-Silva, N., Vander Zanden, M.J., 2012. Twenty years of invasion: a review of round goby *Neogobius melanostomus* biology, spread and ecological implications. J. Fish Biol. 80 (2), 235—285, http://dx.doi.org/10.1111/j.1095-8649.2011.03157.x.

Kültz, D., 2015. Physiological mechanisms used by fish to cope with salinity stress. J. Exp. Biol. 218 (12), 1907—1914, http://dx.doi.org/10.1242/jeb.118695.

Lubzens, E., Bobe, J., Young, G., Sullivan, C.V., 2017. Maternal investment in fish oocytes and eggs: the molecular cargo and its contributions to fertility and early development. Aquaculture 472, 107—143, http://dx.doi.org/10.1016/j.aquaculture.2016.10.029.

Lubzens, E., Young, G., Bobe, J., Cerdà, J., 2010. Oogenesis in teleosts: how fish eggs are formed. Gen. Comp. Endocrinol. 165 (3), 367—389, http://dx.doi.org/10.1016/j.ygcen.2009.05.022.

Mandich, A., Massari, R.A., Bottero, E.S., Pizzicori, P., Goos, E.H., Marino, E.G., 2004. Plasma sex steroid and vitellogenin profiles during gonad development in wild Mediterranean amberjack (*Seriola dumerilii*). Mar. Biol. 144 (1), 127—138, http://dx.doi.org/10.1007/s00227-003-1185-6.

McEvoy, L.A., McEvoy, J., 1992. Multiple spawning in several commercial fish species and its consequences for fisheries management, cultivation and experimentation. J. Fish Biol. 41 (sB), 125—136, http://dx.doi.org/10.1111/j.1095-8649.1992.tb03874.x.

Methven, D.A., Crim, L.W., Norberg, B., Brown, J.A., Goff, G.P., Huse, I., 1992. Seasonal reproduction and plasma levels of sex steroids and vitellogenin in Atlantic halibut (*Hippoglossus hippoglossus*). Can. J. Fish. Aquat. Sci. 49 (4), 754—759, http://dx.doi.org/10.1139/f92-084.

Meunier, B., Yavno, S., Ahmed, S., Corkum, L.D., 2009. First documentation of spawning and nest guarding in the laboratory by the invasive fish, the round goby (*Neogobius melanostomus*). J. Great Lakes Res. 35, 608—612, http://dx.doi.org/10.1016/j.jglr.2009.08.012.

Migaud, H., Robert Mandiki, R., Gardeur, J.-N., Fostier, A., Kestemont, P., Fontaine, P., 2003. Synthesis of sex steroids in final oocyte maturation and induced ovulation in female Eurasian perch, *Perca fluviatilis*. Aquat. Living Res. 16 (4), 380—388, http://dx.doi.org/10.1016/S0990-7440(03)00079-2.

Milla, S., Jalabert, B., Rime, H., Prunet, P., Bobe, J., 2006. Hydration of rainbow trout oocyte during meiotic maturation and in vitro regulation by 17,20 β-dihydroxy-4-pregnen-3-one and cortisol. J. Exp. Biol. 209 (6), 1147—1156, http://dx.doi.org/10.1242/jeb.02094.

Nunes, C., Silva, A., Soares, E., Ganias, K., 2011. The use of hepatic and somatic indices and histological information to characterize the reproductive dynamics of Atlantic Sardine *Sardina pilchardus* from the Portuguese Coast. Mar. Coastal Fish. 3 (1), 127—144, http://dx.doi.org/10.1080/19425120.2011.556911.

Ojaveer, H., Galil, B.S., Lehtiniemi, M., Christoffersen, M., Clink, S., Florin, A.-B., Gruszka, P., Puntila, R., Behrens, J.W., 2015.

Twenty five years of invasion: management of the round goby *Neogobius melanostomus* in the Baltic Sea. Manag. Biol. Invasions 6 (4), 329—339, http://dx.doi.org/10.3391/mbi.2015.6.4.02.

Puntila, R., Strake, S., Florin, A.-B., Naddafi, R., Lehtiniemi, M., Behrens, J.W., Kotta, J., Oesterwind, D., Putnis, I., Smolinski, M.S., Wozniczka, A., Ojaveer, H., Ložys, L., Uspenskiy, A., Yurtseva, A., 2018. Abundance and distribution of round goby (*Neogobius melanostomus*). In: HELCOM Baltic Sea Environment Fact Sheets. http://www.helcom.fi/baltic-sea-trends/environment-fact-sheets/biodiversity/abundance-and-distribution-of-round-goby/, (accessed 15 April 2019).

Sapota, M.R., 2012. NOBANIS — Invasive Alien Species Fact Sheet — *Neogobius melanostomus*. Online Database of the European Network on Invasive Alien Species — NOBANIS, https://www.nobanis.org/globalassets/speciesinfo/n/neogobius-melanostomus/neogobius_melanostomus.pdf, (accessed 27 November 2006).

Skoblina, M.N., 2010. Hydration of oocytes in teleost fishes. Russ. J. Dev. Biol. 41 (1), 1—12, http://dx.doi.org/10.1134/S1062360410010017.

Skóra, K.E., Stolarski, J., 1993. New fish species in the Gulf of Gdansk, *Neogobius* sp [cf. *Neogobius melanostomus* (Pallas 1811)]. Bull. Sea Fish. Inst. 1 (128), 83—84.

Sztobryn, M., Kałas, M., Staskiewicz, A., 1997. Changes of mean sea level and ice conditions in Gdynia as indicators of climate changes in the Gulf of Gdańsk. In: Özsoy, E., Mikaelyan, A. (Eds.), Sensitivity to Change: Black Sea, Baltic Sea and North Sea. NATO ASI Series 2: Environment, vol. 27. Springer, Dordrecht, http://dx.doi.org/10.1007/978-94-011-5758-2_1.

Tomczak, M.T., Sapota, M.R., 2006. The fecundity and gonad development cycle of the round goby (*Neogobius melanostomus* Pallas 1811) from the Gulf of Gdańsk. Oceanol. Hydrobiol. Stud. 35 (4), 353—367, https://www.researchgate.net/publication/230777722, (accessed 15 April 2019).

Tomkiewicz, J., Tybjerg, L., Jespersen, Å., 2003. Micro- and macroscopic characteristics to stage gonadal maturation of female Baltic cod. J. Fish Biol. 62 (2), 253—275, http://dx.doi.org/10.1046/j.1095-8649.2003.00001.x.

Weddle, G.K., Burr, B.M., 1991. Fecundity and dynamics of multiple spawning in darters: an in-stream study of *Etheostoma rafnesquei*. Copeia 419—433, http://dx.doi.org/10.2307/1446591.

Wiegleb, J., Kotterba, P., Hammer, C., Oesterwind, D., 2019. Predation of the round goby (*Neogobius melanostomus* Pallas, 1814) on Atlantic herring eggs in the Western Baltic Sea. Mar. Biol. Res. 14 (9—10), 989—1003, http://dx.doi.org/10.1080/17451000.2019.1577977.

Wright, P.A., Fyhn, J.H., 2001. Ontogeny of nitrogen metabolism and excretion. In: Wright, P.A., Anderson, P. (Eds.), Fish Physiology: Nitrogen Excretion, vol. 20. Acad. Press, San Diego, pp. 149—200. https://www.sciencedirect.com/bookseries/fish-physiology/vol/20.

Young, J.A.M., Marentette, J.R., Gross, C., McDonald, J.I., Verma, A., Marsh-Rollo, S.E., Macdonald, P.D.M., Earn, D.J.D., Balshine, S., 2010. Demography and substrate affinity of the round goby (*Neogobius melanostomus*) in Hamilton Harbour. J. Great Lakes Res. 36 (1), 115—122, http://dx.doi.org/10.1016/j.jglr.2009.11.001.

Zeyl, J.N., Love, O.P., Higgs, D.M., 2014. Evaluating gonadosomatic index as an estimator of reproductive condition in the invasive round goby, *Neogobius melanostomus*. J. Great Lakes Res. 40 (1), 164—171, http://dx.doi.org/10.1016/j.jglr.2013.12.004.